



HELLENIC REPUBLIC  
**National and Kapodistrian  
University of Athens**  
—————EST. 1837—————

SCHOOL OF SCIENCE  
DEPARTMENT OF CHEMISTRY

DOCTORAL THESIS

**Photocatalytic and electrocatalytic hydrogen production with  
dithiolene complexes**

ATHANASIOS ZARKADOULAS  
CHEMIST, MSc

ATHENS

2018





HELLENIC REPUBLIC  
**National and Kapodistrian  
University of Athens**  
—————EST. 1837—————

SCHOOL OF SCIENCE  
DEPARTMENT OF CHEMISTRY

DOCTORAL THESIS

**Photocatalytic and electrocatalytic hydrogen production with  
dithiolene complexes**

ATHANASIOS ZARKADOULAS  
CHEMIST, MSc

ATHENS

2018



# **DOCTORAL THESIS**

Photocatalytic and electrocatalytic hydrogen production with dithiolene complexes

**ATHANASIOS ZARKADOULAS**

**A.M.: 001229**

## **SUPERVISOR:**

C. A. Mitsopoulou, Professor, Department of Chemistry, University of Athens

## **THREE-MEMBER ADVISORY COMMITTEE**

C. A. Mitsopoulou, Professor, Department of Chemistry, University of Athens

I. Papaefstathiou, Associate Professor, Department of Chemistry, University of Athens

P. Paraskevopoulou, Assistant Professor, Department of Chemistry, University of Athens

## **SEVEN-MEMBER EXAMINATION COMMITTEE**

C. A. Mitsopoulou, Professor, Department of Chemistry, University of Athens

I. Papaefstathiou, Associate Professor, Department of Chemistry, University of Athens

P. Paraskevopoulou, Assistant Professor, Department of Chemistry, University of Athens

S. Koinis, Associate Associate Professor, Department of Chemistry, University of Athens

K. Methenitis, Associate Professor, Department of Chemistry, University of Athens

A. Chrissanthopoulos, Assistant Professor, Department of Chemistry, University of Athens

K. Bethanis, Assistant Professor, Department of Biotechnology, Agricultural University of Athens

EXAMINATION DATE 9/2/2018



## **ΔΙΔΑΚΤΟΡΙΚΗ ΔΙΑΤΡΙΒΗ**

Φωτοκαταλυτική και ηλεκτροκαταλυτική παραγωγή υδρογόνου με διθειολενικά σύμπλοκα

**ΑΘΑΝΑΣΙΟΣ ΖΑΡΚΑΔΟΥΛΑΣ**

**A.M.: 001229**

### **ΕΠΙΒΛΕΠΩΝ:**

X. Μητσοπούλου, Καθηγήτρια ΕΚΠΑ

### **ΤΡΙΜΕΛΗΣ ΣΥΜΒΟΥΛΕΥΤΙΚΗ ΕΠΙΤΡΟΠΗ**

X. Μητσοπούλου, Καθηγήτρια, Τμήμα Χημείας ΕΚΠΑ

I. Παπαευσταθίου, Αναπληρωτής Καθηγητής, Τμήμα Χημείας ΕΚΠΑ

Π. Παρασκευοπούλου, Επίκουρη Καθηγήτρια, Τμήμα Χημείας ΕΚΠΑ

### **ΕΠΤΑΜΕΛΗΣ ΕΞΕΤΑΣΤΙΚΗ ΕΠΙΤΡΟΠΗ**

X. Μητσοπούλου, Καθηγήτρια, Τμήμα Χημείας ΕΚΠΑ

I. Παπαευσταθίου, Αναπληρωτής Καθηγητής, Τμήμα Χημείας ΕΚΠΑ

Π. Παρασκευοπούλου, Επίκουρη Καθηγήτρια, Τμήμα Χημείας ΕΚΠΑ

Σ. Κοΐνης, Αναπληρωτής Καθηγητής, Τμήμα Χημείας ΕΚΠΑ

Κ. Μεθενίτης, Αναπληρωτής Καθηγητής, Τμήμα Χημείας ΕΚΠΑ

Α. Χρυσανθόπουλος, Επίκουρος Καθηγητής, Τμήμα Χημείας ΕΚΠΑ

Κ. Μπεθάνης, Επίκουρος Καθηγητής, Τμήμα Βιοτεχνολογίας, Γεωπονικό Πανεπιστήμιο  
Αθηνών

**ΗΜΕΡΟΜΗΝΙΑ ΕΞΕΤΑΣΗΣ 9/2/2018**



## ABSTRACT

The present thesis has been undertaken in the Laboratory of Inorganic Chemistry of National and Kapodistrian University of Athens. It covers literature reports on the application of dithiolene complexes as catalysts in electrocatalytic hydrogen evolution, and some bio-inspired supramolecular systems for homogeneous photocatalytic hydrogen evolution. Experimentally, the preparation, characterization, and investigation of series of nickel bis-dithiolene complexes is reported. These compounds have similar structural and electronic properties that can be tuned in order to establish structure – activity relationship. During this thesis, the first series of complexes is of the type  $[\text{Ni}(\text{S}_2\text{C}_2\text{-}p\text{-C}_6\text{H}_5\text{-R})(\text{S}_2\text{C}_2\text{-}p\text{-C}_6\text{H}_5\text{-R}')] ]$ , where  $\text{R} = \text{R}' = \text{H}$ ,  $\text{R} = \text{OMe}$  and  $\text{R}' = \text{H}$ ,  $\text{R} = \text{R}' = \text{OMe}$ . Crystal structures for compounds with  $\text{R} = \text{OMe}$  and  $\text{R}' = \text{H}$ , and monoanionic  $\text{R} = \text{R}' = \text{OMe}$ . The second series of complexes consists of the monoanionic compounds  $(\text{NBu}_4)[\text{Ni}(\text{bdt})_2]$ ,  $(\text{NBu}_4)[\text{Ni}(\text{tdt})_2]$ , and  $(\text{NBu}_4)[\text{Ni}(\text{mnt})_2]$ , where bdt, tdt, and mnt denote benzene-1,2-dithiolate, toluene-3,4-dithiolate, and maleonitriledithiolate, respectively. The heteroleptic complex  $(\text{NBu}_4)[\text{Ni}(\text{S}_2\text{C}_2\text{Ph}_2)(\text{mnt})]$  has been prepared and its crystal structure has been determined, along with three neutral alkyl-bridged bis-dithiolene compounds  $[\text{Ni}(\text{bdt})_2\text{C}_3]$ ,  $[\text{Ni}(\text{S}_2\text{C}_2\text{Ph}_2)_2\text{C}_3]$ , and  $[\text{Ni}(\text{S}_2\text{C}_2\text{-}p\text{-C}_6\text{H}_4\text{OMe})_2\text{C}_3]$ , where  $\text{C}_3$  denotes a  $-\text{CH}_2\text{CH}_2\text{CH}_2-$  bridge. All complexes have been characterized with spectroscopic and physicochemical methods, namely absorption spectroscopy, IR spectroscopy,  $^1\text{H-NMR}$  spectroscopy, and cyclic voltammetry. The complexes have been employed as proton reducing catalysts in organic media (DMF or MeCN) with organic acids (TFA etc) as the proton source.

**SUBJECT AREA:** homogeneous photocatalysis, electrocatalysis

**KEYWORDS:** photocatalysis, electrocatalysis, dithiolene, nickel, hydrogen



## ΠΕΡΙΛΗΨΗ

### ΦΩΤΟΚΑΤΑΛΥΤΙΚΗ ΚΑΙ ΗΛΕΚΤΡΟΚΑΤΑΛΥΤΙΚΗ ΠΑΡΑΓΩΓΗ ΥΔΡΟΓΟΝΟΥ ΜΕ ΔΙΘΕΙΟΛΕΝΙΚΑ ΣΥΜΠΛΟΚΑ

Η παρούσα διδακτορική διατριβή εκπονήθηκε στο Εργαστήριο Ανόργανης του Εθνικού και Καποδιστριακού Πανεπιστημίου Αθηνών. Περιέχει βιβλιογραφική αναφορά στην εφαρμογή των διθειολενικών συμπλόκων ως καταλύτες στην ηλεκτροκαταλυτική παραγωγή υδρογόνου και μερικά βιομιμητικά υπερμοριακά συστήματα ομογενούς φωτοκαταλυτικής παραγωγής υδρογόνου. Στο πειραματικό μέρος, αναφέρεται η σύνθεση, ο χαρακτηρισμός και η μελέτη διθειολενικών συμπλόκων του νικελίου. Αυτές οι ενώσεις έχουν παραπλήσιες δομικές και ηλεκτρονικές ιδιότητες που μπορούν να ρυθμιστούν ώστε να παρατηρηθούν συσχετισμοί δομής – δραστηριότητας. Η πρώτη σειρά συμπλόκων είναι του τύπου  $[\text{Ni}(\text{S}_2\text{C}_2\text{-}p\text{-C}_6\text{H}_5\text{-R})(\text{S}_2\text{C}_2\text{-}p\text{-C}_6\text{H}_5\text{-R}')] ]$ , όπου  $\text{R} = \text{R}' = \text{H}$ ,  $\text{R} = \text{OMe}$  και  $\text{R}' = \text{H}$ ,  $\text{R} = \text{R}' = \text{OMe}$ . Απομονώθηκαν και επιλύθηκαν οι κρυσταλλικές δομές για τις ενώσεις με  $\text{R} = \text{OMe}$  και  $\text{R}' = \text{H}$  και το μονοανιοντικό σύμπλοκο με τις ομάδες  $\text{R} = \text{R}' = \text{OMe}$ . Η δεύτερη σειρά συμπλόκων περιέχει τα μονοανιοντικά σύμπλοκα  $(\text{NBu}_4)[\text{Ni}(\text{bdt})_2]$ ,  $(\text{NBu}_4)[\text{Ni}(\text{tdt})_2]$  και  $(\text{NBu}_4)[\text{Ni}(\text{mnt})_2]$ , όπου bdt, tdt, and mnt είναι 1,2-βενζοδιθειολάτο, τολουολο-3,4-διθειολάτο, και μαλεονιτριλο-διθειολάτο, αντίστοιχα. Το ετεροληπτικό σύμπλοκο  $(\text{NBu}_4)[\text{Ni}(\text{S}_2\text{C}_2\text{Ph}_2)(\text{mnt})]$  παρασκευάστηκε και η κρυσταλλική του δομή επιλύθηκε, όπως επίσης και τα τρία αλκυλιωμένα και γεφυρωμένα σύμπλοκα  $[\text{Ni}(\text{bdt})_2\text{C}_3]$ ,  $[\text{Ni}(\text{S}_2\text{C}_2\text{Ph}_2)_2\text{C}_3]$  και  $[\text{Ni}(\text{S}_2\text{C}_2\text{-}p\text{-C}_6\text{H}_4\text{OMe})_2\text{C}_3]$ , όπου  $\text{C}_3$  είναι γέφυρα της μορφής  $-\text{CH}_2\text{CH}_2\text{CH}_2-$ . Όλα τα σύμπλοκα χαρακτηρίστηκαν με φασματοσκοπικές και φυσικοχημικές μεθόδους, όπως η φασματοσκοπία απορρόφησης, η φασματοσκοπία υπερύθρου, η φασματοσκοπία μαγνητικού πυρηνικού συντονισμού και η κυκλική βολταμετρία. Τα αναφερθέντα σύμπλοκα εφαρμόστηκαν ως καταλύτες αναγωγής πρωτονίων σε οργανικούς διαλύτες (*N,N'*-διμεθυλοφορμαμίδιο και ακετονιτρίλιο) με οργανικά οξέα (τριφθοροξικό οξύ κ.ά.).

**ΘΕΜΑΤΙΚΗ ΠΕΡΙΟΧΗ:** ομογενής φωτοκατάλυση, ηλεκτροκατάλυση

**ΛΕΞΕΙΣ ΚΛΕΙΔΙΑ:** φωτοκατάλυση, ηλεκτροκατάλυση, διθειολένια, νικέλιο, υδρογόνο

*Dedicated to my parents, Nikos and Maria*

## CONTENTS

<b>PREFACE.....</b>	<b>1</b>
<b>1. CHAPTER 1 INTRODUCTION.....</b>	<b>2</b>
1.1 Hydrogen as a fuel.....	2
1.2 Light-induced hydrogen generation.....	3
<b>2. CHAPTER 2 DITHIOLENE COMPLEXES.....</b>	<b>7</b>
2.1 The MS <sub>4</sub> core.....	7
2.2 Why metal dithiolene complexes as hydrogen evolution catalysts?.....	7
2.3 Synthetic routes to bis-dithiolene complexes.....	8
2.3.1 Symmetrical (homoleptic) bis-dithiolene complexes.....	8
2.3.2 Unsymmetrical (heteroleptic) bis-dithiolene complexes.....	10
2.4 Chemical reactivity of dithiolene complexes.....	12
<b>3. CHAPTER 3 PHOTOCATALYTIC HYDROGEN PRODUCTION.....</b>	<b>14</b>
3.1 Definition of photocatalysis.....	14
3.2 Homogeneous and heterogeneous photocatalysis.....	14
3.3 Mechanisms for hydrogen evolution in homogeneous photocatalytic systems.....	14
3.4 Components of a homogeneous photocatalytic system.....	15
3.4.1 Photosensitizer.....	15
3.4.2 Catalyst.....	16
3.4.3 Sacrificial electron donor.....	17
3.4.4 Solvent.....	18
3.4.5 Effectiveness of a photocatalytic system.....	18
<b>3.5 Homogeneous hydrogen evolving photocatalytic systems from the literature.....</b>	<b>19</b>
3.5.1 Systems employing dithiolene complexes as catalysts.....	19
3.5.2 Supramolecular systems with porphyrins as photosensitizers.....	30
<b>4. CHAPTER 4 ELECTROCATALYTIC HYDROGEN PRODUCTION.....</b>	<b>36</b>
4.1 Definition of electrocatalysis – Homogeneous electrocatalysis.....	36
4.2 Heterogeneous electrocatalysis.....	37
4.3 Components of a homogeneous electrocatalytic system.....	37
4.3.1 Catalyst.....	37
4.3.2 Proton source and solvent.....	38
4.4 Overpotential ( $\eta$ ).....	39
4.5 Faradaic yield.....	40
4.6 Hydrogen evolving electrocatalytic systems from the literature.....	40
4.6.1 Dithiolene complexes as catalysts.....	40
4.6.2 On the stability of dithiolene complexes as electrocatalysts.....	50

<b>5. CHAPTER 5 MATERIALS AND METHODS.....</b>	<b>53</b>
5.1 Starting materials – reagents – solvents .....	53
5.2 Instrumentation.....	53
5.3 X–ray crystal structure determination .....	54
5.4 Density Functional Theory (DFT) calculations.....	55
<b>6. PREPARATION OF COMPOUNDS .....</b>	<b>57</b>
6.1 Preparation of homoleptic dithiolene complexes .....	57
6.1.1 Preparation and characterization of ligands .....	57
6.1.2 Preparation and characterization of complexes .....	57
6.2 Preparation of heteroleptic dithiolene complexes .....	70
6.3 Preparation of bridged dithiolene complexes .....	75
6.4 Preparation of other complexes .....	89
<b>7. CHAPTER 7 APPLICATIONS OF COMPLEXES.....</b>	<b>90</b>
7.1 Electrocatalytic hydrogen production with homoleptic dithiolene complexes .....	90
7.1.1 Catalysts 1, 2, and 3 .....	90
7.1.2 Catalysts 4, 5, and 6 .....	97
7.1.3 Theoretical calculations and discussion.....	108
7.2 Electrocatalytic hydrogen production with heteroleptic dithiolene complex 7.....	125
7.3 Electrocatalytic hydrogen production with bridged dithiolene complexes .....	126
7.4 Photocatalytic hydrogen production.....	128
7.4.1 Discussion .....	130
<b>8. CONCLUSIONS .....</b>	<b>134</b>
<b>9. ABBREVIATIONS – INITIALS – ACRONYMS .....</b>	<b>137</b>
<b>10. APPENDIX.....</b>	<b>139</b>
<b>11. REFERENCES.....</b>	<b>157</b>

## LIST OF FIGURES

Figure 1. Spectrum of solar radiation on Earth [3].	3
Figure 2. Crystal structure of oxygen-evolving photosystem II at a resolution of 1.9 Å [7].	5
Figure 3. Z-scheme of photosynthesis [5].	5
Figure 4. Oxidation states and nomenclature for a dithiolene ligand.	7
Figure 5. Aromatic and ene-dithiolate complexes.	8
Figure 6. UV-Vis spectrum of [Ni(dpdt) <sub>2</sub> ] (a), [Ni(dpdt)(pddt)] (b), [Ni(pddt) <sub>2</sub> ] (c).	12
Figure 7. Oxidation products of diimine dithiolene complexes of Ni, Pd, Pt.	13
Figure 8. Trinuclear complexes mimicking the active site of NiFe hydrogenases.	13
Figure 9. Typical photosensitizers used in homogeneous photocatalytic hydrogen production.	15
Figure 10. Catalysts used in recent works towards photocatalytic hydrogen evolution.	17
Figure 11. Typical sacrificial electron donors.	18
Figure 12. [Ni(S <sub>2</sub> C <sub>2</sub> Ph <sub>2</sub> ) <sub>2</sub> ] catalyst.	19
Figure 13. bis(2-chlorodithiobenzil)nickel(II) catalyst.	20
Figure 14. tris[1-(4-methoxyphenyl)-2-phenyl-1,2-ethylenedithiolenic-S,S]tungsten (VI).	21
Figure 15. monoanion of tris{1-(2-chlorophenyl)-2-phenyl-1,2-dithiolenic-S,S}tungsten(VI).	22
Figure 16. Cobalt dithiolene catalysts studied by Eisenberg and Holland groups.	22
Figure 17. Catalysts studied by Eckenhoff et al. for the reduction of aqueous protons.	24
Figure 18. [Ni(bdt) <sub>2</sub> ] <sup>-</sup> .	25
Figure 19. Iron dithiolene catalysts studied by Lv et al.	26
Figure 20. Dihydrolopic acid (DHLA).	27
Figure 21. Cobalt and nickel binaphthalene dithiolene complex.	27
Figure 22. (a) Changes in H <sub>2</sub> evolution with irradiation time before and after adding extra eosin Y to the photocatalytic system containing cobalt catalyst, (b) Change in the absorption spectra with irradiation for the photocatalytic system containing cobalt catalyst (0.1 mM), eosin Y (0.4 mM), 10% TEA at pH 10.0 in CH <sub>3</sub> CN/H <sub>2</sub> O (1 : 1, v/v). Figure from ref. [79].	28

Figure 23. Tungsten tris–dithiolene hydrogen evolution catalyst.....	29
Figure 24. Proposed hydrogen evolving mechanism with tungsten tris–dithiolene complexes as catalysts.....	30
Figure 25. Complexes prepared by Li et al.....	30
Figure 26. Multinuclear complexes prepared by Song et al. ....	31
Figure 27. Dyads and triads prepared by Poddutoori et al.....	31
Figure 28. Supramolecular hydrogen evolving system studied by Kluwer et al. ....	32
Figure 29. Binuclear porphyrin complexes prepared by Zhang et al.....	32
Figure 30. Molecular devices prepared by Zhang et al.....	33
Figure 31. Dyads studied by the groups of Pryce and Vos.....	34
Figure 32. Dyads studied by the groups of Guldi and Coutsolelos. ....	34
Figure 33. Dyads studied by Natali et al.....	34
Figure 34. Natali's self–assembled triad for photo–induced hydrogen evolution.....	35
Figure 35. Homogeneous electrochemical catalysis: (a) direct electrochemical reaction, (b) redox catalyzed electrochemical reaction. ....	36
Figure 36. Chemically catalyzed electrochemical reaction. ....	36
Figure 37. Covalent grafting of a catalyst onto an electrode surface.....	37
Figure 38. Methyl–ester substituted bis–dithiolene nickel complex reported by Begum et al.....	40
Figure 39. Pentacoordinate iron bis–dithiolene complex prepared by Begum et al. ....	41
Figure 40. Cobalt dithiolene catalysts studied by Eisenberg and Holland groups.....	42
Figure 41. Molybdenum complexes acting as catalysts in proton reduction.....	43
Figure 42. Electrocatalysis of catalyst 1 with a hanging mercury drop working electrode and glassy carbon auxiliary electrode (0.5 mM complex, CH <sub>3</sub> CN–H <sub>2</sub> O:9–1).....	44
Figure 43. Effect of water on CV of catalyst 1 (0.5 mM).....	44
Figure 44. Cobalt aryl–dithiolene catalysts reported by Letko et al. (X = F, Cl, Br, OMe).....	45
Figure 45. Catalytic response for the fluoro– (left), bromo– (center), methoxy– (right) monoanionic cobalt dithiolene complexes in the presence of anilinium (0.3 mM catalyst, 0 – 25 mM acid (black to magenta traces, respectively).....	45

Figure 46. Complexes prepared by the group of Jones.....	47
Figure 47. Heteroleptic complex prepared by Kochem et al. ....	47
Figure 48. Bio-inspired complex reported by the group of Fontecave. ....	48
Figure 49. Tungsten dithiolene complexes prepared by the group of Fontecave. ....	49
Figure 50. Catalyst prepared by the group of Sakai.....	50
Figure 51. $[\text{Ni}(\text{bdt})_2]^-$ .....	51
Figure 52. (A) Voltammograms of $[\text{Ni}(\text{bdt})_2]^-$ with p-bromo-anilinium in MeCN (GCE), (B) Linear sweep voltammogram of $[\text{Ni}(\text{bdt})_2]^-$ (black trace) and subsequent CV using the same electrode (red trace) after rinsing and transfer to fresh acid solution without added Ni catalyst. ....	51
Figure 53. Voltammograms of p-bromo-anilinium with electrodes conditioned by a 3 min electrodeposition. ....	52
Figure 54. $^1\text{H-NMR}$ spectrum of complex 1 in $\text{CDCl}_3$ ( $\delta$ , ppm), showing the aromatic region where the signals for the 20 protons of the complex appear.....	58
Figure 55. $^1\text{H-NMR}$ spectrum of complex 2 in $\text{CDCl}_3$ . ....	59
Figure 56. $^1\text{H-NMR}$ spectrum of complex 3 in $\text{CDCl}_3$ . ....	59
Figure 57. Stacked IR spectra of neutral complexes 1–3.....	61
Figure 58. Stacked IR spectra for anionic complexes $1^- - 3^-$ .....	61
Figure 59. Normalized absorption spectra for neutral complexes 1–3 and monoanionic complexes $1^-$ , $2^-$ , and $3^-$ as tetrabutylammonium salts in DMF solution. ....	63
Figure 60. ORTEP diagram at 30% probability level for compound 2. ....	64
Figure 61. ORTEP diagram at 30% probability level for compound $3^-$ . $\text{NBu}_4^+$ counter-ion is omitted for clarity. ....	64
Figure 62. Normalized cyclic voltammograms for compounds 1–3 in DMF at a scan rate of $100 \text{ mV s}^{-1}$ with $^n\text{Bu}_4\text{NPF}_6$ in DMF under Ar at room temperature (glassy carbon working electrode). ....	68
Figure 63. Normalized cyclic voltammograms for compounds 4, 5, and 6 in MeCN at a scan rate of $100 \text{ mV s}^{-1}$ with $^n\text{Bu}_4\text{PF}_6$ in MeCN under Ar at room temperature. Glassy carbon working electrode, Ag/AgCl reference electrode, Pt-wire counter electrode.....	69
Figure 64. IR spectrum of heteroleptic complex 7 along with the homoleptic counterparts $1^-$ and 6.....	71

Figure 65. Normalized UV–Vis spectra for heteroleptic complex 7 along with its homoleptic counterparts 6 and 1 <sup>-</sup> .....	72
Figure 66. Proposed bonding scheme for compound 7.....	73
Figure 67. Cyclic voltammogram for complex 7 in DMF using a glassy carbon working electrode, Ag/AgCl reference electrode, NBu <sub>4</sub> PF <sub>6</sub> supporting electrolyte, and a Pt wire counter electrode.....	73
Figure 68. ORTEP diagram at 30% probability level for compound 7. The NBu <sub>4</sub> <sup>+</sup> counterion is omitted for clarity. ....	74
Figure 69. ORTEP diagram at 30% probability level for compound 7. The NBu <sub>4</sub> <sup>+</sup> counterion and hydrogen atoms are omitted for clarity.....	74
Figure 70. Packing diagram of a crystal of compound 7. The NBu <sub>4</sub> <sup>+</sup> counterion and hydrogen atoms are omitted for clarity.....	74
Figure 71. <sup>1</sup> H–NMR spectrum of compound 8 in CD <sub>2</sub> Cl <sub>2</sub> .....	77
Figure 72. <sup>1</sup> H–NMR of compound 9 in CD <sub>2</sub> Cl <sub>2</sub> . ....	78
Figure 73. <sup>1</sup> H–NMR of compound 10 in CD <sub>2</sub> Cl <sub>2</sub> . ....	79
Figure 74. IR spectrum of compound 8. ....	80
Figure 75. Stacked IR spectra for compounds 9 and 10. ....	80
Figure 76. Stacked IR spectra for compounds 3, 3 <sup>-</sup> , and 10.....	81
Figure 77. Absorption spectra of compounds 8–10 in DMF solution. ....	82
Figure 78. Cyclic voltammogram of compound 8 in DMF solution under Ar with a glassy carbon working electrode, a Ag/AgCl reference electrode, and a Pt–wire counter electrode at various scan rates with NBu <sub>4</sub> PF <sub>6</sub> supporting electrolyte.....	82
Figure 79. Cyclic voltammogram of compounds 9 and 10 in DMF solution under Ar with a glassy carbon working electrode, a Ag/AgCl reference electrode, and a Pt–wire counter electrode at a scan rate of 100 mV s <sup>-1</sup> with NBu <sub>4</sub> PF <sub>6</sub> supporting electrolyte. Inset: cyclic voltammograms of same compounds under same conditions at a scan rate of 500 mV s <sup>-1</sup> . ....	83
Figure 80. ORTEP diagram at 50% probability level for compound 8. ....	84
Figure 81. ORTEP diagram at 50% probability level for compound 8. ....	85
Figure 82. ORTEP packing figure for compound 8 at 50% probability level. Hydrogen atoms omitted for clarity. ....	85

Figure 83. Crystal structure of 9, as reported by Zhang et al. [134].	86
Figure 84. ORTEP diagram at 50% probability level for compound 10. Hydrogen atoms omitted for clarity.	86
Figure 85. ORTEP diagram at 50% probability level for compound 10 showing planarity of NiS <sub>4</sub> core. Hydrogen atoms omitted for clarity.	87
Figure 86. ORTEP diagram at 50% probability level for compound 10 (stacking of two molecules in the cell). Hydrogen atoms omitted for clarity.	88
Figure 87. Diagram for compound 9 (stacking of two molecules in the cell). Hydrogen atoms omitted for clarity.	88
Figure 88. Cyclic voltammogram of 1 in the presence of increasing equivalents of TFA: no acid, red; 1 equiv, green; 3 equiv, light blue; 5 equiv, burgundy; 10 equiv, dark blue (glassy carbon working electrode).	90
Figure 89. Cyclic voltammogram of 2 in the presence of increasing equivalents trifluoroacetic acid: no acid, red; 1 eq, green; 3 eq, light blue; 5 eq, burgundy; 10 eq, dark blue. Glassy carbon working electrode, scan rate 100 mVs <sup>-1</sup> with NBu <sub>4</sub> PF <sub>6</sub> in DMF.	91
Figure 90. Cyclic voltammogram of 3 in the presence of increasing equivalents trifluoroacetic acid: no acid, red; 1 eq, green; 3 eq, light blue; 5 eq, burgundy; 10 eq, dark blue. Glassy carbon working electrode, scan rate 100 mVs <sup>-1</sup> with NBu <sub>4</sub> PF <sub>6</sub> in DMF.	91
Figure 91. Cyclic voltammogram of trifluoroacetic acid in DMF in the absence of any catalyst. 0 mM, dark blue; 1 mM, red; 3 mM, green; 5 mM, burgundy; 10 mM, light blue. Glassy carbon working electrode, Ag/AgCl reference electrode, platinum wire counter-electrode, scan rate 100 mV s <sup>-1</sup> with NBu <sub>4</sub> PF <sub>6</sub> in DMF.	92
Figure 92. Evolution of the peak potential of the -1/-2 process of catalysts 1 (blue diamonds), 2 (green squares), and 3 (red circles) with log[TFA].	93
Figure 93. Rinse tests for catalyst 2 in the presence of 1 and 10 equiv of TFA: (solid line) in the presence of catalyst; (dashed line) in the absence of catalyst (glassy carbon working electrode).	95
Figure 94. Linear sweep voltammetry of 1 mM catalysts 1 (blue trace) and 2 (red trace) at a glassy carbon electrode in the presence of 10 mM TFA (scan rate 100 mV s <sup>-1</sup> with NBU4PF <sub>6</sub> in DMF).	96
Figure 95. Rinse tests for catalyst 2 in the presence of 10 equiv of TFA: (gray trace) cyclic voltammogram in the presence of catalyst; (red trace) cyclic voltammogram in the absence of	

catalyst starting from $-1.0\text{ V vs Fc}^{+/0}$ after linear sweep voltammetry; (black trace) cyclic voltammogram in the absence of catalyst starting from $-1.0\text{ V vs Fc}^{+/0}$ after 3 min potential application (glassy carbon working electrode). .....	96
Figure 96. Cyclic voltammograms of catalyst 2 in the presence of 10 mM TFA at various scan rates. Inset: linear dependence of $i_{\text{cat.}}$ vs $v^{1/2}$ ( $R^2 = 0.97$ ; glassy carbon working electrode). .....	97
Figure 97. Cyclic voltammogram of catalyst 4 in the presence and absence of $\text{Et}_3\text{NHBF}_4$ . Glassy carbon working electrode, Ag/AgCl reference electrode, platinum wire counter–electrode, scan rate $100\text{ mV} \cdot \text{s}^{-1}$ with $\text{NBu}_4\text{PF}_6$ in MeCN as supporting electrolyte. ....	98
Figure 98. Cyclic voltammograms of 4 (1 mM) in the presence of increasing equivalents of trifluoroacetic acid. Glassy–carbon working electrode, Ag/AgCl reference electrode, platinum wire–counter electrode, scan rate $100\text{ mVs}^{-1}$ with $\text{NBu}_4\text{PF}_6$ in MeCN as the supporting electrolyte.....	98
Figure 99. Cyclic voltammogram of 5 (1 mM) in the presence of increasing equivalents of TFA. Glassy–carbon working electrode, Ag/AgCl reference electrode, platinum–wire counter–electrode, scan rate $100\text{ mVs}^{-1}$ with $\text{NBu}_4\text{PF}_6$ in MeCN as the supporting electrolyte.....	99
Figure 100. Linear fit diagram of $E_p$ vs $\log[\text{TFA}]$ for catalysts 4 and 5. Blue trace: catalyst 4; red trace: catalyst 5. ....	100
Figure 101. Cyclic voltammogram of 6 (1 mM) in the presence of increasing equivalents of TFA. Glassy carbon working electrode, Ag/AgCl reference electrode, platinum wire counter–electrode, scan rate $100\text{ mVs}^{-1}$ with $\text{NBu}_4\text{PF}_6$ in MeCN as supporting electrolyte. ....	100
Figure 102. Evolution of the UV/Vis spectrum of catalyst 4 (0.1 mM) after the addition of 50 mM TFA. Spectra were recorded in deaerated MeCN at 15 min intervals. The inset shows an enlargement of the shoulder region.....	102
Figure 103. UV–Vis spectrum of catalyst 4 (0.1 mM) in the presence of 50 mM TFA in deaerated MeCN after 30 min. Addition of $\text{NEt}_3$ and measurements in 30 min cycles. ....	103
Figure 104. Cyclic voltammogram of catalyst 4 in the presence of 10 mM TFA at various scan rates. Inset: linear dependence of $i_{\text{cat.}}$ on $v^{1/2}$ ( $R^2=0.98$ , glassy–carbon working electrode).....	103
Figure 105. Cyclic voltammogram of catalyst 5 in the presence of 10 mM TFA at various scan rates. Inset: linear dependence of $i_{\text{cat.}}$ on $v^{1/2}$ ( $R^2=0.92$ , glassy carbon working electrode).....	104
Figure 106. Rinse tests for catalyst 4 (glassy–carbon working electrode). Cyclic voltammogram for catalyst 4 in the absence (gray dotted trace) and presence (black trace) of 10 mM TFA in MeCN. Each trace indicates a scan of a rinsed working electrode in a fresh solution of 10 mM	

TFA in MeCN. Red trace: after the measurement of a cyclic voltammogram; green trace: after a linear-sweep voltammogram; blue trace: after a potential of -1.3 V applied for 3 min. ....	104
Figure 107. Cyclic voltammogram for 10 mM 4-Br-anilinium tetrafluoroborate in the absence (dark blue trace) and presence (red trace) of catalyst 4 in MeCN. Green trace indicates scan of a rinsed working electrode in a fresh solution of 10 mM tetrafluoroborate in MeCN (rinse test).	106
Figure 108. Absorption spectrum of [Co(bdt) <sub>2</sub> ](NBu <sub>4</sub> ) (0.2 mM) in the absence (red trace) and presence of tosic acid (65 mM) as a function of time, under Ar, in a 1 – 1 mixture of MeCN – water.....	107
Figure 109. Cuvettes before (left) and after (right) recording the absorbance of a [Co(bdt) <sub>2</sub> ](NBu <sub>4</sub> ) sample, under the same conditions shown previously. ....	107
Figure 110. Calculated structures for intermediates in the proposed hydrogen evolution mechanism for 1.....	113
Figure 111. DFT-calculated structure for intermediate [1(NiH)] <sup>2-</sup> . S – Ni – S dihedral angle is calculated 75.04°.....	114
Figure 112. Atom numbering scheme for catalyst 5.....	118
Figure 113. Calculated structure for intermediate [5(Ni-H)] <sup>2-</sup> . ....	120
Figure 114. Calculated reaction pathway for the hydrogen-evolving step of the mechanism shown in Scheme 31 with catalyst 5. TS denotes transition state and the numbers in parentheses indicate the calculated energy values (kJ mol <sup>-1</sup> ) and the values of the Ni hinge angle (degrees). Significant bond lengths are indicated with arrows.....	121
Figure 115. Cyclic voltammogram of 7 in the presence of increasing equivalents of TFA: no acid, blue; 1 equiv, red; 3 equiv, green; 5 equiv, brown; 10 equiv, light blue; blank, dotted trace; CV after the end of the titration, dashed trace (glassy carbon working electrode).....	125
Figure 116. Cyclic voltammogram of 8 in the presence of increasing equivalents of TFA: no acid, blue; 5 equiv, red; 10 equiv, green; blank, dotted trace (glassy carbon working electrode). .....	126
Figure 117. Cyclic voltammogram of 9 in the presence of increasing equivalents of TFA: no acid, blue; 5 equiv, red; 10 equiv, green; blank, dotted trace (glassy carbon working electrode). .....	127
Figure 118. Cyclic voltammogram of 10 in the presence of increasing equivalents of TFA: no acid, blue; 5 equiv, red; 10 equiv, green; blank, dotted trace (glassy carbon working electrode). .....	128

Figure 119. TON as a function of catalyst concentration with fixed ZnTPP ( $1.0 \times 10^{-4}$ M) and TEA (0.01 M) concentrations. ....	129
Figure 120. UV–Vis spectrum of an Ar–dearated mixture containing 5.0 $\mu$ M catalyst $1^-$ , $10^{-4}$ M ZnTPP, 0.01 M TEA, in DMF – water : 8 – 2 solvent mixture before (blue trace) and after (red trace) irradiation for 20 h with a 1000 W Xe lamp ( $\lambda > 330$ nm). ....	130
Figure 121. Titration of a DMF – water : 8 – 2 solution of catalyst $1^-$ (10.0 $\mu$ M) with aliquots of ZnTPP in the same solvent mixture. ....	131
Figure 122. Titration of a $\text{CH}_2\text{Cl}_2$ solution of catalyst $1^-$ (10.0 $\mu$ M) with aliquots of ZnTPP in the same solvent. ....	131
Figure 123. Emission quenching of ZnTPP (1.0 $\mu$ M) with increasing amounts of nickel catalyst $1^-$ in DMF – water : 8 – 2 solvent mixture. ....	132
Figure 124. Emission quenching of ZnTPP (1.0 $\mu$ M) with increasing amounts of nickel catalyst $1^-$ in $\text{CH}_2\text{Cl}_2$ solvent. ....	132
Figure 125. Stern – Volmer plots for quenching of emission of ZnTPP in $\text{CH}_2\text{Cl}_2$ (blue circles) and in DMF – $\text{H}_2\text{O}$ : 8 – 2 (red diamonds). Inset: linear fit of emission quenching data. ....	133

## LIST OF SCHEMES

Scheme 1. Preparation of homoleptic aromatic bis-1,2-dithiolene complexes. ....	8
Scheme 2. Preparation of ene-1,2-dithiolate complexes. ....	9
Scheme 3. Synthesis of bis-dithiolene complexes with alkylated phosphorus intermediates. ....	10
Scheme 4. Scrambling reaction for the preparation of heteroleptic bis-dithiolene complex. ....	11
Scheme 5. Double substitution reaction for the preparation of heteroleptic bis-dithiolene complex. ....	11
Scheme 6. Oxidation-reduction scrambling reaction for the preparation of mixed ligand bis-dithiolene complexes. ....	11
Scheme 7. Crossed-ligand synthesis of heteroleptic bis-dithiolene complexes. ....	11
Scheme 8. Bis-heteroleptic complex prepared by Anyfantis et al. ....	12
Scheme 9. Template reactions of complexed dithiolene ligands. ....	13
Scheme 10. Oxidative (a) and reductive (b) pathways towards hydrogen evolution. ....	14
Scheme 11. Proposed mechanism for the cleavage of $[W(S_2C_2Ph, C_6H_4-p-OCH_3)_3]$ by $Cu^{2+}$ ions. ....	21
Scheme 12. Hydrogen evolution mechanism with molybdenum dithiolene catalyst. ....	24
Scheme 13. Proposed hydrogen evolving mechanism by Rao et al. [79]. ....	28
Scheme 14. Proposed hydrogen evolution mechanism for the electrocatalytic proton reduction by an iron bis-dithiolene complex. ....	42
Scheme 15. Proposed mechanism for hydrogen evolution mechanism by cobalt aryldithiolene complexes derived by theoretical and electrochemical data (bonds in Å, angles in °). ....	46
Scheme 16. Proton migration from sulfur to cobalt atom (bonds in Å, angles in °). ....	46
Scheme 17. Proposed mechanism for hydrogen evolution with molybdenum dithiolene complexes. ....	49
Scheme 18. Preparation of benzoin. ....	57
Scheme 19. Preparation of neutral bis-aryl-dithiolene nickel complexes. ....	57
Scheme 20. Preparation of anionic complexes bearing 4-methoxy- and un-substituted benzoin. ....	60
Scheme 21. Limiting (A and B) and delocalized (C) structures for a nickel dithiolene complex. ....	66

Scheme 22. Preparation of anionic complexes 4 and 5 bearing methyl- and unsubstituted benzene rings. ....	68
Scheme 23. Preparation of nickel complex 6 with maleonitrile-dithiolate ligands. ....	69
Scheme 24. Preparation of mixed-ligand complex 7. ....	70
Scheme 25. Preparation of compound 8. ....	75
Scheme 26. Preparation of compound 8 (alternate route). ....	76
Scheme 27. Preparation of compounds 9 and 10. ....	76
Scheme 28. Synthetic scheme for the preparation of tetraphenylporphyrin (TPPH <sub>2</sub> ) and subsequent metalation with zinc (ZnTPP). ....	89
Scheme 29. Proposed mechanism for hydrogen evolution with catalyst 1 together with calculated protonation enthalpies and redox potentials (experimentally determined electrochemical potentials are also indicated. Potentials are reported vs Fc <sup>+0</sup> ). ....	110
Scheme 30. Proposed mechanism for hydrogen evolution with catalyst 2 together with calculated protonation enthalpies and redox potentials for cis- and trans- configurations of catalyst 2. Experimentally determined electrochemical potentials are also indicated. Potentials are reported vs Fc <sup>+0</sup> . ....	115
Scheme 31. Proposed hydrogen evolution mechanism for catalysts 4 and 5, along with protonation enthalpies and reduction potentials. Potentials are reported vs. Fc <sup>+0</sup> . ....	116
Scheme 32. Calculated structures of the intermediates in the proposed hydrogen evolution mechanism of compound 5. ....	118
Scheme 33. Proposed hydrogen evolution mechanism for catalyst 6, along with protonation enthalpies and reduction potentials. Potentials are reported vs. Fc <sup>+0</sup> . ....	122

## LIST OF TABLES

Table 1. Higher heating values of common fuels at 25 °C and 1 atm [1].....	2
Table 2. Performance of cobalt dithiolene catalysts .....	23
Table 3. Performance of molybdenum dithiolene catalysts.....	25
Table 4. Commonly used acids and their ionization constants (pK <sub>a</sub> ) in various solvents at 25 °C <sup>a</sup> . .....	38
Table 5. <sup>1</sup> H–NMR data for complex 2 in CDCl <sub>3</sub> .....	59
Table 6. <sup>1</sup> H–NMR data for complex 3 in CDCl <sub>3</sub> .....	60
Table 7. IR data for neutral (1, 2, 3) and anionic complexes (1 <sup>-</sup> , 2 <sup>-</sup> , 3 <sup>-</sup> ) (values in cm <sup>-1</sup> ). .....	62
Table 8. UV–Vis spectroscopic data for complexes 1–3 and their anionic forms.....	64
Table 9. Selected bond lengths (in Å) for complexes 1, 2, 3, 3 <sup>-</sup> .....	65
Table 10. Reduction potentials for complexes 1 – 3.....	68
Table 11. Cyclic voltammetry data for complexes 4–6 in MeCN .....	69
Table 12. IR data values for heteroleptic complex 7, in comparison to homoleptic counterparts 1 <sup>-</sup> and 6.....	71
Table 13. UV–Vis data for complex 7 along with the respective homoleptic complexes.....	72
Table 14. Selected bond distances (Å) and angles (°) for complex 7. ....	75
Table 15. <sup>1</sup> H–NMR data for compound 8 in CD <sub>2</sub> Cl <sub>2</sub> .....	78
Table 16. <sup>1</sup> H–NMR data for compound 10 in CD <sub>2</sub> Cl <sub>2</sub> .....	78
Table 17. <sup>1</sup> H–NMR data for compound 10 in CD <sub>2</sub> Cl <sub>2</sub> .....	79
Table 18. IR data for compound 8. ....	79
Table 19. UV–Vis data for compounds 8, 9, and 10.....	81
Table 20. Electrochemistry data for compounds 8 – 10 .....	84
Table 21. Selected bond lengths (in Å) and bond angles (in °) for compound 8 at 100(2) K with estimated standard deviations in parentheses. ....	85
Table 22. Selected bond lengths (in Å) and bond angles (in °) for compound 10 at 100(2) K with estimated standard deviations in parentheses. ....	87

Table 23. Bulk electrolysis results for complexes 1, 2 and 3 in DMF in the presence of 50 mM trifluoroacetic acid. ....	94
Table 24. Bulk electrolysis results for complexes 4, 5, and 6 in MeCN in the presence of 50 mM trifluoroacetic acid. ....	101
Table 25. Selected structural parameters calculated for intermediates of the hydrogen evolution mechanism for catalyst 1. ....	108
Table 26. Selected structural parameters calculated for intermediates in the hydrogen evolution mechanism of catalyst 5 with values for 4 for comparison. ....	119
Table 27. Calculated structural parameters for intermediate $[5(\text{Ni-H})]^{2-}$ (bond lengths in Å). .	120
Table 28. Hydrogen evolution results for system with ZnTPP (chromophore), $1^-$ (catalyst), TEA (sacrificial electron donor) in DMF – water : 8 – 2 solvent mixture. ....	129
Table 29. Bond lengths [Å] for 2 at 100(2) K with estimated standard deviations in parentheses. ....	139
Table 30. Bond angles [°] for 2 at 100(2) K with estimated standard deviations in parentheses. ....	140
Table 31. Bond lengths [Å] for $3^-$ at 100(2) K with estimated standard deviations in parentheses. ....	142
Table 32. Bond angles [°] for $3^-$ at 100(2) K with estimated standard deviations in parentheses. ....	145
Table 33. Bond lengths (Å) for 7 at 100(2) K with estimated standard deviations in parentheses. ....	151
Table 34. Bond angles (°) for 7 at 100(2) K with estimated standard deviations in parentheses. ....	153
Table 35. Bond lengths (in Å) for compound 8 at 100(2) K with estimated standard deviations in parentheses. ....	154
Table 36. Bond angles (in °) for compound 8 at 100(2) K with estimated standard deviations in parentheses. ....	155
Table 37. Torsion angles (in °) for compound 8 at 100(2) K with estimated standard deviations in parentheses. ....	156

## PREFACE

The present doctoral thesis was undertaken in the Laboratory of Inorganic Chemistry, Department of Chemistry, National and Kapodistrian University of Athens, under the supervision of Prof. of Inorganic Chemistry Christiana Mitsopoulou.

I would like to thank my supervisor Prof. Christiana Mitsopoulou for assigning the topic of this thesis, as well as for her continuing guidance during my undergraduate and graduate studies, giving me the chance to develop as a scientist by expanding the boundaries of my chemical knowledge and critical thinking.

Additionally, I would like to thank Assoc. Prof. Giannis S. Papaefstathiou and Assist. Prof. Patrina Paraskevopoulou for their support and their scientific guidance during this thesis.

I would also like to thank Dr. Vincent Artero for his guidance in electrocatalysis during my stay at his laboratory at LCBM – CEA Grenoble (September – October 2013), as well as Jennifer Fize at the same laboratory for her assistance in experimental setup.

I am indebted to Dr. Martin Field (DYNAMOP, Institut de Biologie Structurale, UMR CNRS, Université Grenoble Alpes) for performing theoretical calculations on catalytic systems, Dr. C. Papatriantafyllopoulou (University of Cyprus, now at NUI Galway), Dr. C. Raptopoulou and Dr. V. Psycharis (NCSR Demokritos), and Assist. Prof. K. Bethanis (Agricultural University of Athens) for determining the crystal structures of the compounds presented in this thesis.

I am also thankful to the Laboratory of Inorganic Chemistry and members of the examination committee, as well as all colleagues and friends from the Laboratory of Inorganic Chemistry for their collaboration and friendship all these years.

Last but not least, I would like to thank all my friends and colleagues from our laboratory, Dr. Eugenia Koutsouri, Dr. Christina Kefalidi, Giorgos Ioannidis, Sofia Balou, Fotis Kamatsos, Eftichia Lioli, Maria Koukouvitaki, Gina Konisti, Maria Drosou, Arsianna Stavradi, as well as Dr. Nikolitsa Lezi and Dr. Stella Kritikou for their continuous support and making life at the lab a lot more bearable.

Finally, I thank my parents Nikos and Maria, and my sisters Vassia, Eva, and Nikol for their full support during the years of my studies at the Department of Chemistry.

# CHAPTER 1

## INTRODUCTION

### 1.1 Hydrogen as a fuel

Increasing CO<sub>2</sub> emissions from human activity on Earth since the Industrial Revolution have led to overall increase in the temperature on the surface of the planet due to greenhouse effect. More specifically, atmospheric CO<sub>2</sub> has increased from ~310 ppm to ~380 ppm during the last five decades (1960–2010) [1]. Theoretical models indicate that after 550 ppm CO<sub>2</sub> concentration, a global warming comparable in size to Ice Age, but in an opposite way.

Hydrogen was first isolated by Henry Cavendish in 1766 and identified as a constituent of water by Antoine Lavoisier in 1783. As early as the 1800s, water splitting by electrolysis has been employed as a way to produce both hydrogen and oxygen.

Hydrogen, being the simplest and lighter atom in the universe, is found with other atoms such as H, N, C, etc. H<sub>2</sub> molecule, when combined with oxidants such as O<sub>2</sub> can sustain combustion, leading thus to its use as a fuel. H<sub>2</sub> also has a mean bond enthalpy of 238 kJ/mol [2] and a higher heating value, ie the maximum amount of energy the fuel can release in the presence of an oxidant, than other widely-used fuels. Thus, hydrogen poses as a promising high-energy value fuel with no environmentally harmful combustion products ( $\text{H}_2 + \frac{1}{2} \text{O}_2 \rightarrow \text{H}_2\text{O}$ ).

**Table 1. Higher heating values of common fuels at 25 °C and 1 atm [1]**

<b>Fuel</b>	<b>Heating value (kJ/g)</b>
hydrogen	141.9
methane	55.5
gasoline	47.5
diesel	44.8
methanol	20.0

## 1.2 Light-induced hydrogen generation

Solar energy is considered inexhaustible contrary to fossil fuels, with more energy in solar light falling on Earth's surface in 1 h ( $1.2 \times 10^5$  TW) than all energy used by mankind in 1 year [1]. Consequently, harnessing all this free and virtually endless energy coming from the sun to sustain chemical transformation is of great scientific interest, both in terms of sustainability and financial reasons.

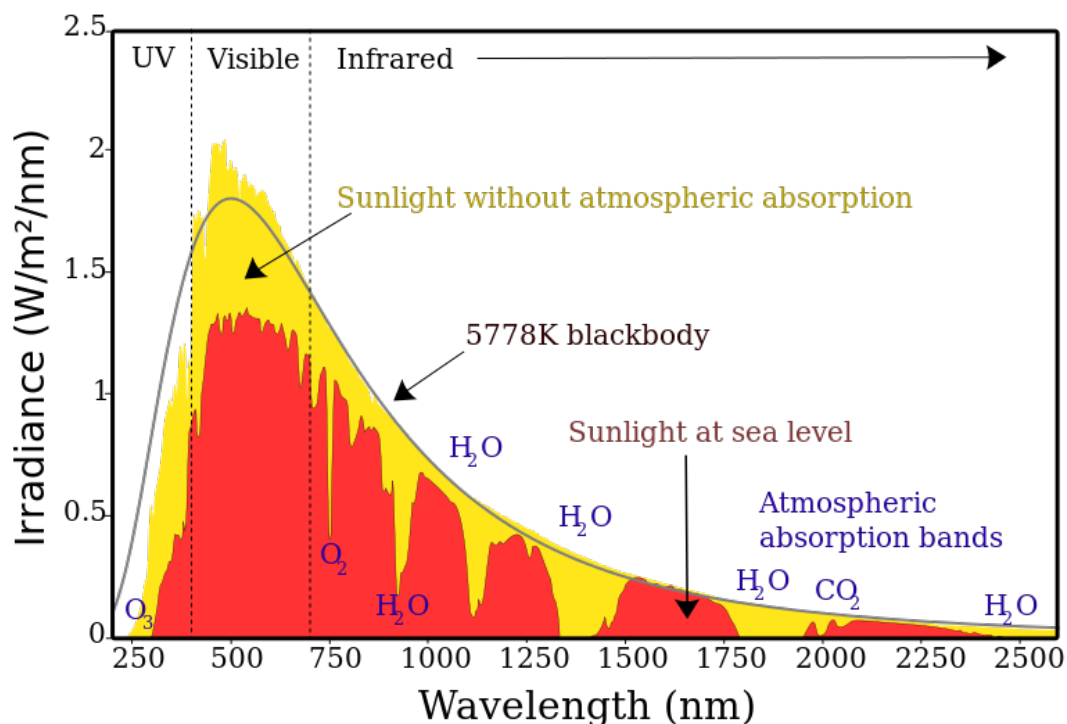
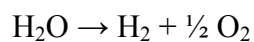


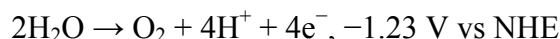
Figure 1. Spectrum of solar radiation on Earth [3].

So, chemists had to mimic the photosynthetic procedure. When taking into consideration photosynthesis, the overall reaction occurring is the following:

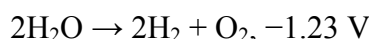


This reaction is both highly endothermic ( $\Delta H = 285.9$  kJ/mol) and endergonic ( $\Delta G = 237.2$  kJ/mol), for a total of two electrons transferred. Since the reaction is not spontaneous ( $\Delta G > 0$ ), it can be driven either photochemically or electrochemically.

If we examine more closely the water splitting reaction through the oxidation and reduction half-reactions of water\* [2]:



we can derive the overall water-splitting reaction:



This potential value corresponds to 1.23 eV of energy per electron transfer, for a total of four electrons. When converted to wavelength, photons with  $\lambda < 1008 \text{ nm}$  belonging in the near infrared area of the spectrum could be suitable for the realization of the water splitting reaction. However, this value corresponds to standard conditions and does not take into account that in such a multi-electron process reaction losses occur and the individual reactions often have high overpotentials. Consequently, photons of higher energy are required, and more specifically those belonging in the visible and ultra-violet area of the spectrum.

In the photosynthetic scheme, water is split during the light period of photosynthesis in chloroplasts and bacteria, leading to oxygen evolution [5,6]:



and plastoquinone (PQ) reduction to plastoquinol (PQH<sub>2</sub>):



In PSII, a photon is absorbed by chlorofyll  $\alpha$  P680, starting a series of electron-transfer reactions. Excited P680 transfers an electron in a pheophytin and a charge separated state is achieved by electron transfer to a quinone Q<sub>A</sub>. Another plastoquinone is protonated and reduced to plastoquinol and released. Oxidized P680 (P680<sup>+</sup>) is reduced by a tyrosine, which in turn is reduced by the oxidation of water in

---

\* These half-reactions can be written in several ways depending on the pH. In basic solution [4]:

the reduction half-reaction of water:  $2\text{H}_2\text{O} + 2\text{e}^- \rightarrow \text{H}_2 + 2\text{OH}^-, -0.83 \text{ V vs NHE}$

and the oxidation half-reaction of water:  $4\text{OH}^- \rightarrow \text{O}_2 + 4\text{e}^- + 2\text{H}_2\text{O}, -0.40 \text{ V vs NHE}$

Eventually the  $\Delta E$  value for the overall water splitting is  $-1.23 \text{ V}$ .

the oxygen evolving center (OEC). Thus, a trans-membrane pH-gradient is formed which promotes ATP synthesis.

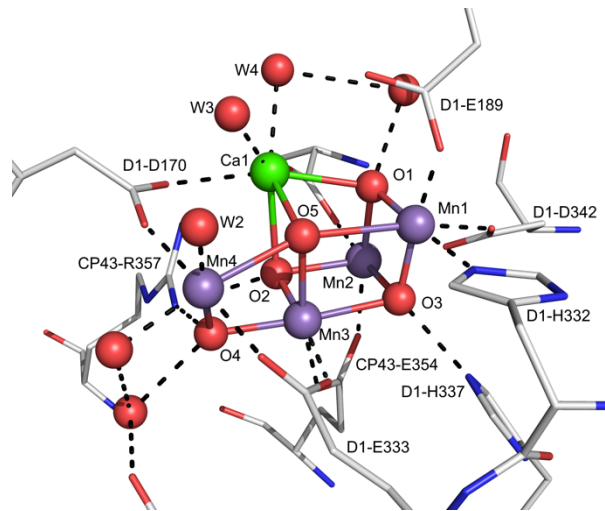


Figure 2. Crystal structure of oxygen-evolving photosystem II at a resolution of 1.9 Å [7].

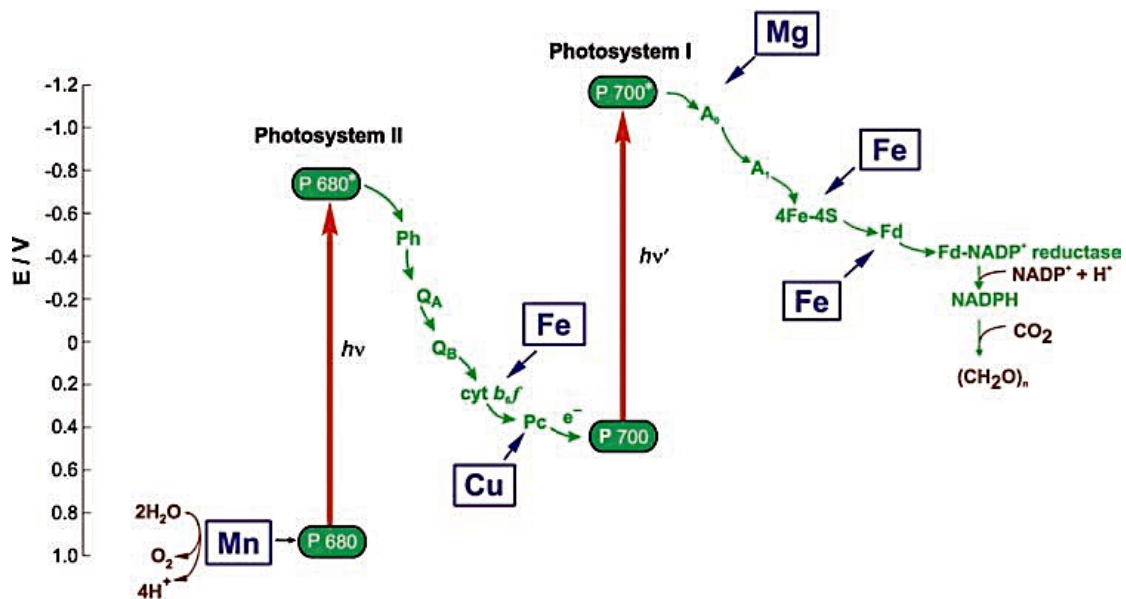


Figure 3. Z-scheme of photosynthesis [5].

In a final step, in the center of PSI where two chlorophylls absorb at 700 nm (P700) create an electron-transfer chain through a Mg-containing chlorophyll ( $A_0$ ) and a quinone ( $A_1$ ) to a 4Fe – 4S cluster. In the next step, ferredoxin (2Fe – 2S cluster, Fd) transfers electrons to  $\text{NADP}^+$  and NADPH is formed, while P700 is regenerated by capturing an electron from reduced plastocyanin.

Thus, artificial photosynthesis and solar hydrogen generation aim to copy the series of electron-transfer reactions observed in photosynthesis. If a solar cell is prepared where overall solar splitting is achieved, the four electrons produced by water oxidation in one part can be used to reduce water in the other part, producing dihydrogen which can then be used as a fuel with water as a combustion product.

## CHAPTER 2

### DITHIOLENE COMPLEXES

#### 2.1 The MS<sub>4</sub> core

The noninnocent nature of the dithiolene ligand framework [8] allows construction of multifunctional complexes because the reversible redox reactions that metal dithiolene complexes undergo can be localized on the metal, leading to reduced metal oxidation states, or on the ligand, depending on the orbital contribution of each fragment [9]. Owing to the unique electronic properties of dithiolene ligands, the electron density of metal–dithiolene complexes is delocalized over the metal–sulfur core, which allows electron storage and the access to several stable anionic oxidation states. The redox noninnocent character of dithiolene ligands is mainly based on their ability to reversibly take up or release electrons, yielding enedithiolate and dithioketone forms with distinct electronic structures and chemical properties, respectively.

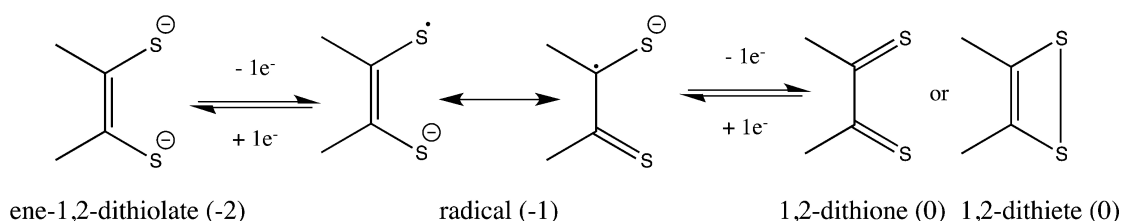


**Figure 4. Oxidation states and nomenclature for a dithiolene ligand.**

Which one of these oxidation states is adopted depends on the substituents on the SCCS moiety of the dithiolene ligand and the nature of the metal. The term 1,2–dithiolene is a general term that describes the ligand framework and its use does not refer to a specific oxidation state on the metal or ligand. The oxidation state and charge localization in metal dithiolene complexes have been the focus of extensive theoretical work [9,10], which has provided insight regarding the chemical reactivity of dithiolene complexes [11] in various applications, including hydrogen evolution in the reductive side of water splitting [12–20].

#### 2.2 Why metal dithiolene complexes as hydrogen evolution catalysts?

i. their synthesis is relatively easy with reactions reaching good to high yields apart from the organic synthesis employed to synthesize the ligands [21,22]

ii. they are coloured and possess extended delocalized systems, whereas they have several different stable oxidation states

iii. the HOMO–LUMO gap, the energy of the MLCT band in the visible region as well as the oxidation and reduction potentials of the complexes can be effectively tuned by altering the substituents of the aromatic rings of the ligands or the metal [23]

iv. the chemical reactivity of either the metal or the sulfur atoms has already been studied both experimentally [24,25] and theoretically [11,26–30].

### 2.3 Synthetic routes to bis–dithiolenes complexes

The preparation of dithiolenes ligands and dithiolenes complexes displays a great deal of synthetic interest [21,23,31,32]. Although numerous starting reagents and synthetic pathways exist, our focus in this work will be on simple aromatic dithiolenes and ene–dithiolate complexes.

#### 2.3.1 Symmetrical (homoleptic) bis–dithiolenes complexes

Symmetrical bis–1,2–dithiolenes complexes can be divided in two great categories:

- the aromatic dithiolenes complexes
- the ene–dithiolate complexes

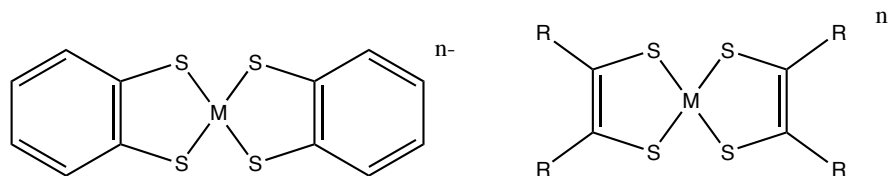
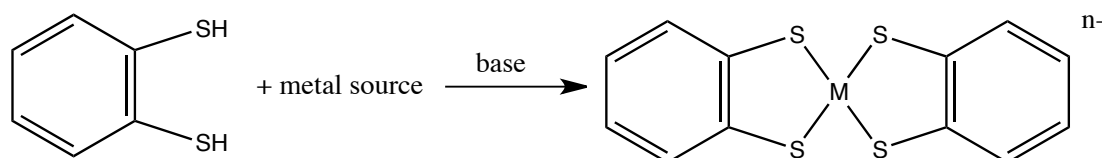


Figure 5. Aromatic and ene–dithiolate complexes.

Aromatic bis dithiolenes complexes are usually prepared by the reaction of the dithiolate salt generated in situ by the reaction of the corresponding dithiol with the appropriate metal source in the presence of a base:

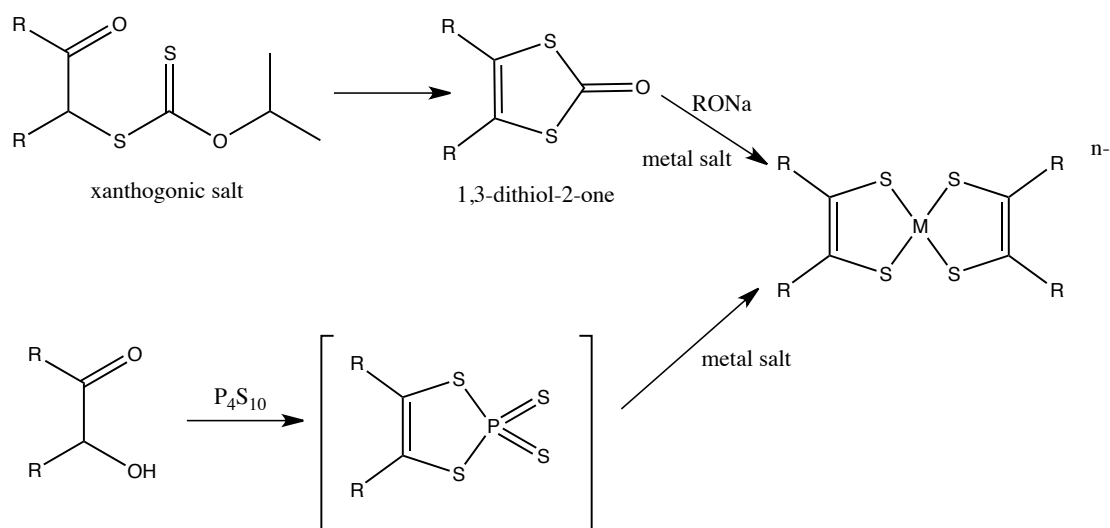


Scheme 1. Preparation of homoleptic aromatic bis–1,2–dithiolenes complexes.

The reaction is usually conducted in polar protic solvents such as methanol and ethanol due to the increased solubility of metal ion salts and dithiolate salts. Oxygen must also not be present due to the air-sensitive nature of intermediate complexes or ligands.

The choice of the base is also important. Early reports used sodium or potassium metals (ie sodium or potassium alkoxides) [33], with presently potassium tert-butoxide ( $t\text{BuOK}$ ) being used as a convenient base [34] since by-product of the preparation of the dithiolate salt is tert-butanol whereas in the case of hydroxide bases ( $\text{NaOH}$ ,  $\text{KOH}$ ) the by-product is water that can interfere with several complexes. The metal salt usually does not interfere with the synthesis, but if anionic species are desired, sodium-alkylammonium or sodium-tetraphenylphosphonium salt metathesis takes place to produce more soluble complexes.

Ene-1,2-dithiolate complexes, however, cannot be prepared in the same manner since the salts of ene-1,2-dithiols are unstable. A “masked” dithiol is used instead, in the form of a 1,3-dithiol-2-one or 1,3-dithiol-2-thione, which is prepared by the ring closure of a xanthogenic salt. In another manner, although less versatile and with lower yields (5–50%), a benzoin can react with  $\text{P}_4\text{S}_{10}$  in refluxing dioxane to produce an intermediate that can be cleaved with a metal ion salt.



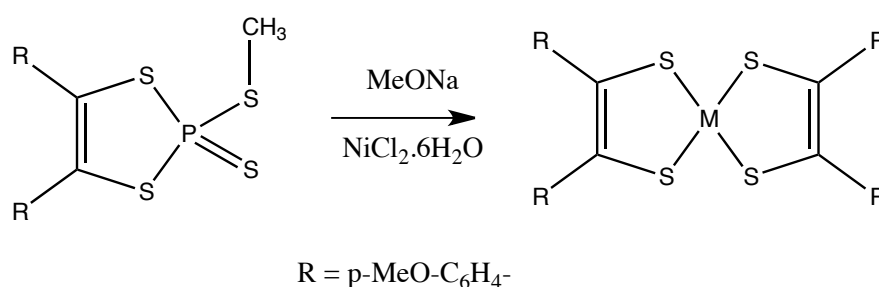
**Scheme 2. Preparation of ene-1,2-dithiolate complexes.**

In the reaction scheme using  $\text{P}_4\text{S}_{10}$ , the neutral complex is formed (usually green in solution). Preparation of anionic complexes can be achieved using reducing agents,

with NaBH<sub>4</sub> being the most convenient, but hydrazine has also been used [13]. Again, salt metathesis produces more soluble products.

In the reaction with 1,3-dithiol-2-one, an anionic form of the complex is usually formed but air-oxidation or iodine oxidation can produce neutral species.

Lately, several more methods have appeared to prepare dithiolene complexes, such as the use of alkylated phosphorus intermediates [22] that upon reaction with a metal salt in the presence of MeONa produce dithiolene complexes.



**Scheme 3. Synthesis of bis-dithiolene complexes with alkylated phosphorus intermediates.**

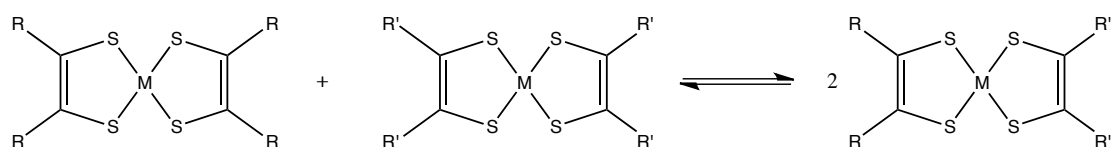
### 2.3.2 Unsymmetrical (heteroleptic) bis-dithiolene complexes

Unsymmetrical bis-dithiolene complexes, especially those comprising a d<sup>8</sup> transition metal ion, exhibit very interesting non-linear optical properties [35–37]. When incorporating two different dithiolene ligands in a complex, each ligand adopts a more defined electronic structure and each reduction can theoretically be localized on each ligand, depending of course on each substituent. One ligand is more easily reduced (acceptor ligand) and the other more easily oxidized (donor ligand).

Another interesting trait of heteroleptic bis-dithiolene complexes is that the resulting complex combines features from the corresponding bis-homoleptic complexes. Thus, the reduction potentials and absorption spectra for a heteroleptic complex are intermediate between the symmetrical precursors [38].

This class of complexes (mostly with Ni) can be prepared via several routes [31], the most important of which are mentioned below:

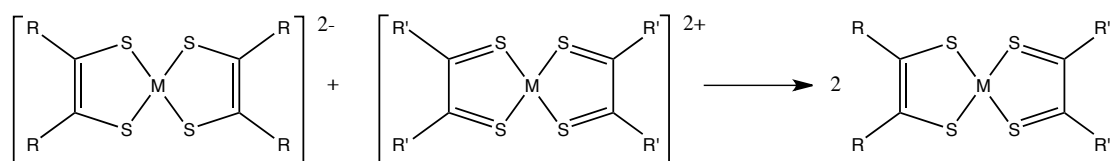
- by refluxing a mixture of two homoleptic complexes (scrambling reaction):



**Scheme 4. Scrambling reaction for the preparation of heteroleptic bis-dithiolene complex.**

This reaction reaches an equilibrium and usually column chromatography is used to isolate the desired compound.

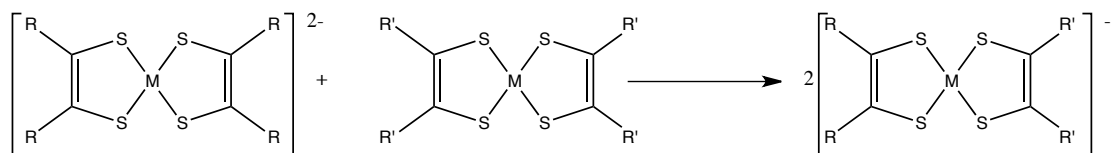
- by refluxing a mixture of a dianionic with a dicationic dithiolene complex:



**Scheme 5. Double substitution reaction for the preparation of heteroleptic bis-dithiolene complex.**

This reaction is often contaminated by double salts were both anionic and cationic complexes coexist.

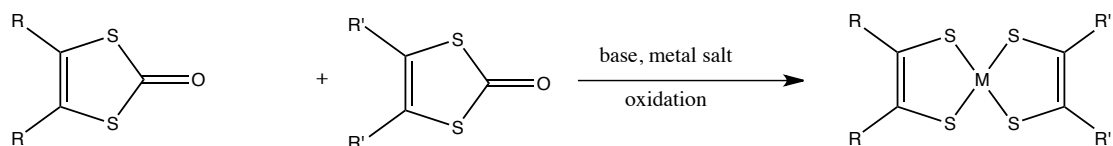
- By an oxidation-reduction scrambling reaction [39,40]:



**Scheme 6. Oxidation-reduction scrambling reaction for the preparation of mixed ligand bis-dithiolene complexes.**

Again, this reaction produces mixtures of complexes and separation of the desired compound is achieved via column chromatography or recrystallization.

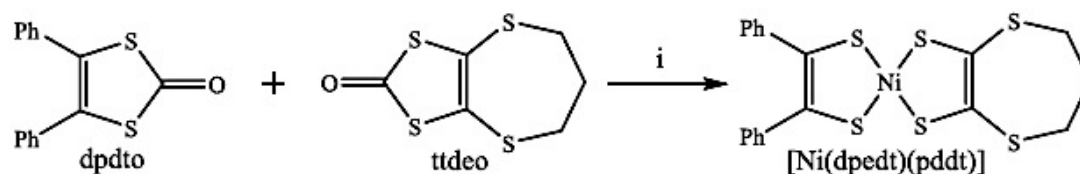
- By mixing 1,3-dithiol-2-ones with a metal salt:



**Scheme 7. Crossed-ligand synthesis of heteroleptic bis-dithiolene complexes.**

Mixtures of all possible complexes are formed, with column chromatography used as a separation technique to isolate the desired complex.

As an example, the latter method has been employed for the preparation of a nickel bis-heteroleptic complex by Anyfantis et al. [41]:



i = 1) MeONa in MeOH; 2) NiCl<sub>2</sub> in MeOH; 3) aq. HCl (35%) in air;

**Scheme 8. Bis-heteroleptic complex prepared by Anyfantis et al.**

This compound exhibits intermediate properties between the homoleptic complexes, as is typical for heteroleptic bis-dithiolene complexes, as evidenced by the spectra shown in the following figure.

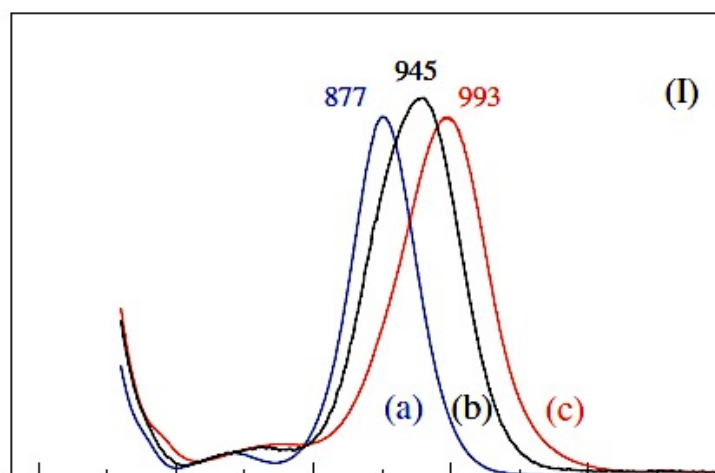


**Figure 6. UV-Vis spectrum of [Ni(dpdt)<sub>2</sub>] (a), [Ni(dpdt)(pddt)] (b), [Ni(pddt)<sub>2</sub>] (c).**

## 2.4 Chemical reactivity of dithiolene complexes

As mentioned earlier, the neutral and reduced forms of dithiolene complexes exhibit reactivity towards nucleophiles, with the electrophilic centers being the sulphur atoms. They can react with oxygen present in the solvent or by oxygen-transfer reactions from other molecules such as dimethylsulphoxide or hydrogen peroxide, to yield sulfinate products [11,25].

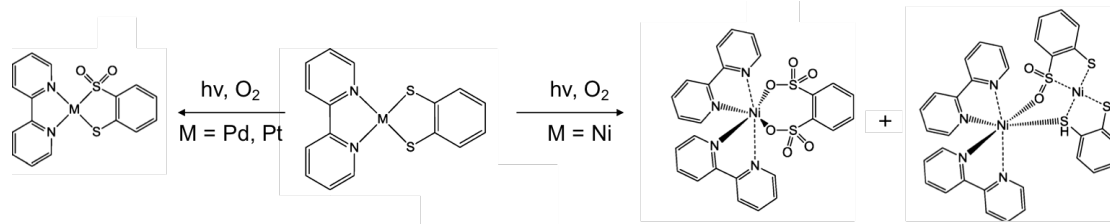
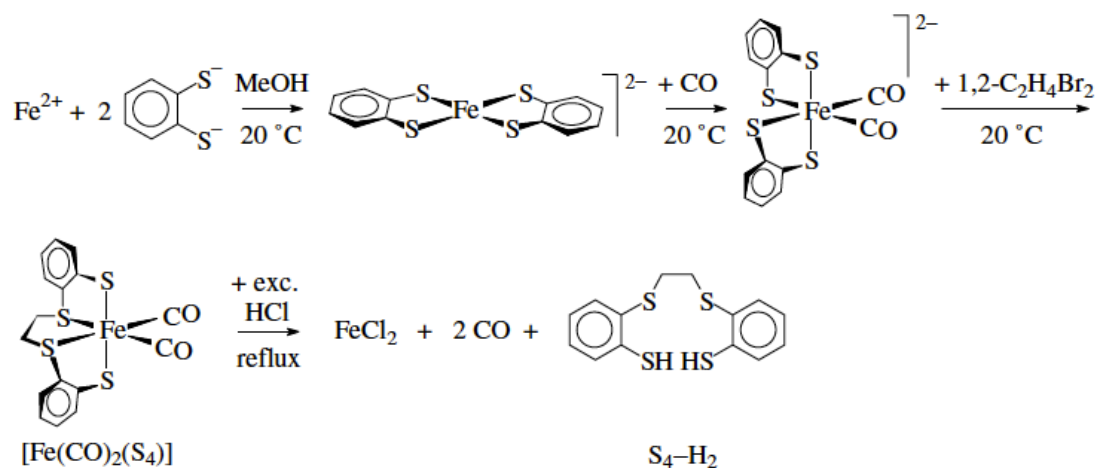


Figure 7. Oxidation products of diimine dithiolene complexes of Ni, Pd, Pt.

More interestingly, nickel dithiolenes in their fully reduced form can undergo alkylation with alkyl halides, a work pioneered by Sellmann [42].



Scheme 9. Template reactions of complexed dithiolene ligands.

These complexes can in turn react with iron moieties to produce multinuclear complexes that act as mimics of NiFe hydrogenases [32,43–51].

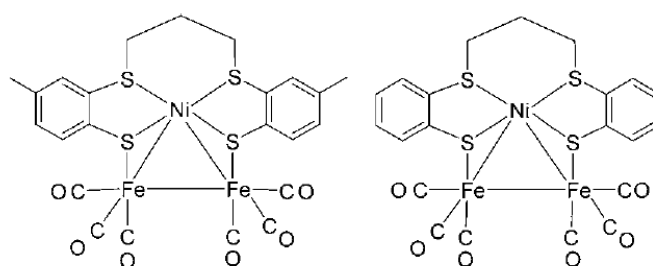


Figure 8. Trinuclear complexes mimicking the active site of NiFe hydrogenases.

## CHAPTER 3

### PHOTOCATALYTIC HYDROGEN PRODUCTION

#### 3.1 Definition of photocatalysis

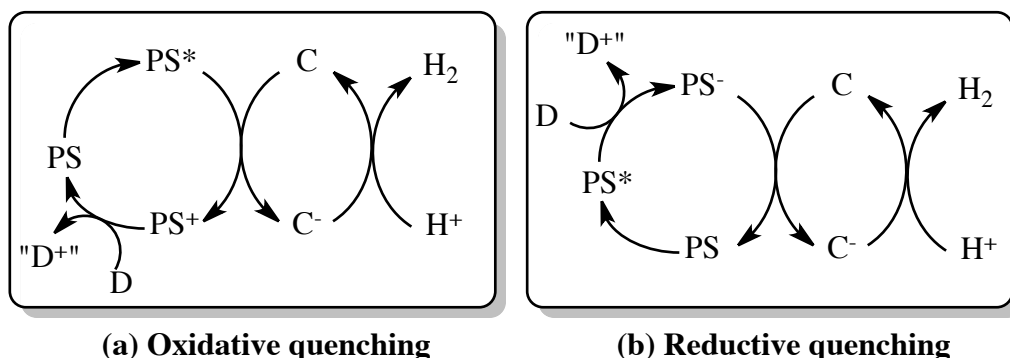
As defined in IUPAC Gold Book [52], photocatalysis is the “change in the rate of a chemical reaction or its initiation under the action of ultraviolet, visible or infrared radiation in the presence of a substance – the photocatalyst – that absorbs light and is involved in the chemical transformation of the reaction partners”. In other words, photocatalysis occurs when photons are absorbed by molecules that take part in the reaction in order to produce a useful chemical species.

#### 3.2 Homogeneous and heterogeneous photocatalysis

Homogeneous catalysis occurs when both the photocatalyst and the substrate can be found in the same phase. When one or more of the components of a photocatalytic system are in a different phase, there is heterogeneous photocatalysis.

#### 3.3 Mechanisms for hydrogen evolution in homogeneous photocatalytic systems

Two ways can be followed to achieve water splitting [53,54]; the reductive side which leads to formation of dihydrogen and the oxidative pathway which leads to dioxygen. Since the focus of this work is the reductive side, only the mechanistic pathways regarding dihydrogen evolution will be displayed.



**Scheme 10. Oxidative (a) and reductive (b) pathways towards hydrogen evolution.**

In both mechanisms, a photosensitizer (PS) absorbs light and reaches an excited state (PS\*). In the oxidative quenching mechanism, the excited state of the photosensitizer is quenched by a catalyst molecule (C) to produce a reduced form of the catalyst (C<sup>-</sup>)

and the oxidized photosensitizer, which in turn receives an electron from a sacrificial electron acceptor (D). The catalyst then provides electrons to protons or to water and hydrogen is produced. In the reductive mechanism, the photosensitizer is first reduced and then provides electrons to the catalyst.

### 3.4 Components of a homogeneous photocatalytic system

#### 3.4.1 Photosensitizer

A photosensitizer (PS) is a molecule that absorbs light in a preferred region of the spectrum. The desired area in which a photosensitizer should absorb photons is the visible and near infrared region. Several types of photosensitizers can be utilized in the photocatalytic splitting of water: organic molecules such as eosin [55] or fluorescein [56] and inorganic metal complexes containing rhenium [57], iridium [58], ruthenium [59], copper [60] or metal porphyrins [61].

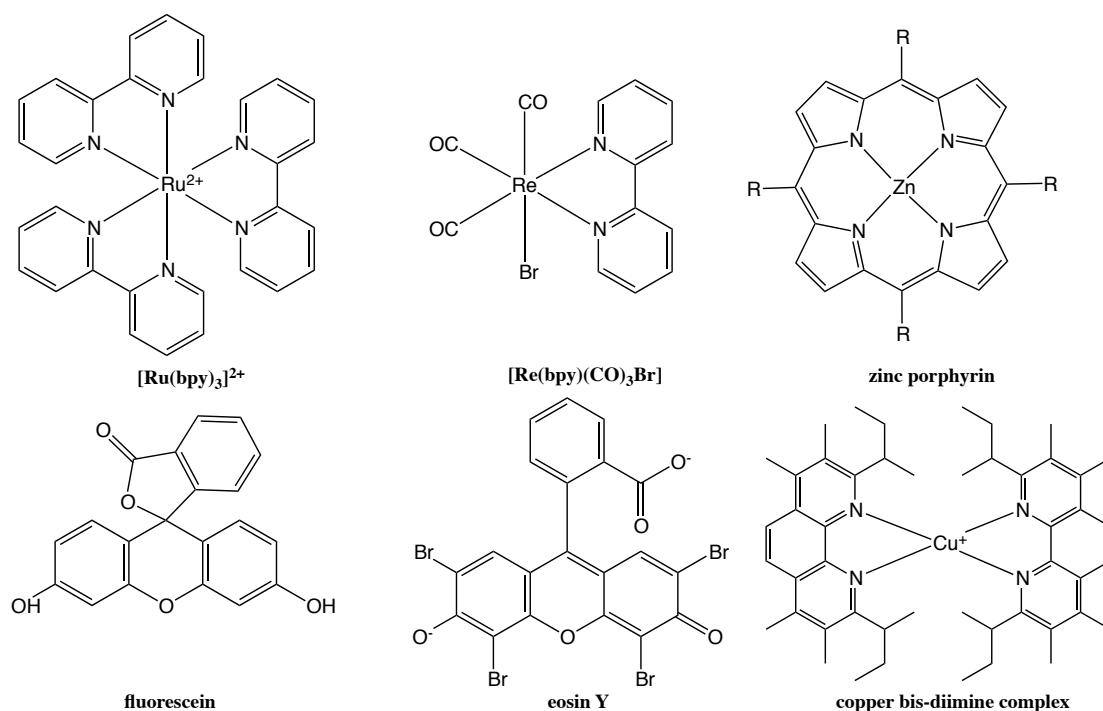


**Figure 9. Typical photosensitizers used in homogeneous photocatalytic hydrogen production.**

A typical photosensitizer must have the following attributes:

- high molar extinction coefficients in the visible area of the absorption spectrum
- stability towards hydrolysis, solvolysis, anation

- reversible oxidation/reduction potentials in order to take part in reversible electron–transfer reactions
- excited state lifetimes suitable for participation in chemical reactions, that is neither too short, nor too long
- low toxicity
- low cost

### **3.4.2 Catalyst**

A catalyst is the molecule responsible for the chemical transformation of reactants into products by lowering energy barriers via alternative reaction pathways. Several complexes have proved suitable catalysts towards hydrogen evolution, mainly cobaloximes [62,63], corroles [64], diphosphine complexes [65], and dithiolene complexes [34,59,66–70]. Most of these catalysts combine middle–transition elements with a relatively robust ligand framework able to sustain the demanding catalytic conditions (different pH values, protonation, solvolysis, etc).

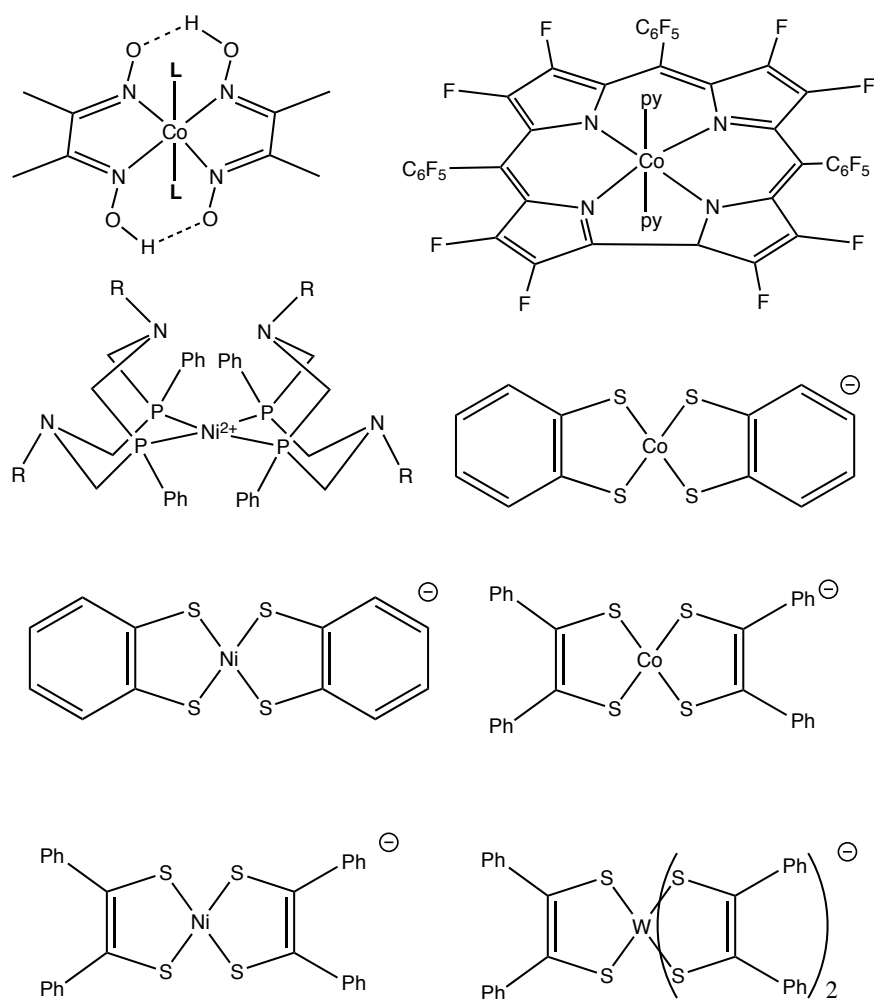


**Figure 10. Catalysts used in recent works towards photocatalytic hydrogen evolution.**

Ideal catalysts should exhibit the following traits:

- reversible oxidation/reduction potentials in order to take part in reversible electron–transfer reactions
- suitable protonation sites either at the metal (typical for cobaloximes which reach the nucleophilic  $\text{Co}^{+1}$  oxidation state), or at the ligands (second coordination sphere, typical of DuBois–type catalysts)
- low toxicity
- low cost

### 3.4.3 Sacrificial electron donor

Sacrificial electron donors provide the electrons required for the return of the oxidized or reduced photosensitizer to its previous state in order for it to participate again in the photocatalytic cycle. More specifically, sacrificial electron donors are usually amines

or substituted amines such as triethylamine (TEA), triethanolamine (TEOA), or ascorbic acid (AA) [71].

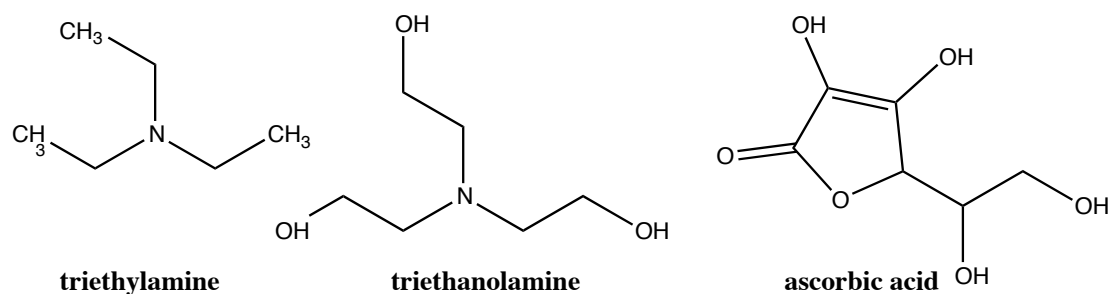


**Figure 11. Typical sacrificial electron donors.**

Although in early studies of homogeneous photocatalytic hydrogen evolving systems not much was known for the action of sacrificial electron donors, later studies have shown that their oxidation produces side-products that can take part in side-reactions that have a great impact on the hydrogen yields. For example, oxidation of triethanolamine produces radical species that interfere with the catalytic cycle [72]. An ideal sacrificial electron donor should have oxidation products that do not impact the performance of the overall reaction scheme.

#### **3.4.4 Solvent**

The choice of solvent is important since all components in a photocatalytic system must be soluble. Furthermore, different solvents have an effect not only on the oxidation/reduction potentials of photosensitizers and catalysts, but also in the formation and preservation of excited states. Finally, whether or not a solvent is polar or non-polar, protic or aprotic, coordinating or not, has an effect on reaction pathways.

#### **3.4.5 Effectiveness of a photocatalytic system**

The effectiveness of a photocatalytic system is usually measured using the turnover number (TON) which is defined based on the catalyst or the photosensitizer, as follows:

$$\text{TON} = \frac{n_{\text{H}_2}}{n_{\text{catalyst}}}$$

Indicative of how fast the catalyst performs is the turnover frequency, defined as follows:

$$\text{TOF} = \frac{\text{TOF}}{t_{\text{irradiation}}}$$

### 3.5 Homogeneous hydrogen evolving photocatalytic systems from the literature

#### 3.5.1 Systems employing dithiolene complexes as catalysts

Hydrogen evolving systems with metal dithiolene complexes have been extensively reviewed in the literature [67], so here only a few representative examples from the early days of research on hydrogen evolution with dithiolene complexes will be shown. Work on dithiolene complexes as hydrogen evolving catalysts begins in the 1980s, with a report from Kisch [16]. In that study, hydrogen evolved when a solution of  $[\text{Ni}(\text{S}_2\text{C}_2\text{Ph}_2)_2]$  in a solvent mixture THF/water:11.5/1 was irradiated with  $\lambda \geq 290$  nm.

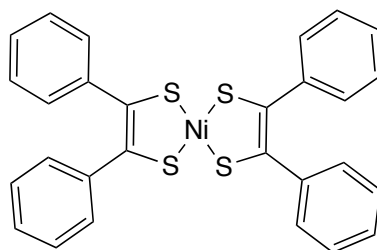
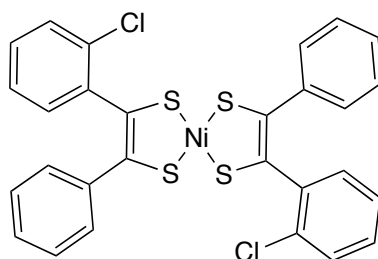


Figure 12.  $[\text{Ni}(\text{S}_2\text{C}_2\text{Ph}_2)_2]$  catalyst.

The amount of the hydrogen produced was 46% after 185 h of irradiation, 100% for 350 h and 225% after 483 h of irradiation with respect to the catalyst, since 1 mol of  $[\text{Ni}(\text{S}_2\text{C}_2\text{Ph}_2)_2]$  leads to the production of 1 mol of hydrogen. Without irradiation there was no hydrogen evolution. Interestingly, when the experiment was carried out in anhydrous THF and for the same hours of irradiation, the production of dihydrogen was 9, 16 and 77%, respectively. This fact implies that the molecules of the solvent must be involved in the catalytic cycle. To investigate the system further, the authors conducted the experiment in  $\text{CCl}_4$  and no hydrogen was evolved. Consequently, the experiment was conducted on a THF/ $\text{D}_2\text{O}$  mixture and mass spectrometry of the gas produced showed that the ratio HD/ $\text{D}_2$  depends on the solvent used. Thus, for THF the ratio was 13 and for MeCN 2.1, the overall D/H ratio being  $\sim 1$  and 2, respectively. This proves that during the catalytic procedure  $\text{D}_2\text{O}$  is split while a hydrogen atom is abstracted from the solvent. In addition, irradiation with  $\lambda \geq 254$  nm favoured the system and produced dihydrogen faster. Finally, since the dianion of  $[\text{Ni}(\text{S}_2\text{C}_2\text{Ph}_2)_2]$

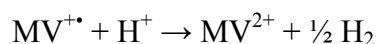
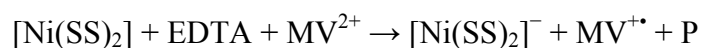
was found in the reaction system, the nature of the active catalyst could not be defined.

At the same time a related asymmetric complex, namely bis(2-chloro-dithio-benzil)nickel (II), was tested for photocatalytic activity with respect to the photoreduction of water by Katakis et al. [73].



**Figure 13. bis(2-chlorodithiobenzil)nickel(II) catalyst.**

In this study, EDTA was used as a sacrificial electron donor while methyl viologen ( $MV^{2+}$ ) served as an electron relay agent. The experiments were conducted in an acetone/water:70/30 mixture. Hydrogen production was observed for  $\lambda \geq 350$  nm. By examining the absorption spectra of the complex and its monoanion in the visible region, the authors deduced that the neutral complex as well as the monoanion can act as the active species. The reactions taking place are the following:



where P represents the products of the oxidation of EDTA, and the production of hydrogen was assumed to be catalyzed both from the neutral and the monoanion form of the complex.

The homogeneous photocleavage of water into hydrogen and oxygen was mentioned for the first time by using as a photocatalyst the non-symmetric homoleptic complex, namely tris[1-(4-methoxyphenyl)-2-phenyl-1,2-ethylenedithiolenic-S,S]tungsten (VI).

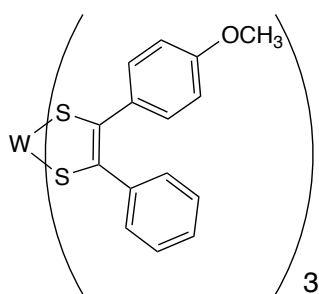
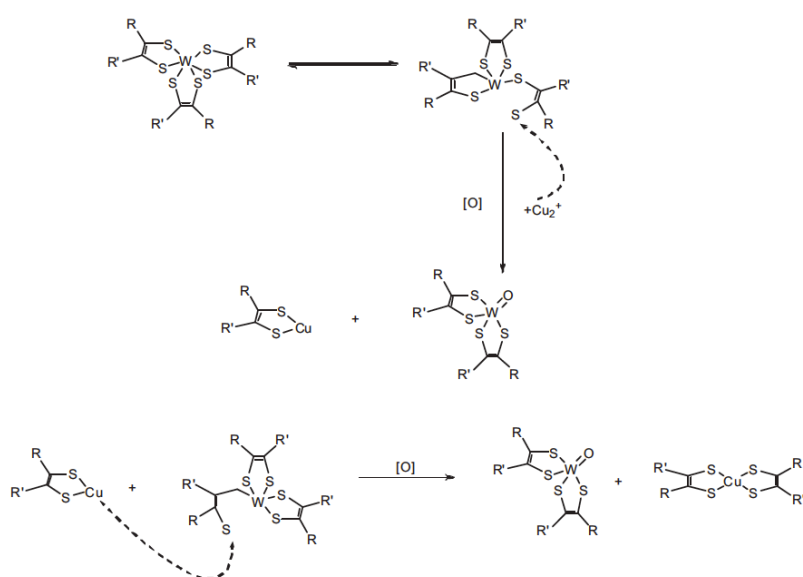


**Figure 14. tris[1-(4-methoxyphenyl)-2-phenyl-1,2-ethylenedithiolenic-S,S]tungsten (VI).**

The illumination of 29 with  $\lambda \geq 350$  nm in acetone/water: 60/40 solutions in the presence of  $MV^{2+}$ , led to dihydrogen and dioxygen production [15]. More than 30 complexes were tested under the same conditions and only three were effective in the photosplitting of water, all of which were non symmetric and carrying an aryl group with a strongly electron-donating substituent in the para-position [19]. However, these trigonal prismatic complexes were unstable in the presence of transition metal ions such as  $Cr^{2+}$ ,  $Cu^{2+}$  even at the ppm concentration level [20].



**Scheme 11. Proposed mechanism for the cleavage of  $[W(S_2C_2Ph,C_6H_4-p-OCH_3)_3]$  by  $Cu^{2+}$  ions.**

From these early studies it became obvious that the reduced species of dithiolene complexes play a pivotal role in hydrogen evolution, since the electrons stored in the reduced metal dithiolene complexes can be transferred to water in a reductive manner to produce hydrogen. For the first time, the monoanion of bis{1-(2-chlorophenyl)-2-phenyl-1,2-dithiolenic-S,S}nickel(II) was observed to act as a catalyst for the catalytic generation of hydrogen from water [73,74]. A few years later, a more detailed research on monoanion of tris{1-(2-chlorophenyl)-2-phenyl-1,2-

dithiolenic-S,S}tungsten(VI) fully demonstrated that this monoanion can catalyze thermally the reduction of water [75].

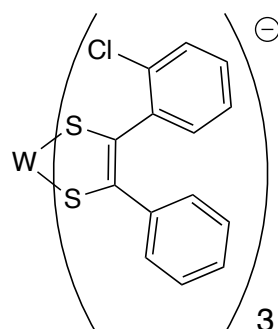


**Figure 15. monoanion of tris{1-(2-chlorophenyl)-2-phenyl-1,2-dithiolenic-S,S}tungsten(VI).**

Spectrometric measurements showed that in mixed acetone/water solutions, this complex reduces to its monoanion.

Dithiolene complexes as catalysts towards photocatalytic proton reduction re-emerged in 2011 from the groups of Eisenberg and Holland [59] with a subsequent extensive study by the same groups. They examined a series of cobalt dithiolene complexes with  $[\text{Ru}(\text{bpy})_3]^{2+}$  as photosensitizer and ascorbic acid/ascorbate buffer in acetonitrile – water solution under irradiation with 520 nm LED lamps.

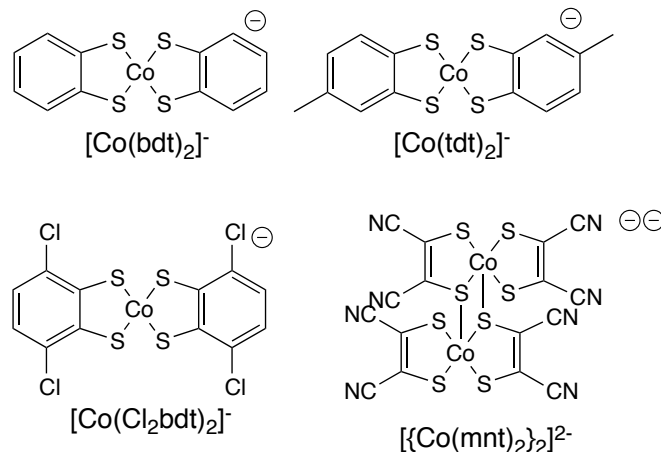
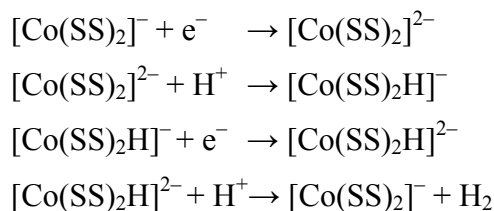


**Figure 16. Cobalt dithiolene catalysts studied by Eisenberg and Holland groups.**

It was found that the complexes with the more electron-withdrawing substituents exhibit the best performance, with the series in terms of activity being  $[\text{Co}(\text{mnt})_2]^- > [\text{Co}(\text{Cl}_2\text{bdt})_2]^- > [\text{Co}(\text{bdt})_2]^- > [\text{Co}(\text{tdt})_2]^-$ . Hydrogen produced was linear to the concentration of the catalyst. The authors proposed that the reductive quenching mechanism is followed, thus suggesting that  $[\text{Ru}(\text{bpy})_3]^{2+}$  is first reduced to  $[\text{Ru}(\text{bpy})_3]^+$  by the ascorbic acid and then the cobalt catalyst is reduced to the dianion with the proposed reaction scheme:



The overall performance of the complexes is summarized in the following table:

**Table 2. Performance of cobalt dithiolene catalysts**

Complex	TON <sup>a</sup>	TOF (h <sup>-1</sup> ) <sup>b</sup>	TOF (h <sup>-1</sup> ) <sup>c</sup>
[Co(bdt) <sub>2</sub> ] <sup>-</sup>	2700	880	225
[Co(tdt) <sub>2</sub> ] <sup>-</sup>	2300	690	192
[Co(Cl <sub>2</sub> bdt) <sub>2</sub> ] <sup>-</sup>	6000	1400	500
[Co(mnt) <sub>2</sub> ] <sup>-</sup>	9000	3400	750

<sup>a</sup>: measured in MeCN/water:1/1, at pH = 4.0 (0.1 M ascorbic acid), 6.5 μM catalyst concentration, 0.5 mM Rubpy, after irradiation for 12 h with green (520 nm) LED, 15 °C

<sup>b</sup>: initial TOF values

<sup>c</sup>: after 12 h

In a similar work, Eckenhoff et al. [76] prepared and studied a series of molybdenum dithiolene complexes for the reduction of aqueous protons. [Ru(bpy)<sub>3</sub>]<sup>2+</sup> was employed as the photosensitizer and ascorbic acid/ascorbate buffer (0.1 M in ascorbic acid, pH = 4.0) in acetonitrile – water solution under irradiation with 460 nm LED lamps. All complexes exhibit good hydrogen evolving activity reaching several hundreds TON, with a cessation of catalytic action after 24 h of irradiation. Addition of fresh Rubpy slightly increased activity but addition of extra catalyst had no effect on hydrogen evolution.

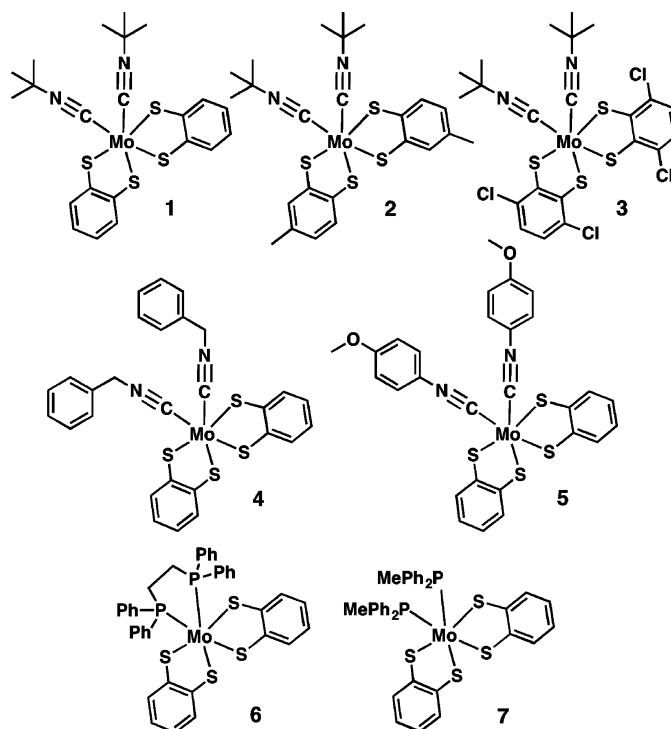
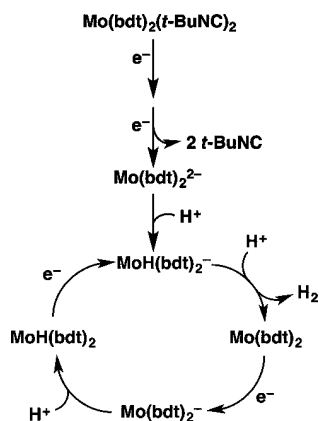


Figure 17. Catalysts studied by Eckenhoff et al. for the reduction of aqueous protons.

After emission quenching studies between the chromophore and catalyst/ascorbic acid, it was proposed that a reductive pathway is followed, as was in the case of cobalt dithiolene complexes.

Mechanistic studies for complex 1 using  $^1\text{H-NMR}$  and UV-Vis spectroscopy showed that after the first reduction, the complex dissociates isocyanide ligands and upon the second reduction the active form of the catalyst  $[\text{Mo}(\text{bdt})_2]^{2-}$  is formed. This intermediate is protonated ( $[\text{Mo}(\text{bdt})_2\text{H}]$ ) and after a second protonation releases dihydrogen and the neutral form  $[\text{Mo}(\text{bdt})_2]$ . A further reduction yields  $[\text{Mo}(\text{bdt})_2]^-$  which is protonated to form  $[\text{Mo}(\text{bdt})_2\text{H}]$  and this in turn upon reduction yields again  $[\text{Mo}(\text{bdt})_2\text{H}]^-$  is reached.



Scheme 12. Hydrogen evolution mechanism with molybdenum dithiolene catalyst.

The overall performance of the molybdenum dithiolene catalysts is summarized in the following table.

**Table 3. Performance of molybdenum dithiolene catalysts**

Complex	TON <sup>a</sup>	TOF (h <sup>-1</sup> ) <sup>b</sup>
1	520	21.67
2	475	19.79
3	100	4.17
4	455	18.96
5	260	10.83
6	402	16.75
7	135	5.62

<sup>a</sup>: measured in MeCN/water:1/1, at pH = 4.0 (0.1 M ascorbic acid), 12 mM catalyst concentration, 0.4 mM Rubpy, after irradiation for 24 h with blue (460 nm) LED, 15 °C

<sup>b</sup>: after 24 h

Several nickel complexes were studied by Das et al. [77], among them bis-1,2-dithiolene nickel, [Ni(bdt)<sub>2</sub>]NBU<sub>4</sub>. Photocatalytic experiments were conducted in aqueous solutions with fluorescein as the photosensitizer, triethanolamine as a sacrificial electron donor at pH = 9.8. When (S<sup>-</sup>CH<sub>2</sub>)<sub>3</sub>CCOO<sup>-</sup> capped CdSe quantum dots were used as photosensitizer, ascorbic acid at pH = 4.5 was used as a sacrificial electron donor. In each case, irradiation was performed with green (520 nm) light emitting diodes.

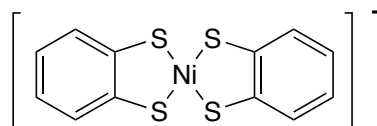


**Figure 18.** [Ni(bdt)<sub>2</sub>]<sup>-</sup>.

Under basic conditions with fluorescein as photosensitizer, [Ni(bdt)<sub>2</sub>]<sup>-</sup> was not active hydrogen evolving catalyst. It was proposed that the reduced form of fluorescein was

reducing enough to transfer an electron to the catalyst. However, in the quantum dot operating system,  $[\text{Ni}(\text{bdt})_2]^-$  showed increased activity reaching a TON of 105300 after 7 days of irradiation and a TOF of 730 after the first 40 h of irradiation (4  $\mu\text{M}$  quantum dot, 1  $\mu\text{M}$  catalyst, 0.5 M aqueous ascorbic acid, 15  $^\circ\text{C}$ , at pH = 4.5).

In a similar context Lv et al. [78] investigated the hydrogen evolving activity of a series of iron dithiolene complexes with CdSe quantum dots as photosensitizers.

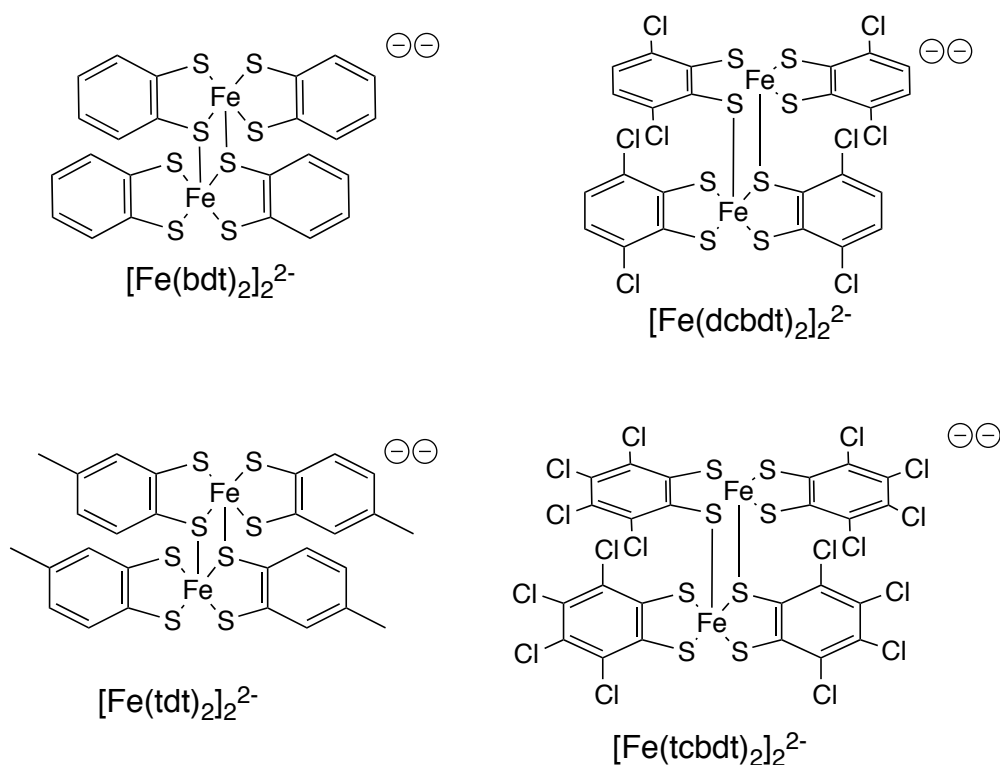


**Figure 19. Iron dithiolene catalysts studied by Lv et al.**

Hydrogen evolution studies were performed in ethanol–aqueous:1–1 solution, with soluble CdSe quantum dots as photosensitizers, ascorbic acid as sacrificial electron donor, under irradiation with 520 nm LEDs. After 80 h of irradiation, TON were 20600, 29400, 15200, and 8000 for catalysts  $[\text{Fe}(\text{bdt})_2]_2^{2-}$ ,  $[\text{Fe}(\text{tdt})_2]_2^{2-}$ ,  $[\text{Fe}(\text{dcbdt})_2]_2^{2-}$ ,  $[\text{Fe}(\text{tcdbdt})_2]_2^{2-}$  per Fe atom. Highest activity was observed for  $[\text{Fe}(\text{tdt})_2]_2^{2-}$ , which is the complex with the most electron–donating substituents on dithiolene ligands.

However, it was found that the water–solubilizing capping agent of the quantum dots (dihydrolic acid, DHLA) displace dithiolene ligands and the dimeric iron dithiolene complexes coexist in equilibrium with the monomeric complexes, in contrast with cobalt dithiolene dimers which dissociate upon reduction [34].

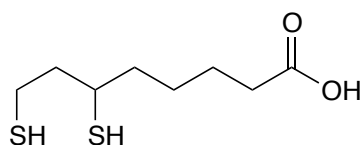


**Figure 20. Dihydrolopic acid (DHLA).**

Thus, the above-mentioned results do not accurately reflect the true activity of iron dithiolene complexes. Using  $\text{Fe}(\text{NO}_3)_3$  as a precatalyst to determine the effect of DHLA substitution on hydrogen evolution activity showed lower activity compared to the systems without  $\text{Fe}(\text{NO}_3)_3$ , indicating that a  $[\text{Fe}(\text{DHLA})_x]$  catalyst also contributes to the observed hydrogen evolution.

After adjustments to each components of the system along with verification that no hydrogen is evolved in the dark, the long-term stability of the catalysts was examined. After 80 h of hydrogen evolution activity, use of the same system led to lower hydrogen yields, both in quantity and rate, with the overall decline of the system ascribed to the depletion of ascorbic acid, instability of  $[\text{Fe}(\text{tdt})_2]^{2-}$ , change in pH. Eventually, the overall activity after addition of excessive DHLA was attributed to the in situ formation of a  $\text{Fe}(\text{DHLA})_x(\text{bdt})_y^{z-}$  catalyst.

Two dithiolene complexes bearing 1'-binaphthalene-2,2'-dithiol and cobalt or nickel have been prepared and employed as hydrogen evolving catalysts [79], coupled with eosin Y as photosensitizer and triethylamine as sacrificial electron donor in aqueous acetonitrile solution (1:1) under irradiation with  $\lambda > 420$  nm.

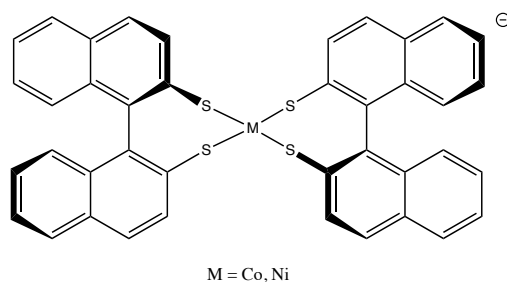


**Figure 21. Cobalt and nickel binaphthalene dithiolene complex.**

Maximum TONs (based on the catalyst) were 495 for the cobalt and 676 for the nickel analogs, after 4 h of irradiation under optimal conditions (0.4 mM eosin Y, 0.1 mM catalyst, 10% triethylamine, pH = 10), giving rise to TOFs of 123.75 and 169. The loss of activity was assigned to the degradation of the chromophore, with the addition of extra photosensitizer after 4 h of irradiation restoring some of the activity of the photocatalytic system.

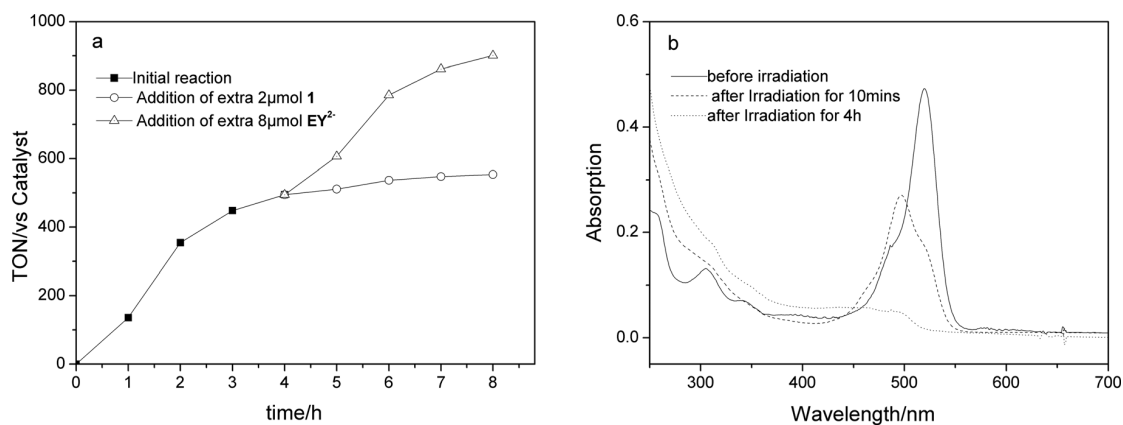
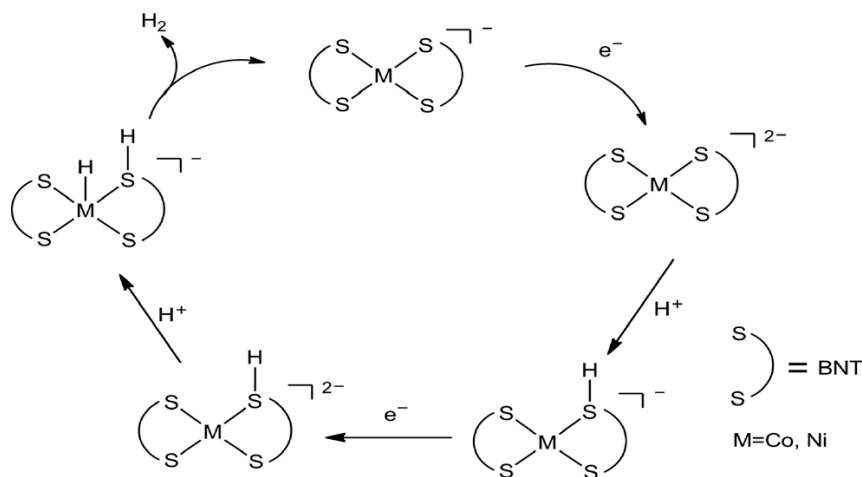


**Figure 22. (a) Changes in H<sub>2</sub> evolution with irradiation time before and after adding extra eosin Y to the photocatalytic system containing cobalt catalyst, (b) Change in the absorption spectra with irradiation for the photocatalytic system containing cobalt catalyst (0.1 mM), eosin Y (0.4 mM), 10% TEA at pH 10.0 in CH<sub>3</sub>CN/H<sub>2</sub>O (1 : 1, v/v). Figure from ref. [79].**

Addition of extra catalyst restored a smaller activity of catalytic activity, indicating that catalyst degradation also has an effect on the overall cessation of activity, albeit to a smaller effect than the photosensitizer.

A possible hydrogen evolution mechanism was proposed following the ECEC scheme, which initially involves reduction of the catalyst to the dianion, subsequent protonation at sulphur, further reduction and protonation at metal. In the final stage, hydrogen is evolved and the monoanionic catalyst is formed again.



**Scheme 13. Proposed hydrogen evolving mechanism by Rao et al. [79].**

The overall better activity of the nickel catalyst versus the cobalt was attributed to the greater emission quenching constant of eosin Y by the nickel complex ( $5.7 \times 10^{12}$  vs  $2.5 \times 10^{12}$  for the cobalt catalyst).

Koutsouri and Mitsopoulou [70] reported on a tungsten tris–dithiolene complex and its monoanion that were active hydrogen evolving catalysts.

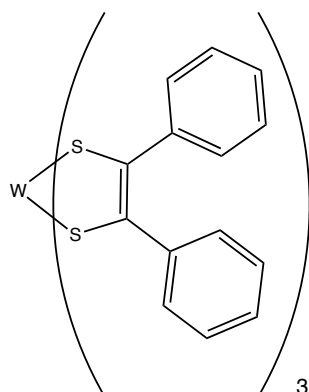


**Figure 23. Tungsten tris–dithiolene hydrogen evolution catalyst.**

Photocatalytic experiments were conducted with  $[\text{Re}(\text{CO})_3(\text{bpy})\text{Br}]$  as the photosensitizer, triethanolamine as sacrificial electron donor, in acetone as solvent, under irradiation with two 10W white LED lamps (400–900 nm), with acetic acid as proton source. The monoanionic catalyst  $[\text{W}(\text{S}_2\text{C}_2\text{Ph}_2)_3]^-$  was used throughout the study due to its better activity. Blank experiments resulted in no hydrogen evolution, apart from a small amount of hydrogen evolved in the absence of catalyst (0.3 TON) attributed to depletion of triethanolamine.

Change of parameters to achieve optimal activity resulted in 16.3 TONs based on catalyst with 0.5 mM Re photosensitizer, 1 M triethanolamine, 0.1 M acetic acid and 6.4  $\mu\text{M}$  catalyst. Addition of further acid resulted in the precipitation of  $\text{HTEOA}^+$ , which is insoluble in acetone and thus catalytic activity was not observed. Interestingly, hydrogen evolution was also observed in the absence of acid, with this assigned to residual protons from the decomposition products of triethanolamine and residual water.

Mercury poisoning experiments did not result in loss of catalytic activity, indicating that catalysis is homogeneous.

A reductive quenching pathway was proposed for the hydrogen evolution mechanism, involving reduction of the excited  $[\text{Re}(\text{CO})_3(\text{bpy})\text{Br}]$  (PS) by TEOA (D), subsequent reduction of the catalyst to the dianion, protonation by the protons from acetic acid (HA), with another reduction and protonation to produce hydrogen and the monoanion of the catalyst.

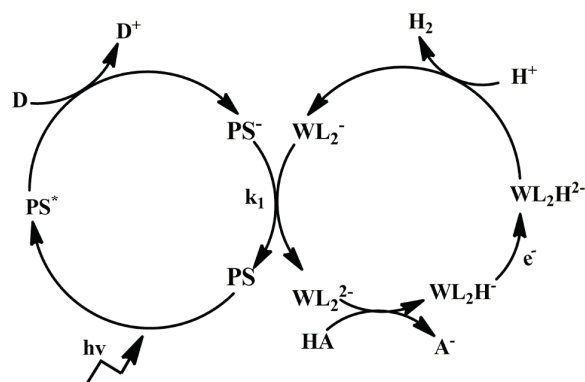


Figure 24. Proposed hydrogen evolving mechanism with tungsten tris–dithiolene complexes as catalysts.

### 3.5.2 Supramolecular systems with porphyrins as photosensitizers

Metalloporphyrins exhibit very promising properties as photosensitizers in photocatalytic hydrogen evolution. Even though several homogeneous systems have been reported [61,80–83], our focus here will be supramolecular systems, i.e. multinuclear assemblies of a porphyrin and a hydrogen evolving catalyst.

In a report from 2008, Li et al. [84] prepared a trinuclear Zn tetraphenylporphyrin – FeFe hydrogenase mimic catalyst complex and studied it towards hydrogen evolution.

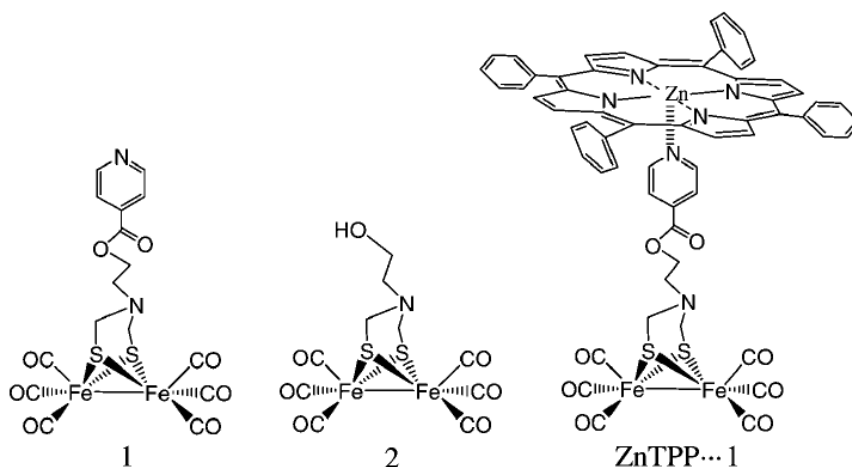
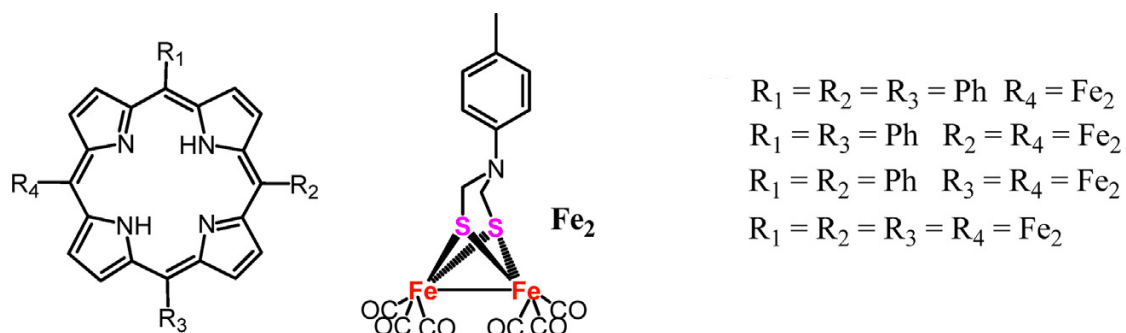


Figure 25. Complexes prepared by Li et al.

It was found that visible light irradiation ( $\lambda > 400$  nm) of an oxygen–free  $\text{CH}_2\text{Cl}_2$  solution of ZnTPP, complex 1, and electron donor ArSH in the presence of  $\text{CF}_3\text{COOH}$  led to the generation of molecular  $\text{H}_2$ , attributed to the in situ formation of ZnTPP–1 adduct. TONs were low, 0.16 based on FeFe catalyst (1) and 16 based on the ZnTPP.

Control experiments where 1 was replaced with 2 did not lead to hydrogen evolution, supporting the claim that the ZnTPP–1 adduct was essential for hydrogen evolution.

In 2009, Song et al. [85] prepared a series of metal free porphyrin – FeFe multinuclear complexes and evaluated their action towards photoinduced hydrogen evolution.



**Figure 26. Multinuclear complexes prepared by Song et al.**

Irradiation with  $\lambda > 400$  nm of a  $\text{CH}_2\text{Cl}_2$  solution with EtSH as electron donor in the presence of  $\text{CF}_3\text{COOH}$  as proton source, containing a complex with  $R_1 = R_2 = R_3 = \text{Ph}$ ,  $R_4 = \text{Fe}_2$ . Hydrogen yield was very low, with a TON of 0.31 after 1 h irradiation.

Poddutoori et al. [86] prepared binuclear and trinuclear complexes containing ZnTPP as photosensitizer, FeFe catalyst and a ferrocene moiety as an electron relay.

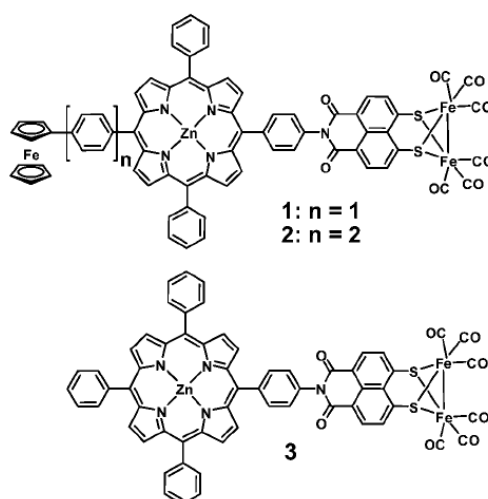


**Figure 27. Dyads and triads prepared by Poddutoori et al.**

Photochemical experiments were conducted under irradiation with  $\lambda = 500\text{--}800$  nm of a  $\text{CH}_2\text{Cl}_2$  solution with  $\text{CF}_3\text{COOH}$  as proton source and 2–mercaptobenzoic acid as sacrificial electron donor. Only triad 2 produced hydrogen (0.56 TON), attributed to the fact that only in this compound the charge–separated excited state is long–lived enough to lead to hydrogen evolution. In the absence of sacrificial electron donor to

regenerate the ferrocene moiety, maximum TON achieved was 1. Such low TONs were attributed to FeFe catalyst instability, as evidenced by CO loss over 8 h of irradiation.

Kluwer et al. [87] studied hydrogen evolution from zinc porphyrins (tetraphenyl and tetra-4-methoxyphenyl) with a binuclear FeFe catalyst bearing coordinating pyridyl phosphines.

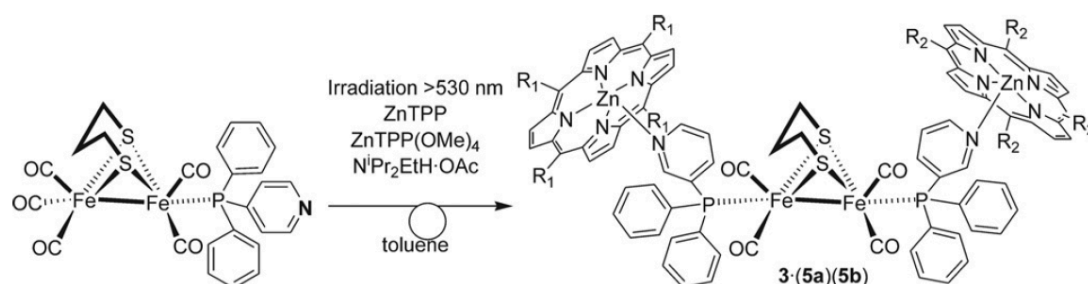


**Figure 28. Supramolecular hydrogen evolving system studied by Kluwer et al.**

When a solution containing 2mM zinc porphyrin and 1mM of catalyst in toluene, with  $^i\text{Pr}_2\text{EtNH.OAc}$  10 mM as proton source and sacrificial electron donor was irradiated with  $\lambda > 530$  nm for 80 min, hydrogen was evolved at a 30% yield (5 TONs) with respect to the proton donor. Both chromophores, ie zinc tetraphenylporphyrin and zinc tetra-4-methoxyphenyl-porphyrin needed to be present on the catalyst for hydrogen to evolve.

Zhang et al. [88] prepared binuclear assemblies using free base, zinc, or magnesium porphyrins coupled with a cobaloxime as proton reducing catalyst.

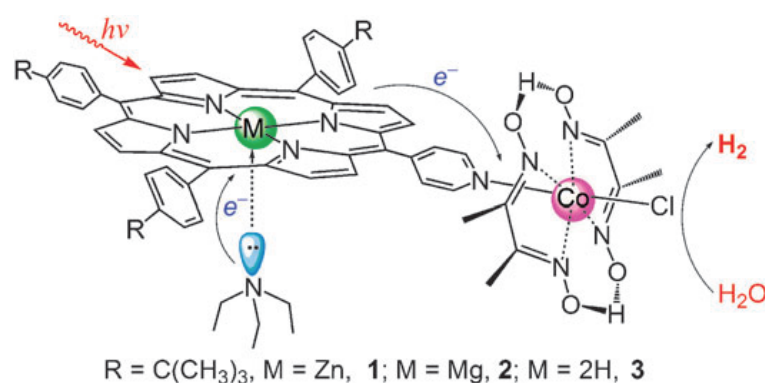


**Figure 29. Binuclear porphyrin complexes prepared by Zhang et al.**

Irradiation ( $\lambda > 400$  nm) in THF- $\text{H}_2\text{O}$ :8-2 solution of each molecular device (1 mM) in the presence of triethylamine as sacrificial electron donor (0.1 M), led to hydrogen evolution only for the zinc porphyrin (TON = 22 after 5 h, TOF = 4,4), while only

trace amounts were detected for the magnesium and free base complexes. Hydrogen was proposed to evolve after generation of Co(I), produced from the quenching of the singlet excited state of the porphyrin by the cobaloxime.

The same group prepared a similar series of compounds [89], with zinc tetraphenylporphyrin bound on an isonicotinamide bridge on the cobaloxime instead of a pyridyl group.

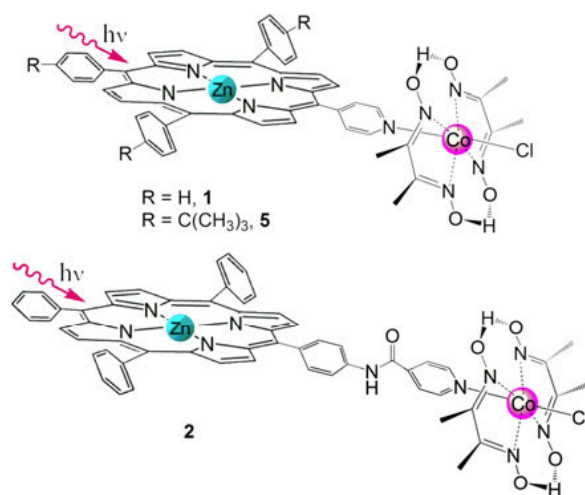


**Figure 30. Molecular devices prepared by Zhang et al.**

Under the same conditions as the previous study (THF–H<sub>2</sub>O:1–1, triethylamine as sacrificial electron donor) improved TONs were achieved, reaching 35 for compound 2 after 12 h irradiation.

Although these early results seemed promising at the time and laid the path for increased interest in supramolecular dyads comprising earth abundant photosensitizers and catalysts, more detailed studies independently by the groups of Guldi and Coutsolelos [90] and Pryce and Vos [91] on similar compounds confirmed that porphyrins failed to act as light–harvesting units and that the lowest energy excited states are in fact cobaloxime–based rather than porphyrin based. Population of these excited states in fact lead to scission of Co – N<sub>pyridyl</sub> bond, leading to rupture of the dyads and no hydrogen evolving. Both in Guldi – Coutsolelo’s and Pryce – Vos’ work negligible amount of hydrogen was evolved, leading to questioning the results obtained earlier by the group of Sun [88,89].

The same conclusions were reached in a study by Natali et al. [92], where study of similar dyads to those reported by Sun, Guldi, Coutsolelos, Pryce, and Vos,

indicated that extremely short-lived charge separated state show little accumulation to lead in hydrogen evolution coming from the dyad.

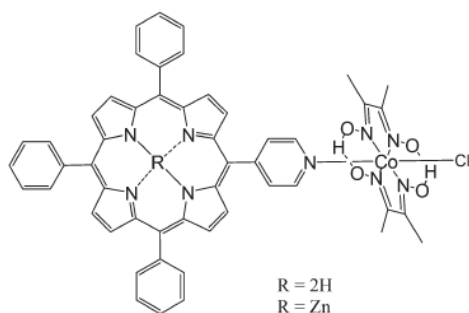


**Figure 31.** Dyads studied by the groups of Pryce and Vos.

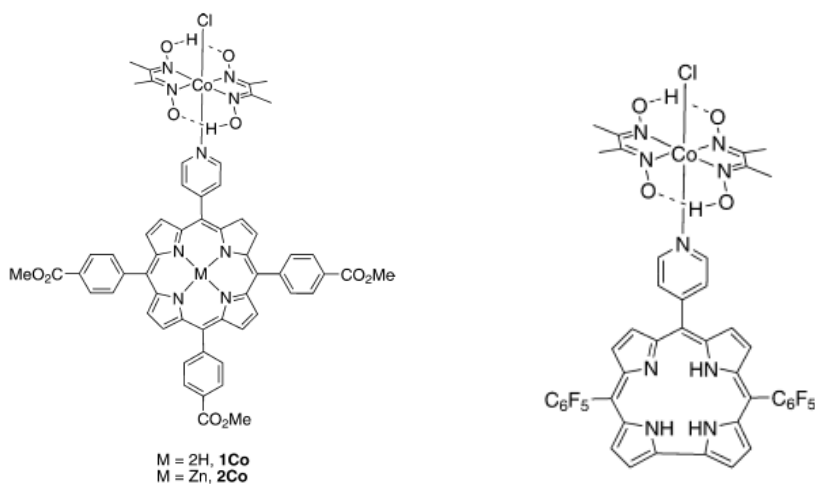


**Figure 32.** Dyads studied by the groups of Guldi and Coutsolelos.

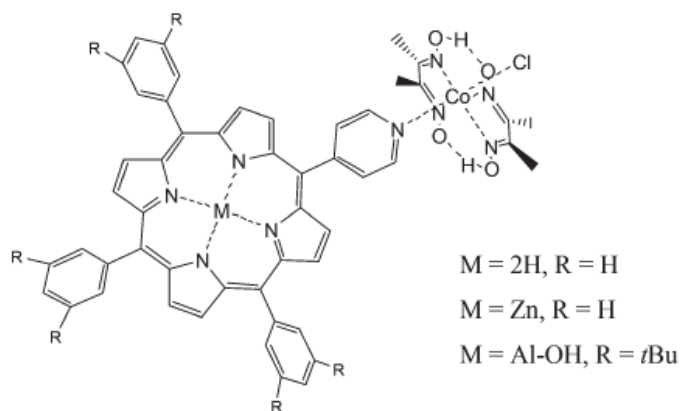


**Figure 33.** Dyads studied by Natali et al.

However, Natali et al. showed that insertion of a Lewis acid such as Al in the porphyrin center [93] can significantly boost the hydrogen evolving activity.

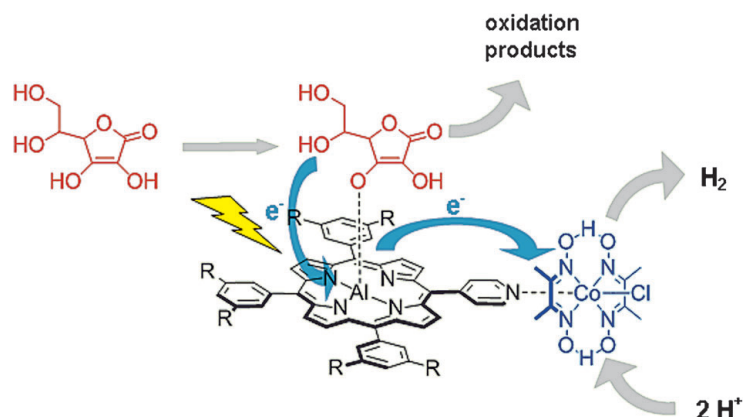


**Figure 34. Natali's self-assembled triad for photo-induced hydrogen evolution.**

More specifically, the triplet excited state of the chromophore is quenched by ascorbic acid acting as a sacrificial electron donor, in acetone–water:7–3 mixture ( $\lambda > 400$  nm), giving rise to good overall hydrogen evolving activity (TOF =  $3.6 \text{ min}^{-1}$  based on the catalyst, TON = 117 for the catalyst). Performance was limited by the reduction of the sensitizer (formation of chlorins) and the hydrogenation of the dimethylglyoximate ligand of the cobaloxime. Eventually, association of several components in solution with a polar solvent mixture is not complete and thus hydrogen is evolved by bimolecular pathways involving the excited photosensitizer and the cobaloxime catalyst.

# CHAPTER 4

## ELECTROCATALYTIC HYDROGEN PRODUCTION

### 4.1 Definition of electrocatalysis – Homogeneous electrocatalysis

Although a strict definition of electrocatalysis hasn't been proposed yet [52], we can approach homogeneous electrocatalysis based on the following figure [94]:

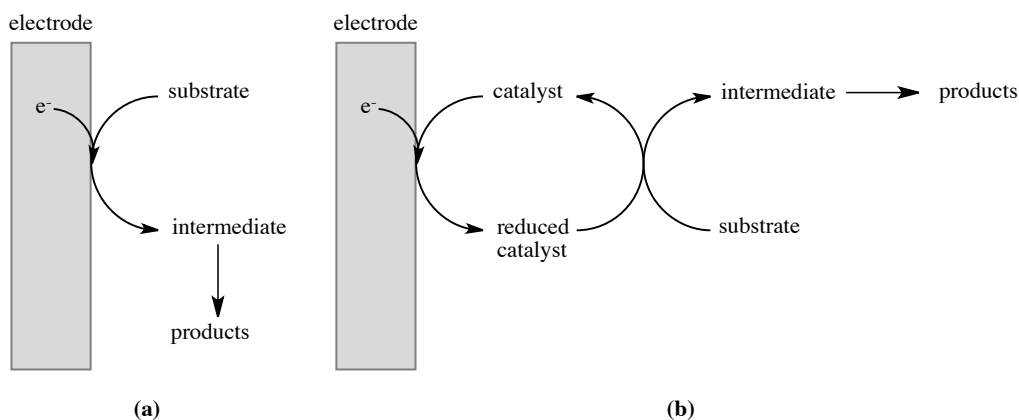


**Figure 35. Homogeneous electrochemical catalysis: (a) direct electrochemical reaction, (b) redox catalyzed electrochemical reaction.**

In the case where no catalysis occurs (Fig. 35a), electrons are directly funnelled into the substrate in an outer-sphere mechanism to create intermediates that lead to products. On the other hand, in a catalyzed electrochemical reaction (Fig. 35b), the catalyst acts as mediator between the electrode and the substrate. However, in this case the active form of the catalyst may interact chemically with the substrate, form an adduct, and thus lead to more selectivity and increased catalytic efficiency. The latter is depicted in the following figure.

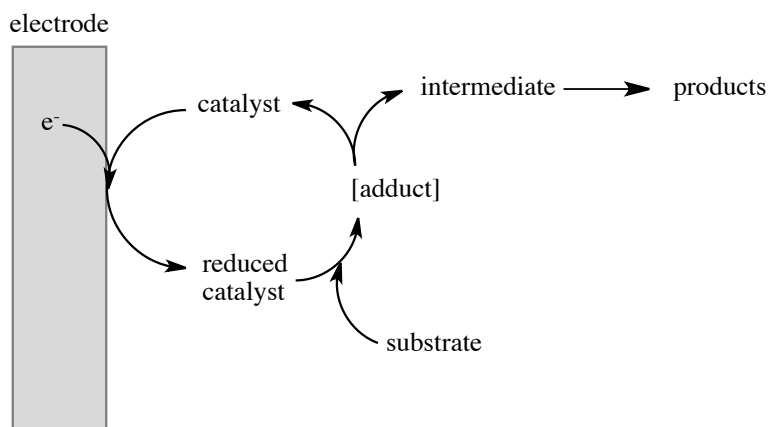


**Figure 36. Chemically catalyzed electrochemical reaction.**

Catalysis occurs when a current is obtained ( $i_{\text{cat.}}$ ) at a potential less negative (when referring to reduction) than when direct electrochemical reaction occurs. Two factors affecting catalysis can be observed at this point:

- the regeneration of the active form of the catalyst must be fast enough in order for catalysis to have acceptable rates
- the formation of an adduct must be faster than the direct electrochemical reaction

## 4.2 Heterogeneous electrocatalysis

Heterogeneous electrocatalysis occurs when a catalyst is deposited or adsorbed on the surface of an electrode. We can experimentally observe if the reaction is inner- or outer-sphere based on the dependence of catalytic activity on the electrode material [95], since an inner-sphere reaction strongly depends on the type of the electrode because there is a direct connection between the catalyst and the electrode surface.

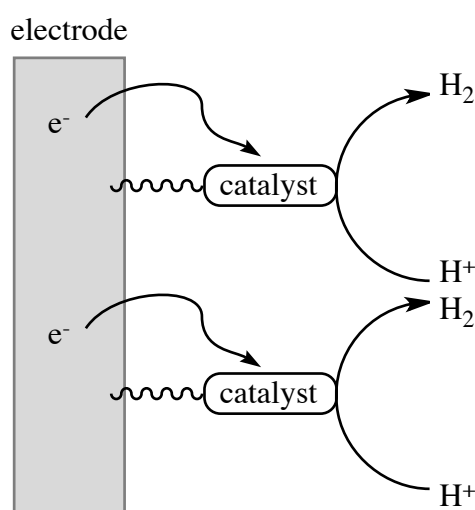


Figure 37. Covalent grafting of a catalyst onto an electrode surface.

## 4.3 Components of a homogeneous electrocatalytic system

### 4.3.1 Catalyst

As in the case of homogeneous photocatalysis, a catalyst must combine some of the following characteristics:

- reversible oxidation/reduction waves in order to take part in reversible electron-transfer reactions

- suitable protonation sites either at the metal or at the ligands (second coordination sphere)
- low toxicity
- low cost

Most of the catalysts applied in photocatalysis can also be employed as electrocatalysts, as will be shown later.

#### 4.3.2 Proton source and solvent

When electrocatalytic experiments are conducted in pure organic solvent, an acid is employed as the proton source. The strength of an acid is dependent on the solvent, due to the different extent of ionization and dissociation of the acid. The most used organic solvents are acetonitrile (MeCN/CH<sub>3</sub>CN) and *N,N*-dimethylformamide (DMF).

**Table 4. Commonly used acids and their ionization constants (pK<sub>a</sub>) in various solvents at 25 °C<sup>a</sup>.**

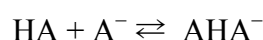
Acid	CH <sub>3</sub> CN	DMF	H <sub>2</sub> O
HClO <sub>4</sub>	2.1	strong	strong
DMFH <sup>+</sup>	6.1		
tosic acid	8.3	2.6	strong
HCl	8.9	3.2	strong
CCl <sub>3</sub> COOH	10.6	3.5	0.7
anilinium	10.7		4.6
CF <sub>3</sub> COOH	12.7	6.0	0.23
Et <sub>3</sub> NH <sup>+</sup>	18.6	9.2	10.75
C <sub>6</sub> H <sub>5</sub> COOH	20.7	12.2	4.19
CH <sub>3</sub> COOH	22.3	13.5	4.76

<sup>a</sup>: values from ref. [68,69,96,97]

Nevertheless, in acetonitrile for most acids the effect of homoconjugation occurs [96,97]. To explain this effect, let us consider the ionization of an acid HA in a solvent such as acetonitrile:

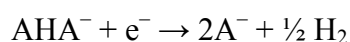


Homoconjugation occurs when the conjugate base  $\text{A}^{-}$  and the acid HA form hydrogen-bonded adducts:



The establishment of the latter equilibrium shifts the ionization equilibrium to the right, increasing thus the concentration of protons released, i.e. the acidity of the acid is increased.

This can complicate the reduction waves observed for an acid, as several reactions can be simultaneously observed apart from the simple reaction  $2\text{H}^{+} + 2\text{e}^{-} \rightarrow \text{H}_2$ , such as:



These reactions occur at different potentials than the simple proton reduction to produce hydrogen, making difficult calculations of the overpotential required for the reduction of protons in the presence of a catalyst.

#### 4.4 Overpotential ( $\eta$ )

Electrocatalysts are often compared in the literature based on catalytic results, namely the turnover number (TON) and turnover frequency (TOF) achieved, but because different research groups assess catalysts at different conditions, direct comparisons cannot be made. The overpotential is another factor of evaluating the performance of a catalyst [97].

The thermodynamically calculated potential required to reduce protons at an electrode is different from the potential found experimentally. In other words, more negative potential value is required to reduce protons than the potential value calculated, indicating that higher-energy electrons must be utilized for the proton reduction reaction to occur at an acceptable rate. The difference between the calculated and

found potentials is called overpotential, introducing in this way a kinetic factor that relates to activation energy.

#### 4.5 Faradaic yield

The faradaic yield or faradaic efficiency measures the yield of an electrochemical reaction. In other words, in a chronoamperometry (Q vs t) experiment where charge (i.e. electrons) is passed through a solution, these electrons are consumed for various reductions to occur. The moles of hydrogen evolved relative to the moles of hydrogen that would evolve if all electrons were consumed for the reaction  $2\text{H}^+ + 2\text{e}^- \rightarrow \text{H}_2$ , expresses the faradaic yield:

$$n_{\text{H}_2, \text{theoretical}} = \frac{Q}{2F}$$

where Q is the charge (in Coulombs) passed through the solution, 2 is for the two-electron reduction of protons, and F is the Faraday constant (96485 C/mol).

Then, the faradaic yield is expressed as the ratio of evolved hydrogen (by means of gas chromatography) and the theoretical moles of hydrogen:

$$\text{Faradaic yield} = \frac{n_{\text{H}_2, \text{measured}}}{n_{\text{H}_2, \text{theoretical}}}$$

#### 4.6 Hydrogen evolving electrocatalytic systems from the literature

##### 4.6.1 Dithiolene complexes as catalysts

An early report by Begum et al. in 2010 [98] involved the preparation and characterization of a methyl-ester substituted bis-dithiolene nickel complex.

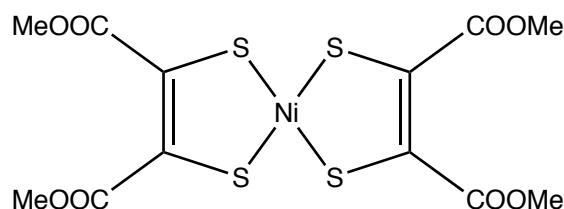


**Figure 38.** Methyl-ester substituted bis-dithiolene nickel complex reported by Begum et al.

This complex was employed as a hydrogen reducing catalyst in acetonitrile with p-toluene sulfonic acid as the proton source on a glassy carbon working electrode. A new peak at  $-0.69$  V vs Ag/AgCl was attributed as the catalytic wave corresponding to proton reduction. Upon increasing acid concentration, the current increased with a

concomitant negative shift of the reduction peak by 8 mV. In the absence of the catalyst, the reduction peak of protons appears at  $-1.71$  V vs Ag/AgCl. Employing a similar nickel complex with cyanide groups instead of carboxy–methylester was found to reduce protons at  $-1.25$  V vs Ag/AgCl. Controlled potential electrolysis at  $-1.00$  V (1 mmol complex, 50 mm acid) induced hydrogen evolution. Immobilization of the same complex was investigated in aqueous solution and it was found that proton reduction occurs at  $-0.71$  V vs Ag/AgCl compared to the reduction of tosic acid occurring  $-1.40$  V vs Ag/AgCl of an untreated electrode. EPR, UV–Vis, and  $^1\text{H}$ –NMR studies indicated that the catalyst protonated at the sulfur atom.

The same group reported a similar compound in 2012 [99], which they as well evaluated as a proton reducing catalyst.

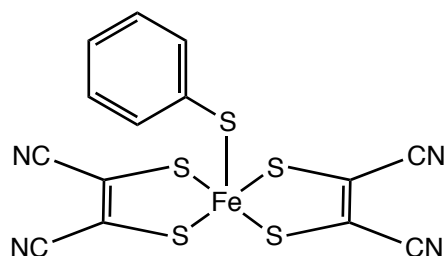
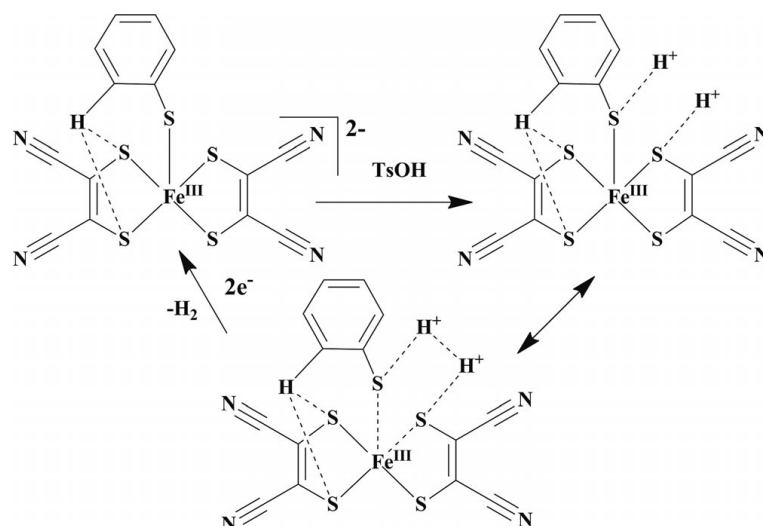


**Figure 39. Pentacoordinate iron bis–dithiolene complex prepared by Begum et al.**

Under the same conditions as in their previous work [98], this iron complex catalyzed proton reduction at  $-0.309$  V vs Ag/AgCl in the presence of tosic acid in acetonitrile. Comparison to a similar compound with bromide as the axial ligand (proton reduction observed at  $-1.1$  V vs Ag/AgCl) led to the proposal of the following mechanism, in which the coordinated benzenethiol acts as a proton relay.



**Scheme 14. Proposed hydrogen evolution mechanism for the electrocatalytic proton reduction by an iron bis-dithiolene complex.**

At the same time [59], the groups of Holland and Eisenberg reported a cobalt bis-dithiolene complex acting as photocatalyst and electrocatalyst. A more detailed study of a series of related cobalt complexes [34] revealed their activity on hydrogen evolution reaction in pure acetonitrile and mixed acetonitrile–water:1–1 complexes, in the presence of trifluoroacetic acid as the proton source on a glassy carbon electrode.

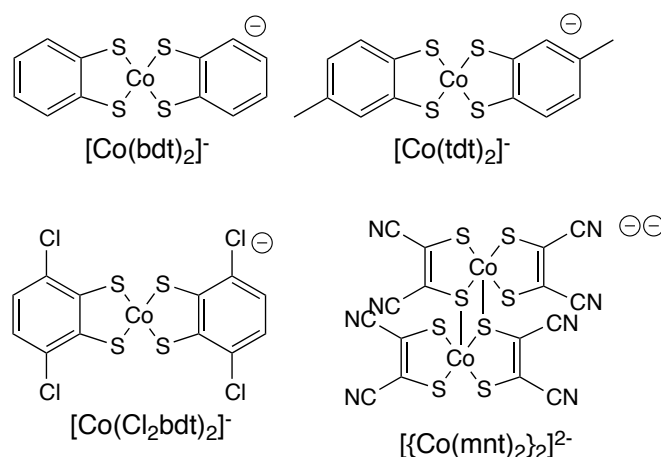


**Figure 40. Cobalt dithiolene catalysts studied by Eisenberg and Holland groups.**

Upon increasing acid concentration, a new wave appeared on the reduction wave of the  $[Co(bdt)_2]^-$  complex, suggesting an ECEC hydrogen evolution mechanism. This mechanism involves initial reduction to the dianion, protonation, another reduction and a final protonation to yield dihydrogen and the monoanionic catalyst. For catalyst  $[Co(Cl_2bdt)_2]^-$  the catalytic wave appears at a more cathodic by 0.25 V potential than the reduction wave of the catalyst. When  $[Co(mnt)_2]^{2-}$  is reduced, it fully

disproportionates to two dianionic complexes which exhibit a catalytic wave at  $-1.40$  V vs SCE, the most negative value of all the series. It was speculated that differences in electrocatalytic activity must depend on the protonation sites of the reduced intermediate for each complex.

At that time, interest in dithiolene complexes re-emerged, as reports on this class of catalysts increased. Eckenhoff et al. [76] reported on a series of molybdenum complexes that act both as photocatalysts and electrocatalysts.

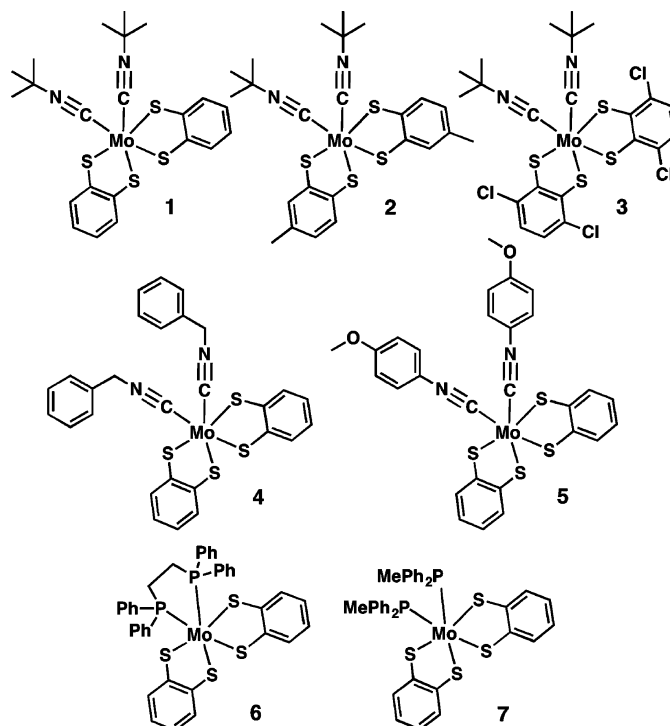


**Figure 41. Molybdenum complexes acting as catalysts in proton reduction.**

In a typical setup,  $0.5$  mM of complex in acetonitrile or  $N,N'$ -dimethylformamide with trifluoroacetic acid as proton source with a glassy carbon electrode. However, since reduction wave of trifluoroacetic acid at the GCE interferes with the reduction of the complex, a hanging drop mercury electrode was employed. This in fact perplexed the voltammograms, with changes appearing possibly due to the effect of mercury on dithiolene ligands.

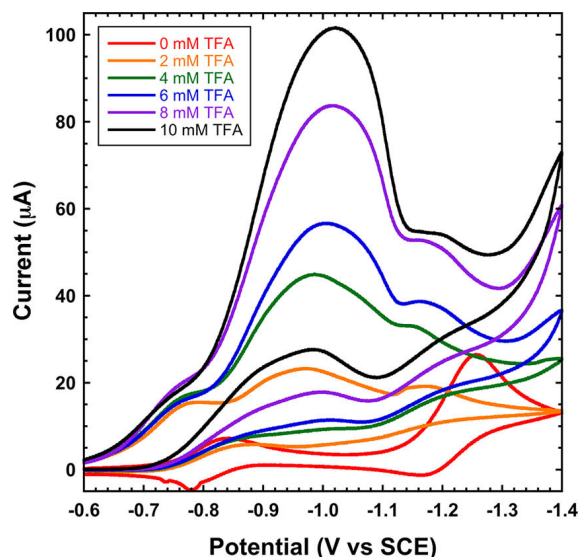


**Figure 42.** Electrocatalysis of catalyst 1 with a hanging mercury drop working electrode and glassy carbon auxiliary electrode (0.5 mM complex, CH<sub>3</sub>CN–H<sub>2</sub>O:9–1).

Catalysis occurs at  $\sim -1$  V vs SCE for most catalysts, with an exemption for catalyst 6 ( $-1.57$  V vs SCE).

The catalysts proved to be unstable in the presence of water, as indicated by recording the cyclic voltammogram in the presence of increasing amounts of water for compound 1, so in overall these results do not provide clear indication of the active catalyst.

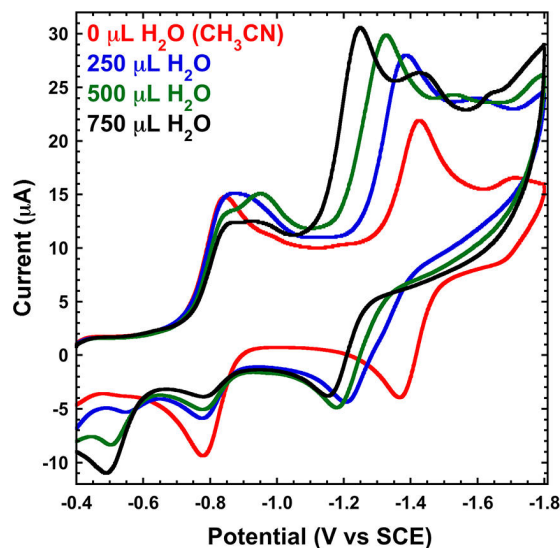


**Figure 43.** Effect of water on CV of catalyst 1 (0.5 mM).

In another report from Letko et al. [66], a series of cobalt–aryldithiolene complexes were prepared, characterized and studied toward electrocatalytic hydrogen evolution in acidic media (anilinium in DMF,  $pK_a = 4.3$  in DMF).

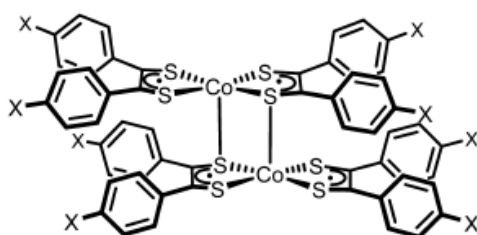


**Figure 44.** Cobalt aryl–dithiolenes catalysts reported by Letko et al. (X = F, Cl, Br, OMe).

Treatment of the dianionic species with stoichiometric quantities of a weak acid afforded dihydrogen and the monoanionic cobalt–diaryldithiolenes species. Addition of acid in the bromo–substituted complex evoked hydrogen evolution at  $-1.45$  V vs  $\text{Fc}^{0/+}$  with a faradaic yield of  $\sim 90\%$  and an overpotential of  $0.35$  V vs  $\text{Fc}^{0/+}$ . The fluoro– and methoxy– derivatives also displayed catalytic activity, the waves occurring at  $-1.37$  and  $-1.46$  V vs  $\text{Fc}^{0/+}$ , respectively.

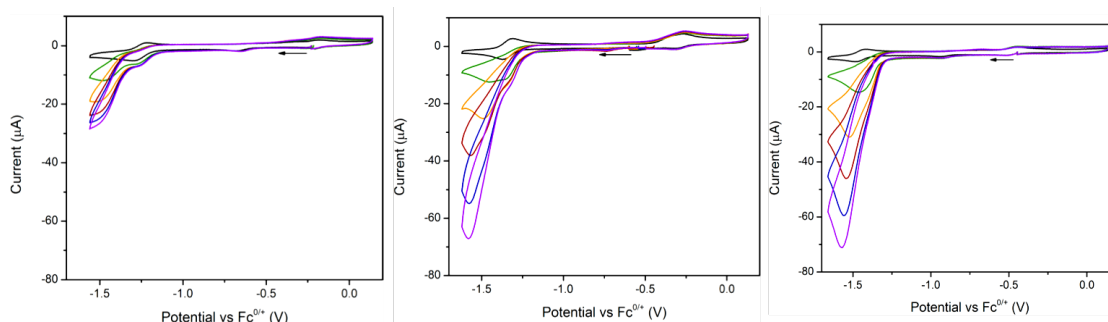
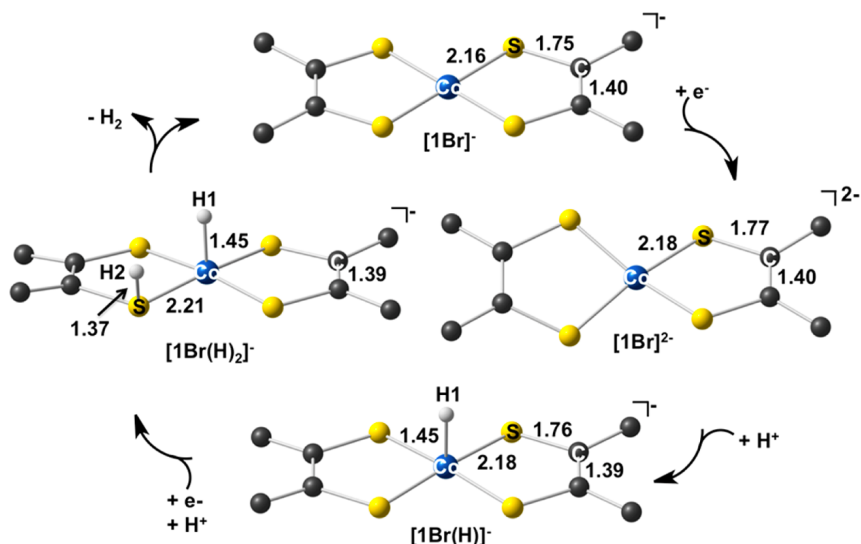


**Figure 45.** Catalytic response for the fluoro– (left), bromo– (center), methoxy– (right) monoanionic cobalt dithiolenes complexes in the presence of anilinium ( $0.3$  mM catalyst,  $0 - 25$  mM acid (black to magenta traces, respectively)).

Employing a weaker acid (dichloroacetic acid,  $\text{pK}_a = 7.2$  in DMF) did not lead to observation of hydrogen evolving activity for all complexes but the methoxy– derivative.

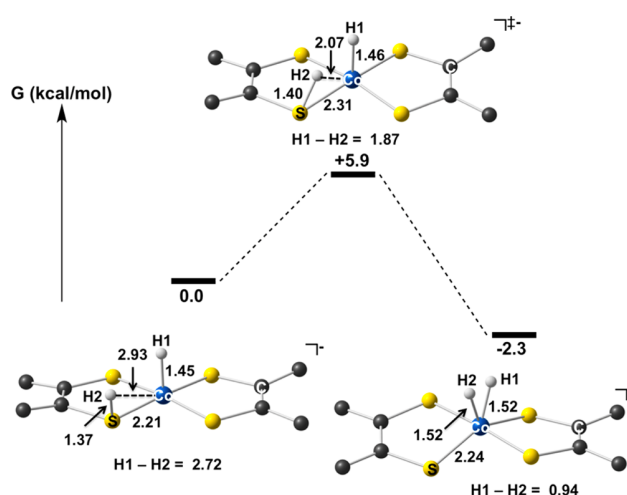
A rinse test involving the GCE was performed and it was found that only  $25\%$  of the catalytic current is present when scanning a fresh acid solution.

DFT studies suggested that hydrogen elimination proceeds through a diprotonated intermediate with a Co–H bond and a protonated S center in an ECEC mechanism, as shown in the following scheme:



**Scheme 15.** Proposed mechanism for hydrogen evolution mechanism by cobalt aryldithiolene complexes derived by theoretical and electrochemical data (bonds in Å, angles in °).

A transition state involving proton migration to the metal has also been observed theoretically, with a computed free energy of 5.9 kcal/mol.



**Scheme 16.** Proton migration from sulfur to cobalt atom (bonds in Å, angles in °).

Catalyst  $[\text{Ni}(\text{bdt})_2]^-$  was investigated toward proton reduction from acetic acid in acetonitrile solution along a series of nickel complexes [77]. The catalytic wave appeared at  $-2.25$  V vs SCE, with no mention of faradaic yield or overpotential value.

The group of Jones [100] reported the preparation, characterization, and hydrogen evolving activity of two nickel diphosphine dithiolate complexes, one comprising a ferrocene moiety as an internal electron relay.

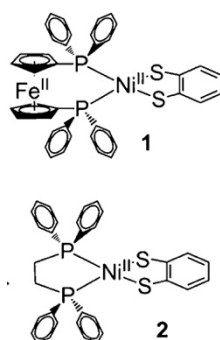


**Figure 46. Complexes prepared by the group of Jones.**

Addition of acetic acid in a tetrahydrofuran 2.6 mM complex 1 solution ( $pK_a = 22.48$  in THF) led to increasing current, indicating catalysis. Faradaic yield was found 99% (stability over 4 h), and compound 2 showed no hydrogen evolving activity even in the presence of the much stronger toxic acid. Rinse tests on the glassy carbon electrode indicated that the catalyst is molecular is not adsorbed. Kinetic analysis revealed a  $[H^+]$ -independent rate constant of  $1240\text{ s}^{-1}$  with a calculated TOF of  $\sim 1200\text{ s}^{-1}$ , with overpotential values of  $0.265 - 0.500\text{ V vs Fc}^{0/+}$ .

An ECEC mechanism was proposed, with the Ni and Fe ions not interacting as indicated by DFT calculations.

Protonation was calculated to be favoured on the Ni (I) center formed upon reduction than the sulphur atom, with a significant tetrahedral distortion of more than  $40^\circ$ . This distortion was concluded essential in the overall hydrogen evolving mechanism, in order for open coordination sites on the distorted intermediate to accommodate protons.

In the same context, Kochem et al. [101] prepared a mixed-ligand nickel complex which contains a pendant amine group as an internal proton relay.

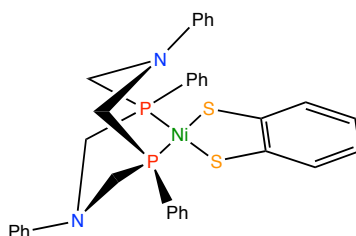


**Figure 47. Heteroleptic complex prepared by Kochem et al.**

Increasing trifluoroacetic acid in a dichloromethane solution (1 mM) of the complex evoked an increase in current, an indication of a catalytic procedure at  $-2.4\text{ V vs Fc}^{0/+}$

with an overpotential of  $-1.6$  V on a glassy carbon electrode. Bulk electrolysis of 3.2 h gave a TON of 30 and a TOF of  $9.3 \text{ h}^{-1}$ .

The hydrogen evolving activity was attributed to the protonation of the Ni (I) formed upon reduction, along with a large geometric rearrangement around the nickel ion.

In the bio-inspired family of complexes, the group of Fontecave [102] reported on a molybdenum oxo-dithiolene complex that act as electrocatalyst in acetonitrile with trifluoroacetic acid as proton source.

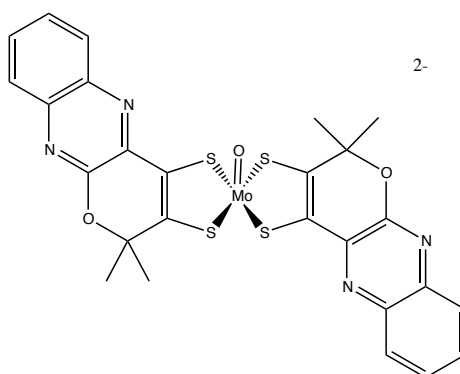
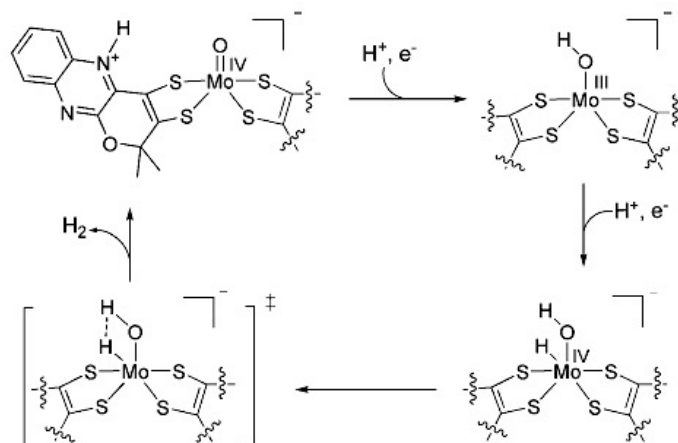


**Figure 48. Bio-inspired complex reported by the group of Fontecave.**

Addition of trifluoroacetic acid triggers the appearance of a wave with a half-wave potential of  $-0.75$  V vs Ag/AgCl, corresponding to an overpotential of  $0.7$  V vs Ag/AgCl. At  $0.1$  M TFA concentration, a TOF value of 1030 at  $-1.3$  V vs Ag/AgCl was calculated, with faradaic yields reaching 92% after 3 h and 86% after 1.5 h.

The proposed mechanism for hydrogen evolution involves N-protonation which facilitates subsequent reductions. Secondly, it was suggested that the Mo-oxo moiety reacts with two electrons and two protons to form a reactive hydrido  $[\text{Mo}^{\text{IV}}\text{OH}(\text{H})-(\text{LH})(\text{L})]$  intermediate.



**Scheme 17. Proposed mechanism for hydrogen evolution with molybdenum dithiolene complexes.**

Evolving the same work, the same group prepared a series of tungsten dithiolene complexes [12] as electrocatalysts.

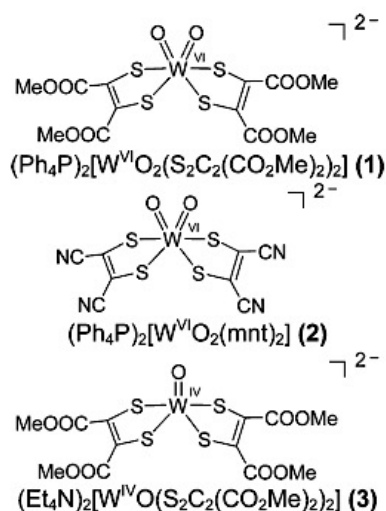


**Figure 49. Tungsten dithiolene complexes prepared by the group of Fontecave.**

Addition of acetic acid in acetonitrile ( $pK_a = 22.3$  in MeCN) solution for each complex, with an onset potential of  $-1.2$  V vs Ag/AgCl. Rinse tests indicated the molecular nature of the catalysts, with overpotentials of  $0.7$ – $0.8$  V vs Ag/AgCl for  $0.1$  M acetic acid.

From controlled potential coulometry at a mercury pool electrode, for a 3h-experiment, faradaic yields of 94%, 75%, and 100% were found for complexes 1, 2, and 3, respectively. Compound 2 is the most efficient, reaching 35 TONs after 3 h with initial TOF of  $12 \text{ h}^{-1}$ .

Experimental results and DFT calculations showed that the dioxo  $W^{VI}O_2(L)_2$  starting complex is a precatalyst, transforming to an active mono-oxo  $W^{IV}O(L)_2$  species, upon reduction/protonation. The mechanism proposed involves two electrons and two protons, cycling between the  $W^{IV}O(L)_2$  species and a reactive hydride  $W^{IV}OH(H)(L)_2$  intermediate. In this W-hydroxo-hydride species the oxygen ligand brings a proton in the vicinity of the reactive metal-bound hydride, thus facilitating protonation of the hydride and further  $H_2$  formation.

In a recent report, the group of Sakai reported a Ni dithiolate water reduction catalyst providing ligand-based proton-coupled electron-transfer pathways [103].

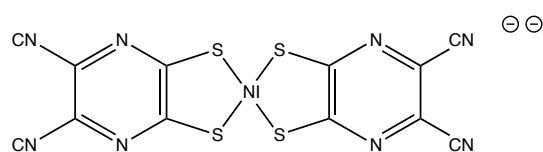


**Figure 50. Catalyst prepared by the group of Sakai.**

The catalyst overpotentials of 0.33–0.4 V at pH = 4–6, reaching a TON of 20000 over 24 h, with a faradaic yield of 92–100% on a glassy carbon electrode. Electrochemical and DFT studies revealed that the diprotonated one electron-reduced species ( $[Ni^{II}(dcpdt)(dcpdtH_2)]^{2-}$  or  $[Ni^{II}(dcpdtH)_2]^-$ ) forms at pH < 6.4 via ligand-based proton coupled electron-transfer (PCET) pathways, leading to electrocatalytic hydrogen evolution without applying highly negative potentials required to generate low-valent nickel intermediates such as Ni (I) or Ni (0).

Rinse tests indicated the homogeneity of catalysis, but it was found that the complex was readily adsorbed on the GCE merely by immersing. X-ray studies, however, revealed that the  $NiS_4$  core is retained even in the adsorbed form of the catalyst. Adsorption was not present on indium tin oxide (ITO) electrodes.

#### 4.6.2 On the stability of dithiolene complexes as electrocatalysts

Taking into consideration the impact of these results, it was not until quite recently that comments on the stability of dithiolene complexes were reported. In an instructive work, Fang et al. [104] reported on the stability of a typical bis-dithiolene catalyst,  $[Ni(bdt)_2]^-$  in the presence of p-bromo-anilinium as an acid ( $pK_a = 9.43$  in acetonitrile).

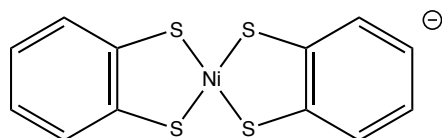


**Figure 51.**  $[\text{Ni}(\text{bdt})_2]^-$ .

Using various conditioning techniques, they showed that films electrodeposited onto glassy carbon electrodes from acidic acetonitrile solutions of  $[\text{Bu}_4\text{N}][\text{Ni}(\text{bdt})_2]$  are active toward electrocatalytic hydrogen production at potentials 0.2–0.4 V positive of untreated electrodes ( $-1.2$  V vs  $\text{Fc}^{0/+}$ ). This activity is preserved after rinsing the electrode and measuring catalysis in a fresh acid solution, with X-ray photoelectron studies showing the presence of Ni and S in the film.

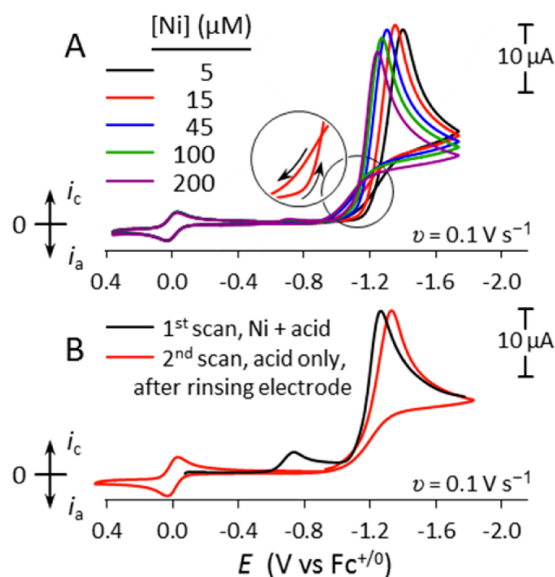


**Figure 52.** (A) Voltammograms of  $[\text{Ni}(\text{bdt})_2]^-$  with p-bromo-anilinium in MeCN (GCE), (B) Linear sweep voltammogram of  $[\text{Ni}(\text{bdt})_2]^-$  (black trace) and subsequent CV using the same electrode (red trace) after rinsing and transfer to fresh acid solution without added Ni catalyst.

A first indication of catalyst decomposition is the crossing between the traces in the cyclic voltammogram (Fig. 52A), verified by a linear sweep voltammogram that deposited the material on the electrode surface which proved catalytically active (Fig. 52B).

In another conditioning procedure, potential was applied at a value where catalysis is observed for 3 min and subsequent measurement of cyclic voltammogram from a negative potential value to avoid oxidation of any deposited material.

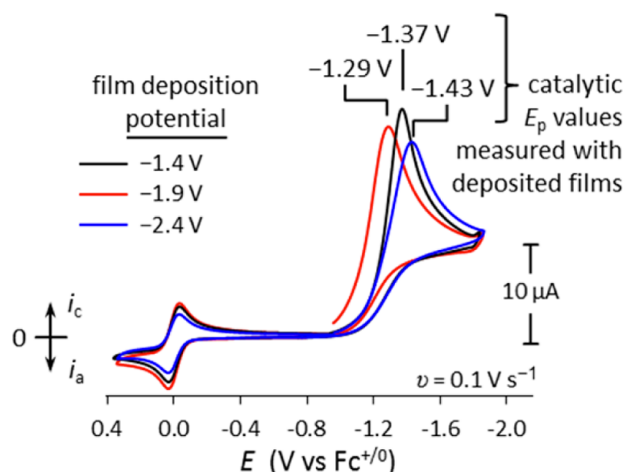


**Figure 53. Voltammograms of p-bromo-anilinium with electrodes conditioned by a 3 min electrodeposition.**

A film on the surface of the GCE was reproducibly generated, showing some catalytic activity.

In the same way, the group of Dempsey [105] re-examined the  $[\text{Co}(\text{bdt})_2]^-$  catalyst reported earlier by Eisenberg [34,59] and found that the complex transforms into an adsorbed film on the electrode upon addition of acid prior to any reduction. Rinse tests verified that this occurs for a variety of acids including substituted aniliniums and TFA, and further studies showed that a black particulate material is formed in the presence of acid. This material upon reduction releases  $[\text{Co}(\text{bdt})_2]^-$  in solution. Thus, they proposed that the hydrogen evolution mechanism proposed by Eisenberg does not fully depict the truth, but an adsorbed intermediate maintaining its molecular nature must also be formed.

Even though the catalysis is not always purely homogeneous with dithiolene complexes, these compounds proved useful catalysts for the fabrication of materials and nanosheets that exhibit proton reducing activity, as reported recently in the literature [106–109].

## CHAPTER 5

### MATERIALS AND METHODS

#### 5.1 Starting materials – reagents – solvents

The following reagents and starting materials were obtained from Alfa Aesar, Merck, or Sigma Aldrich and used as received unless otherwise noted. Solvents used in preparation of compounds were purified when necessary according to literature procedures [110]. Solvents used in electrochemistry and electrocatalytic experiments were HPLC grade and used without further purification. Solvents used in spectroscopy were spectroscopy grade. Water used in experiments was purified through a Milli-Q device. Deuterated solvents were used as received apart from CDCl<sub>3</sub> which was distilled from dry K<sub>2</sub>CO<sub>3</sub> and stored in the dark.

#### 5.2 Instrumentation

IR spectra were recorded in KBr pellets with a 2.0 cm<sup>-1</sup> resolution using a Shimadzu IR Affinity-1 FT-IR spectrometer.

Elemental analyses were conducted using a LECO-183 CHNS analyzer.

NMR spectra were recorded using a Varian Unity Plus instrument (300 MHz) and spectra were corrected with the residual solvent peak as an internal standard.

UV-vis spectra were recorded with Hitachi U-2000 and Varian Cary 3E spectrophotometers in 1.0 cm quartz cuvettes.

Emission spectra were recorded using a RF-5301 Shimadzu spectrometer in 1.0 cm quartz cuvettes.

Electrochemical experiments were performed using an AFCBP1 Pine Instrument Company and Bio-Logic SP300 potentiostat. Cyclic voltammograms were recorded in a two-compartment or one-compartment cell with a glassy carbon working electrode, an Ag/AgCl (KCl 3M) reference electrode, and a platinum wire counter electrode (located in the second compartment). The glassy carbon electrode was polished with diamond paste (1 μm) or alumina (1 μm) on a polishing cloth before each measurement. The solution was purged with argon or nitrogen gas prior to measurements. At the end

of each experiment, sublimed ferrocene was added as an internal standard. *n*-tetrabutylammonium hexafluorophosphate (doubly recrystallized from absolute ethanol) was used as the supporting electrolyte in 0.1 M concentration. Compounds were 1 mM in concentration unless otherwise noted.

Bulk electrolysis was performed in a two-compartment cell with a glassy carbon rod electrode ( $\varnothing$  10 mm, Neyco, Paris, France), an Ag/AgCl reference electrode, and a platinum wire counter electrode (located in the second compartment). The cell was continuously purged with nitrogen ( $5 \text{ mL min}^{-1}$ ), and the output gas was analyzed at 2 min intervals in a PerkinElmer Clarus 500 gas chromatograph using a previously described setup [111].

Photochemical experiments were conducted using an Oriel 1000 W Xe lamp with a UV and IR cutoff filter ( $\lambda > 335 \text{ nm}$ ) in 30 mL scintillation vials. 10 W VK/02001/G/D/230V white LEDs by Spotlights were also used with a luminosity of 700 LM. A typical photochemical hydrogen evolution experiment was conducted as follows: in a 30 mL scintillation vial the catalyst ( $\mu\text{M}$  concentration), the chromophore (0.1 mM), and sacrificial electron donor are dissolved and mixed in the dark using the desired solvent mixture. The mixture is then deaerated via Ar and sealed using rubber septums (Aldrich).

The evolved  $\text{H}_2$  was analyzed by a BRUKER 30-GC (gas chromatographer) with a TCD detector operating at  $150 \text{ }^\circ\text{C}$  and a CP-Molsieve  $5 \text{ \AA}$ , PLOT fused silica column. The gas flow was set at  $10 \text{ mL/min}$ . The oven operated at  $40 \text{ }^\circ\text{C}$  and the injector at  $70 \text{ }^\circ\text{C}$ . The  $50 \mu\text{L}$  gas samples were injected using a Hamilton CO (1710 RN) gastight microliter syringe.

### 5.3 X-ray crystal structure determination

X-ray crystal structures were solved by Dr. C. Papatriantafyllopoulou (University of Cyprus, a SuperNova A Oxford Diffraction diffractometer, equipped with a CCD area detector and a graphite monochromator utilizing Mo  $K\alpha$  radiation ( $\lambda = 0.71073 \text{ \AA}$ ) and Cu  $K\alpha$  radiation ( $\lambda = 1.54184 \text{ \AA}$ )), Dr. C. Raptopoulou and Dr. V. Psycharis (NCSR Demokritos), and Assistant Prof. K. Bethanis (Agricultural University of Athens).

Suitable crystals covered with paratone–N oil were mounted on the tip of glass fibers or scooped up in cryoloops at the end of a copper pin and transferred to a goniostat, where they were cooled for data collection. Empirical absorption corrections (multiscan based on symmetry–related measurements) were applied using CrysAlis RED software [112]. The structures were solved by direct methods with SIR9239 and refined on F2 using full–matrix least squares with SHELXL97 [113]. Software packages used: CrysAlis CCD for data collection [112], CrysAlis RED for cell refinement and data reduction [112], WINGX for geometric calculations [114], and MERCURY for molecular graphics [115]. The non–hydrogen atoms were treated anisotropically, whereas the hydrogen atoms were placed in calculated, ideal positions and refined as riding on their respective carbon atoms.

#### **5.4 Density Functional Theory (DFT) calculations**

DFT calculations were performed by Dr. M. Field (DYNAMO/DYNAMOP, Institut de Biologie Structurale, UMR CNRS, Université Grenoble Alpes). All quantum–chemical calculations were done with a DFT approach using the B3LYP functional and basis sets of triple– $\zeta$  (TZVP) quality. The ORCA program package (version 2.9.1) was employed for all electronic structure calculations [116]. Two approaches were employed for estimation of the relative energies of different species and the energies of the various reactions. In the first, geometry optimizations were performed for all species in a vacuum using the B3LYP functional and a TZVP basis set. Single–point energy calculations were then performed on these optimized vacuum structures using the B3LYP functional and an extended TZVP basis set with extra polarization and diffuse functions. These single–point calculations were performed in both vacuum and DMF solvent using the COSMO implicit solvation method that ORCA implements [117]. In

addition, normal–mode calculations were performed at the vacuum optimized geometries using the B3LYP functional and original TZVP basis set to obtain the appropriate free–energy contributions to the species energies. The latter were estimated as the sum of the singlepoint vacuum energy, the solvation energy (the difference between the single–point solvent and vacuum energies), and the free–energy contribution from the normal–mode calculations. This approach seems to be similar to that used by many workers, including that described by Konezny and co–workers [118]. In the second approach, performed as a check of the first, potential

(rather than free) energies for the reactions were estimated by geometry optimization of all species in DMF solvent using the B3LYP functional and a TZVP basis set, followed by single-point calculations in DMF solvent with the same functional and the larger TZVP basis set.

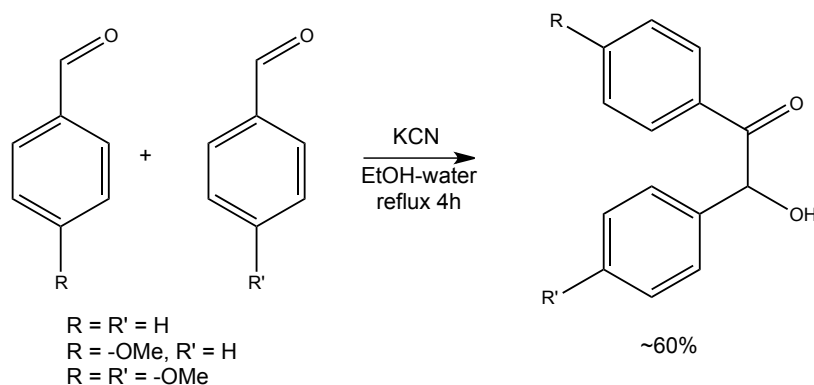
## CHAPTER 6

### PREPARATION OF COMPOUNDS

#### 6.1 Preparation of homoleptic dithiolene complexes

##### 6.1.1 Preparation and characterization of ligands

Benzoin, p-anisoin, and 4-methoxy-benzoin were prepared according to literature procedures [119], based on the condensation of two benzaldehydes in the presence of cyanide as shown below:

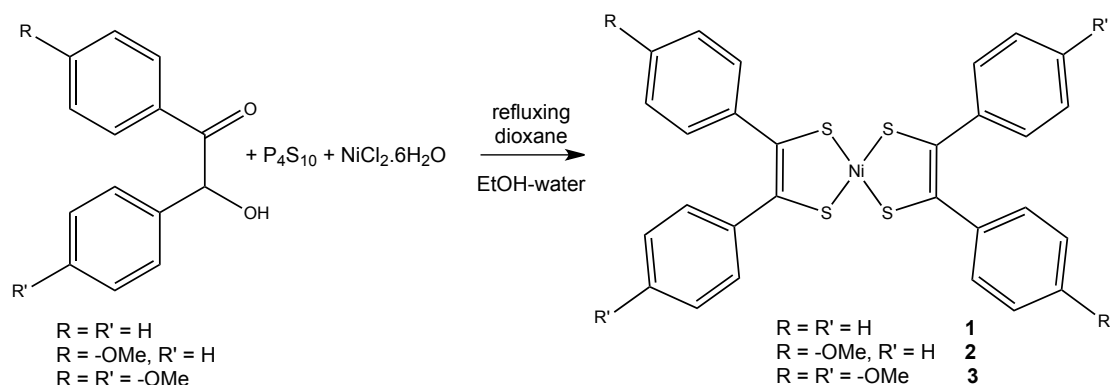


Scheme 18. Preparation of benzoin.

Data for these compounds agree with those reported earlier in the literature.

##### 6.1.2 Preparation and characterization of complexes

Aryl dithiolene complexes were prepared using the benzoin/ $P_4S_{10}$  method of Schrauzer, as modified by Bui et al. [120], with yields reaching 30%:



Scheme 19. Preparation of neutral bis-aryl-dithiolene nickel complexes.

Thus, a series of three complexes was prepared, each bearing none, two, or four methoxy groups. Analytical data are summarized below for each series of complexes:

Anal. Calcd for  $C_{28}H_{20}NiS_4$  (1): C, 61.89; H, 3.71; S, 23.60.

Found: C, 61.92; H, 3.80; S, 23.44.

Anal. Calcd for  $C_{30}H_{24}NiO_2S_4$  (2): C, 59.71; H, 4.01; S, 21.25.

Found: C, 59.58; H, 4.12; S, 21.17.

Anal. Calcd for  $C_{32}H_{28}NiO_4S_4$  (3): C, 57.93; H, 4.25; S, 19.33.

Found: C, 57.81; H, 4.38; S, 19.39.

Anal. Calcd for  $C_{44}H_{56}NNiS_4$  ( $1^-$ ): C, 67.25; H, 7.18; N, 1.78; S, 16.32.

Found: C, 67.18; H, 7.24; N, 1.69; S, 16.41.

Anal. Calcd for  $C_{46}H_{60}NNiO_2S_4$  ( $2^-$ ): C, 65.31; H, 7.15; N, 1.66; S, 15.16.

Found: C, 65.26; H, 7.07; N, 1.75; S, 15.02.

Anal. Calcd for  $C_{48}H_{64}NNiO_4S_4$  ( $3^-$ ): C, 63.63; H, 7.12; N, 1.55; S, 14.16.

Found: C, 63.72; H, 7.20; N, 1.63; S, 14.20.

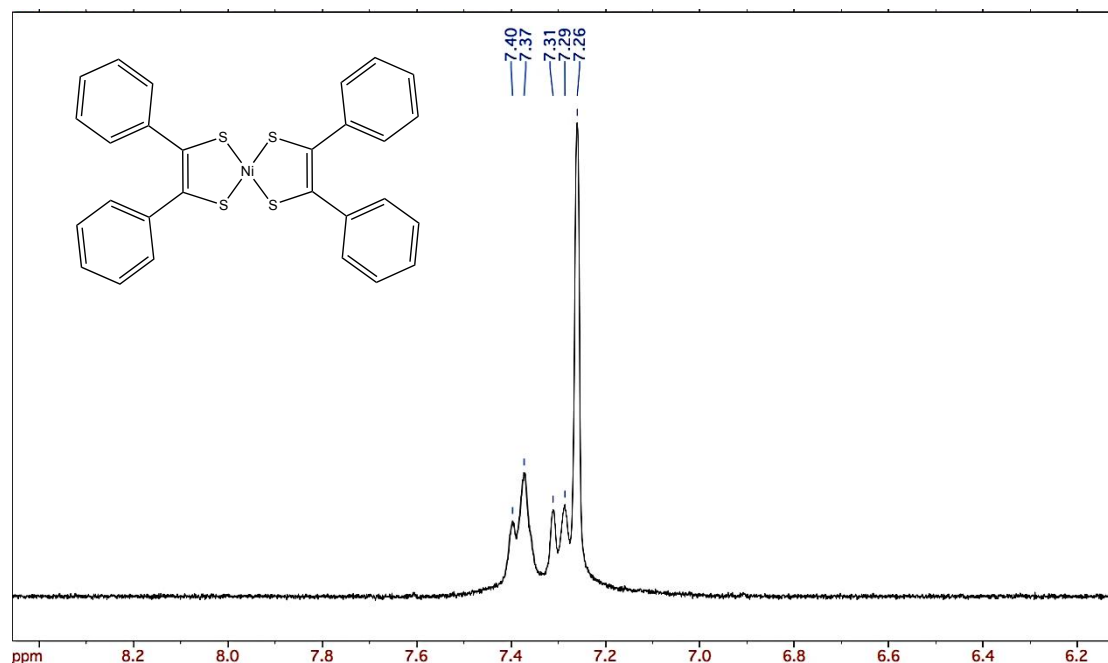


Figure 54.  $^1H$ -NMR spectrum of complex 1 in  $CDCl_3$  ( $\delta$ , ppm), showing the aromatic region where the signals for the 20 protons of the complex appear.

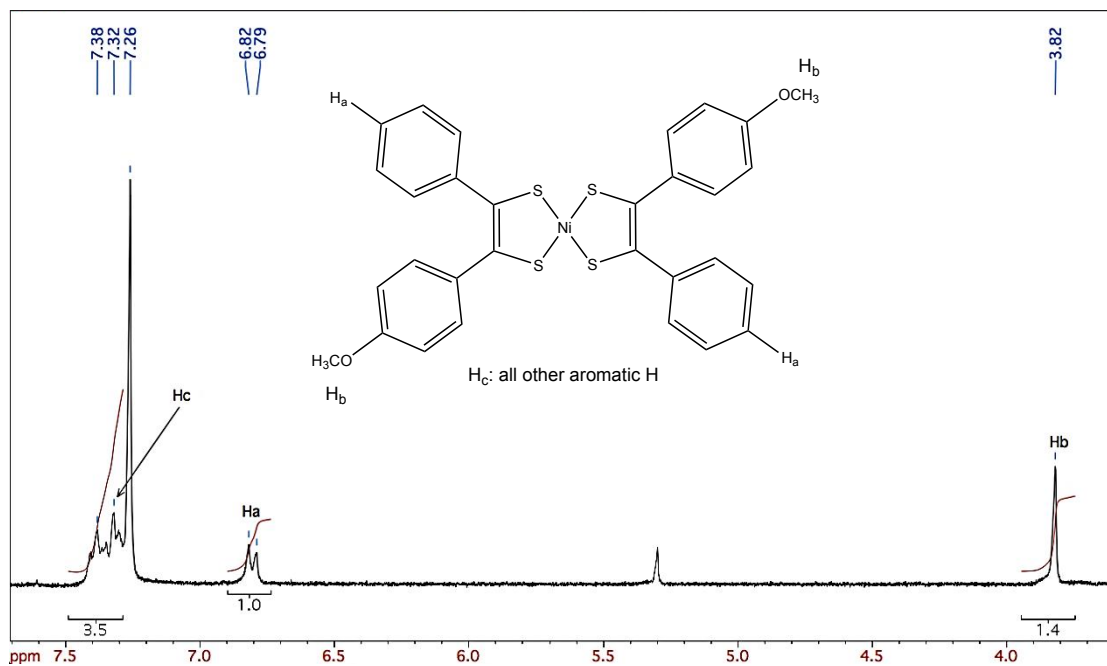


Figure 55. <sup>1</sup>H-NMR spectrum of complex 2 in CDCl<sub>3</sub>.

Table 5. <sup>1</sup>H-NMR data for complex 2 in CDCl<sub>3</sub>

δ (ppm)	multiplicity	H
7.30 – 7.40	m	14
6.8	d	4
3.82	s	6

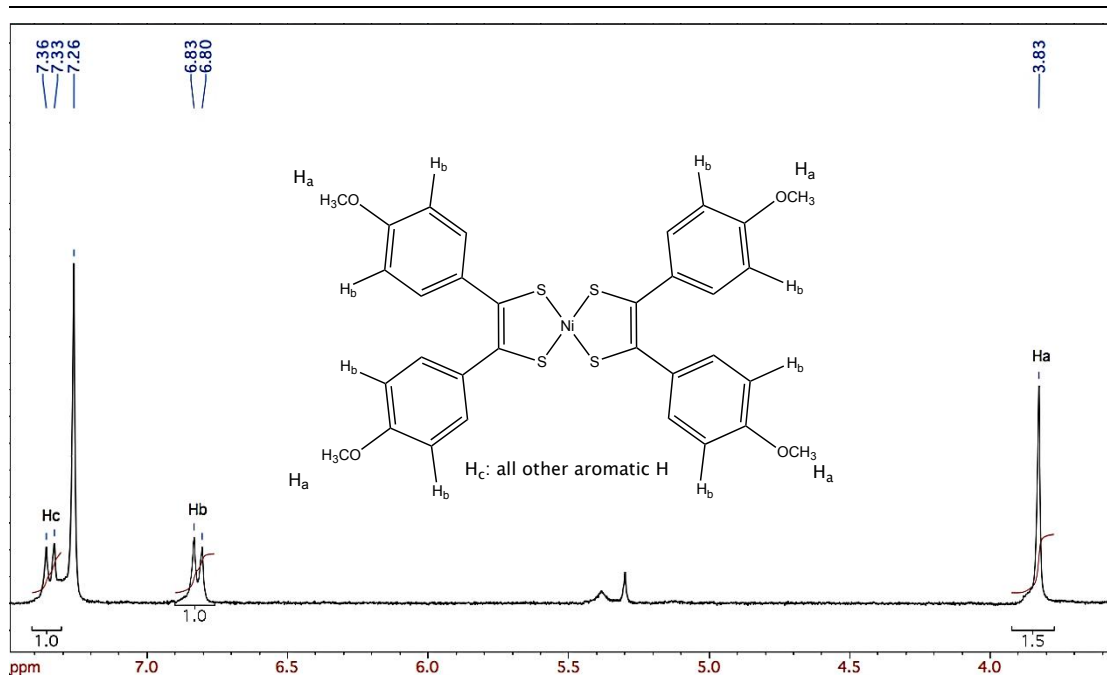
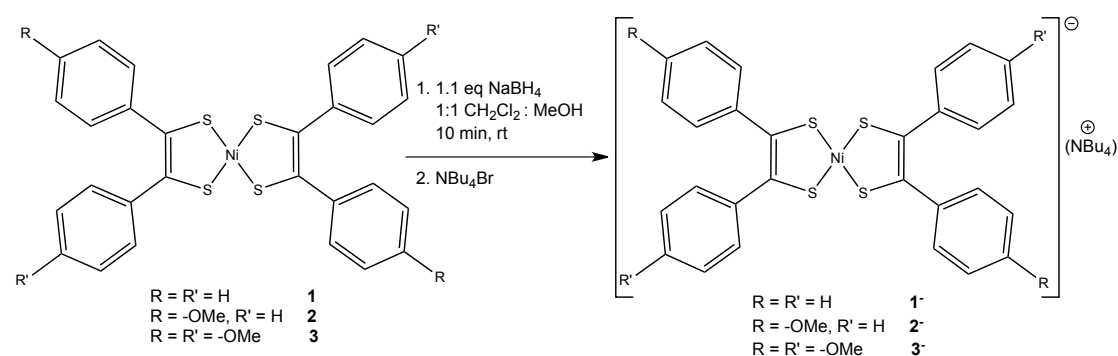


Figure 56. <sup>1</sup>H-NMR spectrum of complex 3 in CDCl<sub>3</sub>.

**Table 6. <sup>1</sup>H-NMR data for complex 3 in CDCl<sub>3</sub>**

δ (ppm)	multiplicity	H
7.35	d	8
6.8	d	8
3.83	s	12

The preparation of monoanionic complexes was achieved in the following general manner: A total of 0.1 mmol of each neutral complex was suspended in a 1:1 mixture of dichloromethane and methanol (30 mL total volume). A total of 1.1 equiv of powdered NaBH<sub>4</sub> was added under stirring, and the green–black suspension gradually turned into a red–brown effervescent solution. The solution was stirred for 10 min until gas evolution ceased, and then 1 equiv of tetra-*n*-butylammonium bromide was added as a solid. The resulting suspension was stirred for 10 min, filtered using a sintered funnel and washed with copious amounts of warm water, methanol, and ether. The resulting solids were dried under vacuum overnight. Yields were quantitative. The anionic compounds are paramagnetic, and thus no NMR spectra were recorded.

**Scheme 20. Preparation of anionic complexes bearing 4-methoxy- and un-substituted benzoinis.**

IR data for the neutral and anionic complexes are shown in the following figures, with corresponding data summarized in Table 7.

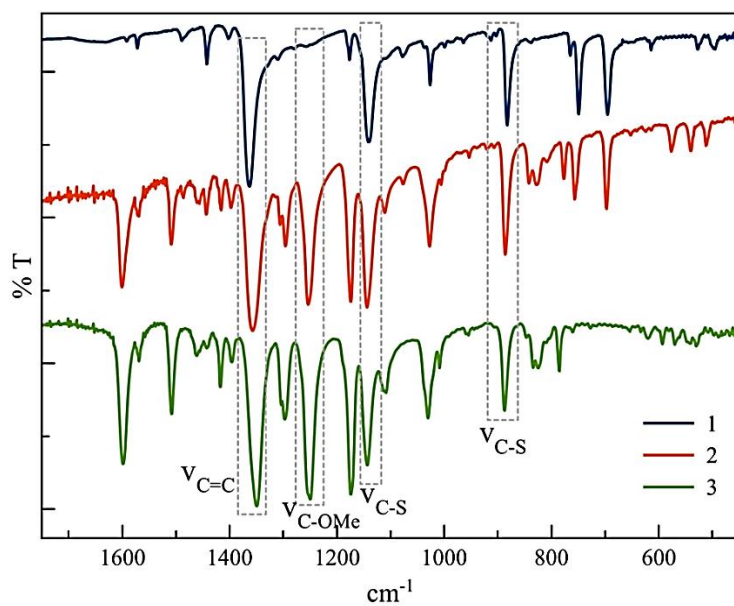


Figure 57. Stacked IR spectra of neutral complexes 1–3.

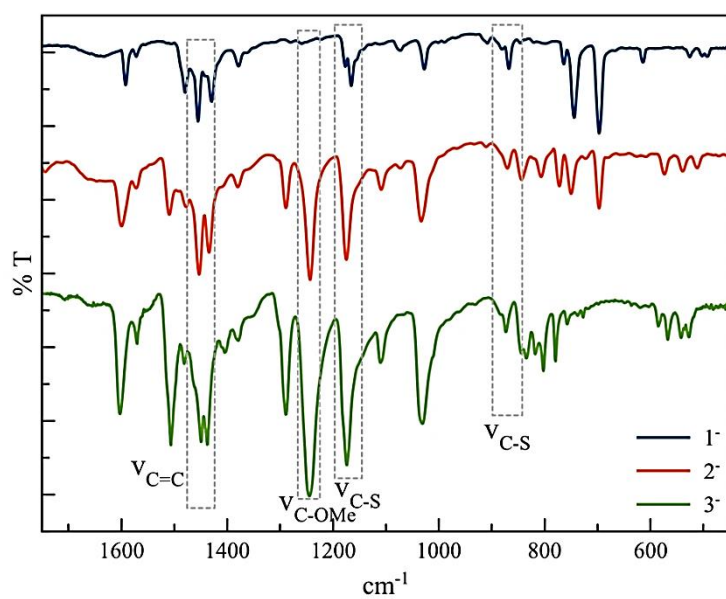


Figure 58. Stacked IR spectra for anionic complexes 1<sup>-</sup> – 3<sup>-</sup>.

**Table 7. IR data for neutral (1, 2, 3) and anionic complexes (1<sup>-</sup>, 2<sup>-</sup>, 3<sup>-</sup>) (values in cm<sup>-1</sup>).**

Complex	$\tilde{\nu}_{C=C}$	$\tilde{\nu}_{C-S}$	$\tilde{\nu}_{C-OMe}$
1	1363 (s)	1140 (s), 882 (w)	–
2	1357 (s)	1144 (s), 886 (w)	1254 (s)
3	1350 (s)	1143 (s), 887 (w)	1249 (s)
1 <sup>-</sup>	1455 (s)	1177 (s), 867 (w)	–
2 <sup>-</sup>	1453 (s)	1175 (s), 871 (w)	1243 (s)
3 <sup>-</sup>	1450 (s)	1174 (s), 874 (w)	1248 (s)

Values obtained from the vibrational spectra are typical for bis-1,2-dithiolene complexes [121,122]. Data reported show a trend within the series, with increasing methoxy substitution of phenyl rings leading to a decrease in  $\tilde{\nu}_{C=C}$  values. A band corresponding to the aryl-OMe vibration ( $\tilde{\nu}_{C-OMe}$ ) is observed around 1250 cm<sup>-1</sup> for the neutral complexes and 1240 cm<sup>-1</sup> for the anionic complexes. This band is absent in the case of unsubstituted compounds 1 and 1<sup>-</sup>. The  $\tilde{\nu}_{C-S}$  values are observed in the region of ~880cm<sup>-1</sup> and follow the opposite trend compared to the  $\tilde{\nu}_{C=C}$  values. Examination of the spectra of the anionic complexes leads to the observation that upon reduction the  $\tilde{\nu}_{C=C}$  values increase and the  $\tilde{\nu}_{C-S}$  values decrease, which is attributed to the fact that in the reduced complexes the ligands possess enedithiolate character [121].

Normalized UV-Vis spectra for complexes 1–3 and their anionic forms (1<sup>-</sup>, 2<sup>-</sup>, 3<sup>-</sup>) were recorded in DMF solution and are shown in the following Figure. All complexes exhibit absorption spectra similar to those reported earlier for similar nickel bis-dithiolene complexes [123].

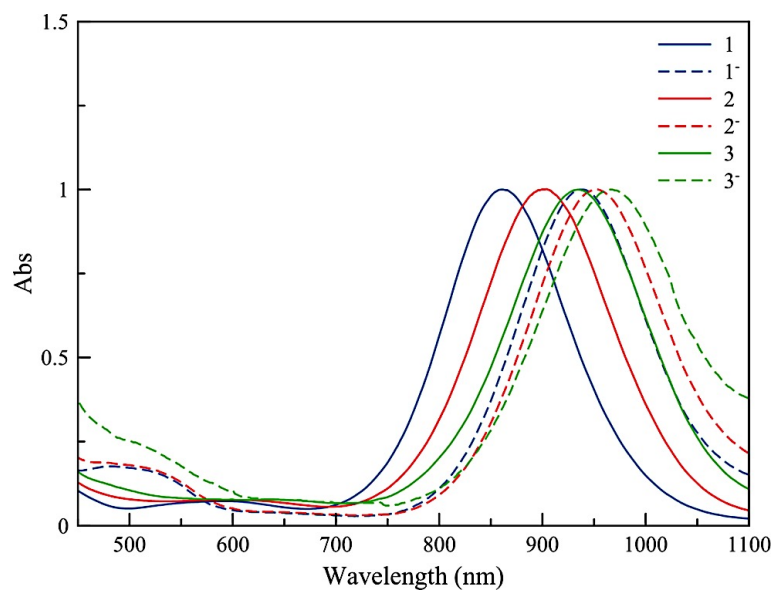


**Figure 59. Normalized absorption spectra for neutral complexes 1–3 and monoanionic complexes 1<sup>-</sup>, 2<sup>-</sup>, and 3<sup>-</sup> as tetrabutylammonium salts in DMF solution.**

All spectra exhibit two major bands around 600 and 900 nm, with the latter being described as  $\pi$ - $\pi^*$  transitions of the dithiolene ligand [124,125]. For 1–3, the prominent band is observed at 860, 902, and 934 nm with molar absorptivity values of 29200, 32100, and 30600  $\text{M}^{-1} \text{cm}^{-1}$ , respectively. Increasing methoxy substitution induces a 30–40 nm bathochromic shift in the near-IR band because the increasing electron-donating effect of additional methoxy groups decreases the highest occupied molecular orbital (HOMO)–lowest unoccupied molecular orbital (LUMO) energy gap of the complex, as reported for similar compounds [124,126]. This trend is also observed in the monoanionic complexes, where the near-IR band bathochromic shifts compared to the corresponding neutral complexes and are located at 938, 953, and 967 nm for 1<sup>-</sup>, 2<sup>-</sup>, and 3<sup>-</sup>, respectively, with molar absorptivity values almost half of those of the neutral complexes, namely, 13900 (1<sup>-</sup>), 15200 (2<sup>-</sup>), and 10000 (3<sup>-</sup>)  $\text{M}^{-1} \text{cm}^{-1}$  (Table 8).

**Table 8.** UV–Vis spectroscopic data for complexes 1–3 and their anionic forms.

Complex	$\lambda_{\text{max}}$ . (nm)	$\epsilon$ ( $\text{M}^{-1} \text{cm}^{-1}$ )
1	860	29200
2	902	32100
3	934	30600
1 <sup>-</sup>	938	13900
2 <sup>-</sup>	953	15200
3 <sup>-</sup>	967	10000

Single crystals suitable for structure determination were isolated for complexes 2 and 3<sup>-</sup> (Figures 58 and 59, respectively). Selected bond distances are presented in Table 9.

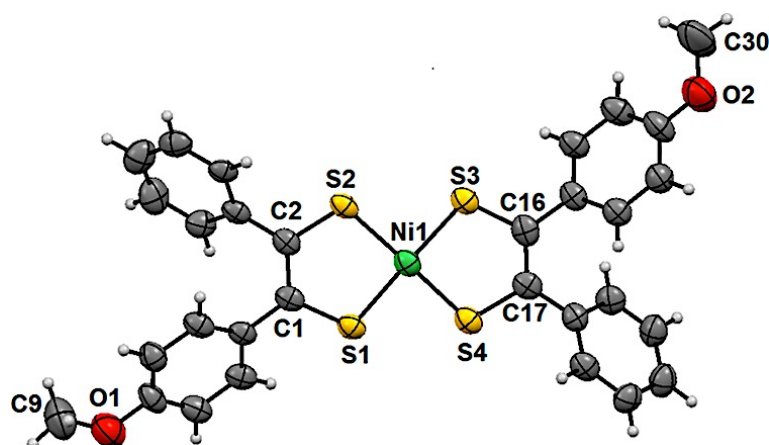


**Figure 60.** ORTEP diagram at 30% probability level for compound 2.

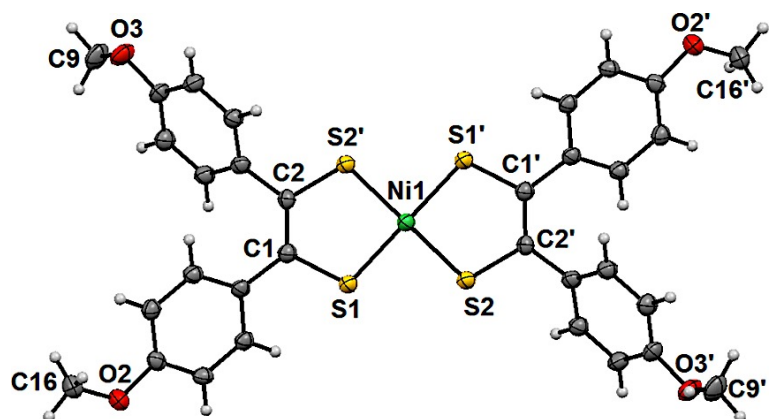


**Figure 61.** ORTEP diagram at 30% probability level for compound 3<sup>-</sup>.  $\text{NBu}_4^+$  counter-ion is omitted for clarity.

**Table 9. Selected bond lengths (in Å) for complexes 1, 2, 3, 3<sup>-</sup>.**

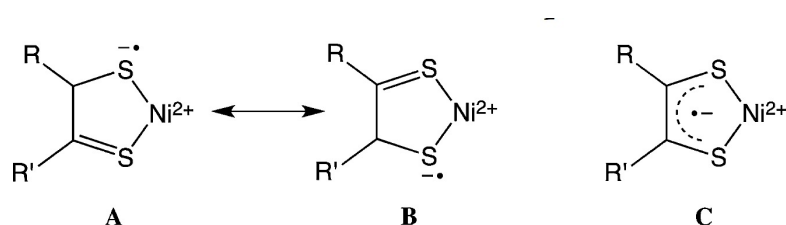
Bond <sup>a</sup> /Compound	1 <sup>[124]</sup>	2	3 <sup>[22]</sup>	3 <sup>-</sup>
Ni1 – S1	2.1209	2.130(2)	2.1222(6)	2.1416(5)
Ni1 – S2	2.1227	2.129(2)	2.1217(6)	2.1292(6)
Ni1 – S3	2.1209	2.128(2)	2.1341(6)	2.1510(5)
Ni1 – S4	2.1227	2.115(2)	2.1182(6)	2.1358(6)
C1 – S1	1.716	1.699(6)	1.717(2)	1.744(2)
C2 – S2	1.703	1.711(6)	1.703(2)	1.742(2)
C16 – S3	1.716	1.707(6)	1.717(2)	1.745(2)
C17 – S4	1.703	1.714(7)	1.710(2)	1.743(3)
C1 – C2	1.388(3)	1.423(8)	1.394(3)	1.368(3)
C16 – C17	1.388(3)	1.402(9)	1.391(3)	1.362(2)
S1–Ni1–S2	0	0	5°	4.89°
S3–Ni1–S4				

<sup>a</sup> for the sake of comparison, numbering for 3 is in accordance with 2, i.e. bond in 2/bond in 3. Ni1–S2 / Ni1–S2', Ni1–S3 / Ni1–S1', Ni–S4 / Ni–S2, C2–S2 / C2–S2', C16–S3 / C1'–S1', C17–S4 / C2'–S2, C16–C17 / C1'–C2', S1–Ni1–S2 / S1–Ni1–S2', S3–Ni1–S4 / S2–Ni1–S1'

Both complexes crystallize in the  $P\bar{1}$  crystal group. To the best of our knowledge, 2 is the first example of an asymmetric phenyl–substituted bis(dithiolene) complex to be structurally characterized. The neutral form of 3<sup>-</sup>, i.e., 3, was reported earlier by Arumugam et al. [22]. The structure of the complexes is representative for the nickel bis(dithiolene) system, with an almost perfectly planar configuration of the NiS<sub>4</sub> core for both complexes. Bond lengths (Ni–S, C–S, and C–C) are comparable to those reported for analogous complexes, with the average Ni–S bonds in the literature [127] being 2.101–2.223 Å, the S–C bonds 1.642–1.777 Å, and the C–C bonds 1.284–1.520 Å.

It is of interest to compare how the addition of methoxy groups affects the bond lengths of complexes 1–3. The Ni–S and C–S bonds remain practically unaffected, but the C1–C2 and C16–C17 bonds vary notably. In complex 1, the C–C bond distance of the dithiolene moiety (C1–C2 and C16–C17) is ~1.388 Å, and the addition of one methoxy group leads to a significant elongation of the same bonds (1.423 and

1.402 Å). However, the addition of one more methoxy group to the remaining phenyl ring leads to intermediate bond lengths (1.394 and 1.391 Å), so in terms of the C–C<sub>ene</sub> bond length, the trend is 1 < 3 < 2. The noninnocence of the dithiolene ligands in neutral nickel bis(dithiolene) complexes 1–3 involves the coordination of two radical anionic ligands to a nickel(II) ion [10]. The radical anionic nature of the coordinated dithiolene ligand is well depicted by the two extreme resonant forms A and B in Scheme 20, where for simplicity only one of the coordinated ligands is depicted, with one sulfur atom with radical–anion character and the other one engaged in a thioketone function. Form C depicts the delocalized nature of the coordinated ligand as a sum of forms A and B, where the electron density is distributed over the five–atom NiS<sub>2</sub>C<sub>2</sub> ring.



**Scheme 21. Limiting (A and B) and delocalized (C) structures for a nickel dithiolene complex.**

When  $R = R'$ , the negative charge is delocalized in a symmetrical manner over the SCCS core (form C). Actually, this is also supported from the aforementioned trend for the C–C<sub>ene</sub> bond length, indicating that the two symmetric complexes 1 and 3 adopt a structure where the charge is evenly distributed over the NiS<sub>2</sub>C<sub>2</sub> core (form C, Scheme 20). Moreover, it has been proven by S K–edge X–ray absorption spectroscopy data combined with theoretical calculations that if the contribution of the metal  $d_{xz}$  orbital dials up to 25%, then 0.4 of an electron spin is located in each ligand, with the metal orbital acting as a superexchange pathway between the two partially spin–polarized ligands [128]. When  $R \neq R'$ , as in our case for complex 2 ( $R =$  phenyl and  $R' = 4$ –methoxyphenyl), one of the first two resonance forms must contribute more to the bonding scheme. While differences in the C–S and Ni–S bond lengths are within experimental error, the C–C bonds provide insight into the electronic structure of 2. As mentioned earlier, 2 exhibits elongated C1–C2 and C16–C17 bonds, an indication that in 2 the C–C bond resembles a single bond. Thus, one of the two first structures (forms A and B) of Scheme 20 better describes the structure of 2. On the basis of the fact that the thiolate sulfur atom is richer in electron

density than the thioketone sulfur atom, which facilitates protonation, we propose that the bonding scheme in catalyst 2 is best described by form B (R = phenyl and R' = 4-methoxyphenyl) of Scheme 21.

A comparison between the neutral and monoanionic complexes 3 and 3<sup>-</sup> at first reveals a shortening of the C1–C2 and C16–C17 bonds with a concomitant elongation of the C–S and Ni–S bonds. This trend has been observed for the [Ni(S<sub>2</sub>C<sub>2</sub>Me<sub>2</sub>)<sub>2</sub>]<sup>0/1-/2-</sup> series in a detailed study by Lim et al.[129] DFT and vibrational data indicate that the reduction is a ligand-based event and leads to electronic saturation of the ligand, with the dianionic extreme being better described as two dianionic ene-dithiolate ligands coordinated to a nickel(II) ion. Thus, a shortening of the C–C bonds is anticipated as these bonds acquire a double-bond character, which is further corroborated by the increased wavenumber values observed in the IR spectra for the vibration of C–C bonds. Elongation of the C–S bonds is attributed to the loss of dithioketone character upon reduction.

The electrochemical behavior of all complexes was investigated with CV in DMF in the presence of <sup>n</sup>Bu<sub>4</sub>NPF<sub>6</sub> as the supporting electrolyte. Examination of either the monoanionic or neutral compounds revealed the same behavior so only the electrochemical characteristics of the neutral compounds are reported here. Two well-defined reversible redox events are observed, corresponding to the one- and two-electron reductions of complexes 1–3, as documented in the literature for compound 1 [130]. The introduction of methoxy groups on the phenyl rings has an effect on the reduction potential because the methoxy electron-donating groups lead to increased electron density on the sulfur atoms. A trend can be observed where the most difficult complex to reduce is 3 and the easiest to reduce is 1.

Reduction potential values are in the range of –0.274 to –0.370 V vs Fc<sup>+0</sup> for the first reduction to the monoanion (0/1<sup>-</sup> process) and –1.260 to –1.325 V vs Fc<sup>+0</sup> for the second reduction to the dianion (1<sup>-</sup>/2<sup>-</sup> process). Although the behavior is similar to the respective cobalt compound [66], the reductions of 3 are found at less negative potential values than those of the cobalt analogue complexes. Normalized cyclic voltammograms are shown in Figure 62, and reduction potentials can be found in Table 10.

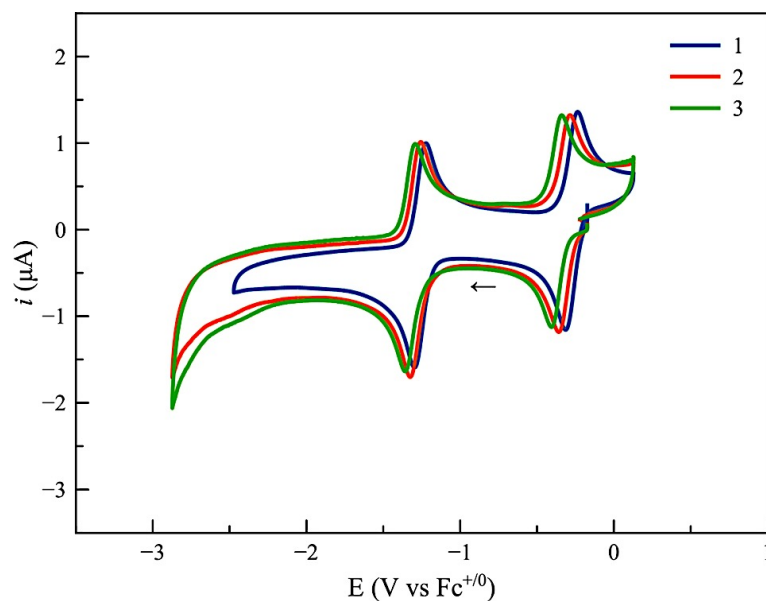
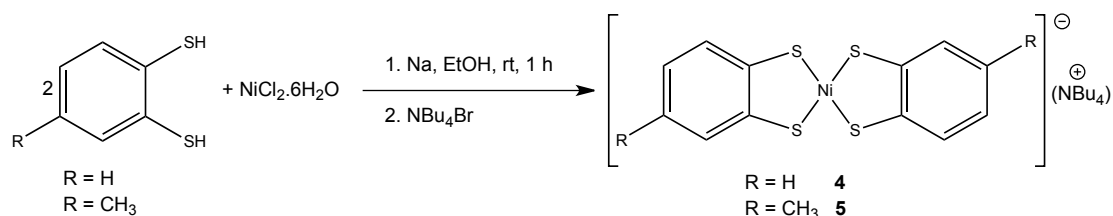


**Figure 62.** Normalized cyclic voltammograms for compounds 1–3 in DMF at a scan rate of  $100 \text{ mV s}^{-1}$  with  ${}^n\text{Bu}_4\text{NPF}_6$  in DMF under Ar at room temperature (glassy carbon working electrode).

**Table 10.** Reduction potentials for complexes 1 – 3.

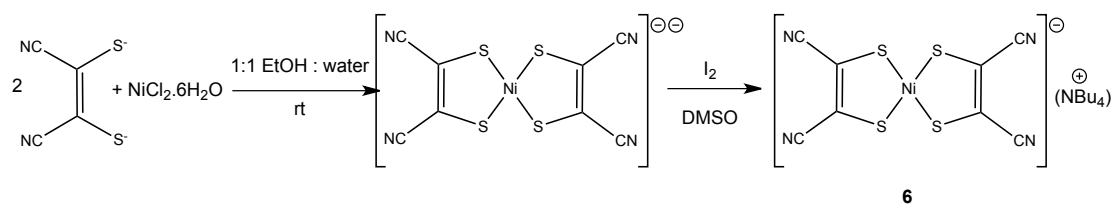
Compound	$E \text{ vs Fc}^{+/0}$	
	neutral/monoanion	monoanion/dianion
1	-0.274	-1.260
2	-0.319	-1.289
3	-0.370	-1.325

The homoleptic complexes bearing benzene–1,2–dithiolate ligands were prepared using literature procedures [33], by deprotonating the corresponding dithiol in absolute ethanol using Na instead of K as a base:



**Scheme 22.** Preparation of anionic complexes 4 and 5 bearing methyl– and unsubstituted benzene rings.

The complex bearing maleonitrile–dithiolate ligand was prepared from the  $\text{I}_2$  – oxidation of the corresponding dianionic complex, as mentioned in the literature [131]:



**Scheme 23. Preparation of nickel complex 6 with malonitrile–dithiolate ligands.**

Analytical data for these complexes agree with those reported in the literature.

Cyclic voltammetry of the aforementioned complexes was recorded in acetonitrile solution with a glassy carbon working electrode. Data are summarized in Table 11 and normalized cyclic voltammograms are shown in Figure 63.

**Table 11. Cyclic voltammetry data for complexes 4–6 in MeCN**

Compound	$E$ vs $\text{Fc}^{+/0}$	
	monoanion/dianion	dianion/trianion
4	-0.92	–
5	-0.95	–
6	-0.08	-2.00

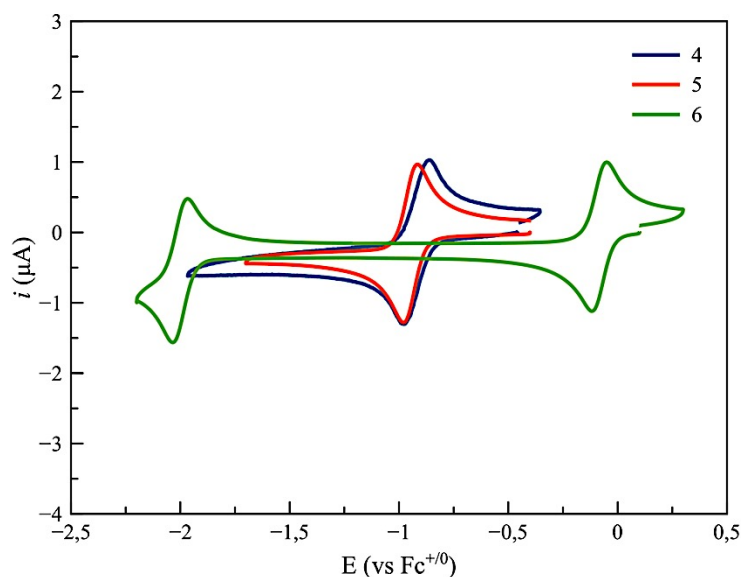


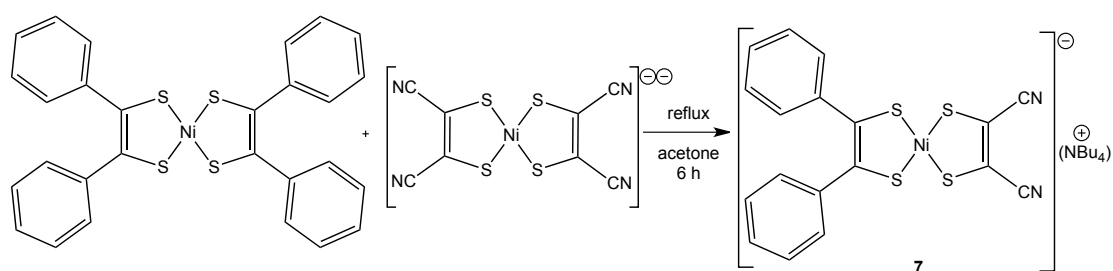
**Figure 63. Normalized cyclic voltammograms for compounds 4, 5, and 6 in MeCN at a scan rate of  $100 \text{ mV s}^{-1}$  with  ${}^n\text{Bu}_4\text{PF}_6$  in MeCN under Ar at room temperature. Glassy carbon working electrode, Ag/AgCl reference electrode, Pt-wire counter electrode.**

For 4 and 5, one fully reversible redox process is observed, which corresponds to the reduction of the monoanion to the dianionic compound. The reduction occurs at

slightly negative potentials,  $-0.92$  V vs.  $\text{Fc}^{+/0}$  for 4 and  $-0.95$  V vs.  $\text{Fc}^{+/0}$  for 5. The small negative shift (30 mV) for the reduction potential of 5 compared to that of 4 can be rationalized in terms of the electron-donating effect of the methyl group that renders the sulfur atoms more electron-rich. Compound 6 exhibits two well-defined redox waves, corresponding to the formation of the one- and two-electron-reduced species. The potential values of  $-0.08$  V vs.  $\text{Fc}^{+/0}$  and  $-2.00$  V vs.  $\text{Fc}^{+/0}$  correspond to the formation of the dianion and trianion, respectively. The electron-withdrawing effect of the maleonitrile-dithiolate ligand on 6 allows its accommodation of one more electron, leading to the formation of the trianionic species which is not observed for compounds 4 and 5 in the scanned potential range.

## 6.2 Preparation of heteroleptic dithiolene complexes

Complex 7 (*vide infra*) was prepared using a scrambling oxidation-reduction reaction, upon which the neutral complex 1 reacts with dianionic  $6^-$  (i.e.  $[\text{Ni}(\text{mnt})_2]^{2-}$ ) to afford the monoanionic mixed-ligand species [132], in the following procedure:



**Scheme 24. Preparation of mixed-ligand complex 7.**

250 mg  $(\text{NBu}_4)_2[\text{Ni}(\text{mnt})_2]$  and 165 mg of compound 1 are dissolved in 75 mL acetone and the resulting solution is refluxed for 6 h. The mixture is then left to cool to room temperature and the solvent is removed under vacuum without heating. The resulting brown residue is subjected in column chromatography (Silica 60). Elution with  $\text{CHCl}_3$  afforded first unreacted 1 (green band) and elution with  $\text{CHCl}_3$  – acetone : 8 – 2 afforded the desired compound (brown band). Recrystallization of the product was effected by slow evaporation of a solution (acetone – hexane : 1 – 2) yielding black needle-like crystals of compound 7 suitable for X-rays analysis. Yield: 77 %.

Anal. Calcd for  $\text{C}_{34}\text{H}_{46}\text{N}_3\text{NiS}_4$ : C, 59.73 ; H, 6.78; S, 18.76. Found: C, 59.86; H, 6.68; S, 17.59.

Since the resulting compound is paramagnetic,  $^1\text{H-NMR}$  spectra were not recorded. The IR spectrum, however, in comparison to the respective homoleptic counterparts, is reported in Figure 64.

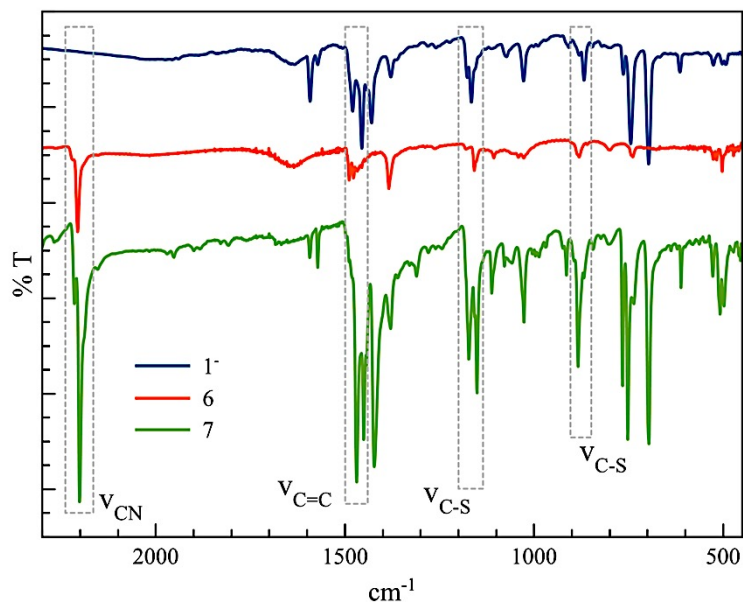


**Figure 64.** IR spectrum of heteroleptic complex 7 along with the homoleptic counterparts 1<sup>-</sup> and 6.

Wavenumber values for the heteroleptic complex are typical of bis-dithiolene nickel complexes [121], with the most characteristic  $\tilde{\nu}_{\text{CN}}$  band observed at  $2202\text{ cm}^{-1}$ , found at approximately  $5\text{ cm}^{-1}$  less than the same band observed for the symmetrical complex 6. Stretch  $\tilde{\nu}_{\text{C=C}}$  values are found at the region of  $1450\text{--}1470\text{ cm}^{-1}$ , and  $\tilde{\nu}_{\text{C-S}}$  are observed at  $\sim 1173$  and  $883\text{ cm}^{-1}$ .

**Table 12.** IR data values for heteroleptic complex 7, in comparison to homoleptic counterparts 1<sup>-</sup> and 6.

Complex	$\tilde{\nu}_{\text{C=C}}$	$\tilde{\nu}_{\text{C-S}}$	$\tilde{\nu}_{\text{CN}}$
1 <sup>-</sup>	1455 (s)	1177 (s), 867 (w)	–
6	1435 (s)	1158 (s), 881 (w)	2207 (s), 2222 (sh)
7	1469 (s)	1173 (s), 883 (w)	2202 (s), 2215 (sh)

The absorption spectrum of compound 7 was recorded in DMF and several bands are observed in the 400 – 1100 nm region. More specifically, two weak bands located at 510 nm and 638 nm with molar absorptivity values of  $2020$  and  $1180\text{ M}^{-1}\text{ cm}^{-1}$  with

the most prominent band at 910 nm ( $10300 \text{ M}^{-1} \text{ cm}^{-1}$ ) assigned to  $\pi - \pi^*$  dithiolene ligand transitions (Figure 65).

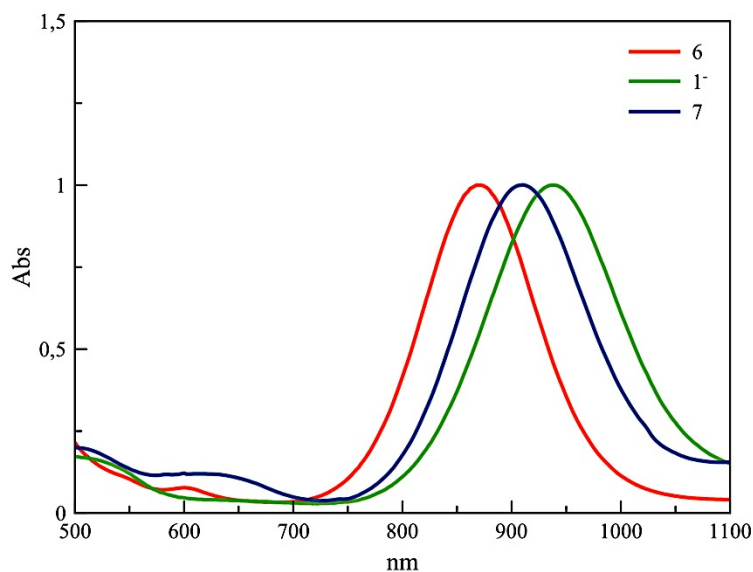


**Figure 65.** Normalized UV-Vis spectra for heteroleptic complex 7 along with its homoleptic counterparts 6 and  $1^-$ .

The main band at 910 nm is found at an intermediate wavelength between the homoleptic complexes, the observed value in proximity with the theoretical calculated of 904 nm by the empirical equation  $\lambda_{\text{heteroleptic}} = (\lambda_{\text{homoleptic 1}} + \lambda_{\text{homoleptic 2}})/2$  ([41] and references therein). UV-Vis data for complex 7 in comparison to the respective homoleptic complexes are summarized in Table 13.

**Table 13.** UV-Vis data for complex 7 along with the respective homoleptic complexes.

Complex	$\lambda_{\text{max.}}$ (nm)	$\epsilon$ ( $\text{M}^{-1} \text{ cm}^{-1}$ )
$1^-$	938	13900
6	870	6200
7	910	10300

The less prominent band at 638 nm, however, is not observed for the corresponding homoleptic species (Figure 65). It is proposed that this band corresponds to a mixed-metal-ligand-to-ligand transition (MMLLT) with metal participation, since the difference in the electronic structure of the ligands cancels the delocalized bonding scheme usually observed for bis-1,2-dithiolene complexes. In fact, for this compound it has been suggested that the mnt ligand is present in the dithiolate form due to the

electron-accepting properties of the nitrile groups, while the other ligand in the dithioketone form [40], as reported for similar push – pull complexes [31,38,126].

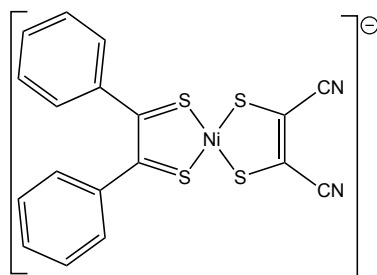


**Figure 66. Proposed bonding scheme for compound 7.**

Cyclic voltammetry in DMF showed a reversible reduction wave observed at  $-0.758$  V vs  $\text{Fc}^{+/0}$ , corresponding to the reduction of the complex to the dianion. No reversible oxidation wave was found at room temperature measurements, indicating that the neutral species is unstable in solution, further corroborated by reports in the literature for similar complexes [132]. Reduction to the dianionic form occurs at considerably more positive potential compared to its homoleptic counterpart **1** ( $-1.26$  V vs  $\text{Fc}^{+/0}$ ).

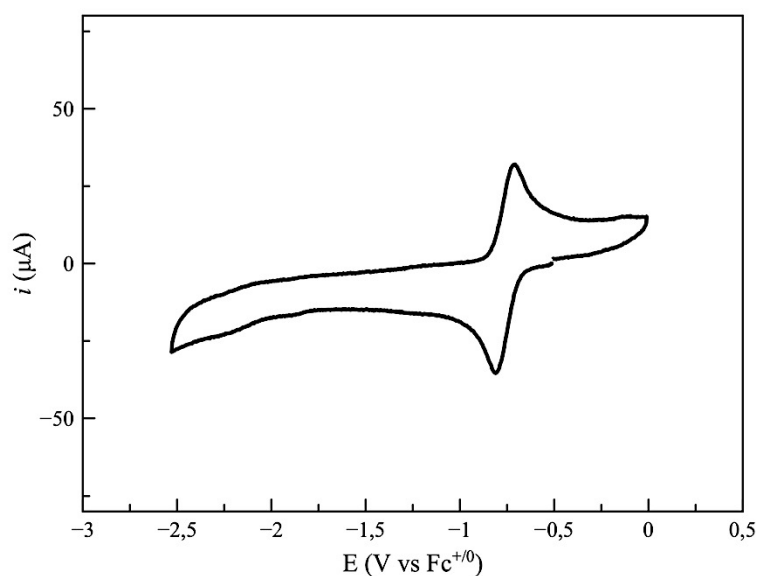


**Figure 67. Cyclic voltammogram for complex 7 in DMF using a glassy carbon working electrode, Ag/AgCl reference electrode,  $\text{NBu}_4\text{PF}_6$  supporting electrolyte, and a Pt wire counter electrode.**

Complex **7** crystallizes in the P21/n space group. All atoms of  $\text{NiS}_4$  core are located on the same plane, imposing a square planar geometry around the Ni ion, with a small twist in the torsion angle of the mnt and diphenyl–ethylene–dithiolene ligand (Figure 69). Packing in the crystal reveals the shortest S – S distance  $4.263 \text{ \AA}$ , the mnt ligand

being adjacent to the phenyl rings on the ligand of the other complex in the unit cell (Figure 70).

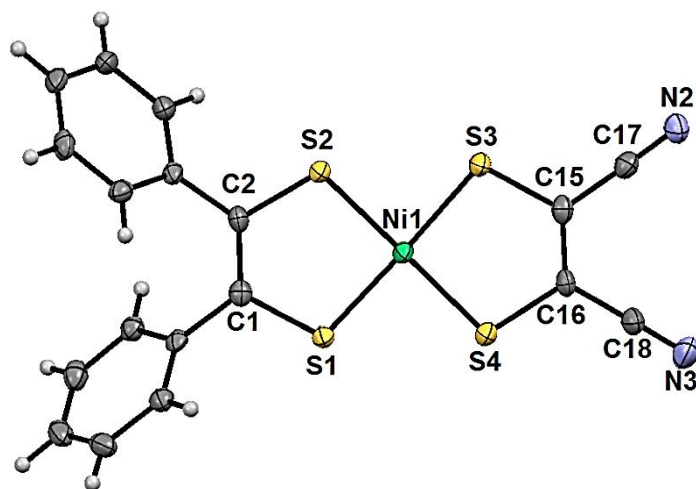


Figure 68. ORTEP diagram at 30% probability level for compound 7. The  $\text{NBu}_4^+$  counterion is omitted for clarity.

Selected crystallographic data for complex 7 are summarized in Table 18 and full data for the same compound are shown in Tables in the Appendix.

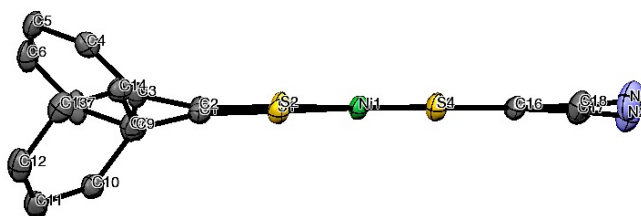


Figure 69. ORTEP diagram at 30% probability level for compound 7. The  $\text{NBu}_4^+$  counterion and hydrogen atoms are omitted for clarity.

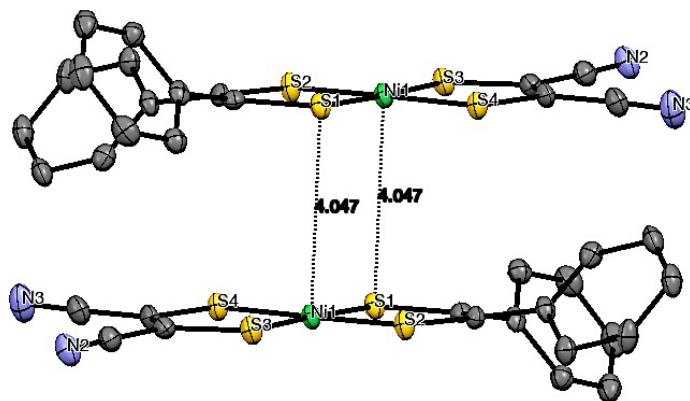


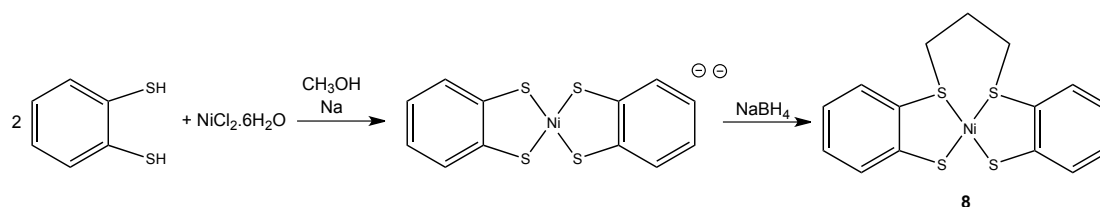
Figure 70. Packing diagram of a crystal of compound 7. The  $\text{NBu}_4^+$  counterion and hydrogen atoms are omitted for clarity.

Bond lengths are typical for similar complexes [121], with the average Ni–S bonds in the literature [127] being 2.101–2.223 Å, the S–C bonds 1.642–1.777 Å, and the C–C bonds 1.284–1.520 Å.

**Table 14. Selected bond distances (Å) and angles (°) for complex 7.**

Ni1 – S1	2.1413(9)	Ni1 – S3	2.1490(9)
Ni1 – S2	2.1351(9)	Ni1 – S4	2.1538(9)
C1 – S1	1.727(3)	C1 – C2	1.361(5)
C2 – S2	1.734(3)	C15 – C16	1.355(5)
C15 – S3	1.730(4)	C17 – N2	1.149(5)
C16 – S4	1.741(3)	C18 – N3	1.141(5)
S1 – Ni1 – S2	90.70(4)	S2 – Ni1 – S3	87.20(4)
S1 – Ni1 – S3	177.49(4)	S2 – Ni1 – S4	179.10(4)
S1 – Ni1 – S4	88.87(3)	S3 – Ni2 – S4	93.24(4)

### 6.3 Preparation of bridged dithiolene complexes

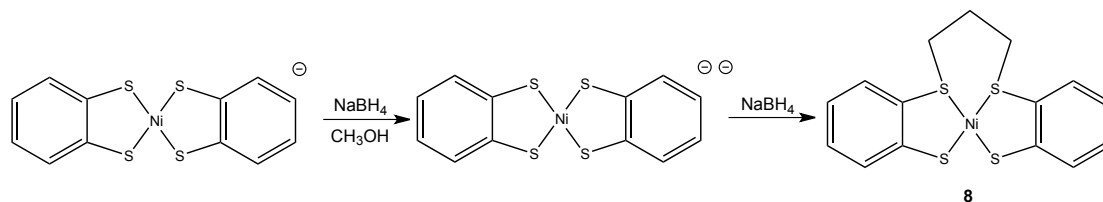


**Scheme 25. Preparation of compound 8.**

A modification of a literature procedure [133] was followed for the preparation of compound 8: In a Shlenck flask under Ar 97 mg (4.22 mmol) Na are dissolved in 15 mL methanol under stirring. 243  $\mu$ L (300 mg, 2.11 mmol) of benzene-1,2-dithiol are added and the solution is left under stirring for 15 min and subsequently 250 mg (1.05 mmol) of NiCl<sub>2</sub>.6H<sub>2</sub>O are added to the above solution. The mixture turns instantly brown and left under stirring for 15 min. The flask is opened under Ar and 39 mg (10.52 mmol) NaBH<sub>4</sub> are added to the mixture and stirred for 15 min. Next, 1,3-dibromopropane is added to the mixture (107  $\mu$ L, 1.055 mmol) and the resulting orange – brown suspension is left under stirring for 3 h. Filtration under vacuum and washing with ether afforded an orange – brown solid. Upon slow evaporation of a dichloromethane – methanol : 2 – 1 mixture afforded red – brown needles suitable for

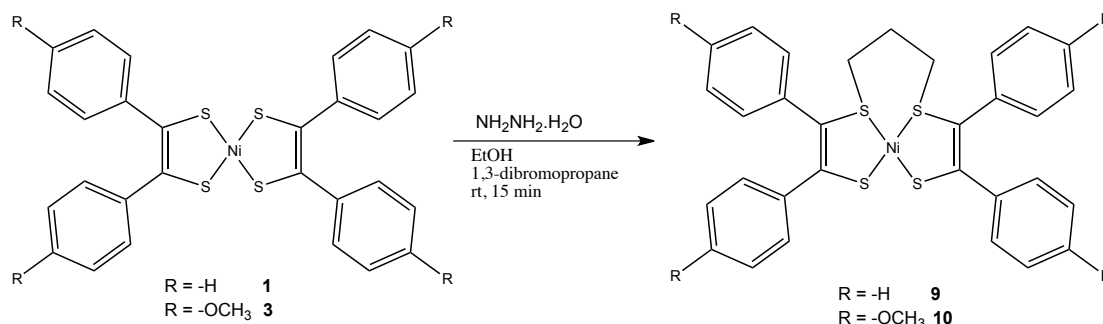
X-ray studies. Yield: 38%. Anal. Calcd for  $C_{15}H_{24}NiS_4$ : C, 47,26 ; H, 3,7; S, 33,64. Found: C, 47,8; H, 3,42; S, 33,92.

The same compound can be prepared in a different manner reaching higher yields:



**Scheme 26. Preparation of compound 8 (alternate route).**

145.4 mg (0.25 mmol) of  $(NBU_4)[Ni(bdt)_2]$  are suspended in 15 mL methanol and 95 mg (2.5 mmol)  $NaBH_4$  are added to the green suspension. The mixture turns gradually dark red and after effervescence stops 26  $\mu$ L (0.26 mmol) of 1,3-dibromopropane are added to the red solution. Immediately an orange – brown solid separates. The mixture is left under stirring for 3 h and filtration under vacuum affords an orange – brown solid. Yield: 80%.



**Scheme 27. Preparation of compounds 9 and 10.**

In an Erlenmeyer flask 100 mg (0.15 mmol) of compound 1 are dissolved under stirring in 7.33 mL (0.25 mmol) hydrazine hydrate. The red solution is stirred for 15 min. Subsequently, 15.2  $\mu$ L (0.16 mmol) of 1,3-dibromopropane are added and after 15 min stirring, a green – brown precipitate is formed. The mixture is filtered under vacuum and the resulting solid is recrystallized from a dichloromethane – methanol : 2 – 1 mixture to afford brown needles of 9. Yield: 44%. Anal. Calcd for  $C_{31}H_{26}NiS_4$ : C, 63.59; H, 4.48; S, 21.91. Found: C, 63.87; H, 4.91; S, 21.52.

Same procedure was followed for compound 9, yielding 46% of orange – brown needles suitable for X-ray diffraction study. Anal. Calcd for  $C_{35}H_{34}NiO_4S_4$ : C, 59.58; H, 4.86; S, 18.18. Found: C, 58.32; H, 4.35; S, 18.54.

Preparations for compound 8 in the literature [133] involved reaction of  $\text{Na}_2[\text{Ni}(\text{bdt})_2]$  with one equivalent of the alkylating agent 1,3-dibromopropane. However, it is well established that the dianionic forms of nickel bis-dithiolene complexes are air-sensitive and require inert Ar atmosphere. We were able to prepare the aforementioned compound in a more straightforward manner, without the need for strict deaerated conditions, by generating in situ the dianionic complex  $[\text{Ni}(\text{bdt})_2]^{2-}$  via  $\text{NaBH}_4$  reduction, reaching higher yields.

In a similar context, 9 has been prepared in the literature via  $\text{NaBH}_4$  reduction of the neutral compound 1 reaching 72% yield [134]. However, in our hands the best results leading to the desired compound with minimal effort and a simple recrystallization purification, were obtained by the use of hydrazine hydrate [135] as a stronger reducing agent that creates a strong reducing environment, inhibiting thus the in situ formed  $1^{2-}$  formed from being oxidized by air.

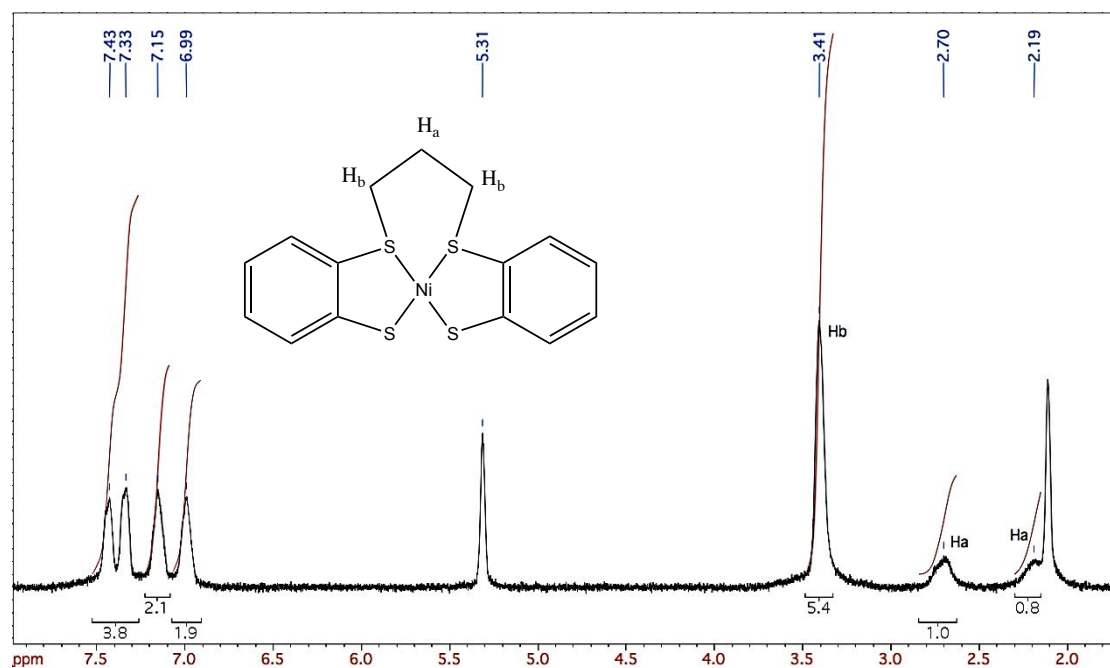


Figure 71.  $^1\text{H-NMR}$  spectrum of compound 8 in  $\text{CD}_2\text{Cl}_2$ .

The  $^1\text{H-NMR}$  spectrum of compound 8 exhibits three sets of signals; in the aromatic region ( $\sim 7\text{--}7.5$  ppm), four multiplets corresponding to the eight aromatic protons on the benzene rings, while two separate signals can be observed for the  $-\text{SCH}_2\text{CH}_2\text{CH}_2\text{S}-$  hydrogen signals (2.19 and 2.70 ppm). This separation of signals for this group of protons has been attributed to the fluxional nature of the alkyl bridge in

solution [43,133]. Finally, the singlet at 3.41 ppm is assigned to the remaining four protons of the  $-SCH_2CH_2CH_2S-$  bridge. Data are summarized in Table 17.

**Table 15.**  $^1H$ -NMR data for compound 8 in  $CD_2Cl_2$ .

$\delta$ (ppm)	multiplicity	H
6.99–7.43	m	8
3.41	s	4
2.70, 2.19	m	2

The  $^1H$ -NMR of compounds 9 and 10 show a similar pattern; a set of signals in the aromatic proton region along with signals around  $\sim 2$ –4 ppm assigned to the protons on the alkyl bridge.

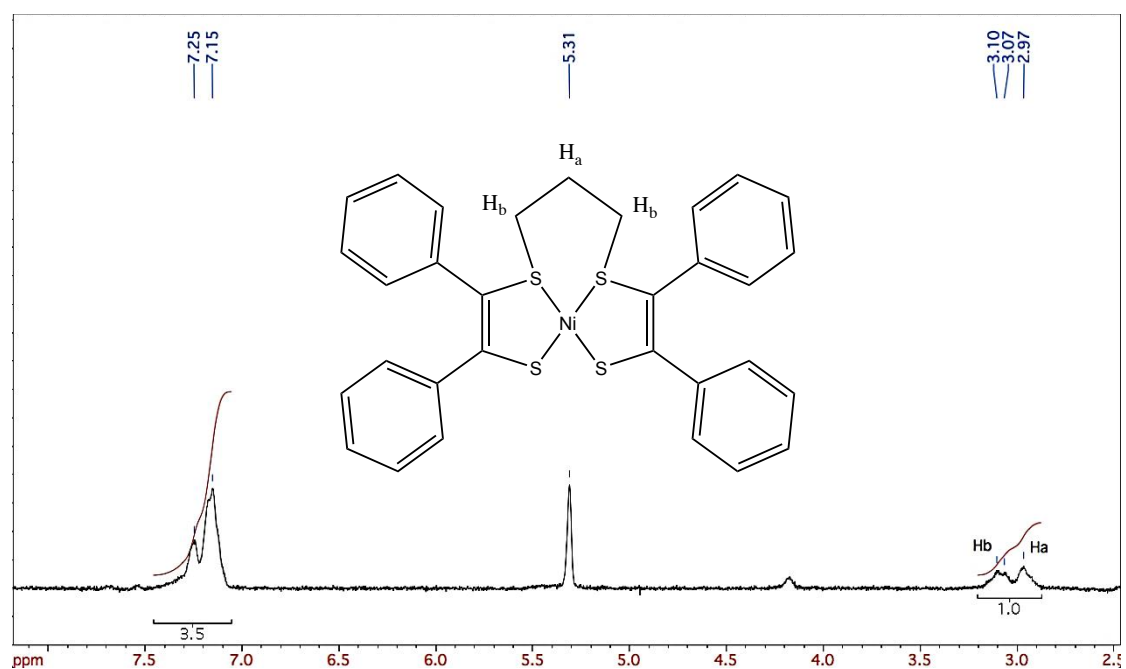


**Figure 72.**  $^1H$ -NMR of compound 9 in  $CD_2Cl_2$ .

**Table 16.**  $^1H$ -NMR data for compound 10 in  $CD_2Cl_2$ .

$\delta$ (ppm)	multiplicity	H
7.15–7.25	m	20
3.05	m	4
2.97	m	2

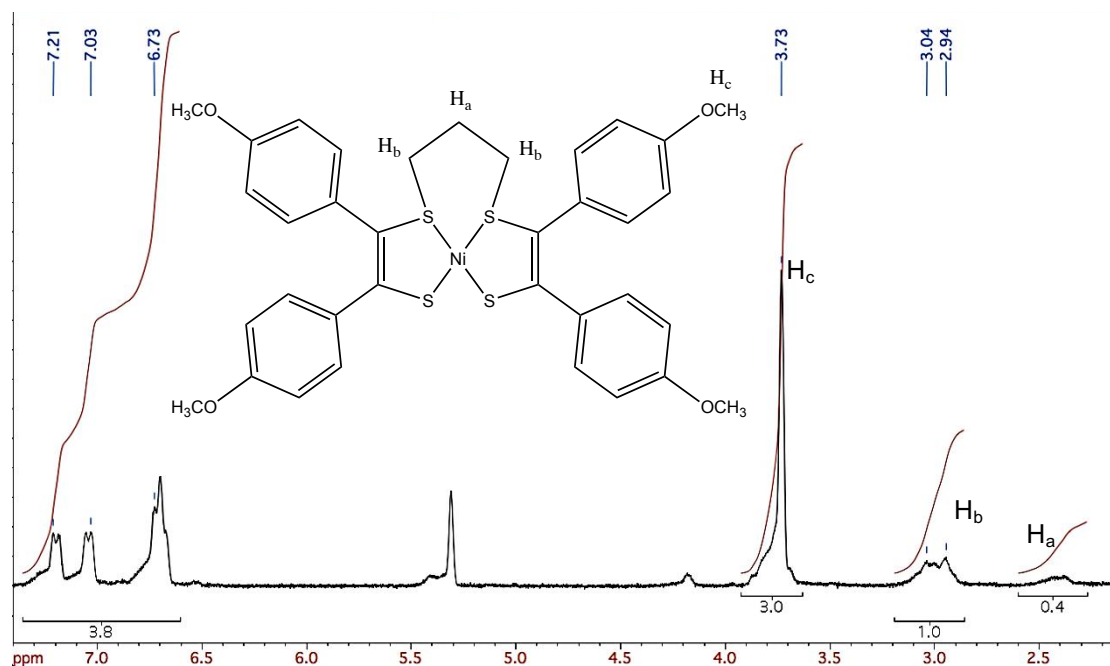


Figure 73.  $^1\text{H-NMR}$  of compound 10 in  $\text{CD}_2\text{Cl}_2$ .

Table 17.  $^1\text{H-NMR}$  data for compound 10 in  $\text{CD}_2\text{Cl}_2$ .

$\delta$ (ppm)	multiplicity	H
6.73–7.21	m	16
3.73	s	12
3.04, 2.94	m	4
2.42	m	2

The IR spectrum of complex 8 exhibits bands resembling those for the unbridged complex 4. Assignments to transitions for the bands observed have been made based on data reported for compound 4 in the literature [136].

Table 18. IR data for compound 8.

Band	Assignment
666 (m), 743 (s), 761 (s), 1102 (s)	$\tilde{\nu}_{\text{C-S}}$
1286 (w)	$\tilde{\nu}_{\text{C=C}} + \tilde{\nu}_{\text{C-S}}$

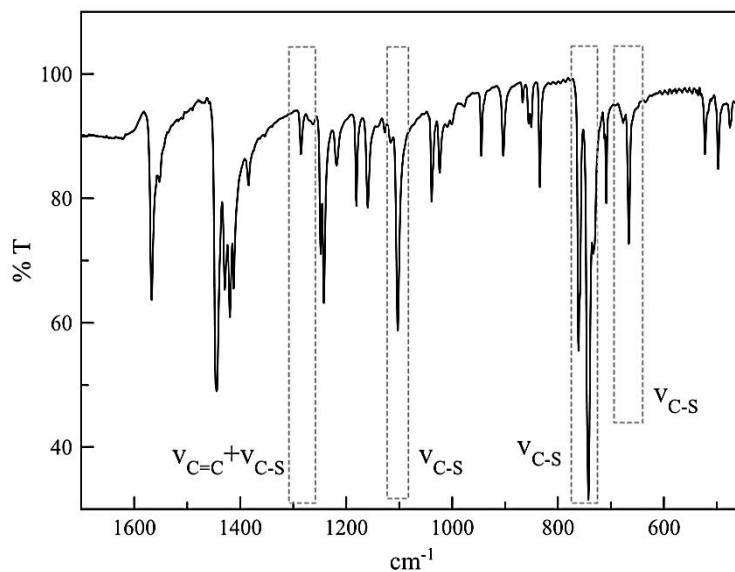


**Figure 74. IR spectrum of compound 8.**

The IR spectra of compounds 9 and 10 are shown in Figure 74 and an overlay of spectra of compounds 3, 3<sup>-</sup>, and 10 for comparison are shown in Figure 75. Direct comparison of each band of the alkylated compound 10 cannot be made with the precursor 3 or the related 3<sup>-</sup>, due to the different symmetry of each compound.

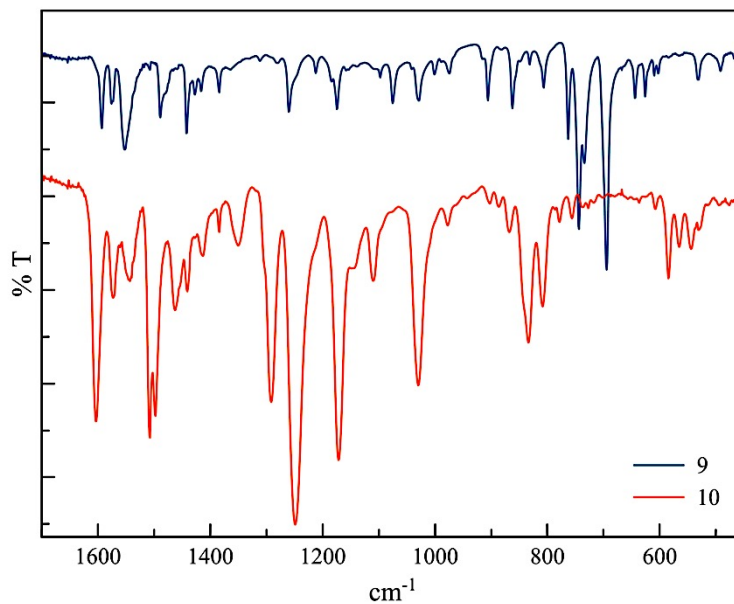


**Figure 75. Stacked IR spectra for compounds 9 and 10.**

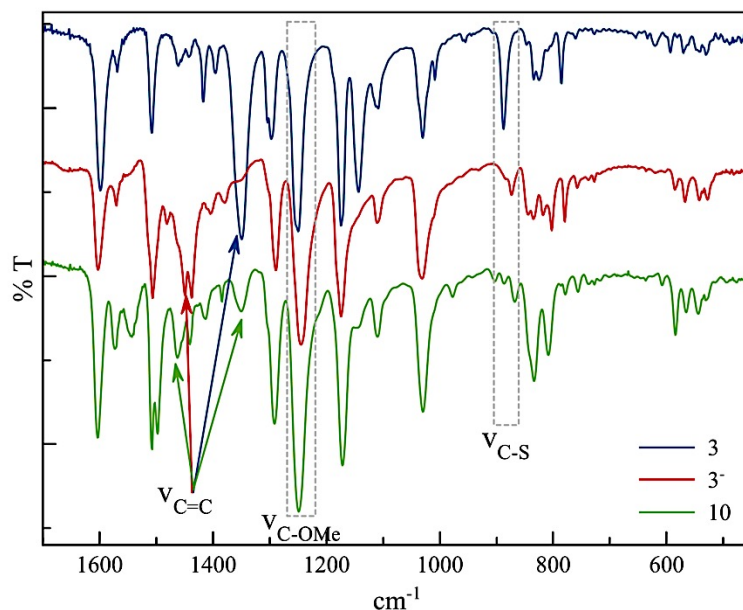


**Figure 76. Stacked IR spectra for compounds 3, 3', and 10.**

The absorption spectra of the bridged complexes display two main bands in the visible region; the first occurs at 492, 527, and 520 nm for compounds 8, 9, and 10, respectively, with molar absorptivity values of  $150 - 580 \text{ M}^{-1} \text{ cm}^{-1}$ . The second band is located at 669 nm for 8, 636 nm for 9, and 629 nm for 10 with low molar absorptivity values ( $56 - 130 \text{ M}^{-1} \text{ cm}^{-1}$ ).

Such low molar absorptivity values indicate that these transitions cannot be assigned to charge-transfer transitions, the latter being the case for the un-bridged compounds 4, 1, and 3, that display an intense CT band at the near-IR region (900 – 1000 nm). Thus, alkylation at two adjacent sulfur sites of the  $\text{NiS}_4$  ring must induce loss of electron delocalization over the whole  $\text{NiS}_4$ , giving rise to more localized electron structures in comparison to the un-bridged counterparts.

**Table 19. UV-Vis data for compounds 8, 9, and 10.**

Complex	$\lambda_{\text{max}}$ (nm)	$\epsilon$ ( $\text{M}^{-1} \text{ cm}^{-1}$ )
8	492	150
	669	56
9	527	210
	636	59
10	520	580
	629	130

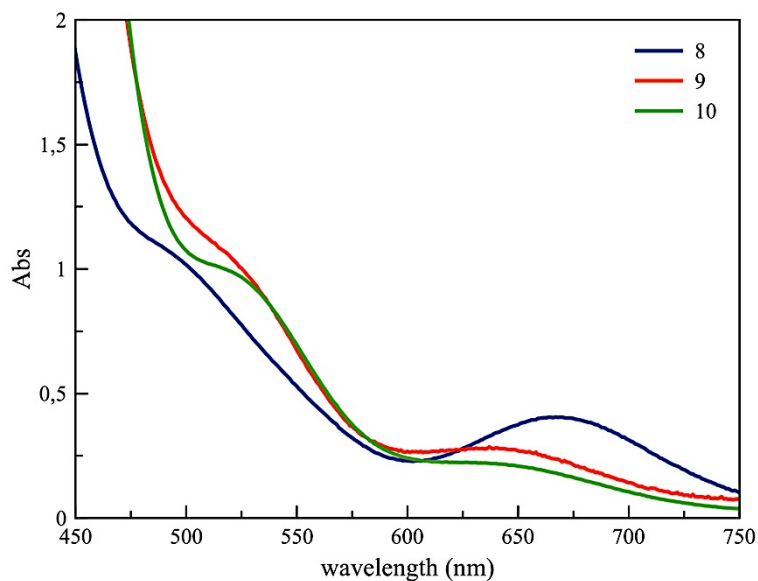


**Figure 77. Absorption spectra of compounds 8–10 in DMF solution.**

The cyclic voltammograms for the bridged compounds 8, 9, and 10 were recorded in DMF solution.

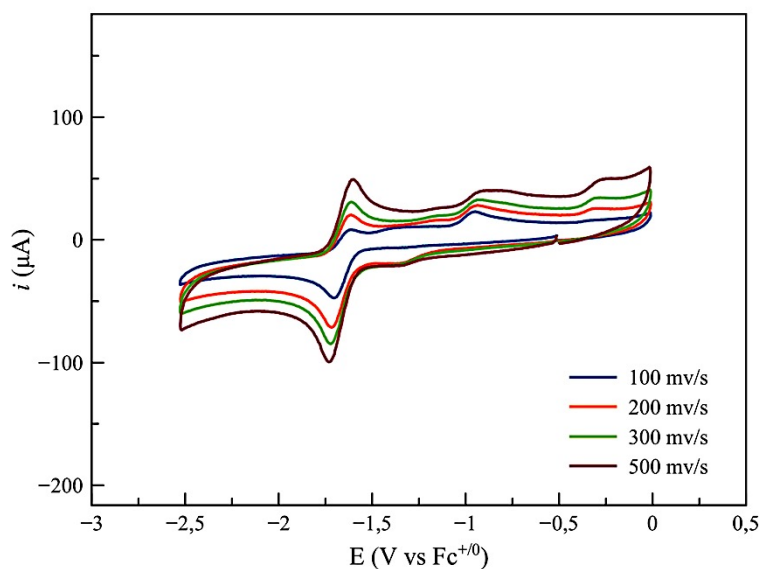


**Figure 78. Cyclic voltammogram of compound 8 in DMF solution under Ar with a glassy carbon working electrode, a Ag/AgCl reference electrode, and a Pt-wire counter electrode at various scan rates with  $\text{NBu}_4\text{PF}_6$  supporting electrolyte.**

Compound 8 exhibits a single cathodic wave at  $-1.70 \text{ V vs Fc}^{+/0}$ , followed by one prominent anodic wave at  $-1.62 \text{ V vs Fc}^{+/0}$  correlated to the first cathodic wave observed. One more anodic wave at  $0.94 \text{ V vs Fc}^{+/0}$  is observed at low scan rates ( $100 \text{ mV s}^{-1}$ , blue trace, Figure 78). Increasing scan rate up to  $500 \text{ mV s}^{-1}$  reveals increased reversibility for the anodic wave correlated to the first reduction to the monoanion,

indicating that the process at  $-1.70$  V vs  $\text{Fc}^{+/0}$  involves a structural reorganisation of the molecule upon reduction, attributed to the scission of one or two S – C bonds of the

$-\text{CH}_2\text{CH}_2\text{CH}_2-$  alkyl moiety. Dealkylation upon reduction has also been reported for similar Ni compounds bearing dimethyl–propane as a bridging group [137], although in the present case the solvent (DMF) must have a deteriorating effect on dealkylation procedure compared to the reversibility ( $\text{MeCN}$ ,  $E_{1/2} \approx -2$  V vs  $\text{Fc}^{+/0}$ ) observed in the literature for the similar dimethyl–propane compound [137]. The same compound in THF solution displayed only irreversible redox events [138].

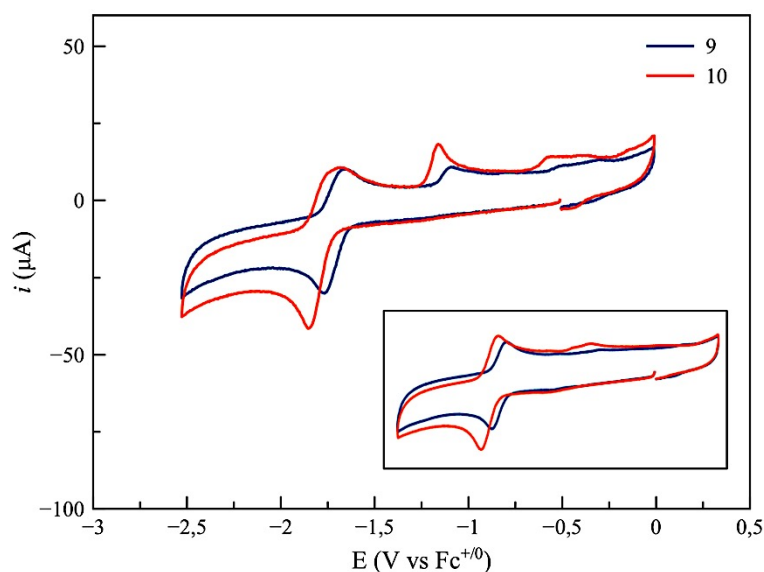


**Figure 79.** Cyclic voltammogram of compounds 9 and 10 in DMF solution under Ar with a glassy carbon working electrode, a Ag/AgCl reference electrode, and a Pt–wire counter electrode at a scan rate of  $100 \text{ mV s}^{-1}$  with  $\text{NBu}_4\text{PF}_6$  supporting electrolyte. Inset: cyclic voltammograms of same compounds under same conditions at a scan rate of  $500 \text{ mV s}^{-1}$ .

Compounds 9 and 10 exhibit a similar behavior, at similar potential values. One partially reversible wave is observed for each compound, at  $E_{1/2} = -1.72$  V vs  $\text{Fc}^{+/0}$  and  $E_{1/2} = -1.77$  V vs  $\text{Fc}^{+/0}$  for 9 and 10, respectively, corresponding to the reduction of the neutral compounds to their monoanions. As in the case of compound 8, reversibility of the anodic wave increases upon increasing scan rate to  $500 \text{ mV s}^{-1}$  (Figure 79, inset), indicating a structural impact accompanying the reduction.

Compared to the respective un–bridged analogs 4, 1, and 3, all three compounds 8 – 10 display different electrochemical behavior. More specifically, 8 displays a wave by  $\sim 1$  V more negative values compared to 4 [69,139], while 9 and 10 display only one

reduction when 1 and 3 display two reversible reductions to the dianionic form [68,135], approximately at 500 mV more negative potential values. A first indication from these observations is that all three complexes 8 – 10 are harder to reduce than the corresponding unbridged compounds, implicating that there is already electron density on the NiS<sub>4</sub> core trapped by the alkyl bridge; upon further reduction, the complex loses its structural integrity and most likely dealkylation occurs. Secondly, within the series 9 and 10, the methoxy-substituted complex is harder to reduce, as has already been observed for the unbridged complexes 1 and 3 [68]. Electrochemistry data are summarized in Table 20.

**Table 20. Electrochemistry data for compounds 8 – 10**

Compound	<i>E</i> vs Fc <sup>+0</sup>
	monoanion/dianion
8	-1.70 ( <i>E</i> <sub>p,c</sub> )
9	-1.72 ( <i>E</i> <sub>1/2</sub> )
10	-1.74 ( <i>E</i> <sub>1/2</sub> )

Crystal structures were also determined for bridged complexes 8–10. The crystal structure of 8 was reported in the literature [133] but was determined again for the scope of this study (Figure 80).

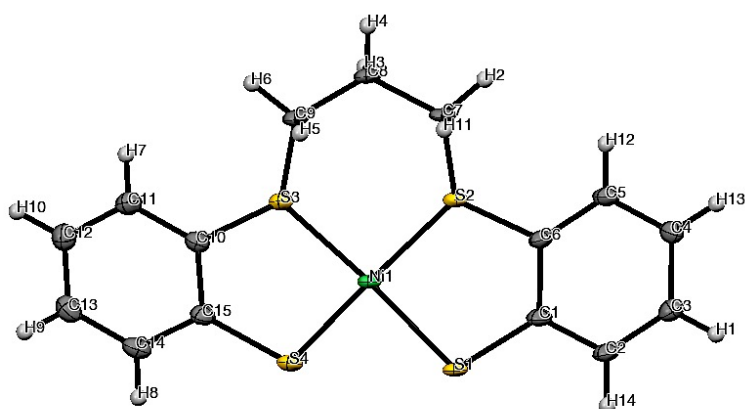


**Figure 80. ORTEP diagram at 50% probability level for compound 8.**

Compound 8 crystallizes in the P121/c1 crystal system. Ni–S bonds are in the expected values for similar nickel dithiolene complexes [127], with average values of 2.156 – 2.173 Å, appearing slightly elongated by 0.02 Å compared to the unbridged complex 4 [140]. All S – Ni – S angles approach the 90° value, with a deviation from

square planar geometry around nickel ion reflected on the approximately 25° torsion angle (C6 – S2 – Ni1 – S1, Figure 81) which is absent in the unbridged compound [140].

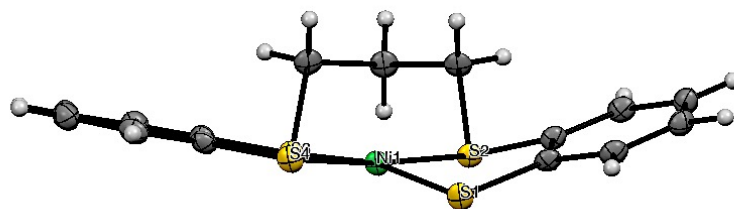


**Figure 81.** ORTEP diagram at 50% probability level for compound 8.

This tetrahedral distortion in similar compounds [134] has been explained in terms of the more localized electron structure compared to the un-bridged compound.

Packing reveals the shortest distance 3.453 Å between Ni1 and S2 of another molecule in the cell (Figure 82).

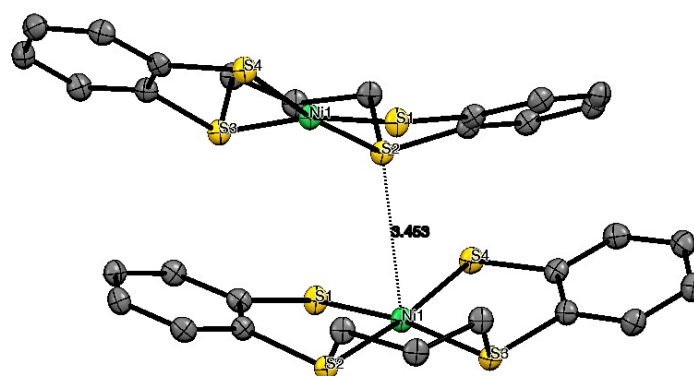


**Figure 82.** ORTEP packing figure for compound 8 at 50% probability level. Hydrogen atoms omitted for clarity.

Selected bond lengths (Å) and angles (°) are summarized below.

**Table 21.** Selected bond lengths (in Å) and bond angles (in °) for compound 8 at 100(2) K with estimated standard deviations in parentheses.

Ni1 – S3	2.1557(6)	Ni1 – S4	2.1616(6)
Ni1 – S1	2.1702(7)	Ni1 – S2	2.1728(6)
S1 – C1	1.7617(19)	S2 – C6	1.7819(18)
S3 – Ni1 – S4	92.41(2)	S3 – Ni1 – S1	168.83(2)
S4 – Ni1 – S1	88.06(2)	S3 – Ni1 – S2	90.84(2)
S4 – Ni1 – S2	173.55(2)	S1 – Ni2 – S2	89.83(2)

A similar structure adopt the remaining two bridged complexes, namely 9 and 10. The crystal structure of compound 9 has been reported in 1992 by Zhang et al. [134].

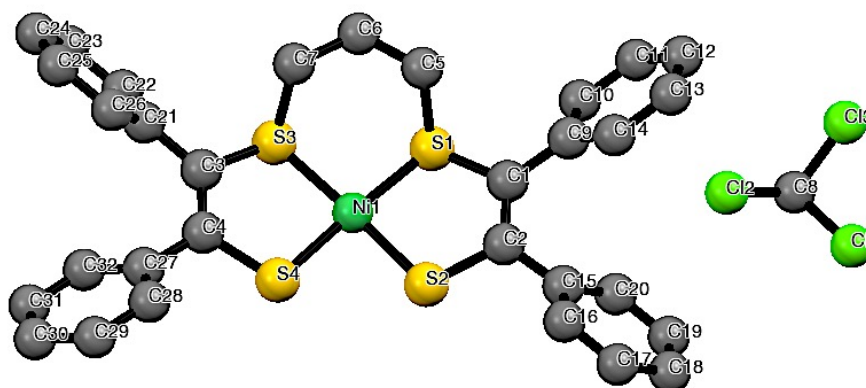


Figure 83. Crystal structure of 9, as reported by Zhang et al. [134].

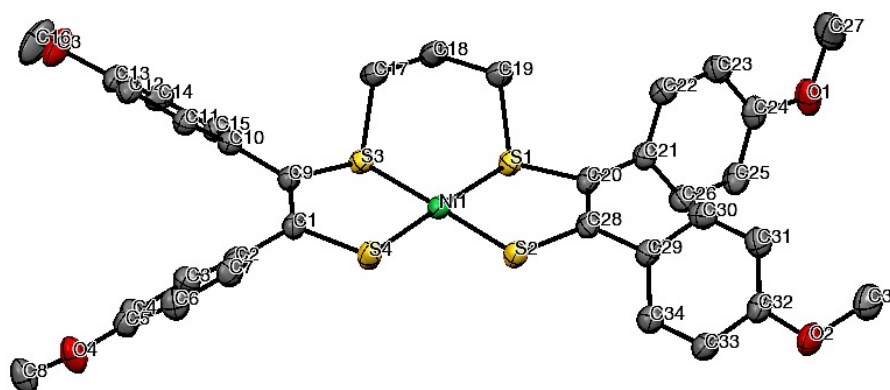


Figure 84. ORTEP diagram at 50% probability level for compound 10. Hydrogen atoms omitted for clarity.

The X-ray structure reveals a square planar geometry around the nickel ion (Figure 85), with all S – Ni – S angles approaching  $90^\circ$  (Table 22). Bond lengths are in typical range for nickel bis-dithiolene complexes [127], with average values of 2.153–2.162 Å. Bonds between  $S_{alkyl}$  and Ni (Ni1 – S1 and Ni1 – S3) are by  $\sim 0.01$  Å longer than the other Ni – S bonds (Ni1 – S2 and Ni1 – S4), a trend also observed for the corresponding C – S bonds; C20 – S1 and C9 – S3 are longer than C28 – S2 and C1 – S4 by  $\sim 0.02$  Å. Additionally, all C – S bonds are longer than the corresponding bonds in either 3 ( $\sim 1.71$  Å) or  $3^-$  ( $\sim 1.74$  Å) [68], indicating loss of dithioketone character upon sulfur alkylation. The C – C –ene bonds in 10 ( $\sim 1.35$  Å) are shorter than the corresponding bonds in 3 ( $\sim 1.39$  Å) but closer to the values of  $3^-$  ( $\sim 1.36$  Å) [68]. The above data indicate that upon alkylation of the dianionic compound  $3^{2-}$ , the resulting compound 10 exhibits a localized electronic structure with C – C –ene bonds

possessing double bond character. Thus, we propose that the alkylated ligand framework both in complexes 9 and 10 is best described by an dianionic enethiolate form coordinated to a Ni(II) center.

**Table 22.** Selected bond lengths (in Å) and bond angles (in °) for compound 10 at 100(2) K with estimated standard deviations in parentheses.

Ni1 – S1	2.1619(9)	Ni1 – S3	2.1622(9)
Ni1 – S2	2.1527(9)	Ni1 – S4	2.164(1)
C20 – S1	1.782(3)	C1 – C9	1.353(5)
C28 – S2	1.758(3)	C20 – C28	1.349(5)
C9 – S3	1.773(3)	C1 – S4	1.755(3)
S1 – Ni1 – S2	90.33(3)	S2 – Ni1 – S3	178.94(4)
S1 – Ni1 – S3	90.54(3)	S2 – Ni1 – S4	88.58(3)
S1 – Ni1 – S4	177.86(4)	S3 – Ni1 – S4	90.53(3)

Ni – S bond length values of 9 are in the same range as in 10 (~1.16 Å) [134], but C – S bonds follow the same trend as in compound 10, ie elongated C – S<sub>alkyl</sub> bonds compared to the remaining two C – S bonds.

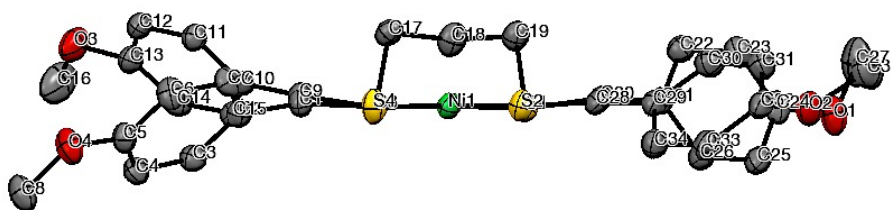


**Figure 85.** ORTEP diagram at 50% probability level for compound 10 showing planarity of NiS<sub>4</sub> core. Hydrogen atoms omitted for clarity.

Stacking of compound 10 reveals the shortest intermolecular S – S bond being 3.561 Å, in contrast to 9 (shortest S – S intermolecular bond is 3.561 Å, Figure 87) and 8 (shortest intermolecular distance Ni – S 3.453 Å).

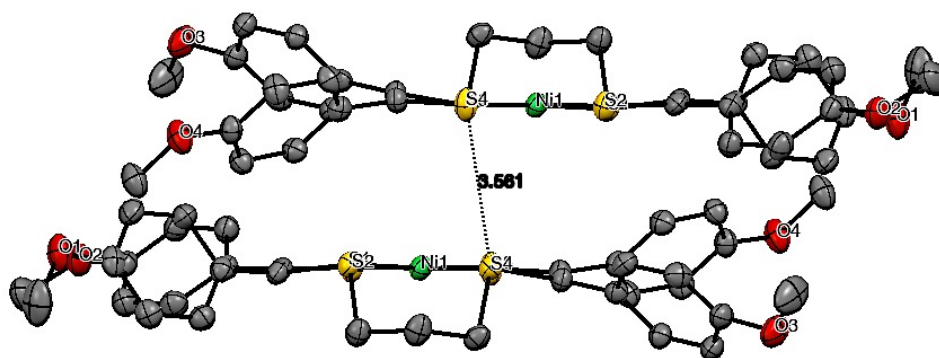


Figure 86. ORTEP diagram at 50% probability level for compound 10 (stacking of two molecules in the cell). Hydrogen atoms omitted for clarity.

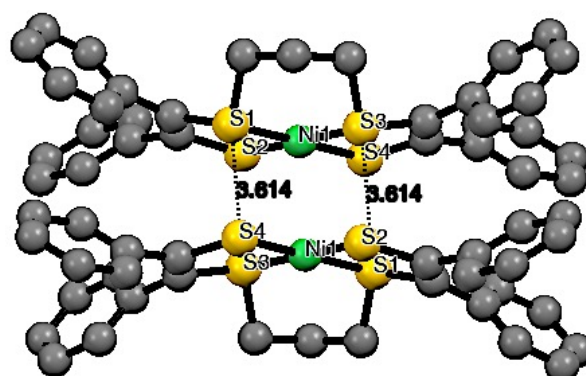
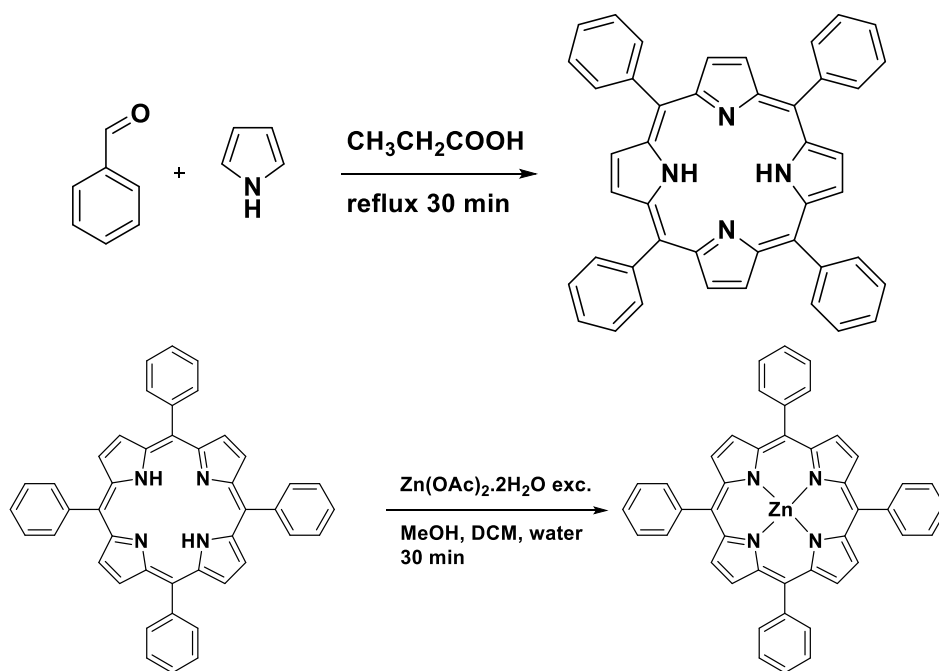


Figure 87. Diagram for compound 9 (stacking of two molecules in the cell). Hydrogen atoms omitted for clarity.

## 6.4 Preparation of other complexes

Free base tetraphenyl porphyrin was prepared by the method of Adler and Longo [141], by the condensation of pyrrole with benzaldehyde in the presence of refluxing propionic acid. Subsequent metalation with zinc was effected using a literature method [142]. Analytical data for these complexes match those reported in the literature.



**Scheme 28.** Synthetic scheme for the preparation of tetraphenylporphyrin (TPPH<sub>2</sub>) and subsequent metalation with zinc (ZnTPP).

## CHAPTER 7

### APPLICATIONS OF COMPLEXES

#### 7.1 Electrocatalytic hydrogen production with homoleptic dithiolene complexes

##### 7.1.1 Catalysts 1, 2, and 3

Trifluoroacetic acid (TFA;  $pK_a = 6.0$  in DMF) has been employed as the proton source in hydrogen evolution experiments for catalysts 1 – 3. The addition of TFA aliquots to solutions of catalyst 1, 2, or 3 in DMF triggers the appearance of catalytic waves that grow at potentials significantly more cathodic than the reversible redox potential corresponding to the formation of the dianionic species. For complex 1, two catalytic processes are observed at approximately  $-1.75$  and  $-1.9$  V vs  $Fc^{+/0}$  (midwave potentials; see Figure 88) measured at the middle of the catalytic waves for 5 mM TFA concentration.

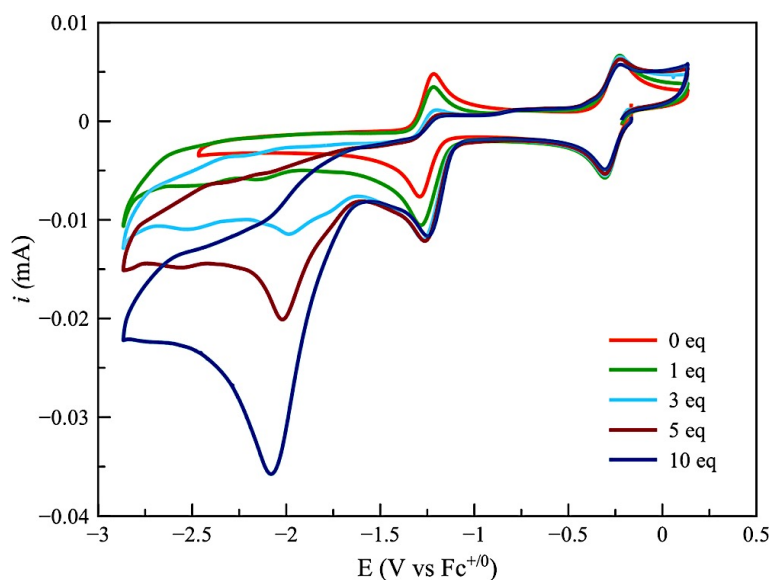


**Figure 88.** Cyclic voltammogram of 1 in the presence of increasing equivalents of TFA: no acid, red; 1 equiv, green; 3 equiv, light blue; 5 equiv, burgundy; 10 equiv, dark blue (glassy carbon working electrode).

Catalysts 2 and 3 exhibit the same behavior:

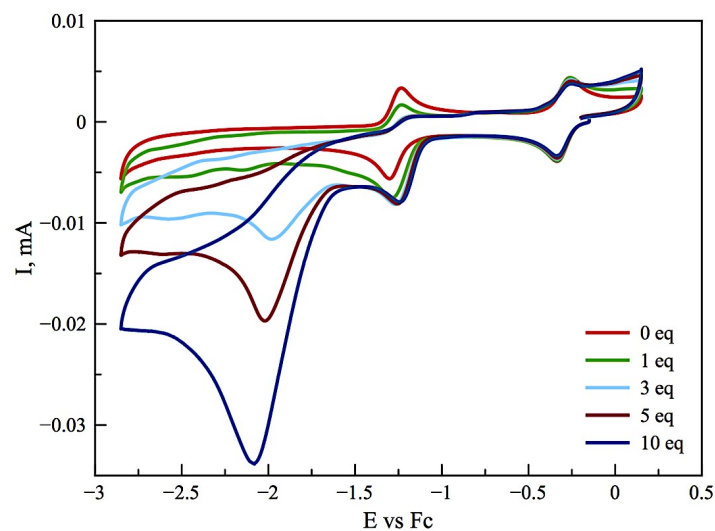


**Figure 89.** Cyclic voltammogram of **2** in the presence of increasing equivalents trifluoroacetic acid: no acid, red; 1 eq, green; 3 eq, light blue; 5 eq, burgundy; 10 eq, dark blue. Glassy carbon working electrode, scan rate  $100 \text{ mVs}^{-1}$  with  $\text{NBu}_4\text{PF}_6$  in DMF.

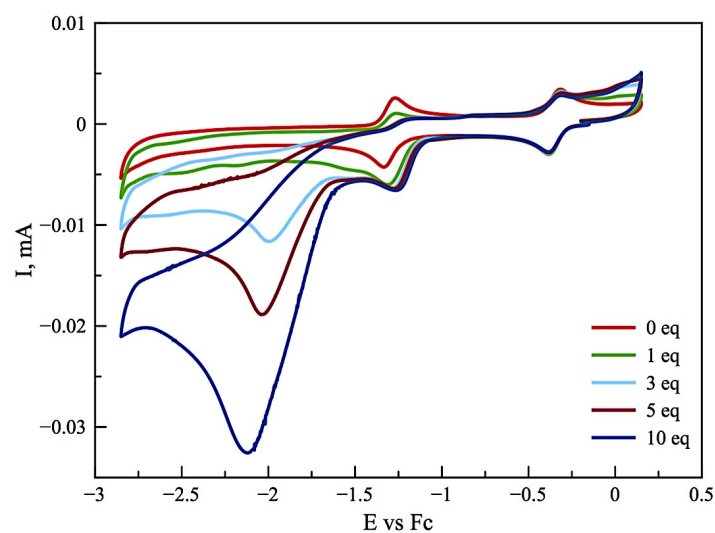


**Figure 90.** Cyclic voltammogram of **3** in the presence of increasing equivalents trifluoroacetic acid: no acid, red; 1 eq, green; 3 eq, light blue; 5 eq, burgundy; 10 eq, dark blue. Glassy carbon working electrode, scan rate  $100 \text{ mVs}^{-1}$  with  $\text{NBu}_4\text{PF}_6$  in DMF.

Direct reduction of TFA at the glassy carbon electrode occurs at potentials more negative than  $-2.2 \text{ V vs Fc}^{+/0}$ .

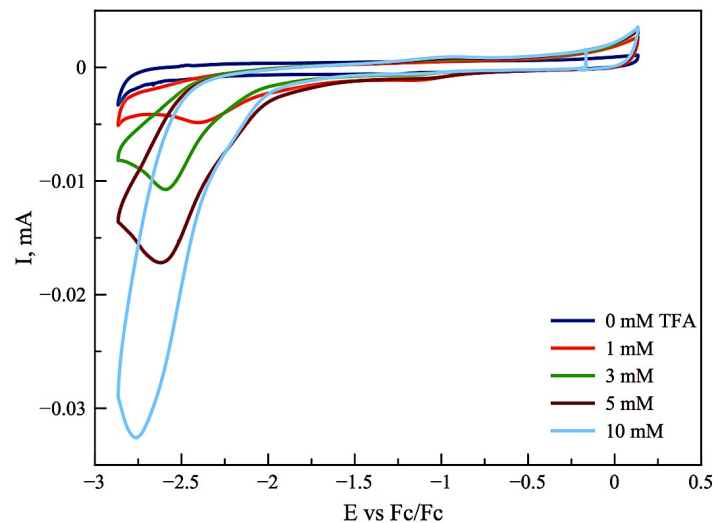


**Figure 91.** Cyclic voltammogram of trifluoroacetic acid in DMF in the absence of any catalyst. 0 mM, dark blue; 1 mM, red; 3 mM, green; 5 mM, burgundy; 10 mM, light blue. Glassy carbon working electrode, Ag/AgCl reference electrode, platinum wire counter–electrode, scan rate 100 mV s<sup>-1</sup> with NBu<sub>4</sub>PF<sub>6</sub> in DMF.

We can therefore conclude that both catalytic waves are mediated by the nickel–based catalysts. For comparison, similar cobalt and nickel dithiolene complexes (with maleonitriledithiolate or 1,2–benzenedithiolate ligands) exhibit only one wave in the presence of organic acids [34,59,104].

As the acid concentration increases and reaches 10 mM, the process with a half–wave potential of –1.75 V saturates and the process with a half–wave potential of –1.9 V prevails. The equilibrium potential for the reduction of TFA (5 mM) into H<sub>2</sub> in DMF is –0.94 V vs Fc<sup>+0</sup> and was calculated using the method described in refs [49,97] using the following equation:

$$E_{1/2} = E_{H^+/H_2}^0 - \frac{2.303RT}{F} pK_a + \epsilon_D - \frac{RT}{2F} \ln \frac{C_0}{C_{H_2}}$$

with the following values in DMF:

$$E_{H^+/H_2}^0 = -0.62 \text{ V vs } Fc^{+/0}, C_{H_2} = 1.9 \text{ mM}, \epsilon_D = 40 \text{ mV},$$

$$pK_a = 6.0 \text{ for TFA}, C_0 = 5 \text{ mM TFA}$$

This value allows overpotential requirements of 0.81 and 0.96 V to be determined at the midwave potentials for the two above–mentioned processes, respectively. The aforementioned trend is followed by complexes 2 and 3 with similar overpotential

requirements. At the same time, there is a concomitant loss of the reversibility of the 1-/2- redox process, indicating that a fast chemical reaction, likely protonation, takes place after reduction to the dianion. This is in accordance with the fact that the sulfur atoms, which act as intramolecular proton relays/protonation sites, are nucleophilic enough for protonation to occur only when the complex is fully reduced [66,143]. The peak potential of the cathodic wave ( $E_p$ ) moves toward more positive potentials with increasing amounts of protons, as expected for such an EC process [144]. Plotting  $E_p$  as a function of  $\log[\text{TFA}]$  for catalysts 1–3 results in linear relationships between these two quantities with slopes of 37.5, 47.6, and 50.5 mV per log unit, respectively.

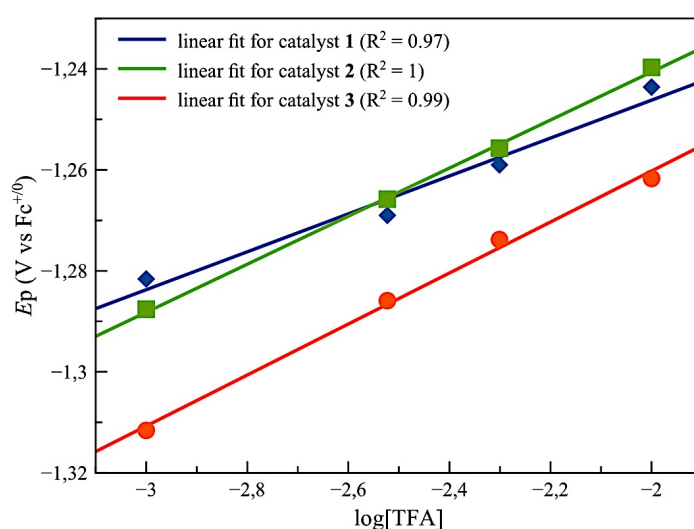


**Figure 92.** Evolution of the peak potential of the 1-/2- process of catalysts 1 (blue diamonds), 2 (green squares), and 3 (red circles) with  $\log[\text{TFA}]$ .

Protonation constant ( $k_{\text{H}^+}$ ) values of  $1.78 \times 10^5$ ,  $3.51 \times 10^7$ , and  $4.31 \times 10^7 \text{ s}^{-1}$  could then be determined using the following equation for the initial protonation step following the 1-/2- reduction process [94,145].

$$E_p = E^0 - 0.78 \frac{RT}{F} + \frac{RT \ln 10}{2F} \log \left( \frac{RT k_{\text{H}^+} [\text{TFA}]}{Fv} \right)$$

However, the current enhancement observed at the 1-/2- cathodic peak for catalysts 1–3 (53, 41, and 53%, respectively) in the presence of 10 mM TFA is larger than the ~11% increase of the peak current expected for an EC process [94], suggesting that a catalytic process might also occur at this potential value.

The production of hydrogen was confirmed using controlled potential bulk electrolysis in DMF at  $-1.67 \text{ V vs Fc}^{+/0}$ , corresponding to the onset potential of the

first catalytic wave mentioned above. The concentrations of the catalyst and TFA were 1 and 50 mM, respectively. Bulk electrolysis was performed for 3 h using a glassy carbon rod electrode, and the evolved hydrogen was quantified by gas chromatography. A faradaic yield of 66–83% is observed for all three complexes, with the highest value for the asymmetric complex 2. Complex 2 also performs best with a TON of 25, compared to 15 and 12 for 1 and 3, respectively.

**Table 23. Bulk electrolysis results for complexes 1, 2 and 3 in DMF in the presence of 50 mM trifluoroacetic acid.**

Compound	TON	Faradaic yield <sup>a</sup>
1	15	0.66
2	25	0.83
3	12	0.74
2 <sup>b</sup>	47	0.23

<sup>a</sup> bulk electrolysis was performed at  $-1.67$  V vs  $\text{Fc}^{+/0}$ , for a 3 h period, catalyst concentration 1 mM

<sup>b</sup> catalyst concentration was 0.1 mM

Bulk electrolysis using a mercury pool electrode resulted in less efficiency for all complexes, with a hydrogen sulfide smell evolving after the end of the experiment, which indicates a degree of catalyst degradation. In order to find out if a catalytic process occurs at the potential corresponding to the formation of the dianion, as enhancement of the peak current implies, bulk electrolysis experiments were also performed at  $-1.3$  V vs  $\text{Fc}^{+/0}$  for complexes 1 and 2. Catalysts 1 and 2 achieved 2 and 1 TONs corresponding to hydrogen evolution with 57% and 34% faradaic yield, respectively, indicating that this catalytic process is rather reduced but not missing, in accordance with DFT calculations.

Taking into consideration that the hydrogen–evolving systems reported up to now with dithiolene catalysts perform better when the catalyst is in lower concentration (micromolar for photocatalysis and  $10^{-4}$  M for electrocatalysis [34,59,76]), we also employed catalyst 2 with a concentration of 0.1 mM. The TON (determined from gas chromatography measurements) increased to 47 for the same time of bulk electrolysis (glassy carbon electrode, 3 h), with the faradaic yield dropping to 23%.

Thus, we propose that higher catalyst concentrations could lead to destructive pathways between two dithiolene catalyst molecules. CV measurements performed on the bulk

electrolysis solution at the end of the experiment display features similar to those of Figure 88. Furthermore, the addition of iodine in the bulk electrolysis solution after the end of the experiment resulted in a color change from red to green, indicating oxidation of the red anionic species to the green neutral.

In order to investigate whether decomposition of the catalyst occurs on the surface of the electrode, an implication of heterogeneous catalysis, rinse test experiments were performed in which, after three distinct experiments detailed below, the working electrode was rinsed with solvent and immersed again in a fresh solution of acid in order to examine whether a catalytic activity remains in the absence of catalyst in solution. First, the glassy carbon working electrode was conditioned through measurement of a single cyclic voltammogram in acidic solutions of catalyst 2. Little current enhancement was observed in CV measurements for the rinsed electrode.

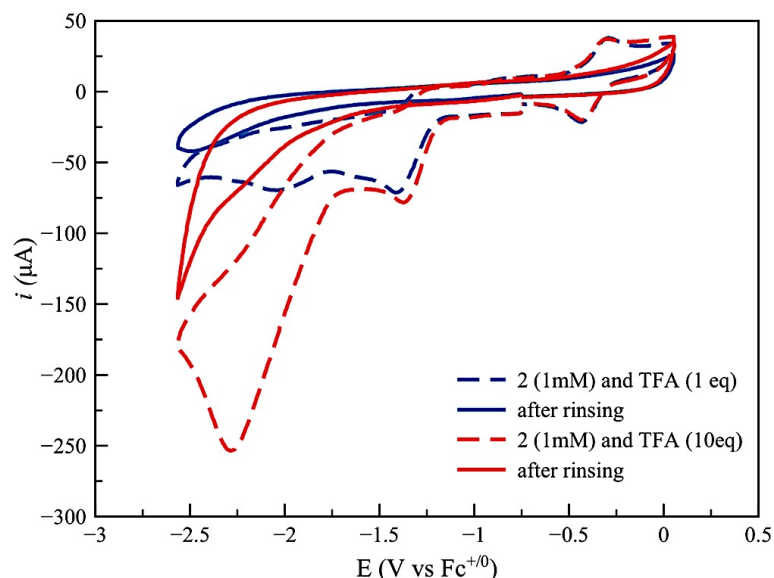


**Figure 93.** Rinse tests for catalyst 2 in the presence of 1 and 10 equiv of TFA: (solid line) in the presence of catalyst; (dashed line) in the absence of catalyst (glassy carbon working electrode).

Second, a linear sweep voltammogram from  $-0.5$  to  $-1.7$  V vs  $\text{Fc}^{+/0}$  was measured in the presence of catalyst.

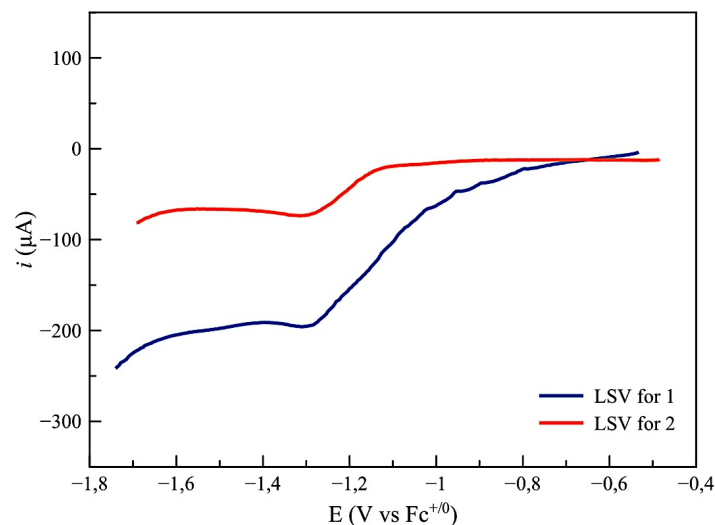


**Figure 94.** Linear sweep voltammetry of 1 mM catalysts 1 (blue trace) and 2 (red trace) at a glassy carbon electrode in the presence of 10 mM TFA (scan rate 100 mV s<sup>-1</sup> with NBU4PF<sub>6</sub> in DMF).

This procedure should avoid reoxidation of the deposit (therefore cleaning the electrode surface) during the backward scan. However, a subsequent CV measurement starting from -1.0 V vs Fc<sup>+0</sup> showed no current enhancement (red trace) in the potential region, where catalysis occurs in the presence of catalyst (dotted gray trace).

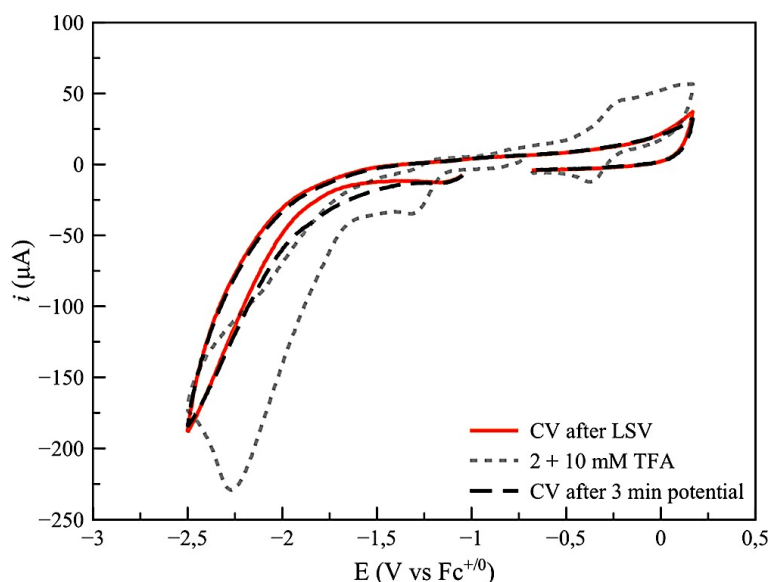


**Figure 95.** Rinse tests for catalyst 2 in the presence of 10 equiv of TFA: (gray trace) cyclic voltammogram in the presence of catalyst; (red trace) cyclic voltammogram in the absence of catalyst starting from -1.0 V vs Fc<sup>+0</sup> after linear sweep voltammetry; (black trace) cyclic

voltammogram in the absence of catalyst starting from  $-1.0\text{ V vs Fc}^{+/0}$  after 3 min potential application (glassy carbon working electrode).

Third, another conditioning procedure previously [104] reported to demonstrate deposition of NiS onto a glassy carbon electrode for a similar  $[\text{Ni}(\text{bdt})_2]^-$  complex was used. The working electrode was poised for 3 min at a constant potential negative to the potential of the 1-/2- process and corresponding to the onset of the catalytic wave ( $-1.65\text{ V vs Fc}^{+/0}$ ). The subsequent recording of the cyclic voltammogram (Figure 95, black trace) indicated that there was little enhancement of the catalytic wave in the absence of catalyst. The same behavior was observed with catalyst 1.

Finally, the linear dependence of  $i_{\text{cat.}}$  on the square root of the scan rate indicated a homogeneous, diffusion-controlled process [145].

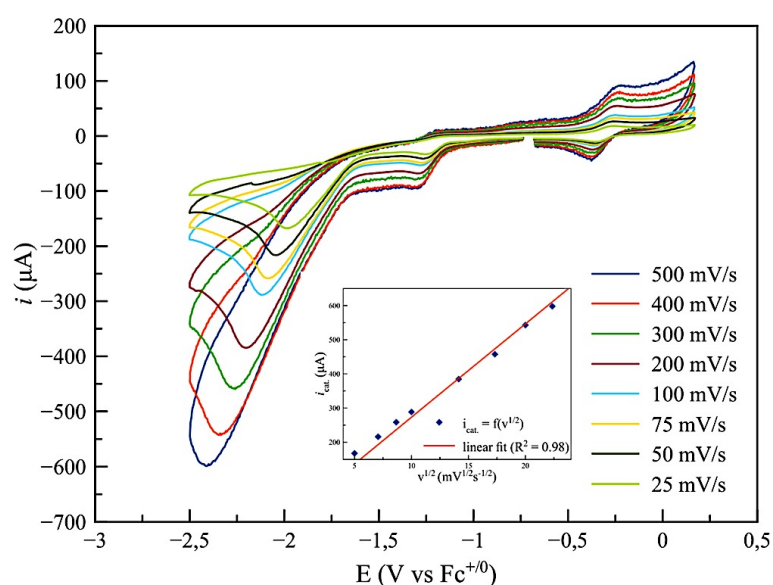


**Figure 96.** Cyclic voltammograms of catalyst 2 in the presence of 10 mM TFA at various scan rates. Inset: linear dependence of  $i_{\text{cat.}}$  vs  $v^{1/2}$  ( $R^2 = 0.97$ ; glassy carbon working electrode).

All of the above experiments indicate that, under the experimental conditions reported in this work, homogeneous catalysis occurs at the surface of the electrode.

### 7.1.2 Catalysts 4, 5, and 6

Trifluoroacetic acid (TFA,  $\text{pK}_a=12.7$  in MeCN) was employed as the proton source in the hydrogen-evolution experiments. Initial experiments with triethylammonium tetrafluoroborate ( $\text{pK}_a = 18.6$  in MeCN) did not reveal any catalytic activity because triethylammonium is too weak an acid in the chosen solvent.

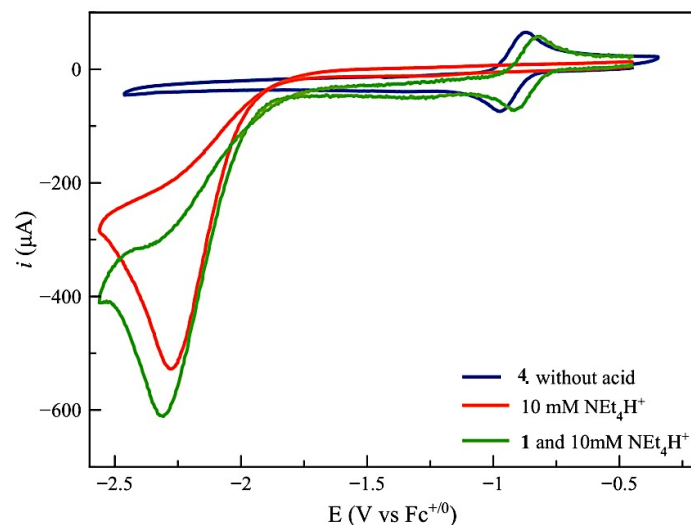


**Figure 97.** Cyclic voltammogram of catalyst 4 in the presence and absence of  $\text{Et}_3\text{NHBF}_4$ . Glassy carbon working electrode,  $\text{Ag}/\text{AgCl}$  reference electrode, platinum wire counter-electrode, scan rate  $100 \text{ mV} \cdot \text{s}^{-1}$  with  $\text{NBu}_4\text{PF}_6$  in  $\text{MeCN}$  as supporting electrolyte.

Catalysts 4 and 5 behave similarly in the presence of TFA. The catalytic wave occurs at potentials more negative than those required for the reduction of the monoanionic complex to the dianion. Upon addition of acid, the reversibility of the redox couple for the complex is also lost. A concomitant shift of the reduction wave towards less negative potential values with increasing acid concentration is also observed.

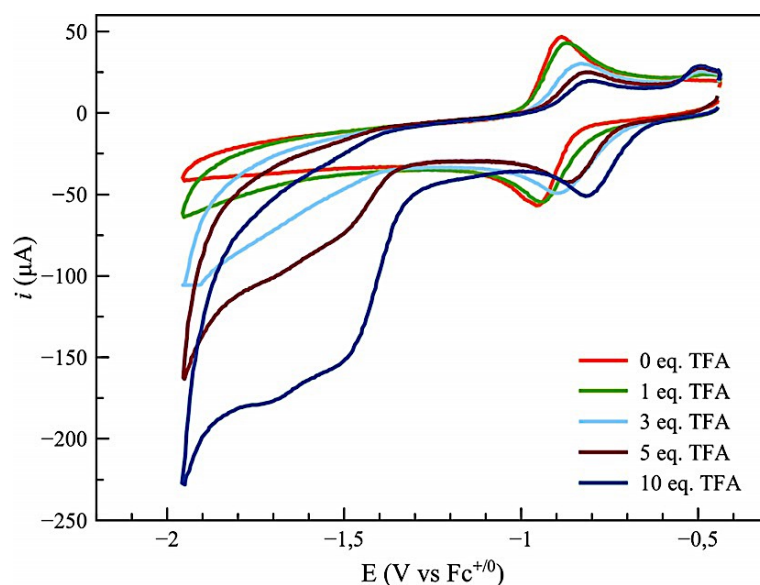


**Figure 98.** Cyclic voltammograms of 4 (1 mM) in the presence of increasing equivalents of trifluoroacetic acid. Glassy-carbon working electrode,  $\text{Ag}/\text{AgCl}$  reference electrode, platinum

wire-counter electrode, scan rate  $100 \text{ mVs}^{-1}$  with  $\text{NBu}_4\text{PF}_6$  in MeCN as the supporting electrolyte.

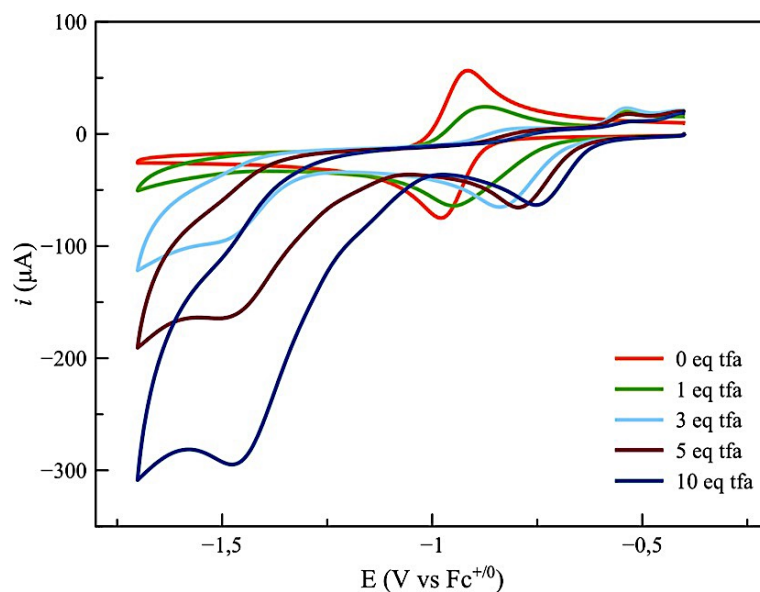


**Figure 99.** Cyclic voltammogram of 5 (1 mM) in the presence of increasing equivalents of TFA. Glassy-carbon working electrode, Ag/AgCl reference electrode, platinum-wire counter-electrode, scan rate  $100 \text{ mVs}^{-1}$  with  $\text{NBu}_4\text{PF}_6$  in MeCN as the supporting electrolyte.

Altogether, these data suggest that the dianionic form rapidly reacts with a proton to form a novel catalytically active species. For catalyst 4, if the acid concentration reaches 5 mM, two distinct processes can be observed, with half-wave potentials of  $-1.42$  and  $-1.68 \text{ V vs. Fc}^{+/0}$ . The equilibrium reduction potential for TFA in MeCN into protons (5 mM) was calculated to be  $-0.83 \text{ V vs. Fc}^{+/0}$  by using the method described earlier for catalysts 1 – 3. The overpotential requirements for these processes were calculated as  $0.587 \text{ V}$  and  $0.907 \text{ V}$ , respectively.

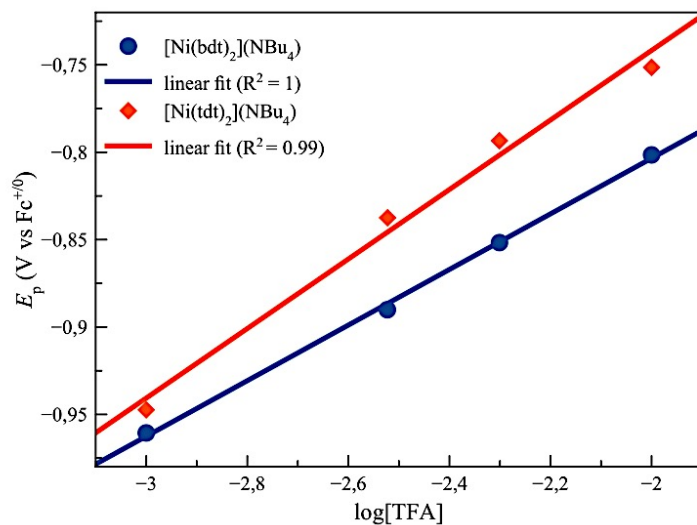


**Figure 100.** Linear fit diagram of  $E_p$  vs  $\log[\text{TFA}]$  for catalysts 4 and 5. Blue trace: catalyst 4; red trace: catalyst 5.

In contrast, catalyst 5 exhibits only the first of these waves with a half-wave potential of  $-1.3$  V vs.  $Fc^{+/0}$ , corresponding to an overpotential requirement of 0.467.

For catalyst 6, the catalytic wave appears at potential values close to the potential required for the reduction of the complex to the trianion, with a mid-wave potential value of  $-1.40$  V vs.  $Fc^{+/0}$  if the acid concentration is 5 mM.

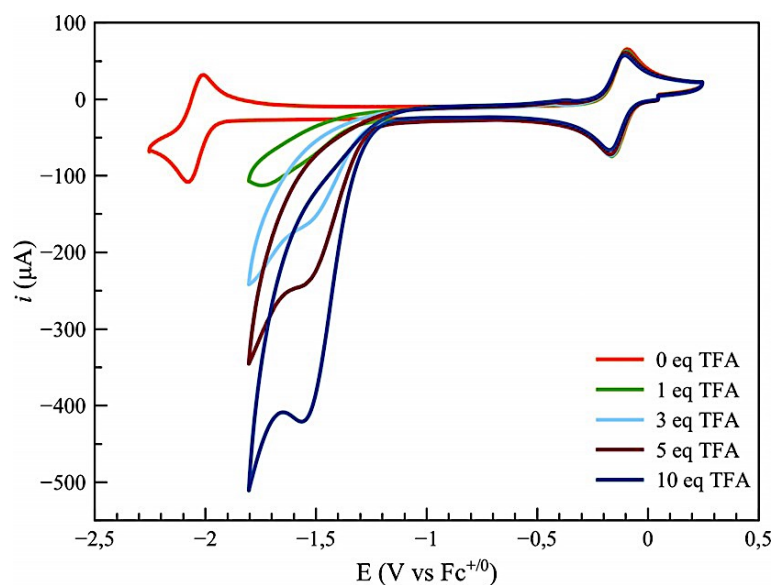


**Figure 101.** Cyclic voltammogram of 6 (1 mM) in the presence of increasing equivalents of TFA. Glassy carbon working electrode, Ag/AgCl reference electrode, platinum wire counter-electrode, scan rate  $100 \text{ mVs}^{-1}$  with  $\text{NBu}_4\text{PF}_6$  in MeCN as supporting electrolyte.

The reversibility of the 3-/2- couple is maintained and no shift of the anodic wave to less negative potential values is observed. This behavior is in contrast to that of catalysts 4 and 5. The overpotential requirement for this process is 0.567 V.

Hydrogen-evolution measurements were performed in MeCN by using a controlled-potential bulk-electrolysis setup with a glassy-carbon rod electrode in MeCN for a 3 h period at a potential of -1.2V vs.  $\text{Fc}^{+/0}$  for all the complexes. The evolved hydrogen was quantified by gas chromatography. Catalyst 5 performs best, with a TON of 158, compared to TONs of 113 and 6 for catalysts 4 and 6, respectively. The Faradaic yield was 71% for 4, 88% for 5, and 34% for 6.

**Table 24. Bulk electrolysis results for complexes 4, 5, and 6 in MeCN in the presence of 50 mM trifluoroacetic acid.**

Compound	TON	Faradaic yield <sup>a</sup>
4	113	0.71
5	158	0.88
6	6	0.34

<sup>a</sup> bulk electrolysis was performed at -1.2V vs  $\text{Fc}^{+/0}$  for a 3 h period, catalyst concentration 0.1 mM

The shift of the reduction potential towards less negative values that is observed for catalysts 4 and 5 as the concentration of TFA increases can be interpreted as the consequence of either an EC or a CE mechanism (with E denoting an electron-transfer step and C indicating a chemical reaction—here, protonation). In the first case, protonation is triggered by reduction whereas in the latter the complex is protonated first.

To investigate this process, a solution of each catalyst (0.1 mM) in deaerated MeCN was monitored by absorption spectroscopy after the addition of a large excess of TFA (50 mM).

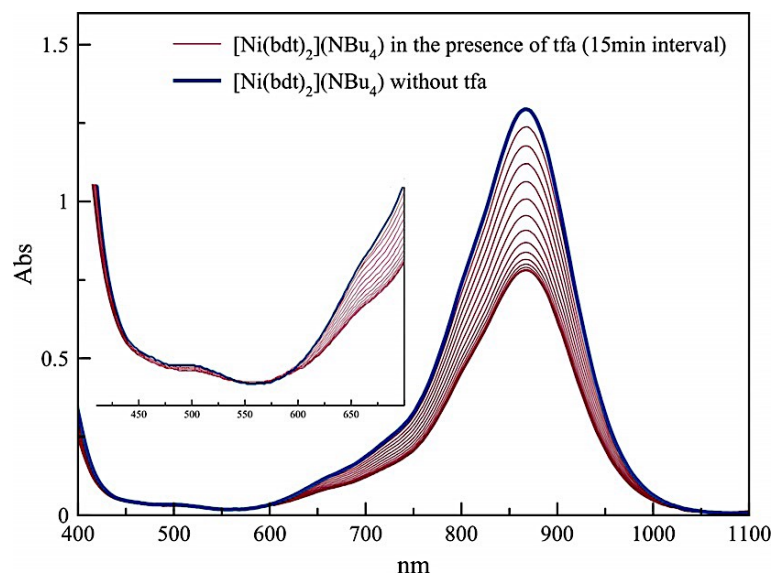


**Figure 102.** Evolution of the UV/Vis spectrum of catalyst 4 (0.1 mM) after the addition of 50 mM TFA. Spectra were recorded in deaerated MeCN at 15 min intervals. The inset shows an enlargement of the shoulder region.

The band at 866 nm in the presence of acid exhibits a hypochromic shift as a function of time. The presence of isobestic points (inset) indicates the formation of one new species which absorbs at similar wavelengths, with a more pronounced shoulder at 800 nm compared to the spectrum of the sample without acid. Such a behavior indicates the slow formation of a protonated species. As this band at 800 nm has been assigned to an intravalence charge–transfer (IVCT) transition involving the radical anionic ligand  $[(L\cdot)M(L)] \leftrightarrow [(L)M(L\cdot)]$  [30], we propose that protonation occurs at the sulfur. This procedure is partially reversed if a base soluble in  $CH_3CN$  is added (e.g., trimethylamine).

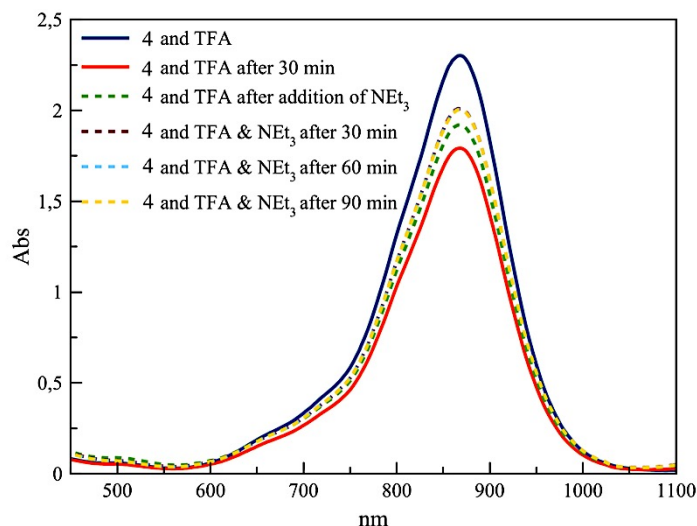


**Figure 103.** UV–Vis spectrum of catalyst 4 (0.1 mM) in the presence of 50 mM TFA in deaerated MeCN after 30 min. Addition of  $\text{NEt}_3$  and measurements in 30 min cycles.

The formation of protonated species is therefore possible, although such a process is extremely slow in comparison with the cyclic voltammetry timescale. We therefore conclude that formation of protonated species  $4\text{H}^+$  and  $5\text{H}^+$  proceeds through EC mechanisms.

The linear dependence of  $i_{\text{cat}}$  (where  $i_d$  denotes the current of the catalytic wave) on the square root of the scan rate ( $v^{1/2}$ ) indicates a diffusion–controlled homogeneous process for both catalysts 4 and 5, as shown in the following Figures.

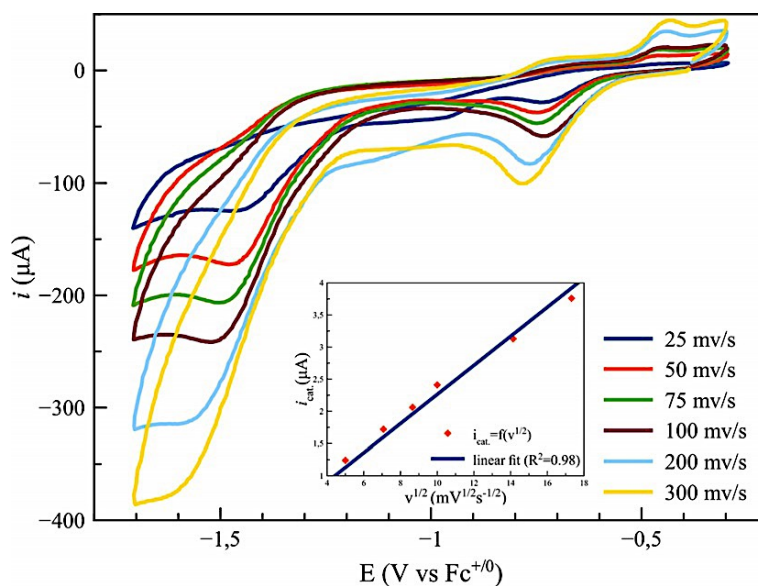


**Figure 104.** Cyclic voltammogram of catalyst 4 in the presence of 10 mM TFA at various scan rates. Inset: linear dependence of  $i_{\text{cat}}$  on  $v^{1/2}$  ( $R^2=0.98$ , glassy–carbon working electrode).

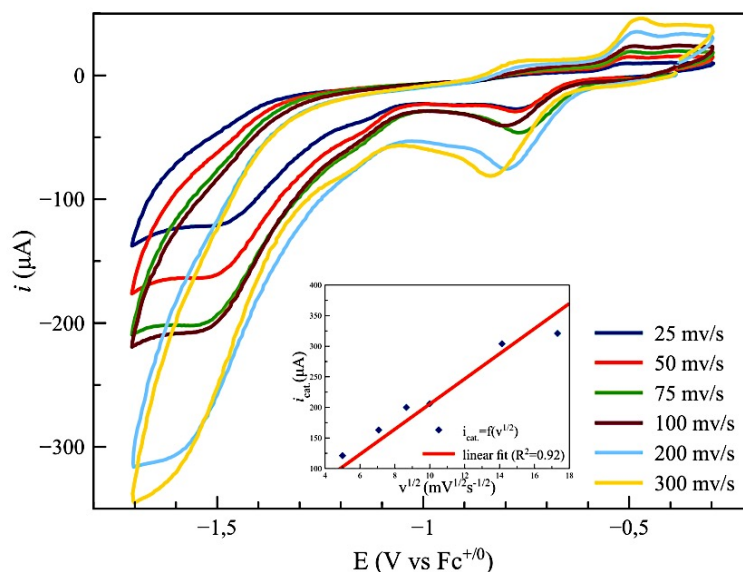


**Figure 105.** Cyclic voltammogram of catalyst 5 in the presence of 10 mM TFA at various scan rates. Inset: linear dependence of  $i_{\text{cat}}$  on  $v^{1/2}$  ( $R^2=0.92$ , glassy carbon working electrode).

To confirm this point, we performed three rinse tests for catalyst 4, in the same manner as mentioned earlier for Ni–bis(aryldithiolene) catalysts 1 – 3.

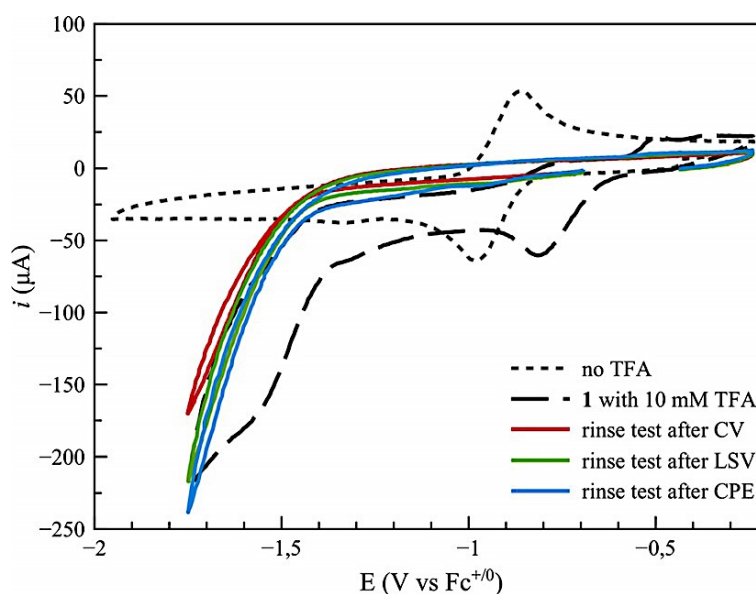


**Figure 106.** Rinse tests for catalyst 4 (glassy-carbon working electrode). Cyclic voltammogram for catalyst 4 in the absence (gray dotted trace) and presence (black trace) of 10 mM TFA in MeCN. Each trace indicates a scan of a rinsed working electrode in a fresh solution of 10 mM TFA in MeCN. Red trace: after the measurement of a cyclic voltammogram; green trace: after a linear-sweep voltammogram; blue trace: after a potential of  $-1.3$  V applied for 3 min.

Initially the electrode was rinsed after a cyclic voltammetry scan, and the electrode was transferred to a fresh solution of acid. Then, a cyclic voltammogram was recorded starting at a negative potential ( $-0.7$  V vs.  $\text{Fc}^{+/0}$ ) to avoid oxidative

redissolution of any deposited material. Almost no catalytic current was observed. Second, a linear sweep voltammogram of the catalyst in the presence of TFA was measured. This procedure was used to definitively exclude oxidative redissolution of any deposit during the reverse scan. However, a subsequent CV measurement starting from  $-0.7$  V vs.  $\text{Fc}^{+/0}$  did not show any catalytic behavior distinct from that of the pristine electrode. As a last conditioning method, a potential of  $-1.3$  V vs.  $\text{Fc}^{+/0}$  was applied for 3 min, with a subsequent measurement of a cyclic voltammogram starting from  $-0.7$  V vs.  $\text{Fc}^{+/0}$ . Again, no catalysis was observed, indicating that catalysis under these conditions is of a homogeneous nature. The same was observed for catalyst 5.

Significant attention has been drawn to whether electrocatalysis in organic solvents is of homogeneous or heterogeneous nature. More specifically, several studies on similar dithiolene- or thiolate-containing systems have shown that under reductive conditions a molecular catalyst may decompose to form a material which deposits on the surface of the electrode and is responsible for the catalytic performance [12,59,66,104,146–148]. Several diagnostic criteria have been used to identify if a process is truly catalytic, most notably rinse tests in which the electrode, after a scan or a potential has been applied for a period of time, is transferred to a fresh solution containing only the acid. The rinse test experiments performed for catalysts 4 and 5 clearly support homogeneous/molecular  $\text{H}_2$  evolution catalysis. Recently, Fang et al. in a meticulous study reported on the processes that take place if 4 is employed as an electrocatalyst in the presence of 4-bromo-anilinium tetrafluoroborate ( $\text{pK}_a=9.43$  in MeCN) [104]. We were able to reproduce their findings with minor differences owing to instrumentation and experimental conditions.

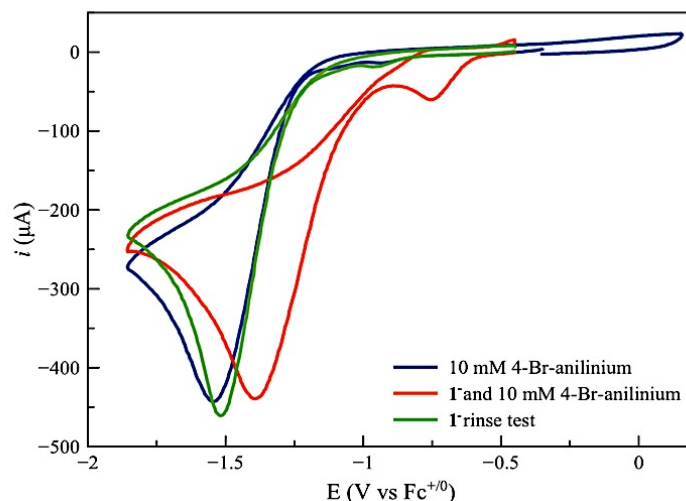


**Figure 107.** Cyclic voltammogram for 10 mM 4-Br-anilinium tetrafluoroborate in the absence (dark blue trace) and presence (red trace) of catalyst 4 in MeCN. Green trace indicates scan of a rinsed working electrode in a fresh solution of 10 mM tetrafluoroborate in MeCN (rinse test).

Based on the different strength (3.27 pKa units) of the acids used (TFA by us and 4-bromoanilinium by Fang et al.) we propose that even though under reductive conditions and in the presence of acid catalyst, 4 decomposes as shown by Fang et al., the degree of decomposition relies on the strength of the acid, with stronger acids leading to an extended degree of catalyst decomposition.

In this context, we examined the behavior of the cobalt analogue of 4,  $[\text{Co}(\text{bdt})_2](\text{NBu}_4)$  that has been reported as a catalyst for the reduction of protons by the groups of Eisenberg and Holland [34,59]. If investigated in a MeCN/water 1:1 mixture under anaerobic conditions in the presence of p-toluenesulfonic acid (0.2 mM  $[\text{Co}(\text{bdt})_2](\text{NBu}_4)$ , 65 mM p-toluenesulfonic acid), decomposition occurs. This can be seen from the absorption spectrum, in which there is a decrease in absorbance with a concomitant increase in baseline, and a grayblack precipitate is formed.

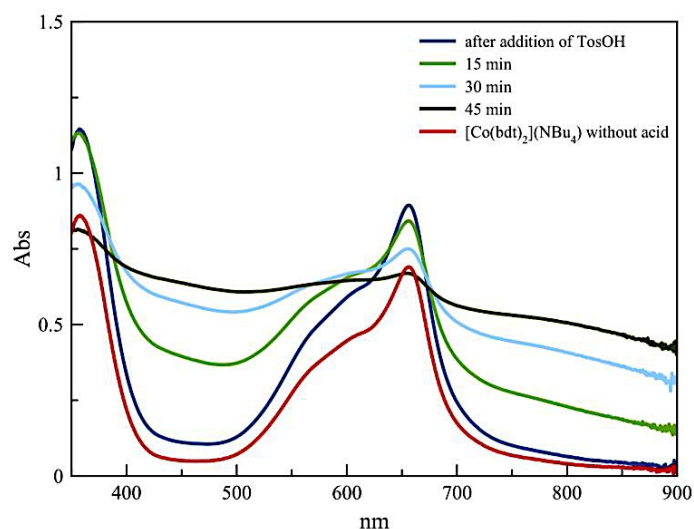


**Figure 108.** Absorption spectrum of  $[\text{Co}(\text{bdt})_2](\text{NBu}_4)$  (0.2 mM) in the absence (red trace) and presence of tosic acid (65 mM) as a function of time, under Ar, in a 1 – 1 mixture of MeCN – water.

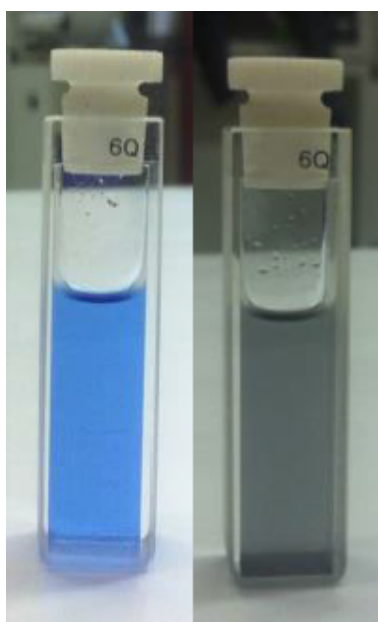


**Figure 109.** Cuvettes before (left) and after (right) recording the absorbance of a  $[\text{Co}(\text{bdt})_2](\text{NBu}_4)$  sample, under the same conditions shown previously.

This can be rationalized in terms of the increased acidity of p-toluenesulfonic acid in MeCN/water mixtures [149,150], which leads to the degradation of the dithiolene complex. According to a recent paper [105], the black precipitate is of molecular nature and contains the protonated form of  $[\text{Co}(\text{bdt})_2]^-$ . These findings imply that both

Ni- and Co- dithiolene complexes behave differently in the presence of acid [106,151].

### 7.1.3 Theoretical calculations and discussion

DFT calculations were employed to investigate the possible reaction pathways for hydrogen evolution by catalysts 1–3 and their monoanions. The electronic structure of all of the stationary points along the reaction path were characterized, and the redox potentials of the electron-transfer steps as well as the energies of the proton-transfer processes were calculated. Although these computed energies can be different from the experimental values, often by as much as 300 mV [152] the calculations, nevertheless, provide invaluable insight into what is observed experimentally. The geometries of the neutral complexes and their monoanions were fully optimized in DMF from their experimental single-crystal X-ray structures, as determined herein and in the literature [124]. The calculated geometries in solvent are in good agreement with the experimental ones, with the calculated bond lengths and angles within 0.01 Å and 2°,

respectively. There is an exception for the Ni–S bond lengths, which are overestimated by as much as 0.04 Å, but this is anticipated with DFT calculations. Calculated structural parameters, namely, bond lengths and S–Ni–S dihedral angles for complex 1, its monoanion, and all of its intermediates, are summarized in Table 25.

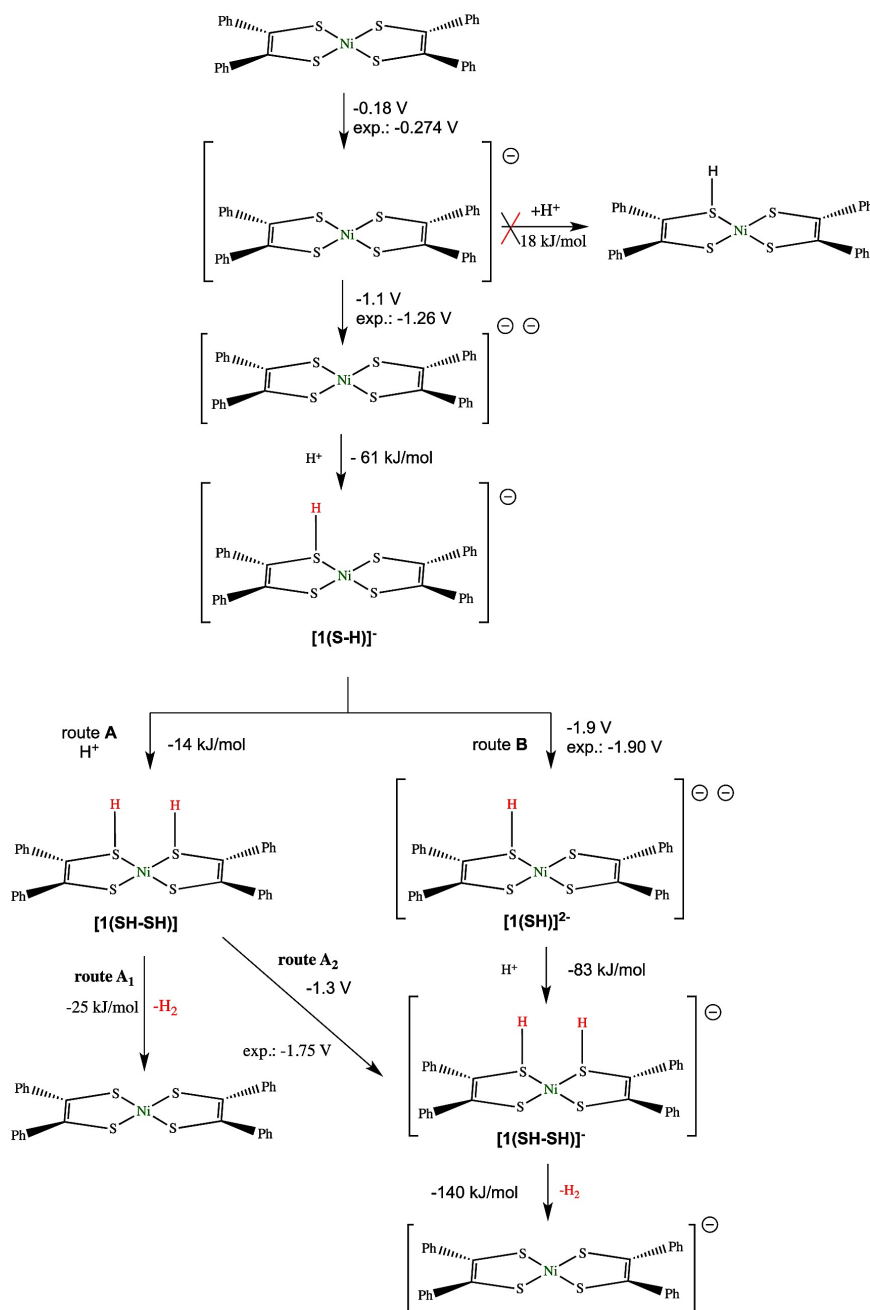
**Table 25. Selected structural parameters calculated for intermediates of the hydrogen evolution mechanism for catalyst 1.**

Parameter <sup>a</sup>	[1] <sup>[124]</sup>	[1] <sup>−</sup>	[1] <sup>2−</sup>	[1(S–H)] <sup>−</sup>	[1(S–H)] <sup>2−</sup>	[1(SH–SH)]	[1(SH–SH)] <sup>−</sup>
Ni1 – S1	2.160	2.184	2.222	2.227	2.404	2.230	2.369
Ni1 – S2	2.161	2.183	2.213	2.237	2.374	2.200	2.310
Ni1 – S3	2.160	2.185	2.219	2.185	2.312	2.205	2.335
Ni1 – S4	2.161	2.186	2.219	2.203	2.311	2.236	2.335
C1 – S1	1.722	1.757	1.790	1.803	1.804	1.806	1.805
C2 – S2	1.721	1.755	1.778	1.770	1.769	1.769	1.765
C16 – S3	1.722	1.758	1.783	1.782	1.777	1.771	1.772
C17 – S4	1.721	1.755	1.763	1.783	1.787	1.805	1.804
C1 – C2	1.392	1.364	1.356	1.351	1.360	1.348	1.359
C16 – C17	1.392	1.364	1.353	1.350	1.361	1.349	1.360

S1 – H	–	–	–	1.352	1.351	1.353	1.352
S4 – H	–	–	–			1.352	1.352
S–Ni–S dihedral angle	0	0	0.8°	2.32°	20.44°	8.87°	39.93°

<sup>a</sup> numbering scheme is the same as Figure 60 assuming protonation at S1 and S4. Bond lengths are given in Å.

The proposed mechanism for the  $2e^-/2H^+$  reduction/protonation of 1 leading to evolution of hydrogen is shown in Scheme 29. All of the protonation energies were computed with respect to the  $CF_3COOH/CF_3COO^-$  couple, and the standard redox potential,  $E^\circ$ , was calculated using the relation  $E^\circ = (-\Delta G^\circ/nF) - E^\circ_{ref}$ , where  $\Delta G^\circ$  is the free energy of reduction,  $n$  is the number of electrons being transferred,  $F$  is the Faraday constant, and  $E^\circ_{ref}$  is the absolute reduction potential of the ferrocene couple computed at the same level of theory.



**Scheme 29.** Proposed mechanism for hydrogen evolution with catalyst 1 together with calculated protonation enthalpies and redox potentials (experimentally determined electrochemical potentials are also indicated. Potentials are reported vs  $\text{Fc}^{+/0}$ ).

As Scheme 29 indicates, the mechanism initially involves reduction to the monoanion followed by reduction to the dianion, and the next step is protonation of the latter, which proceeds downhill by  $61\text{ kJ mol}^{-1}$ . Overall, this scheme agrees with the experimental findings in which hydrogen is produced after formation of the dianion, and it is also identified as the favorable path compared with protonation of the monoanion, yielding  $[1(\text{SH})]$ , a process computed to be endothermic by as much as  $18\text{ kJ mol}^{-1}$ . Moreover, protonation of the monoanion at the nickel atom is less

favorable to  $[1(\text{SH})]^-$  by  $74 \text{ kJ mol}^{-1}$ . These calculations indicate that the most favorable protonation site of the dianion of 1 is on any one of the sulfur atoms of the dithiolene ligands rather than the nickel atom. Indeed, the nickel-protonated counterpart  $[1(\text{NiH})]^-$  is less stable by  $64 \text{ kJ mol}^{-1}$  than  $[1(\text{SH})]^-$  (Scheme 29). After the first protonation, two different steps can take place; either a second protonation via a thermoneutral reaction ( $-14 \text{ kJ mol}^{-1}$ ) (route A) or reduction and then protonation (route B).

Protonation of  $[1(\text{SH})]^-$  (route A) leads only to one intermediate, which is doubly protonated on two sulfur atoms on distinct dithiolene rings, namely,  $[1(\text{SH}-\text{SH})]$ . Hydrogen evolution from this state to afford complex 1 is slightly exergonic by  $-25 \text{ kJ mol}^{-1}$  (route A1, Scheme 29) in accordance with the experimental evidence of catalytic hydrogen evolution at the potential of the 1-/2- process.  $[1(\text{SH}-\text{SH})]$  is calculated to be more stable than the state where both protons are on sulfur atoms of the same chelate ring by  $32 \text{ kJ mol}^{-1}$ . Subsequent reduction with a potential of  $-1.3 \text{ V}$  vs  $\text{Fc}^{+/0}$  (compared to experimental  $-1.75 \text{ V}$  vs  $\text{Fc}^{+/0}$ ) leads to the reduced diprotonated intermediate  $[1(\text{SH}-\text{SH})]^-$  (route A2, Scheme 29). This intermediate can also be reached via the alternative route B because the singly protonated  $[1(\text{SH})]^-$  is reduced at  $-1.9 \text{ V}$  vs  $\text{Fc}^{+/0}$  (compared to the  $-1.9 \text{ V}$  vs  $\text{Fc}^{+/0}$  experimentally observed) to produce  $[1(\text{SH})]^{2-}$ . For this reduction process, one has a unique singly protonated singly reduced species but two singly protonated doubly reduced species that are close in energy. The singly reduced species has the proton on a sulfur atom, whereas the two doubly reduced species have protons on either a sulfur atom or the metal. In each case, however, reduction occurs primarily on the sulfur atoms ( $>1$  electron gain in charge) with small compensating changes on the other atoms. For the doubly reduced species with sulfur protonation, the protonated sulfur atom gains an amount of negative charge similar to those of the other three sulfur atoms. By comparison to the sulfur-protonated doubly reduced species, the proton atom gains  $\sim -0.30$  units of charge in the metal-protonated doubly reduced species, indicative of its hydride nature.

The calculations indicate that  $[1(\text{SH})]^{2-}$  is more stable than  $[1(\text{NiH})]^{2-}$  by only  $1 \text{ kJ mol}^{-1}$ , thereby not excluding the possibility of nickel-ion protonation. However, the next step protonation of the dianion yields the species  $[1(\text{SH}-\text{SH})]^-$ , in an energetically downhill process of  $-83 \text{ kJ mol}^{-1}$  with respect to  $[1(\text{SH})]^{2-}$ . This

monoanionic species is  $19 \text{ kJ mol}^{-1}$  more stable than the one with two protons on the same sulfur ligand, and no stable species protonated at nickel was observed. Other studies have suggested that a nickel hydride intermediate is formed before hydrogen evolution [153], but this is probably due to the differences in the electronic properties of the dithiolene ligands that were employed. From this point, evolution of hydrogen proceeds via an exothermic reaction by  $-140 \text{ kJ mol}^{-1}$ , yielding the monoanion of complex 1, which therefore acts as the catalyst for the reduction of  $\text{H}^+$ .

According to experimental data, the two routes compete at low ratios of acid to catalyst (1–3 equiv of acid), whereas at higher ratios ( $\geq 10$  equiv), route A saturates and route B appears dominant. The calculated structures for the intermediates along with the catalytic cycle are shown in Figure 110. Holding the potential value at  $-1.67 \text{ V vs Fc}^{+/0}$  in the bulk electrolysis experiment makes route A prevail because route B requires significantly more negative potential values.

In route B, formation of the protonated  $[\text{1}(\text{NiH})]^{2-}$  species is possible, but no stable species protonated at both sulfur and nickel could be found, as mentioned before. These findings are in contrast to the ones for the related cobalt dithiolene complexes. In fact, extensive studies on cobalt dithiolenes by Letko et al. [66] revealed that a Co–H intermediate species is formed in the hydrogen evolution cycle. More specifically, the monoanionic cobalt species is reduced to the dianion, and protonation occurs at the cobalt ion. Subsequent reduction and protonation leads to a (Co–H)/(S–H) diprotonated species that releases dihydrogen. However, herein it is proposed that in nickel aryldithiolene complexes the protonation and redox effects are located mainly on the ligand framework because of the decreased contribution of nickel orbitals:  $\sim 25\%$  Ni 3d orbitals for all three oxidation states of the similar  $[\text{Ni}(\text{S}_2\text{C}_2\text{Me}_2)_2]$  complexes [128], as opposed to  $62\%$  for cobalt complexes [66]. As observed earlier [129] for the similar compound  $[\text{Ni}(\text{S}_2\text{C}_2\text{Me}_2)_2]$  across the 0/1–/2–oxidation states, the redox events take place on the ligands because of the increased contribution of S  $3_{\text{pz}}$  in the  $5b_{2g}$  molecular orbital, even though the nickel contribution increases upon reduction to the dianion. Herein it is proposed that this is also the case for the nickel dithiolene complexes under study.

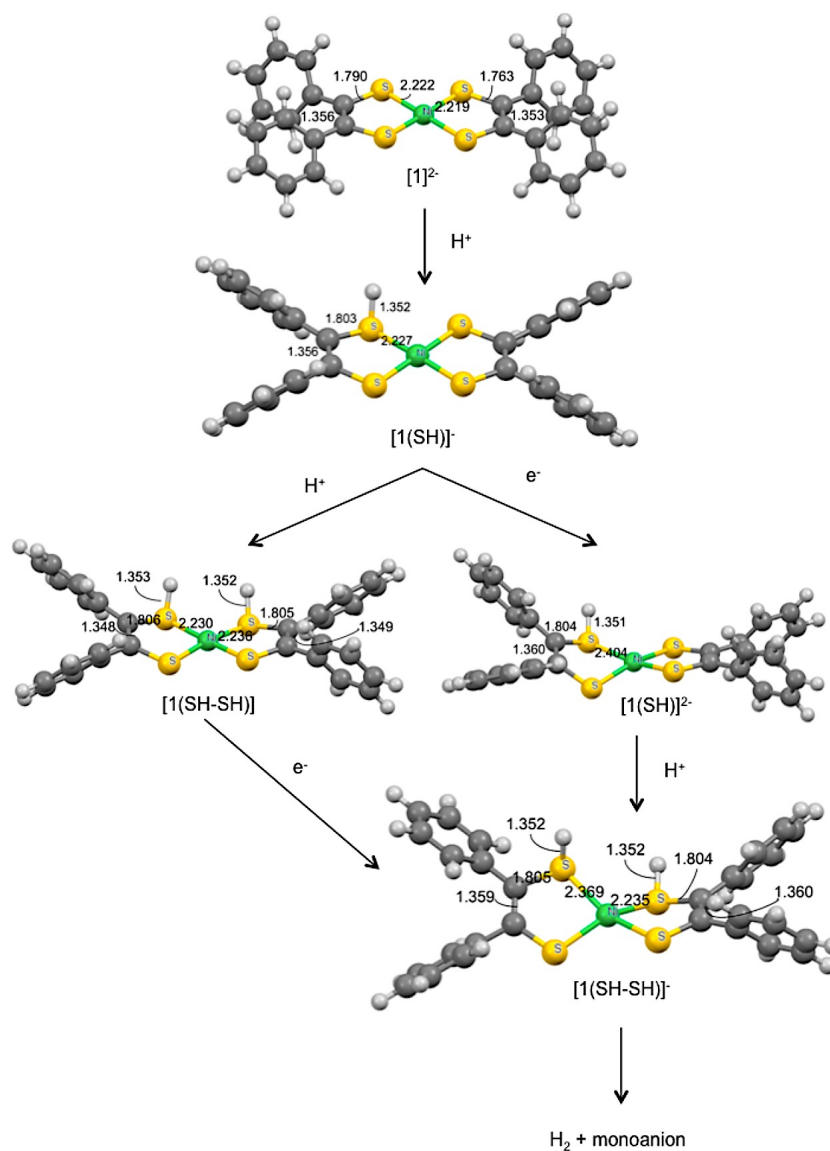


**Figure 110.** Calculated structures for intermediates in the proposed hydrogen evolution mechanism for 1.

Upon protonation after reduction to the dianionic state  $[1]^{2-}$ , only a minor tetrahedral distortion is observed ( $2.32^\circ$ ) for intermediate  $[1(\text{SH})]^-$ . Subsequent protonation as discussed before (route A) leads to a more distorted structure ( $8.87^\circ$  for  $[1(\text{SH-SH})]$ ). In route B, the generated  $[1(\text{SH})]^{2-}$  exhibits a dihedral S–Ni–S angle of  $20.44^\circ$ , whereas the corresponding  $[1(\text{NiH})]^{2-}$  intermediate (Figure 111) exhibits a calculated S–Ni–S dihedral angle of  $75.04^\circ$ . When the diprotonated and reduced state  $[1(\text{SH-SH})]^-$  is reached, the dihedral angle is calculated to be  $39.93^\circ$ , which is much larger than that in the neutral form.

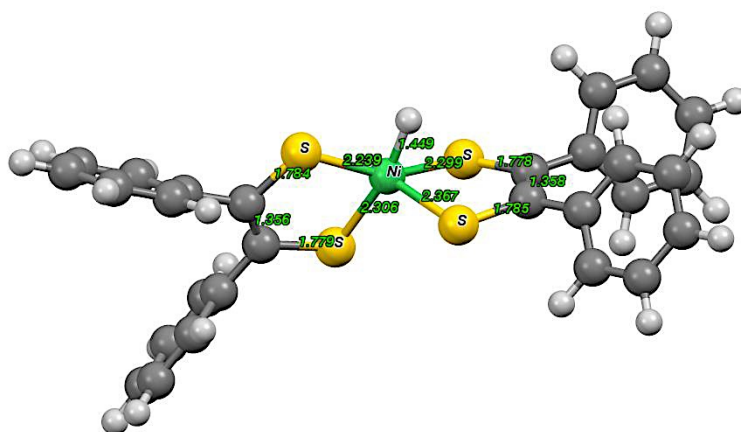


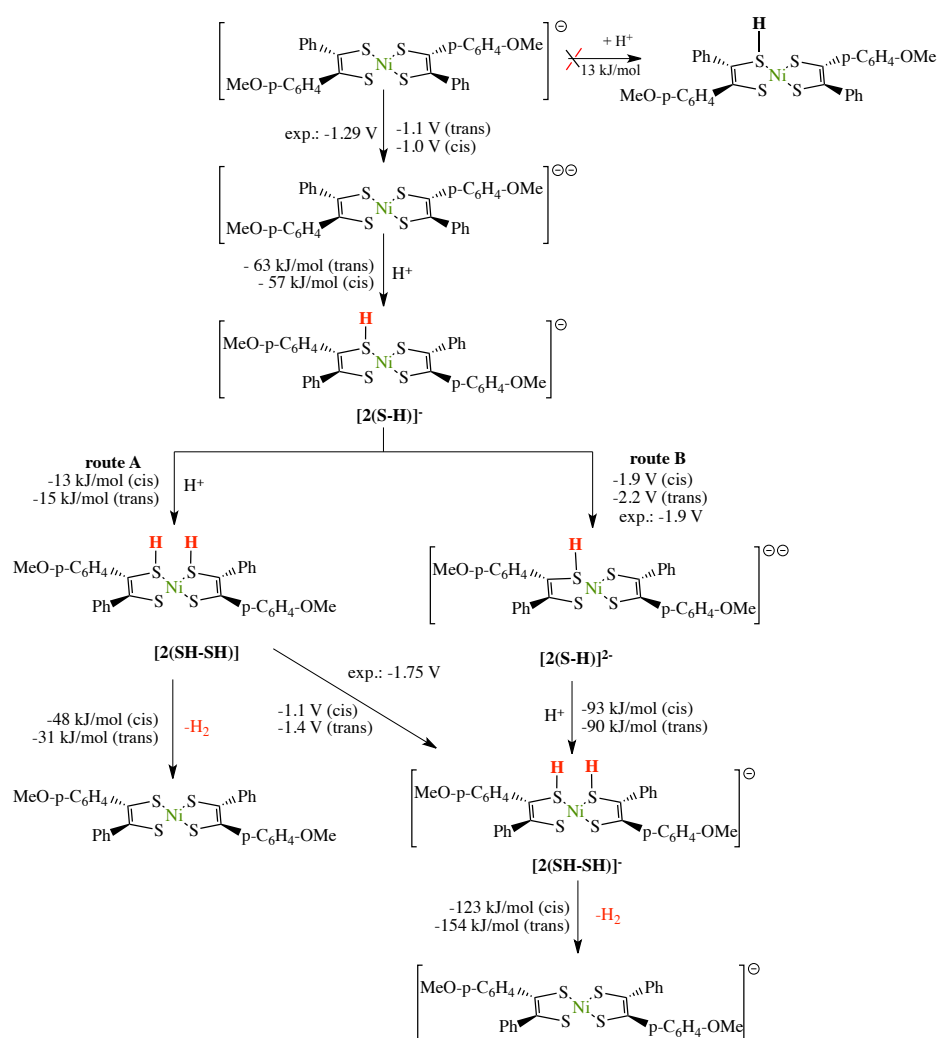
**Figure 111.** DFT-calculated structure for intermediate  $[1(\text{NiH})]^{2-}$ . S – Ni – S dihedral angle is calculated 75.04°.

Another important parameter is the H $\cdots$ H distance in the protonated intermediates, which increases from 3.0 Å in  $[1(\text{SH}-\text{SH})]$  to 4.0 Å in  $[1(\text{SH}-\text{SH})]^-$ . Additional studies, including explicit dynamics of the complexes, are therefore required to identify the mechanism for hydrogen evolution from these species. Alternatively, transient cleavage of a Ni–S bond, as observed in some higher energy species in the course of our DFT studies (data not shown), with hydrogen passage via the nickel might be envisaged.

For the symmetric tetramethoxy complex 3, the mechanism proposed is the same as that for 1 with analogous intermediates.

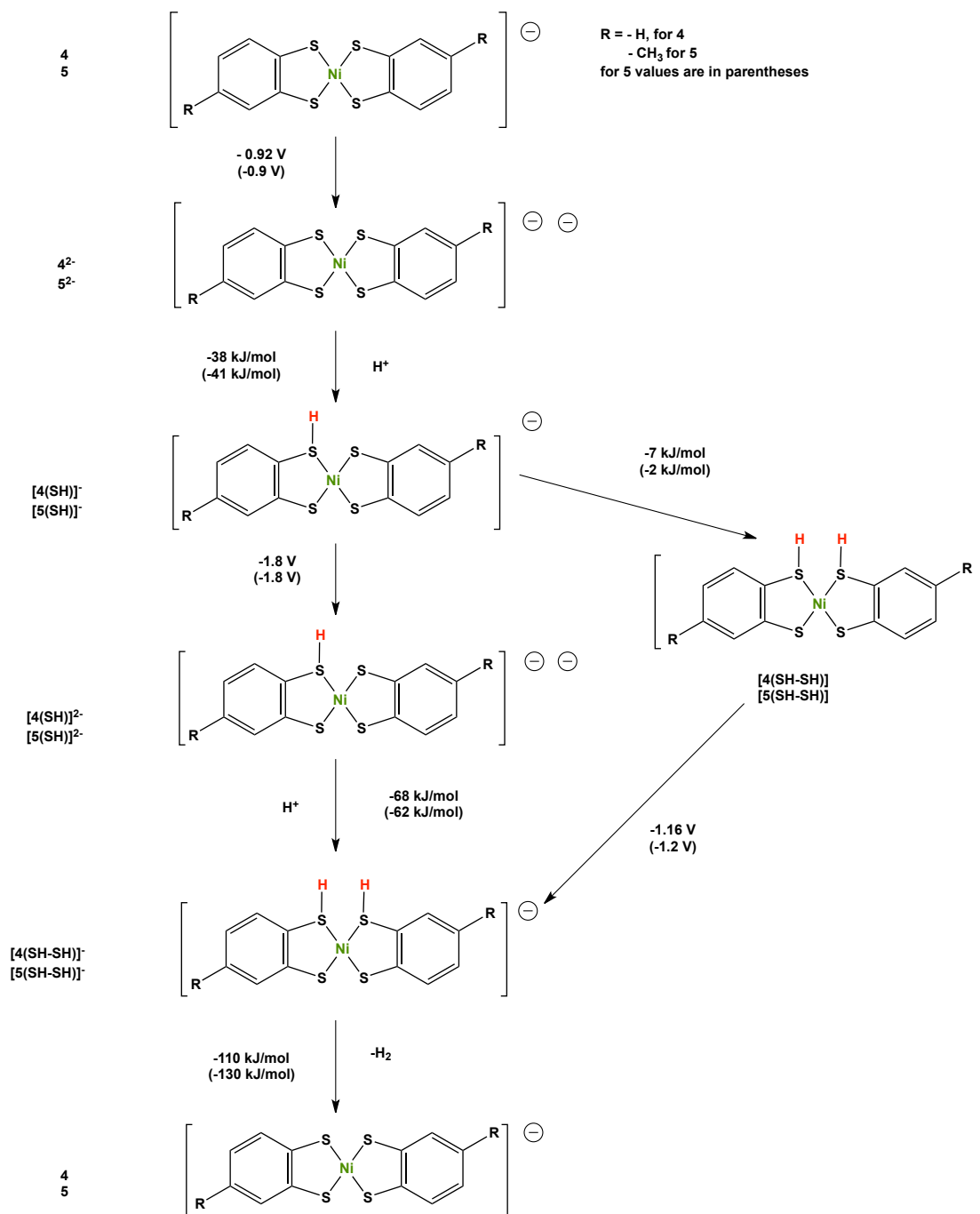
In the case of the asymmetric dithiolene complex 2, the same general mechanism is proposed (Scheme 30). Metal dithiolene complexes with asymmetric dithiolene ligands show fluxional behavior in solution [154]. This prompted us to calculate the intermediates of both the cis and trans isomers. Similar  $\Delta G$  values for reactions involving the protonated intermediates were found for the isomers, but there is a difference in the reduction potential values, with the trans isomer and its protonated forms exhibiting more negative reduction potentials. Overall, these calculated values compare well with the experimental data. In the final step where hydrogen is evolved by this catalyst, the trans-protonated complex releases hydrogen in a more exergonic process ( $-154 \text{ kJ mol}^{-1}$ ) in comparison to the cis form of the complex ( $-123 \text{ kJ mol}^{-1}$ ). This difference suggests that the electron-donating ability of the trans methoxy groups preferentially enriches the sulfur atom that participates in the protonation, and this is proposed to be the sulfur atom proximal to the (4-

methoxyphenyl)phenyl group of 2. However, on the basis of the calculated values, both isomers can be expected to be active catalysts, with the observed activity being a suitable average of the process for both. Moreover, theoretical data indicate that asymmetric substitution of the phenyl groups reflects on the charges of the sulfur atoms, with the atoms S1 and S3 (Figure 60) always being more negative compared to atoms S2 and S4 (actually the slight differences are 0.02, 0.01, and 0.03e for the neutral form, monoanion, and dianion, respectively). This discrepancy between the reduction potential and free-energy values for the trans and cis isomers along with the different structural features that the asymmetric complex exhibits can account for the fact that 2 is a better catalyst than 1 and 3, with the series eventually being  $2 > 3 > 1$ .



**Scheme 30. Proposed mechanism for hydrogen evolution with catalyst 2 together with calculated protonation enthalpies and redox potentials for cis- and trans- configurations of catalyst 2. Experimentally determined electrochemical potentials are also indicated. Potentials are reported vs  $Fc^{+/0}$ .**

DFT calculations were also employed to investigate the reaction intermediates and reaction pathways for catalysts 4–6. The proposed mechanism for hydrogen evolution for catalysts 4 and 5 is shown in Scheme 31.

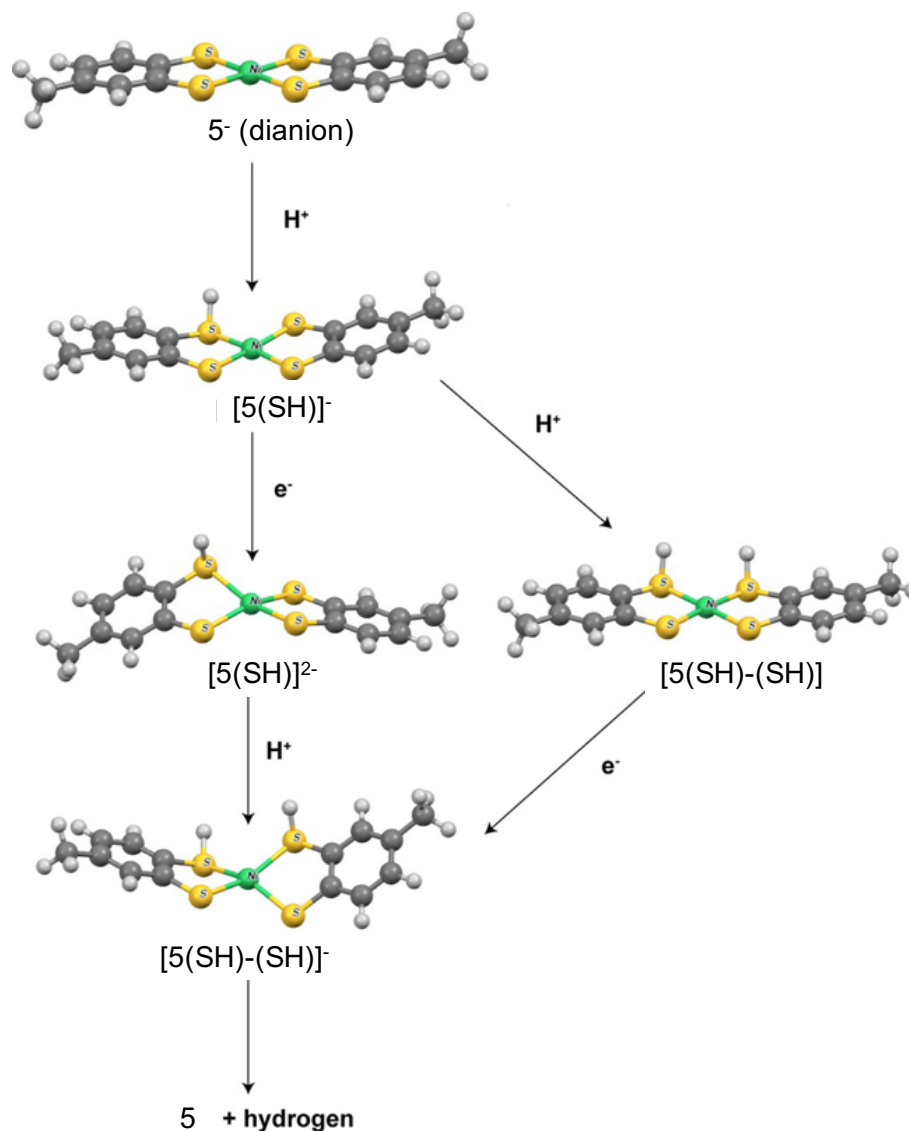


Scheme 31. Proposed hydrogen evolution mechanism for catalysts 4 and 5, along with protonation enthalpies and reduction potentials. Potentials are reported vs.  $\text{Fc}^{+/0}$ .

Catalyst 4 is first reduced to the dianion and then protonation occurs in an exergonic step ( $-38 \text{ kJ mol}^{-1}$ ). The protonation at a sulfur atom to form  $[4(\text{SH})]^-$  is more favorable than protonation at the nickel center (forming  $[4(\text{NiH})]^-$ ) by  $66 \text{ kJ mol}^{-1}$ . Direct protonation of 4 is found slightly endergonic ( $16 \text{ kJ mol}^{-1}$ ) to yield  $[4(\text{SH})]$  which is more stable than  $[4(\text{NiH})]$  by  $91 \text{ kJ mol}^{-1}$ .  $[4(\text{SH})]$  can then be reduced to  $[4(\text{SH})]^-$  with a potential of  $-0.06 \text{ V vs. Fc}^{+/0}$ . In the next step,  $[4(\text{SH})]^-$  reduces to  $[4(\text{SH})]^{2-}$  with a calculated potential of  $-1.8 \text{ V vs. Fc}^{+/0}$ .  $[4(\text{NiH})]^{2-}$  is also observed with a similar stability as  $[4(\text{SH})]^{2-}$  within  $3 \text{ kJ mol}^{-1}$ . Another protonation ( $-68 \text{ kJ mol}^{-1}$ ) leads to  $[4(\text{SH-SH})]^-$  which is only observed if protons are on distinct ligands.  $[4(\text{SH-SH})]^-$  can also be reached by protonation of  $[4(\text{SH})]^-$  ( $-7 \text{ kJ mol}^{-1}$ ) to yield  $[4(\text{SH-SH})]$  and subsequent reduction ( $-1.16 \text{ V vs. Fc}^{+/0}$ ). From  $[4(\text{SH-SH})]^-$ , hydrogen is evolved in an exergonic reaction ( $-110 \text{ kJ mol}^{-1}$ ) to yield the monoanionic catalyst 4. Hydrogen evolution from  $[4(\text{SH-SH})]$  is calculated to be slightly endergonic ( $16 \text{ kJ mol}^{-1}$ ). Despite this, the process is likely to be entropically driven by the evolution of the dissociated  $\text{H}_2$  molecule as a gas—an effect that is not adequately taken into account in the thermodynamic computation.

Catalyst 5 follows a similar pathway for the hydrogen–evolution reaction, with similar intermediates, protonation enthalpies, and redox potentials, as shown in Scheme 31. The entity  $5^{2-}$  (ie the dianionic dithiolene complex) can be protonated in an exergonic process ( $-41 \text{ kJ mol}^{-1}$ ) to yield  $[5(\text{SH})]^-$  which is more stable than  $[5(\text{NiH})]^-$  by  $76 \text{ kJ mol}^{-1}$ . Further reduction of  $[5(\text{SH})]^-$  ( $-1.8 \text{ V vs. Fc}^{+/0}$ ) yields  $[5(\text{SH})]^{2-}$ , which is favored compared to  $[5(\text{NiH})]^{2-}$  by  $12 \text{ kJ mol}^{-1}$ . Alternatively, direct protonation of  $[5(\text{SH})]^-$  ( $2 \text{ kJ mol}^{-1}$ ) yields  $[5(\text{SH-SH})]$  which is then reduced to give  $[5(\text{SH-SH})]^-$ . On the other hand, an exothermic protonation of  $[5(\text{SH})]^{2-}$  ( $-62 \text{ kJ mol}^{-1}$ ) leads to the doubly sulfur–protonated intermediate  $[5(\text{SH-SH})]^-$  that is more stable than  $[5(\text{NiH-SH})]^-$  by only  $6 \text{ kJ mol}^{-1}$ , indicating that participation of nickel ion in this step cannot be excluded. Finally, in a highly exergonic reaction ( $-130 \text{ kJ mol}^{-1}$ ) hydrogen is evolved and monoanionic 5 is formed.

The structures of the calculated intermediates are shown in Scheme 32. The calculated structures for the monoanionic and dianionic states of 5 in MeCN are in agreement with those experimentally reported in references [155–157], with calculated bond lengths within  $0.04 \text{ \AA}$  of the experimental values.



**Scheme 32.** Calculated structures of the intermediates in the proposed hydrogen evolution mechanism of compound 5.

The calculated value for the Ni hinge angle for 5 differs significantly from the experimental value of  $0^\circ$ , but for the dianionic compound the calculated value of  $0^\circ$  is in agreement with the experimental value. Calculated structural parameters for compound 5, its dianion, and all calculated intermediates are summarized in Table 26 with the numbering scheme applied shown in Figure 112.

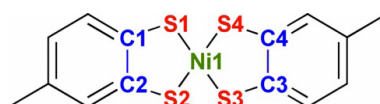


**Figure 112.** Atom numbering scheme for catalyst 5.

**Table 26. Selected structural parameters calculated for intermediates in the hydrogen evolution mechanism of catalyst 5 with values for 4 for comparison.**

Parameter <sup>a</sup>	[5] <sup>-</sup>	[5] <sup>2-</sup>	[5(S-H)] <sup>-</sup>	[5(S-H)] <sup>2-</sup>	[5(SH-SH)]	[5(SH-SH)] <sup>-</sup>
Ni – S1	2.193	2.229	2.255	2.436	2.260	2.353
Ni – S2	2.198	2.234	2.234	2.371	2.208	2.325
Ni – S3	2.199	2.229	2.199	2.325	2.211	2.347
Ni – S4	2.197	2.234	2.222	2.336	2.253	2.363
C1 – S1	1.758	1.776	1.802	1.802	1.797	1.801
C2 – S2	1.758	1.775	1.768	1.762	1.772	1.769
C3 – S3	1.760	1.775	1.774	1.777	1.773	1.773
C4 – S4	1.758	1.775	1.777	1.777	1.801	1.803
S1 – H1	–	–	1.351	1.352	1.353	1.351
S4 – H2			–	–	1.352	1.350
Ni hinge angle	7.5°	0.8°	5.2°	27.1°	2.4°	37.9°

The numbering scheme is the same as in Figure 112 with protonation at S1 and S4. Bond lengths are given in Å. The Ni hinge angle is the angle between the Ni–S1–S2 and Ni–S3–S4 planes.

Protonation of the dianionic catalyst (i.e., [5]<sup>2-</sup>) at S1 leads to a small tetrahedral distortion which is reflected in the value of the Ni hinge angle (5.28°) and an elongation of the C1–S1 bond by 0.026 Å for [5(SH)]<sup>-</sup>. Further reduction yields [5(SH)]<sup>2-</sup>, which exhibits an even more distorted structure with a hinge angle of 27.18° and elongated Ni – S bonds, among which Ni – S1 is the longest (2.436 Å). In the alternate route in which [5(SH)]<sup>-</sup> is protonated prior to reduction, the distortion diminishes and a hinge angle of 2.48° is reached with minor elongation of the Ni – S1 bond. However, if the doubly protonated and reduced state [5(SH–SH)]<sup>-</sup> is achieved, a high degree of distortion is observed (37.98°) with a concomitant elongation of the Ni – S bonds; the C – S bonds also appear longer, approximately 1.8 Å for C1 – S1 and C4 – S4, and 1.77 Å for the remaining C – S bonds. The calculated structure of intermediate [5(NiH)]<sup>2-</sup> and calculated parameters are shown below.

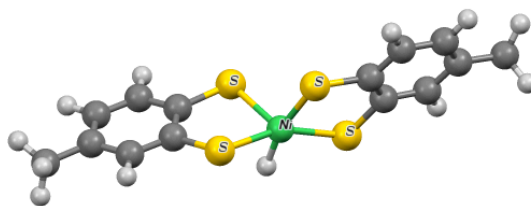


**Figure 113.** Calculated structure for intermediate  $[5(\text{Ni-H})]^{2-}$ .

**Table 27.** Calculated structural parameters for intermediate  $[5(\text{Ni-H})]^{2-}$  (bond lengths in Å).

Parameter <sup>a</sup>	$[5(\text{Ni-H})]^{2-}$
Ni1 – S1	2.372
Ni1 – S2	2.294
Ni1 – S3	2.251
Ni1 – S4	2.310
C1 – S1	1.776
C2 – S2	1.780
C3 – S3	1.777
C4 – S4	1.773
Ni1 – H1	1.447
S–Ni–S dihedral angle	72.24°

Bond lengths are given in Å. The Ni hinge angle is the angle between the planes defined by the atoms Ni–S1–S2 and Ni–S3–S4.

Further theoretical investigation of the hydrogen-evolving step reveals an intramolecular reaction pathway that involves one intermediate and two transition states (TS). We did not consider intermolecular schemes here, such as those involving acid, as these would require supplementary theoretical approaches that are beyond the scope of this study. The intramolecular reaction profile for 5 is depicted in Figure 114.

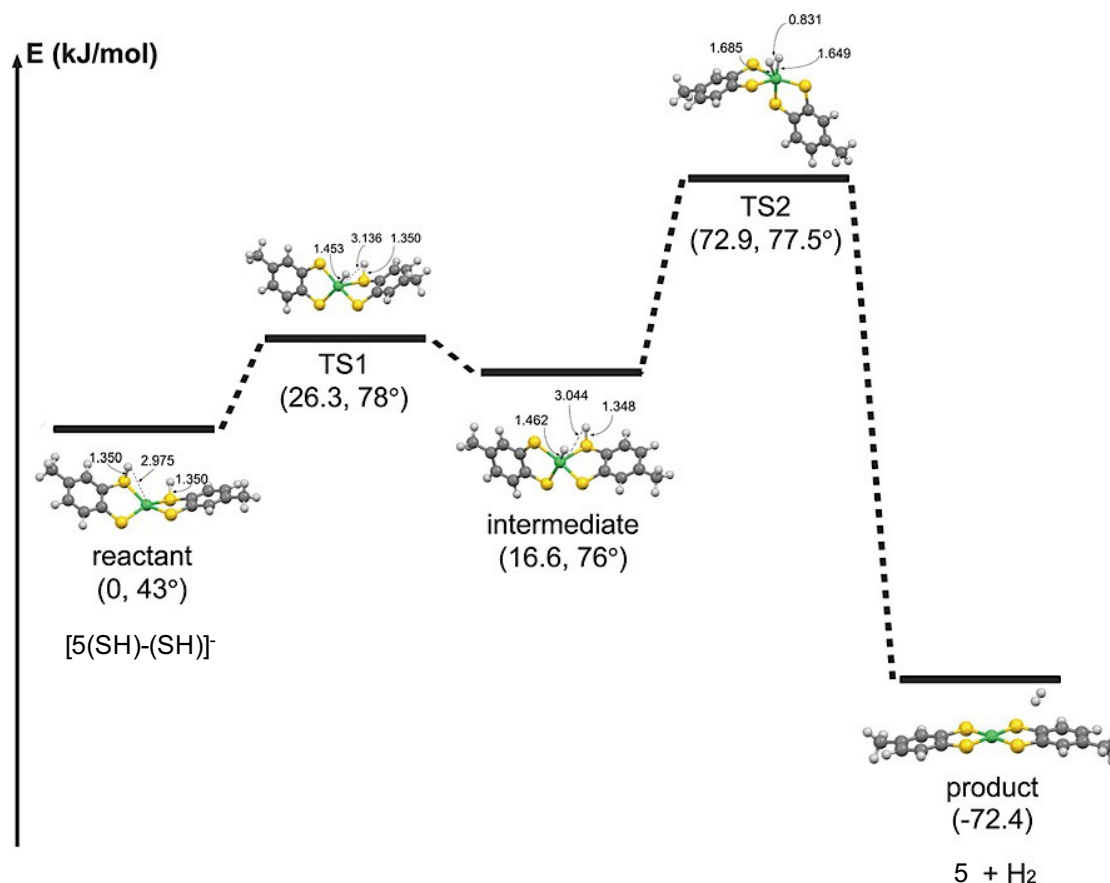
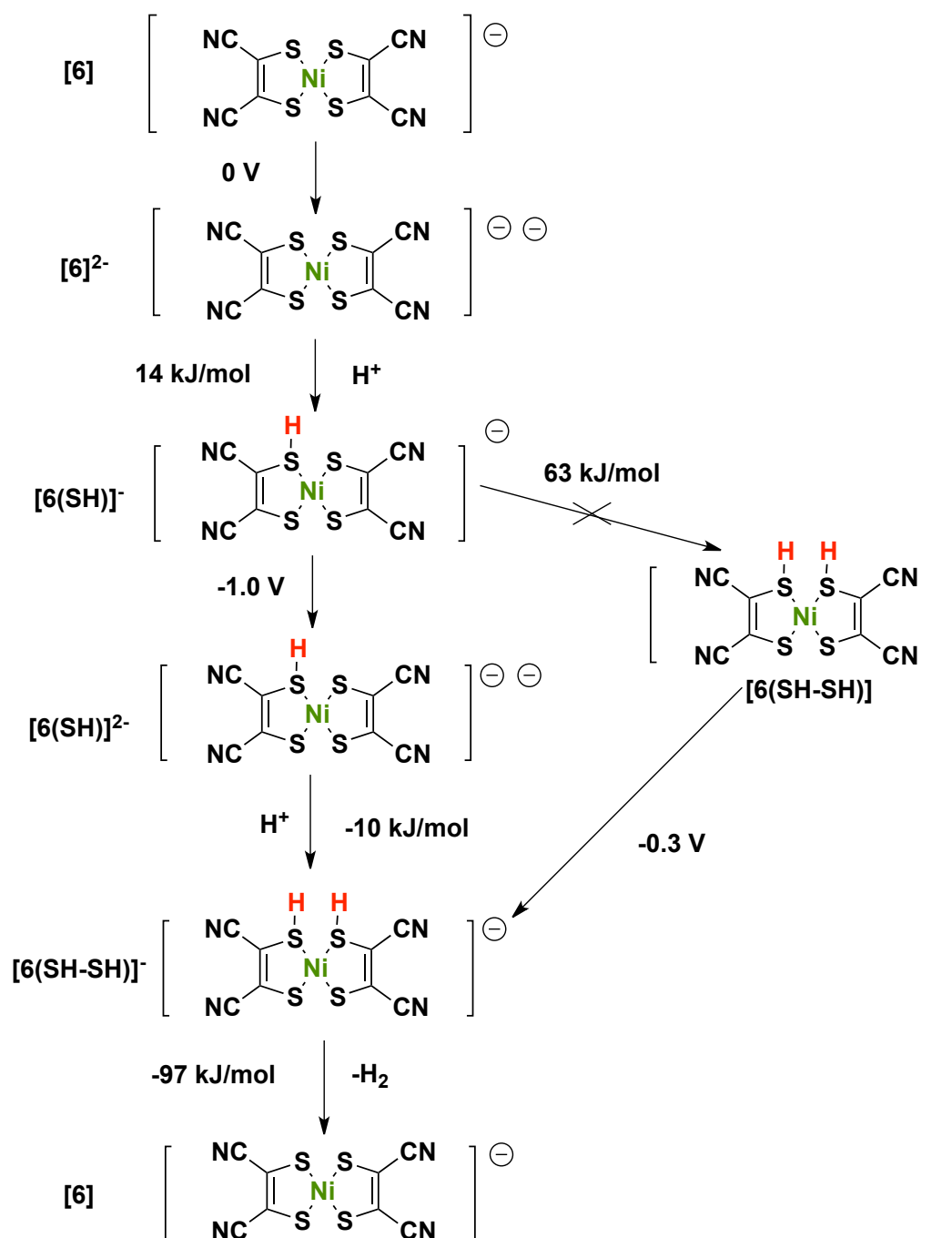


**Figure 114.** Calculated reaction pathway for the hydrogen-evolving step of the mechanism shown in Scheme 31 with catalyst 5. TS denotes transition state and the numbers in parentheses indicate the calculated energy values ( $\text{kJ mol}^{-1}$ ) and the values of the Ni hinge angle (degrees). Significant bond lengths are indicated with arrows.

Very similar structures and energies are calculated for compound 4 within experimental errors. Starting from  $[5(\text{SH}-\text{SH})]^-$  as the reactant (Ni hinge angle  $42.78^\circ$ ), the first transition state (TS1) is reached, which is located  $26.3 \text{ kJ mol}^{-1}$  uphill and is more distorted with a hinge angle of  $77.88^\circ$ . At the same time, a H atom migrates from a sulfur atom to the nickel ion leading to a Ni – H bond to yield an intermediate with a slightly relaxed  $76^\circ$  hinge angle and S – H and Ni – H bond lengths of  $1.35 \text{ \AA}$  and  $1.46 \text{ \AA}$ , respectively. The proton and the hydride ion are within  $3.044 \text{ \AA}$ , significantly closer than in TS1 ( $3.136 \text{ \AA}$ ). Migration of the second proton to the nickel ion results in the formation of the second transition state (TS2), with an activation energy of  $56.3 \text{ kJ mol}^{-1}$ . In TS2, the hinge angle increases to  $77.58^\circ$  and both Ni – H bonds are significantly longer than the nickel–hydride distance in the intermediate ( $\approx 1.65 \text{ \AA}$  vs.  $\approx 1.46 \text{ \AA}$ ), in line with the formation of a coordinated  $\text{H}_2$

molecule with 0.831 Å H – H distance. From TS2, the reaction proceeds downhill to yield dihydrogen and the monoanionic catalyst 5.

Compound 6 is the least active catalyst in the series but the calculated intermediates resemble those of catalysts 4 and 5.



Scheme 33. Proposed hydrogen evolution mechanism for catalyst 6, along with protonation enthalpies and reduction potentials. Potentials are reported vs.  $Fc^{+/0}$ .

More specifically, protonation at sulfur occurs if 6 has been reduced to the dianion. This is a slightly endergonic process ( $14 \text{ kJ mol}^{-1}$ ) and yields the intermediate  $[6(\text{SH})]^-$ . Protonation at nickel produces the less stable (by  $73 \text{ kJ mol}^{-1}$ ) species  $[6(\text{NiH})]^-$  and is not favorable. Protonation at sulfur of the monoanionic state is strongly unfavorable ( $101 \text{ kJ mol}^{-1}$ ), but  $[6(\text{SH})]^-$  can be reduced ( $-1.0 \text{ V vs. Fc}^{+/0}$ ) to yield  $[6(\text{SH})]^{2-}$  which is more stable than the nickel-protonated species  $[6(\text{NiH})]^{2-}$  by  $22 \text{ kJ mol}^{-1}$ . Further protonation in an exergonic reaction ( $-10 \text{ kJ mol}^{-1}$ ) yields  $[6(\text{SH-SH})]^-$  which is more stable than  $[6(\text{NiH-SH})]^-$  by  $21 \text{ kJ mol}^{-1}$ . From the  $[6(\text{SHSH})]^-$  state, hydrogen can evolve in an exothermic process ( $-97 \text{ kJ mol}^{-1}$ ). For this compound, theoretical data suggest that protonation can also occur on the nitrogen atoms of the dithiolene ligands. This can be explained in terms of the electron-withdrawing effect of the  $\text{mnt}^{2-}$  ligand, in which the  $-\text{CN}$  groups strip the sulfur atoms of electron density. Thus, the species  $[6(\text{SH})]^-$  is more stable by  $5 \text{ kJ mol}^{-1}$  than the  $[6(\text{NH})]^-$  species. Further reduction yields the respective singly reduced species, and the sulfur-protonated  $[6(\text{SH})]^-$  is more stable than  $[6(\text{NH})]^-$  by  $51 \text{ kJ mol}^{-1}$ . When the doubly reduced species are reached,  $[6(\text{SH})]^{2-}$  and  $[6(\text{NH})]^{2-}$ , the sulfur-protonated species is more stable by  $15 \text{ kJ mol}^{-1}$ . In general, although protonation at nitrogen is plausible for this complex, the sulfur-protonated intermediate is calculated to be more stable.

Calculations confirm a kinetic preference for the monoprotonated monoreduced intermediate to be produced through a sequential downhill EC route, rather than from a CE pathway. The calculated enthalpies for the protonation of 4 and 5 are slightly endergonic ( $16 \text{ kJ mol}^{-1}$  and  $24 \text{ kJ mol}^{-1}$ , respectively) in line with the slow rate of protonation observed in the presence of excess acid. Reduction potentials for  $[4(\text{SH})]$  and  $[5(\text{SH})]$  are calculated to be  $-0.06 \text{ V}$  and  $0 \text{ V vs. Fc}^{+/0}$ , respectively. Such positive values can, however, drive the CE pathway forward, especially as the concentration of acid increases. In addition, catalysts 4 and 5 have similar calculated routes for hydrogen evolution and these two pathways nicely correspond to the two catalytic processes identified experimentally in the corresponding cyclic voltammograms.  $\text{H}_2$  evolution occurring in the first process therefore likely results from a double protonation of the dianionic species, followed by reduction of this deprotonated monoreduced species. This process can thus be described as an ECCE sequence. The

second catalytic process goes through the reduction of the monoprotonated derivative of the monoreduced species and occurs at a more negative potential.

Experimentally, catalysts 4 and 5 display distinct electrocatalytic behaviors in their cyclic voltammograms. Catalyst 5 exhibits only one catalytic wave whereas 4 shows two waves with lower catalytic peak currents. Such differences indicate that catalysis in the first process is slower for 4 than for 5. As a consequence, one might expect that the diffusion–reaction layer at the surface of the electrode is not fully depleted in protons at the top of the first wave so that there is still some substrate available for the second process occurring at the more negative potential. In contrast, fast catalysis by 5 completely consumes protons so that none are left to be reduced in the second process. Based on the calculated thermodynamic values, only one pathway towards hydrogen evolution is feasible for complex 6. This supports the observation of only one catalytic wave at the cyclic voltammogram of 6 in the presence of acid.

What becomes clear from the above observations is that protonation at sulfur induces elongation of the respective C – S and Ni – S bonds, along with the significant geometrical distortions that the reduction process imposes on the catalyst. This is in accordance with what was previously reported [118]. The dithiolene complexes under study are almost planar but their geometries seem to distort significantly during proton reduction as indicated by both experimental and theoretical data from this and previous work [68]. Actually, variation in the Ni hinge angle seems to be of importance because reduced intermediates and transition states that eventually lead to the evolution of hydrogen exhibit tetrahedral distortion. The significant elongation of Ni – S bonds for the reduced protonated species  $[5(\text{SH})]^{2-}$  and  $[5(\text{SH}-\text{SH})]^{-}$  reveals that each proton added affects the electronic structure of the ligand framework. More specifically, the delocalized nature of the dithiolate ligands is altered and the Ni – S bonds acquire a bonding nature resembling that of Ni–S<sub>thiolate</sub> analogs. This is reflected in bond lengths because the calculated Ni – S bonds for  $[5(\text{SH})]^{2-}$  (2.325–2.436 Å) are close to those of similar  $[\text{Ni}(\text{SPh})_4]^{2-}$  species reported in the literature (2.293–2.331 Å) [158].

We have been able to locate a pathway for intramolecular proton–hydride coupling that leads to the formation of a metal–bound H<sub>2</sub> molecule. The activation energy of this process was calculated to be approximately 60 kJ mol<sup>-1</sup>, a value that is in agreement with studies of similar H<sub>2</sub>–evolving catalysts [12,159–161] and enzymes

[162]. As H<sub>2</sub> elimination is entropically favored, it is likely that the metastable H<sub>2</sub>-bound molecule is not a true intermediate in the catalytic mechanism. In addition, competition with direct intermolecular hydride-proton coupling involving a proton donor from the bulk (e.g., TFA) cannot be excluded. Accurate modeling of such a process requires more elaborate methods, such as hybrid quantum chemical/molecular mechanical approaches [163].

## 7.2 Electrocatalytic hydrogen production with heteroleptic dithiolene complex

### 7

Addition of TFA aliquots in a DMF solution of complex 7 induces the appearance of a cathodic wave which at [TFA] = 10 mM has  $E_{1/2} = -1.65$  V vs Fc<sup>+0</sup>. This wave is assigned to the catalytic reduction of protons with complex 7 as a catalyst.

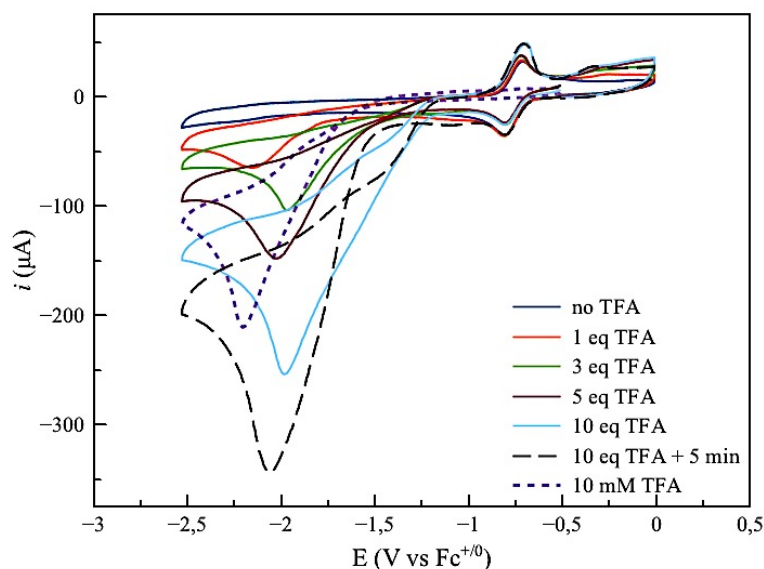


**Figure 115.** Cyclic voltammogram of 7 in the presence of increasing equivalents of TFA: no acid, blue; 1 equiv, red; 3 equiv, green; 5 equiv, brown; 10 equiv, light blue; blank, dotted trace; CV after the end of the titration, dashed trace (glassy carbon working electrode).

This complex exhibits similar behavior with homoleptic compound 1, where the catalytic wave appears at a half-wave potential of  $-1.9$  V vs Fc<sup>+0</sup>, an indication of a similar reaction pathway, as protonation occurs after reduction to the dianion, with a single process appearing at the catalysis region. Catalyst 1 exhibits two catalytic waves at low TFA concentration, up to 5 mM. However, there is no loss of reversibility on the  $-1/-2$  reduction wave upon protonation, which occurred at the unbridged catalysts 1–3, but still a small current enhancement is observed at the  $-1/-2$  reduction wave.

Cyclic voltammetry at the end of the experiment (dashed trace, Figure 115) reveals an enhancement in the catalytic current at the process at  $-1.9\text{ V vs Fc}^{+/0}$ . At the same time, the crossing of anodic and cathodic scan combined with the increase in catalytic current indicates that the catalyst further reacts with TFA at the CV timescale and maybe decomposes at the electrode surface, as seen for other NiSS complexes [98,104,146], proposing thus that TFA might be too strong an acid and promotes decomposition of 7.

### 7.3 Electrocatalytic hydrogen production with bridged dithiolene complexes

Compound 7 was employed towards proton reduction in DMF with TFA as a proton source. Aliquots of a TFA stock solution in DMF were added in a solution of complex 8 (1 mM).

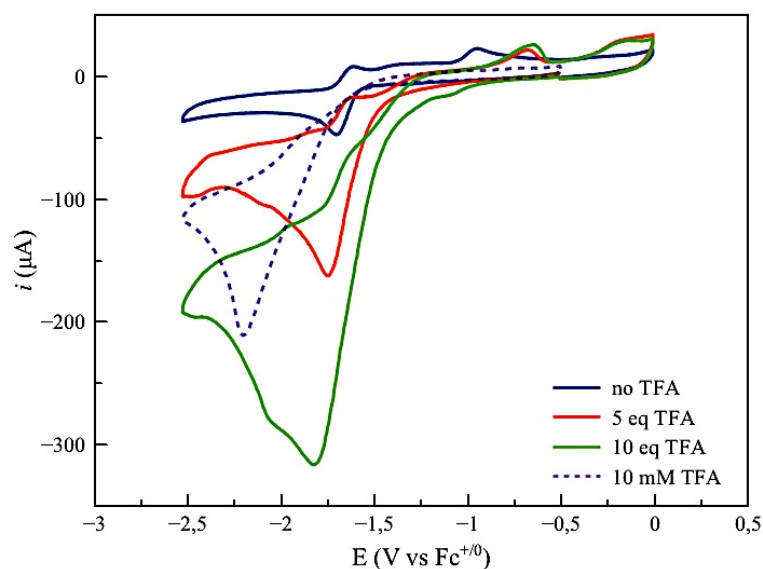


**Figure 116. Cyclic voltammogram of 8 in the presence of increasing equivalents of TFA: no acid, blue; 5 equiv, red; 10 equiv, green; blank, dotted trace (glassy carbon working electrode).**

The catalytic wave grows on the the  $8/8^-$  reduction wave of the catalyst. At the same time, the anodic wave shifts by  $\sim 300\text{ mV}$  towards positive values, indicating that the oxidation of the protonated – reduced species formed after catalysis is distorted and easier to reduce. The alkylated catalyst 8 behaves differently compared to catalyst 4 [69]; Catalyst 4, albeit investigated in MeCN where TFA is significantly weaker ( $\text{pK}_a^{\text{DMF}} = 6.0$ ,  $\text{pK}_a^{\text{MeCN}} = 12.7$ ), shows a shift of the reduction wave towards more positive potential values, indication of a CE process, which does not occur for catalyst 8 where reduction to the dianion is not required for the appearance of catalytic wave.

Therefore, the more localized electronic structure of catalyst 8 vs catalyst 4 may allow a different pathway to take place, preferably via an electron-rich reduced Ni(I) state or an electron-density richer S atom.

As the TFA concentration reaches 10 mM, the catalytic wave grows at a half-wave potential of  $-1.6$  V vs  $\text{Fc}^{+/0}$ , with the concomitant appearance of a second wave at  $E_{p,c} = -2$  V vs  $\text{Fc}^{+/0}$ . Since the direct reduction of TFA (dotted trace) is observed at  $-2.2$  V vs  $\text{Fc}^{+/0}$ , close to the catalytic wave due to the presence of the catalyst, participation of the direct reduction process cannot also be excluded, even though an enhancement takes place in the catalytic cathodic current at  $-1.82$  V vs  $\text{Fc}^{+/0}$ .

Both catalysts 9 and 10 behave in a similar manner upon addition of increasing equivalents of TFA in DMF solution (Figures 117 and 118 for 9 and 10, respectively).

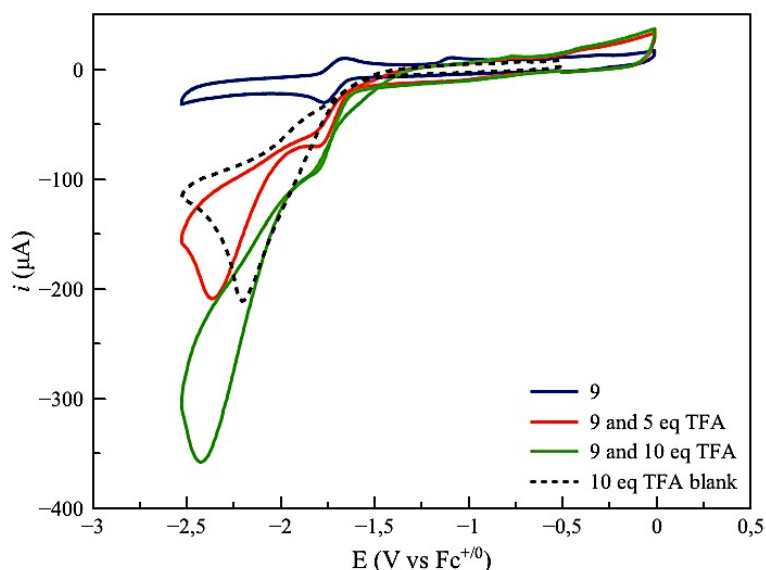


**Figure 117.** Cyclic voltammogram of 9 in the presence of increasing equivalents of TFA: no acid, blue; 5 equiv, red; 10 equiv, green; blank, dotted trace (glassy carbon working electrode).

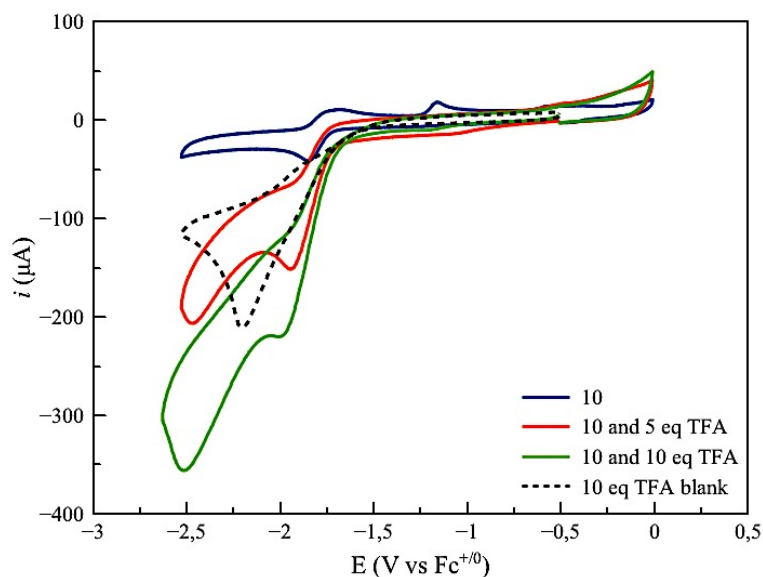


**Figure 118.** Cyclic voltammogram of 10 in the presence of increasing equivalents of TFA: no acid, blue; 5 equiv, red; 10 equiv, green; blank, dotted trace (glassy carbon working electrode).

The catalytic wave with half-wave potential of  $-1.7$  V vs  $\text{Fc}^{+/0}$  (5 mM TFA) grows on the 0/–1 reduction for each complex, the same that applies for catalyst 8 but different compared to un-bridged catalysts. As in the case of 8, it is proposed that S atoms and/or Ni ion are sufficient nucleophilic in this ligand framework, so only one reduction is required for protonation to occur. However, the crossing of anodic and cathodic scan as well as the negative shift of the direct TFA reduction despite the catalytic current enhancement, imply a modification of the surface of the electrode. The same action of acids on NiS-containing complexes has been reported in the literature [104,146,164], with suggested deterioration pathways leading to Ni=S-containing compounds or amorphous Ni/S films, depending on the strength of the acid [105,146].

#### 7.4 Photocatalytic hydrogen production

The interaction of catalyst  $1^-$  with zinc tetraphenylporphyrin as chromophore was investigated in terms of hydrogen evolving activity in mixed DMF – water : 8 – 2 mixture due to the low solubility of both compounds in increased water to DMF ration. Triethylamine (TEA) was used as a sacrificial electron donor and irradiation was kept for 20 h for all experiments. Use of either catalyst  $2^-$  or  $3^-$  led to no hydrogen evolution.

Initially, the concentration of chromophore (ZnTPP) was kept constant at  $1.0 \times 10^{-4}$  M and TEA at 0.01 M. Variation of catalyst concentration revealed the optimum value at the micromolar range  $5.0 \mu\text{M}$  with a TON of  $\sim 16.5$ , with over  $9.0 \times 10^{-5}$  or lower than  $5.0 \times 10^{-6}$  M showing only traces or no amount of hydrogen at all.

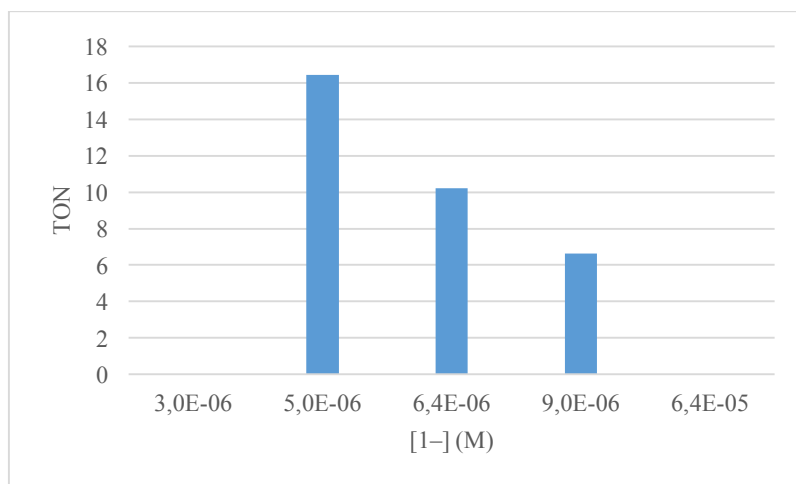


**Figure 119.** TON as a function of catalyst concentration with fixed ZnTPP ( $1.0 \times 10^{-4}$  M) and TEA (0.01 M) concentrations.

Variation of ZnTPP concentration in the next series of experiments was limited by the poor solubility of ZnTPP when water was introduced into the solvent mixture. Thus, only two concentration values could be obtained; when  $[\text{ZnTPP}] = 8.0 \times 10^{-5}$  M (catalyst kept at  $5 \mu\text{M}$ , TEA 0.01 M)  $\sim 7.5$  TON were obtained, while increasing the chromophore concentration to  $3.0 \times 10^{-4}$  M led to significant precipitation of ZnTPP.

Increase in TEA concentration to either 0.1 or 1 M had detrimental effect on the hydrogen evolution activity. Results for photochemical induced evolution are summarized in the following Table.

**Table 28.** Hydrogen evolution results for system with ZnTPP (chromophore),  $\text{I}^-$  (catalyst), TEA (sacrificial electron donor) in DMF – water : 8 – 2 solvent mixture.

[ZnTPP]	[I <sup>-</sup> ]	[TEA]	H <sub>2</sub> (mL)	t <sub>irr.</sub> (h)	TON
$1 \cdot 10^{-4}$	$9 \cdot 10^{-6}$	0.01 M	0.04	20	6.64
	$6.4 \cdot 10^{-6}$	0.01 M	0.044	20	10.21
	$5 \cdot 10^{-6}$	0.01 M	0.055	20	16.43
	$3 \cdot 10^{-6}$	0.01 M	traces	20	–
	$6.4 \cdot 10^{-5}$	0.01 M	0	20	–
$8 \cdot 10^{-5}$	$5 \cdot 10^{-6}$	0.01 M	0.025	20	7.47
$3 \cdot 10^{-4}$	$5 \cdot 10^{-6}$	0.01 M	precipitation of	–	–

## ZnTPP

$1 \cdot 10^{-4}$	$5 \cdot 10^{-6}$	0.1 M	0.02	20	5.98
$1 \cdot 10^{-4}$	$5 \cdot 10^{-6}$	1 M	0	20	–

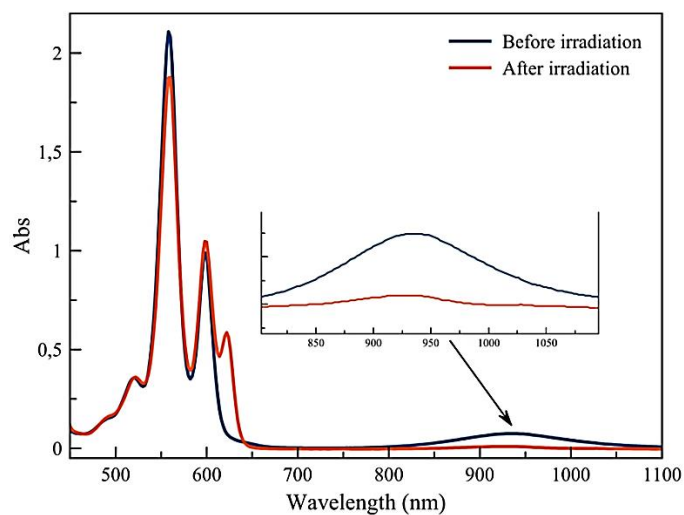


**Figure 120.** UV–Vis spectrum of an Ar–dearated mixture containing  $5.0 \mu\text{M}$  catalyst  $1^-$ ,  $10^{-4}$  M ZnTPP, 0.01 M TEA, in DMF – water : 8 – 2 solvent mixture before (blue trace) and after (red trace) irradiation for 20 h with a 1000 W Xe lamp ( $\lambda > 330$  nm).

The UV–Vis spectrum of a cuvette containing the hydrogen evolution system before and after 20 h irradiation reveals the almost completely diminished band of catalyst at 938 nm and the appearance of a new band at 622 nm (Q band) for the metalloporphyrin, assigned to the (partial) reduction/decomposition of ZnTPP [89] due to excess TEA and continuous irradiation.

### 7.4.1 Discussion

To further probe the system, titration experiments were performed initially in DMF – water : 8 – 2 solvent mixture.

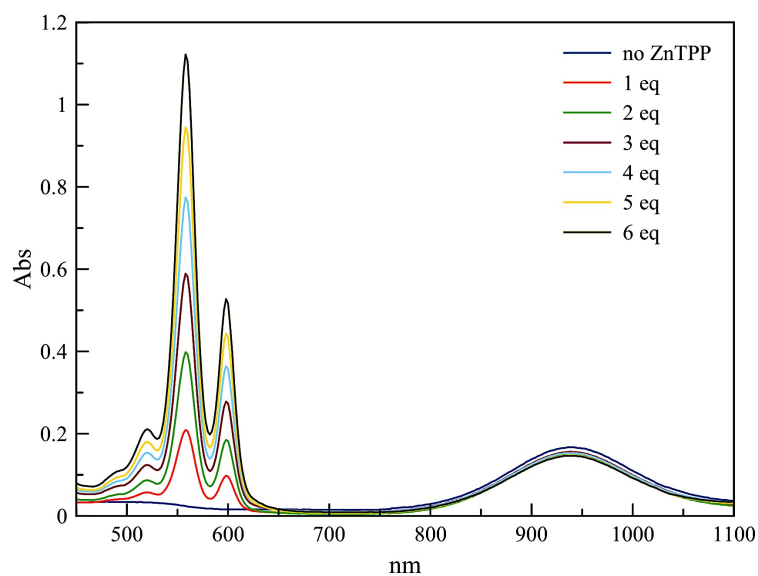


**Figure 121.** Titration of a DMF – water : 8 – 2 solution of catalyst  $1^-$  ( $10.0 \mu\text{M}$ ) with aliquots of ZnTPP in the same solvent mixture.

Increasing ZnTPP concentration doesn't affect the band of the nickel dithiolene catalyst at 938 nm but –as expected– leads to appearance of the Q bands in the region 500 – 600 nm for ZnTPP.

When the same experiment is conducted in a less polar, non–donor solvent such as dichloromethane, there is a significant difference in absorbance spectra, with the most prominent being a 6 nm blue–shift in the catalyst band at 938 nm.

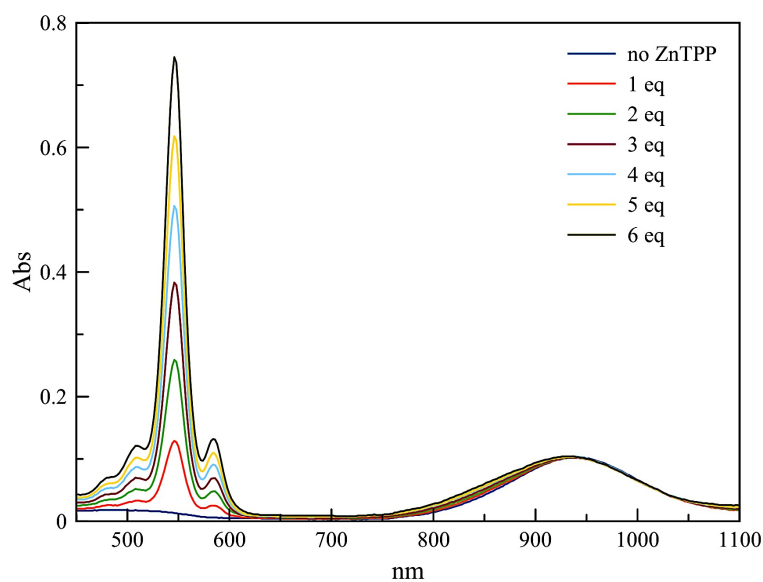


**Figure 122.** Titration of a  $\text{CH}_2\text{Cl}_2$  solution of catalyst  $1^-$  ( $10.0 \mu\text{M}$ ) with aliquots of ZnTPP in the same solvent.

This observation implies a ground state interaction of the nickel anionic catalyst with the  $ZnN_4$  core of the ZnTPP chromophore.

Steady state emission quenching of the emission of ZnTPP by increasing amounts of  $I^-$  in both DMF – water : 8 – 2 and  $CH_2Cl_2$  suggests the same observation.

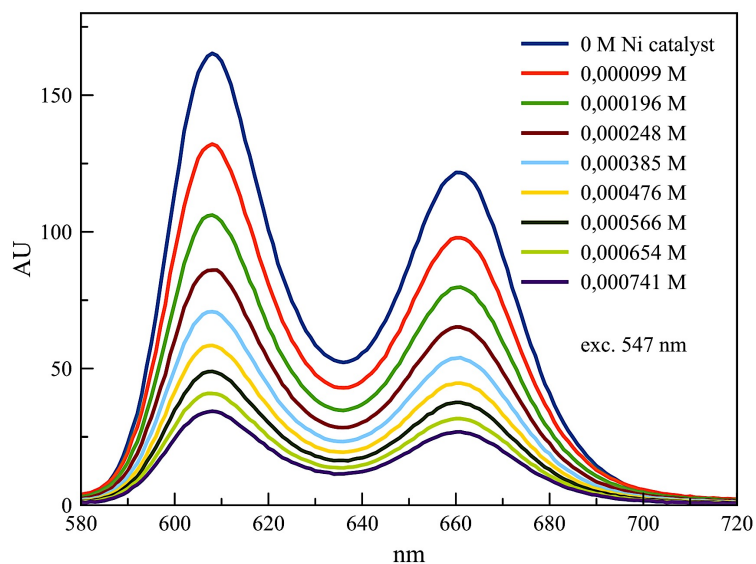


**Figure 123. Emission quenching of ZnTPP (1.0 μM) with increasing amounts of nickel catalyst  $I^-$  in DMF – water : 8 – 2 solvent mixture.**

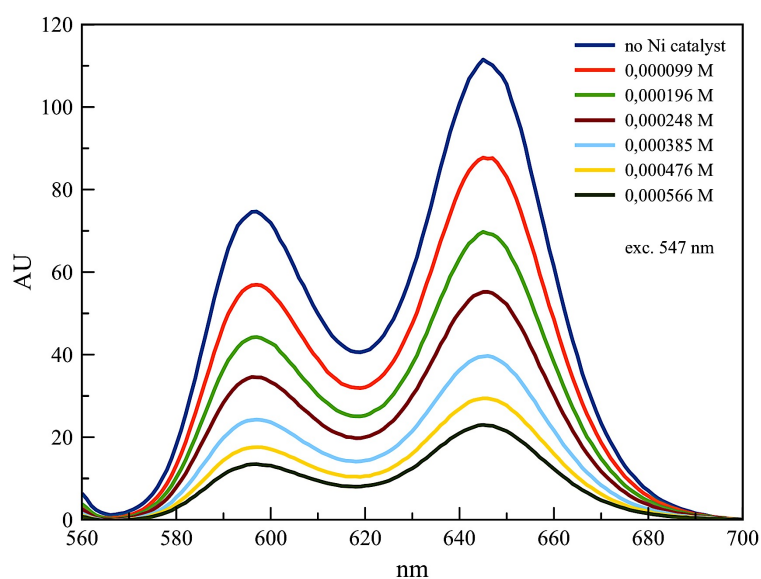


**Figure 124. Emission quenching of ZnTPP (1.0 μM) with increasing amounts of nickel catalyst  $I^-$  in  $CH_2Cl_2$  solvent.**

Plotting  $I_0/I$  vs  $[I^-]$  to obtain Stern – Volmer quenching data reveals an almost linear regression for data obtained in DMF – water : 8 – 2 mixtures but a significant upward curvature is obtained for data obtained in  $\text{CH}_2\text{Cl}_2$ .

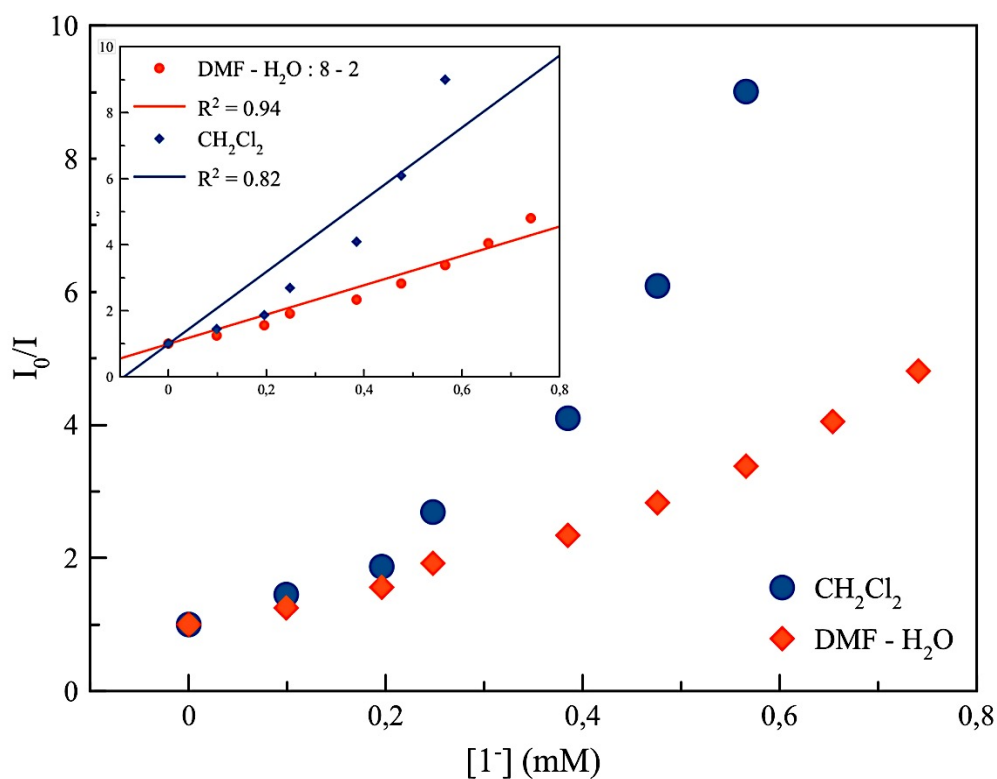


**Figure 125.** Stern – Volmer plots for quenching of emission of ZnTPP in  $\text{CH}_2\text{Cl}_2$  (blue circles) and in DMF –  $\text{H}_2\text{O}$  : 8 – 2 (red diamonds). Inset: linear fit of emission quenching data.

Such a behavior is indicative of the chromophore being quenched both by collisions with the catalyst and by ground–state complex formation with the same quencher [165].

In fact, a similar interaction between ZnTPP or CoTPP with  $[\text{Ni}\{\text{S}_2\text{C}_2(\text{CF}_3)_2\}_2]$  has been documented in the literature [166]. In that study, both ZnTPP and CoTPP interacted with  $[\text{Ni}\{\text{S}_2\text{C}_2(\text{CF}_3)_2\}_2]$ , to form 1: 1 complexes with near–infrared charge–transfer bands. The cobalt analog was isolated and possessed a Co – S bond, but reaction with ZnTPP led to production of a mixture of  $\text{ZnTPP}^+$  and  $[\text{Ni}\{\text{S}_2\text{C}_2(\text{CF}_3)_2\}_2]^-$ , based on the strong oxidating character of the latter. Since catalyst  $I^-$  is a much weaker oxidant than the  $-\text{CF}_3$  analog and based on all spectroscopic results we propose that hydrogen evolution proceeds via a charge–transfer intermediate, the formation of which is hindered in polar donor solvents such as the solvent mixture used.

## CONCLUSIONS

In the present thesis, the preparation, characterization (UV-Vis,  $^1\text{H-NMR}$ , IR, electrochemistry) and application as hydrogen evolution catalysts of ten nickel-bis dithiolene complexes (compounds 1–10) have been performed.

Complexes 1 – 3 are of the type  $[\text{Ni}(\text{S}_2\text{C}_2\text{-}p\text{-C}_6\text{H}_5\text{-R})(\text{S}_2\text{C}_2\text{-}p\text{-C}_6\text{H}_5\text{-R}')] ]$  where  $\text{R} = \text{R}' = \text{H}$  (compound 1),  $\text{R} = \text{OMe}$ ,  $\text{R}' = \text{H}$  (compound 2),  $\text{R} = \text{R}' = \text{OMe}$  (compound 3). Crystal structures for compounds 2 and 3<sup>-</sup> have been determined, with compound 2 being the first example of an asymmetric phenyl-substituted bis(dithiolene) complex to be structurally characterized. The respective monoanionic tetrabutylammonium salts have also been prepared using  $\text{NaBH}_4$ .

Monoanionic complexes 4 – 6 are  $(\text{NBu}_4)[\text{Ni}(\text{bdt})_2]$  (compound 4),  $(\text{NBu}_4)[\text{Ni}(\text{tdt})_2]$  (compound 5), and  $(\text{NBu}_4)[\text{Ni}(\text{mnt})_2]$  (compound 6).

One heteroleptic complex (compound 7)  $(\text{NBu}_4)[\text{Ni}(\text{S}_2\text{C}_2\text{Ph}_2)(\text{mnt})]$  has been prepared and its crystal structure has been determined.

Three neutral alkyl-bridged bis-dithiolene compounds  $[\text{Ni}(\text{bdt})_2\text{C}_3]$  (compound 8),  $[\text{Ni}(\text{S}_2\text{C}_2\text{Ph}_2)_2\text{C}_3]$  (compound 9), and  $[\text{Ni}(\text{S}_2\text{C}_2\text{-}p\text{-C}_6\text{H}_4\text{OMe})_2\text{C}_3]$  (complex 10).

All complexes have been employed as proton reducing catalysts in organic media (DMF or MeCN) with organic acids (TFA etc) as proton source. The first series of complexes (compounds 1–3) are active catalysts with good faradaic yields, reaching 83% for 2 (47 TONs) but relatively high overpotential requirements (0.91 and 1.55 V measured at the middle of the catalytic wave for two processes observed depending on the different routes of the mechanism). The similarity of the experimental data regardless of whether the neutral or anionic form of the complexes is used, indicates that the neutral form acts as a precatalyst. On the basis of detailed DFT calculations, the proposed mechanism reveals two different main routes after protonation of the dianion of the catalyst in accordance with the experimental data, revealing the role of the concentration of the acid and the influence of the methoxy groups. Protonation at sulfur seems to be more favorable than that at the metal, which is in marked contrast with the catalytic mechanism proposed for analogous cobalt dithiolene complexes.

The second series of complexes (compounds 4–6) were employed as electrocatalysts in MeCN, with TFA as the proton source. All complexes are active catalysts with

TONs reaching 113, 158, and 6 for (NBu<sub>4</sub>)[Ni(bdt)<sub>2</sub>] (4), (NBu<sub>4</sub>)[Ni(tdt)<sub>2</sub>](NBu<sub>4</sub>), (5) and (NBu<sub>4</sub>)[Ni(mnt)<sub>2</sub>] (6), respectively. The Faradaic yield for the hydrogen evolution reaction reaches 88% for 5, which also displays the minimal overpotential requirement value (467 mV) within the series. Two pathways for H<sub>2</sub> evolution can be hypothesized that differ in the sequence of protonation and reduction steps. DFT calculations are in agreement with experimental data and indicate that protonation at sulfur follows the reduction to the dianion. Hydrogen evolves from the di-reduced-deprotonated form via a highly distorted nickel hydride intermediate.

Compound 7 was employed as electrocatalyst in DMF with TFA as proton source, displaying catalytic activity similar to catalyst 1, i.e. catalysis occurs after the reduction of catalyst to the dianion. However, in the presence of low concentration of TFA

(10 mM) decomposition of the molecular compounds occurs as shown from cyclic voltammetry experiments.

Alkylated compounds 8–10 display quasi- or irreversible one-electron reductions with data indicating that de-alkylation occurs. Nevertheless, these complexes exhibit a catalytic wave for proton reduction that grows directly on the 0/1- reduction wave of each catalyst. This result implies that sulfur and/or Ni atoms are nucleophilic enough at the first monoanionic state and can be protonated. Again, decomposition of the catalysts after reduction in the presence of acid still occurs, as evidenced by the evolution of cyclic voltammetry experiments.

Rinse tests performed on the catalysts under various reductive conditions indicate a direct correlation of the strength of the acid (reflected in the pK<sub>a</sub>) and the stability of the molecular structure of the catalyst. DFT studies performed suggest that hydrogen evolution most likely occurs via highly distorted intermediates, as evidenced by calculated S – Ni – S planes. Complexes with electron-donating groups (2 and 5) contribute positively to catalysis by directing protonation at specific sulfur sites or persevering more distorted intermediate transition states. However, the same hydrogen-promoting distortion ultimately leads to the decomposition of each catalyst and large overpotential requirements. Stronger acids than TFA in MeCN such as aniliniums accelerate the decomposition of catalysts, but weaker acids (e.g. <sup>+</sup>NEt<sub>3</sub>H) do not always protonate the reduced forms of the catalysts, with main decomposition

pathways possibly involving C–S bond rupture or the formation of NiS<sub>x</sub> films which may be electrocatalytically active.

Attempts to stabilize the complexes by alkylation of adjacent sulfur atoms (8–10) does not lead to very stable catalysts, at least at the same reductive conditions as unbridged catalysts. Although alkylation is a way of “trapping” the electron-rich structure of dianionic dithiolene complexes, as evidenced by only one reduction wave upon which catalysis occurs, still TFA is too strong an acid in DMF.

Examination of a heteroleptic complex to investigate whether protonation and/or catalysis is located on one of the two different ligands resulted in a behavior similar to homoleptic catalysts, indicating that most probably protonation of catalyst 7 occurs after reduction to the dianion and protonation of sulfur atoms adjacent to phenyl rings.

Photocatalytic hydrogen evolution with zinc tetraphenylporphyrin as chromophore and catalyst 1<sup>-</sup> with trimethylamine as sacrificial electron donor leads to low activity in the polar solvent system of DMF – water : 8 – 2. Spectroscopic studies indicate that there is a ground state interaction between the ZnN<sub>4</sub> and NiS<sub>4</sub> core of the two molecules, evidenced by non-linear Stern–Volmer plots in polar donor solvents. Activity of this system is underway in less polar solvents such as CH<sub>2</sub>Cl<sub>2</sub> using organic acids as proton source instead of water.

## ABBREVIATIONS – INITIALS – ACRONYMS

NHE	Normal hydrogen electrode
ATP	Adenosine triphosphate
HOMO	Highest occupied molecular orbital
LUMO	Lowest occupied molecular orbital
MLCT	Metal-to-ligand charge transfer
UV – Vis	Ultra violet – visible
PS	Photosensitizer
TEA	Triethylamine
TEOA	Triethanolamine
AA	Ascorbic acid
THF	Tetrahydrofuran
EDTA	Ethylene-diamine-tetra-acetic acid
MV	Methyl viologen
LED	Light emitting diode
bdt	Benzene-1,2-dithiolate
tdt	Toluene-3,4-dithiolate
mnt	Maleonitrile-dithiolate
dpedt	Diphenyl-ethylene-dithiolate
TON	Turnover number
TOF	Turnover frequency
DHLA	Dihydrolopic acid
ECEC	Electron transfer-chemical reaction-electron transfer-chemical reaction
bpy	2,2'-bipyridine
TPP	Tetraphenylporphyrin
Fc	Ferrocene
DMF	N,N'-dimethylformamide
EPR	Electron paramagnetic resonance
GCE	Glassy carbon electrode
SCE	Saturated calomel electrode
DFT	Density functional theory

TFA	Trifluoroacetic acid
ITO	Indium-tin oxide
GC	Gas chromatography
CV	Cyclic voltammetry
EC	Electron transfer-chemical reaction
LSV	Linear sweep voltammetry
CPE	Controlled potential electrolysis
CE	Chemical reaction-electron transfer
IVCT	Intra-valence charge transfer
TS	Transition state
ECCE	Electron transfer-chemical reaction-electron transfer-chemical reaction

## APPENDIX

**Table 29. Bond lengths [ $\text{\AA}$ ] for 2 at 100(2) K with estimated standard deviations in parentheses.**

Label	Distances
Ni(1)–S(4)	2.115(2)
Ni(1)–S(3)	2.1276(19)
Ni(1)–S(2)	2.129(2)
Ni(1)–S(1)	2.1296(19)
S(1)–C(1)	1.700(7)
S(2)–C(2)	1.711(6)
S(3)–C(16)	1.707(7)
S(4)–C(17)	1.714(6)
O(1)–C(8)	1.379(8)
O(1)–C(9)	1.453(12)
O(2)–C(28)	1.348(9)
O(2)–C(30)	1.479(11)
C(1)–C(2)	1.424(8)
C(1)–C(3)	1.466(8)
C(2)–C(10)	1.468(9)
C(3)–C(7)	1.382(9)
C(3)–C(4)	1.400(8)
C(4)–C(5)	1.387(9)
C(5)–C(8)	1.379(10)
C(6)–C(8)	1.367(10)
C(6)–C(7)	1.402(9)
C(10)–C(11)	1.389(9)
C(10)–C(15)	1.404(8)
C(11)–C(12)	1.381(9)
C(12)–C(13)	1.408(11)
C(13)–C(14)	1.366(11)
C(14)–C(15)	1.377(10)
C(16)–C(17)	1.401(9)
C(16)–C(25)	1.483(9)
C(17)–C(18)	1.471(9)
C(18)–C(23)	1.393(9)
C(18)–C(19)	1.397(8)
C(19)–C(20)	1.366(10)
C(20)–C(21)	1.387(10)

C(21)–C(22)	1.405(10)
C(22)–C(23)	1.388(10)
C(24)–C(29)	1.390(9)
C(24)–C(25)	1.403(9)
C(25)–C(26)	1.388(9)
C(26)–C(27)	1.370(9)
C(27)–C(28)	1.402(10)
C(28)–C(29)	1.348(10)

**Table 30. Bond angles [°] for 2 at 100(2) K with estimated standard deviations in parentheses.**

Label	Angles
S(4)–Ni(1)–S(3)	91.14(7)
S(4)–Ni(1)–S(2)	175.00(7)
S(3)–Ni(1)–S(2)	90.36(7)
S(4)–Ni(1)–S(1)	87.25(7)
S(3)–Ni(1)–S(1)	178.13(8)
S(2)–Ni(1)–S(1)	91.17(7)
C(1)–S(1)–Ni(1)	106.5(2)
C(2)–S(2)–Ni(1)	105.6(2)
C(16)–S(3)–Ni(1)	105.5(2)
C(17)–S(4)–Ni(1)	106.4(2)
C(8)–O(1)–C(9)	118.8(7)
C(28)–O(2)–C(30)	115.8(7)
C(2)–C(1)–C(3)	123.0(6)
C(2)–C(1)–S(1)	117.8(5)
C(3)–C(1)–S(1)	119.2(5)
C(1)–C(2)–C(10)	123.4(5)
C(1)–C(2)–S(2)	118.8(5)
C(10)–C(2)–S(2)	117.8(4)
C(7)–C(3)–C(4)	118.6(6)
C(7)–C(3)–C(1)	121.2(5)
C(4)–C(3)–C(1)	120.2(6)
C(5)–C(4)–C(3)	120.2(6)
C(8)–C(5)–C(4)	119.7(6)
C(8)–C(6)–C(7)	118.7(7)
C(3)–C(7)–C(6)	121.2(6)
C(6)–C(8)–C(5)	121.4(6)

C(6)–C(8)–O(1)	121.7(7)
C(5)–C(8)–O(1)	116.9(6)
C(11)–C(10)–C(15)	119.0(6)
C(11)–C(10)–C(2)	121.2(5)
C(15)–C(10)–C(2)	119.8(6)
C(12)–C(11)–C(10)	120.4(6)
C(11)–C(12)–C(13)	120.3(7)
C(14)–C(13)–C(12)	118.6(7)
C(13)–C(14)–C(15)	121.9(7)
C(14)–C(15)–C(10)	119.7(7)
C(17)–C(16)–C(25)	123.7(6)
C(17)–C(16)–S(3)	119.3(5)
C(25)–C(16)–S(3)	117.0(5)
C(16)–C(17)–C(18)	126.9(6)
C(16)–C(17)–S(4)	117.6(5)
C(18)–C(17)–S(4)	115.5(5)
C(23)–C(18)–C(19)	118.1(6)
C(23)–C(18)–C(17)	120.9(6)
C(19)–C(18)–C(17)	120.9(6)
C(20)–C(19)–C(18)	120.9(6)
C(19)–C(20)–C(21)	121.7(7)
C(20)–C(21)–C(22)	118.1(7)
C(23)–C(22)–C(21)	120.1(6)
C(22)–C(23)–C(18)	121.1(6)
C(29)–C(24)–C(25)	120.5(6)
C(26)–C(25)–C(24)	118.2(6)
C(26)–C(25)–C(16)	121.3(6)
C(24)–C(25)–C(16)	120.4(6)
C(27)–C(26)–C(25)	120.7(6)
C(26)–C(27)–C(28)	120.2(6)
C(29)–C(28)–O(2)	124.3(7)
C(29)–C(28)–C(27)	119.9(6)
O(2)–C(28)–C(27)	115.4(6)
C(28)–C(29)–C(24)	120.4(7)

---

**Table 31. Bond lengths [Å] for 3<sup>-</sup> at 100(2) K with estimated standard deviations in parentheses.**

Label	Distances
Ni(1)–S(2)#1	2.1292(6)
Ni(1)–S(2)	2.1292(6)
Ni(1)–S(1)#1	2.1416(5)
Ni(1)–S(1)	2.1416(5)
Ni(2)–S(4)	2.1358(6)
Ni(2)–S(4)#2	2.1358(6)
Ni(2)–S(3)#2	2.1510(5)
Ni(2)–S(3)	2.1510(5)
S(1)–C(1)	1.744(2)
S(2)–C(2)#1	1.743(2)
S(3)–C(17)	1.746(2)
S(4)–C(25)#2	1.744(2)
O(1)–C(21)	1.378(3)
O(1)–C(24)	1.420(3)
O(2)–C(15)	1.378(3)
O(2)–C(16)	1.423(3)
O(3)–C(6)	1.373(3)
O(3)–C(9)	1.423(3)
O(4)–C(29)	1.370(3)
O(4)–C(32)	1.429(3)
N(1)–C(37)	1.519(3)
N(1)–C(33)	1.524(3)
N(1)–C(41)	1.528(3)
N(1)–C(45)	1.527(3)
C(1)–C(2)	1.367(3)
C(1)–C(10)	1.482(3)
C(2)–C(3)	1.483(3)
C(2)–S(2)#1	1.743(2)
C(3)–C(8)	1.395(3)
C(3)–C(4)	1.403(3)
C(4)–C(5)	1.374(3)
C(4)–H(4)	0.9300
C(5)–C(6)	1.393(4)
C(5)–H(5)	0.9300
C(6)–C(7)	1.394(3)
C(7)–C(8)	1.384(3)

C(7)–H(7)	0.9300
C(8)–H(8)	0.9300
C(9)–H(9A)	0.9600
C(9)–H(9B)	0.9600
C(9)–H(9C)	0.9600
C(10)–C(11)	1.389(3)
C(10)–C(13)	1.415(3)
C(11)–C(12)	1.393(3)
C(11)–H(11)	0.9300
C(12)–C(15)	1.395(3)
C(12)–H(12)	0.9300
C(13)–C(14)	1.380(3)
C(13)–H(13)	0.9300
C(14)–C(15)	1.385(4)
C(14)–H(14)	0.9300
C(16)–H(16A)	0.9600
C(16)–H(16B)	0.9600
C(16)–H(16C)	0.9600
C(17)–C(25)	1.361(3)
C(17)–C(18)	1.487(3)
C(18)–C(19)	1.390(4)
C(18)–C(23)	1.401(3)
C(19)–C(20)	1.394(3)
C(19)–H(19)	0.9300
C(20)–C(21)	1.394(3)
C(20)–H(20)	0.9300
C(21)–C(22)	1.385(4)
C(22)–C(23)	1.383(3)
C(22)–H(22)	0.9300
C(23)–H(23)	0.9300
C(24)–H(24A)	0.9600
C(24)–H(24B)	0.9600
C(24)–H(24C)	0.9600
C(25)–C(26)	1.486(3)
C(25)–S(4)#2	1.744(2)
C(26)–C(27)	1.390(3)
C(26)–C(31)	1.400(3)
C(27)–C(28)	1.389(3)

C(27)–H(27)	0.9300
C(28)–C(29)	1.391(4)
C(28)–H(28)	0.9300
C(29)–C(30)	1.400(4)
C(30)–C(31)	1.384(3)
C(30)–H(30)	0.9300
C(31)–H(31)	0.9300
C(32)–H(32A)	0.9600
C(32)–H(32B)	0.9600
C(32)–H(32C)	0.9600
C(33)–C(34)	1.514(4)
C(33)–H(33A)	0.9700
C(33)–H(33B)	0.9700
C(34)–C(35)	1.530(4)
C(34)–H(34A)	0.9700
C(34)–H(34B)	0.9700
C(35)–C(36)	1.516(4)
C(35)–H(35A)	0.9700
C(35)–H(35B)	0.9700
C(36)–H(36A)	0.9600
C(36)–H(36B)	0.9600
C(36)–H(36C)	0.9600
C(37)–C(38)	1.524(3)
C(37)–H(37A)	0.9700
C(37)–H(37B)	0.9700
C(38)–C(39)	1.520(4)
C(38)–H(38A)	0.9700
C(38)–H(38B)	0.9700
C(39)–C(40)	1.525(3)
C(39)–H(39A)	0.9700
C(39)–H(39B)	0.9700
C(40)–H(40A)	0.9600
C(40)–H(40B)	0.9600
C(40)–H(40C)	0.9600
C(41)–C(42)	1.522(4)
C(41)–H(41A)	0.9700
C(41)–H(41B)	0.9700
C(42)–C(43)	1.527(3)

C(42)–H(42A)	0.9700
C(42)–H(42B)	0.9700
C(43)–C(44)	1.527(4)
C(43)–H(43A)	0.9700
C(43)–H(43B)	0.9700
C(44)–H(44A)	0.9600
C(44)–H(44B)	0.9600
C(44)–H(44C)	0.9600
C(45)–C(46)	1.526(3)
C(45)–H(45A)	0.9700
C(45)–H(45B)	0.9700
C(46)–C(47)	1.497(4)
C(46)–H(46A)	0.9700
C(46)–H(46B)	0.9700
C(47)–C(48)	1.510(4)
C(47)–H(47A)	0.9700
C(47)–H(47B)	0.9700
C(48)–H(48A)	0.9600
C(48)–H(48B)	0.9600
C(48)–H(48C)	0.9600

Symmetry transformations used to generate equivalent atoms:

(1)  $-x, -y, -z$  (2)  $-x+2, -y, -z+1$

**Table 32. Bond angles [°] for 3<sup>-</sup> at 100(2) K with estimated standard deviations in parentheses.**

Label	Angles
S(2)#1–Ni(1)–S(2)	180.0
S(2)#1–Ni(1)–S(1)#1	89.22(2)
S(2)–Ni(1)–S(1)#1	90.78(2)
S(2)#1–Ni(1)–S(1)	90.78(2)
S(2)–Ni(1)–S(1)	89.22(2)
S(1)#1–Ni(1)–S(1)	180.0
S(4)–Ni(2)–S(4)#2	180.000(1)
S(4)–Ni(2)–S(3)#2	90.85(2)
S(4)#2–Ni(2)–S(3)#2	89.15(2)
S(4)–Ni(2)–S(3)	89.15(2)
S(4)#2–Ni(2)–S(3)	90.85(2)
S(3)#2–Ni(2)–S(3)	179.999(2)

C(1)–S(1)–Ni(1)	105.96(8)
C(2)#1–S(2)–Ni(1)	105.89(8)
C(17)–S(3)–Ni(2)	105.43(8)
C(25)#2–S(4)–Ni(2)	105.69(8)
C(21)–O(1)–C(24)	117.47(19)
C(15)–O(2)–C(16)	116.75(19)
C(6)–O(3)–C(9)	116.7(2)
C(29)–O(4)–C(32)	116.4(2)
C(37)–N(1)–C(33)	111.2(2)
C(37)–N(1)–C(41)	106.99(19)
C(33)–N(1)–C(41)	110.74(18)
C(37)–N(1)–C(45)	111.32(19)
C(33)–N(1)–C(45)	105.66(18)
C(41)–N(1)–C(45)	110.96(19)
C(2)–C(1)–C(10)	126.5(2)
C(2)–C(1)–S(1)	118.17(18)
C(10)–C(1)–S(1)	115.25(16)
C(1)–C(2)–C(3)	127.7(2)
C(1)–C(2)–S(2)#1	119.15(18)
C(3)–C(2)–S(2)#1	113.16(16)
C(8)–C(3)–C(4)	117.3(2)
C(8)–C(3)–C(2)	123.0(2)
C(4)–C(3)–C(2)	119.5(2)
C(5)–C(4)–C(3)	121.3(2)
C(5)–C(4)–H(4)	119.4
C(3)–C(4)–H(4)	119.4
C(4)–C(5)–C(6)	120.7(2)
C(4)–C(5)–H(5)	119.7
C(6)–C(5)–H(5)	119.7
O(3)–C(6)–C(5)	116.0(2)
O(3)–C(6)–C(7)	125.0(2)
C(5)–C(6)–C(7)	119.0(2)
C(8)–C(7)–C(6)	119.8(2)
C(8)–C(7)–H(7)	120.1
C(6)–C(7)–H(7)	120.1
C(7)–C(8)–C(3)	121.9(2)
C(7)–C(8)–H(8)	119.1
C(3)–C(8)–H(8)	119.1

O(3)–C(9)–H(9A)	109.5
O(3)–C(9)–H(9B)	109.5
H(9A)–C(9)–H(9B)	109.5
O(3)–C(9)–H(9C)	109.5
H(9A)–C(9)–H(9C)	109.5
H(9B)–C(9)–H(9C)	109.5
C(11)–C(10)–C(13)	116.9(2)
C(11)–C(10)–C(1)	122.9(2)
C(13)–C(10)–C(1)	120.1(2)
C(10)–C(11)–C(12)	122.2(2)
C(10)–C(11)–H(11)	118.9
C(12)–C(11)–H(11)	118.9
C(11)–C(12)–C(15)	119.2(2)
C(11)–C(12)–H(12)	120.4
C(15)–C(12)–H(12)	120.4
C(14)–C(13)–C(10)	121.6(2)
C(14)–C(13)–H(13)	119.2
C(10)–C(13)–H(13)	119.2
C(13)–C(14)–C(15)	120.0(2)
C(13)–C(14)–H(14)	120.0
C(15)–C(14)–H(14)	120.0
O(2)–C(15)–C(14)	115.3(2)
O(2)–C(15)–C(12)	124.6(2)
C(14)–C(15)–C(12)	120.0(2)
O(2)–C(16)–H(16A)	109.5
O(2)–C(16)–H(16B)	109.5
H(16A)–C(16)–H(16B)	109.5
O(2)–C(16)–H(16C)	109.5
H(16A)–C(16)–H(16C)	109.5
H(16B)–C(16)–H(16C)	109.5
C(25)–C(17)–C(18)	125.0(2)
C(25)–C(17)–S(3)	118.78(18)
C(18)–C(17)–S(3)	116.04(16)
C(19)–C(18)–C(23)	117.7(2)
C(19)–C(18)–C(17)	121.1(2)
C(23)–C(18)–C(17)	121.2(2)
C(18)–C(19)–C(20)	122.0(2)
C(18)–C(19)–H(19)	119.0

C(20)–C(19)–H(19)	119.0
C(19)–C(20)–C(21)	118.8(2)
C(19)–C(20)–H(20)	120.6
C(21)–C(20)–H(20)	120.6
O(1)–C(21)–C(22)	115.6(2)
O(1)–C(21)–C(20)	124.2(2)
C(22)–C(21)–C(20)	120.2(2)
C(23)–C(22)–C(21)	120.1(2)
C(23)–C(22)–H(22)	119.9
C(21)–C(22)–H(22)	119.9
C(22)–C(23)–C(18)	121.1(2)
C(22)–C(23)–H(23)	119.5
C(18)–C(23)–H(23)	119.5
O(1)–C(24)–H(24A)	109.5
O(1)–C(24)–H(24B)	109.5
H(24A)–C(24)–H(24B)	109.5
O(1)–C(24)–H(24C)	109.5
H(24A)–C(24)–H(24C)	109.5
H(24B)–C(24)–H(24C)	109.5
C(17)–C(25)–C(26)	126.3(2)
C(17)–C(25)–S(4)#2	119.24(18)
C(26)–C(25)–S(4)#2	114.45(16)
C(27)–C(26)–C(31)	117.6(2)
C(27)–C(26)–C(25)	122.6(2)
C(31)–C(26)–C(25)	119.7(2)
C(28)–C(27)–C(26)	121.9(2)
C(28)–C(27)–H(27)	119.1
C(26)–C(27)–H(27)	119.1
C(27)–C(28)–C(29)	119.8(2)
C(27)–C(28)–H(28)	120.1
C(29)–C(28)–H(28)	120.1
O(4)–C(29)–C(28)	125.5(2)
O(4)–C(29)–C(30)	115.3(2)
C(28)–C(29)–C(30)	119.2(2)
C(31)–C(30)–C(29)	120.1(2)
C(31)–C(30)–H(30)	119.9
C(29)–C(30)–H(30)	119.9
C(30)–C(31)–C(26)	121.3(2)

C(30)–C(31)–H(31)	119.3
C(26)–C(31)–H(31)	119.3
O(4)–C(32)–H(32A)	109.5
O(4)–C(32)–H(32B)	109.5
H(32A)–C(32)–H(32B)	109.5
O(4)–C(32)–H(32C)	109.5
H(32A)–C(32)–H(32C)	109.5
H(32B)–C(32)–H(32C)	109.5
C(34)–C(33)–N(1)	116.3(2)
C(34)–C(33)–H(33A)	108.2
N(1)–C(33)–H(33A)	108.2
C(34)–C(33)–H(33B)	108.2
N(1)–C(33)–H(33B)	108.2
H(33A)–C(33)–H(33B)	107.4
C(33)–C(34)–C(35)	110.3(2)
C(33)–C(34)–H(34A)	109.6
C(35)–C(34)–H(34A)	109.6
C(33)–C(34)–H(34B)	109.6
C(35)–C(34)–H(34B)	109.6
H(34A)–C(34)–H(34B)	108.1
C(36)–C(35)–C(34)	112.3(2)
C(36)–C(35)–H(35A)	109.1
C(34)–C(35)–H(35A)	109.1
C(36)–C(35)–H(35B)	109.1
C(34)–C(35)–H(35B)	109.1
H(35A)–C(35)–H(35B)	107.9
C(35)–C(36)–H(36A)	109.5
C(35)–C(36)–H(36B)	109.5
H(36A)–C(36)–H(36B)	109.5
C(35)–C(36)–H(36C)	109.5
H(36A)–C(36)–H(36C)	109.5
H(36B)–C(36)–H(36C)	109.5
N(1)–C(37)–C(38)	115.2(2)
N(1)–C(37)–H(37A)	108.5
C(38)–C(37)–H(37A)	108.5
N(1)–C(37)–H(37B)	108.5
C(38)–C(37)–H(37B)	108.5
H(37A)–C(37)–H(37B)	107.5

C(39)–C(38)–C(37)	111.6(2)
C(39)–C(38)–H(38A)	109.3
C(37)–C(38)–H(38A)	109.3
C(39)–C(38)–H(38B)	109.3
C(37)–C(38)–H(38B)	109.3
H(38A)–C(38)–H(38B)	108.0
C(38)–C(39)–C(40)	114.0(2)
C(38)–C(39)–H(39A)	108.7
C(40)–C(39)–H(39A)	108.7
C(38)–C(39)–H(39B)	108.7
C(40)–C(39)–H(39B)	108.7
H(39A)–C(39)–H(39B)	107.6
C(39)–C(40)–H(40A)	109.5
C(39)–C(40)–H(40B)	109.5
H(40A)–C(40)–H(40B)	109.5
C(39)–C(40)–H(40C)	109.5
H(40A)–C(40)–H(40C)	109.5
H(40B)–C(40)–H(40C)	109.5
C(42)–C(41)–N(1)	114.8(2)
C(42)–C(41)–H(41A)	108.6
N(1)–C(41)–H(41A)	108.6
C(42)–C(41)–H(41B)	108.6
N(1)–C(41)–H(41B)	108.6
H(41A)–C(41)–H(41B)	107.5
C(41)–C(42)–C(43)	110.5(2)
C(41)–C(42)–H(42A)	109.5
C(43)–C(42)–H(42A)	109.5
C(41)–C(42)–H(42B)	109.5
C(43)–C(42)–H(42B)	109.5
H(42A)–C(42)–H(42B)	108.1
C(44)–C(43)–C(42)	111.2(2)
C(44)–C(43)–H(43A)	109.4
C(42)–C(43)–H(43A)	109.4
C(44)–C(43)–H(43B)	109.4
C(42)–C(43)–H(43B)	109.4
H(43A)–C(43)–H(43B)	108.0
C(43)–C(44)–H(44A)	109.5
C(43)–C(44)–H(44B)	109.5

H(44A)–C(44)–H(44B)	109.5
C(43)–C(44)–H(44C)	109.5
H(44A)–C(44)–H(44C)	109.5
H(44B)–C(44)–H(44C)	109.5
C(46)–C(45)–N(1)	117.3(2)
C(46)–C(45)–H(45A)	108.0
N(1)–C(45)–H(45A)	108.0
C(46)–C(45)–H(45B)	108.0
N(1)–C(45)–H(45B)	108.0
H(45A)–C(45)–H(45B)	107.2
C(47)–C(46)–C(45)	114.4(2)
C(47)–C(46)–H(46A)	108.7
C(45)–C(46)–H(46A)	108.7
C(47)–C(46)–H(46B)	108.7
C(45)–C(46)–H(46B)	108.7
H(46A)–C(46)–H(46B)	107.6
C(46)–C(47)–C(48)	113.7(3)
C(46)–C(47)–H(47A)	108.8
C(48)–C(47)–H(47A)	108.8
C(46)–C(47)–H(47B)	108.8
C(48)–C(47)–H(47B)	108.8
H(47A)–C(47)–H(47B)	107.7
C(47)–C(48)–H(48A)	109.5
C(47)–C(48)–H(48B)	109.5
H(48A)–C(48)–H(48B)	109.5
C(47)–C(48)–H(48C)	109.5
H(48A)–C(48)–H(48C)	109.5
H(48B)–C(48)–H(48C)	109.5

---

Symmetry transformations used to generate equivalent atoms:  
(1)  $-x, -y, -z$  (2)  $-x+2, -y, -z+1$

**Table 33. Bond lengths (Å) for 7 at 100(2) K with estimated standard deviations in parentheses.**

Label	Distances
Ni(1)–S(2)	2.1351(9)
Ni(1)–S(1)	2.1413(9)
Ni(1)–S(3)	2.1490(9)
Ni(1)–S(4)	2.1538(9)
S(1)–C(1)	1.727(3)
S(2)–C(2)	1.734(3)

S(3)–C(15)	1.730(4)
S(4)–C(16)	1.741(3)
N(1)–C(23)	1.514(4)
N(1)–C(27)	1.519(4)
N(1)–C(31)	1.524(4)
N(1)–C(19)	1.530(4)
N(2)–C(17)	1.149(5)
N(3)–C(18)	1.141(5)
C(1)–C(2)	1.361(5)
C(1)–C(9)	1.484(5)
C(2)–C(3)	1.483(5)
C(3)–C(4)	1.398(5)
C(3)–C(8)	1.403(5)
C(4)–C(5)	1.389(5)
C(5)–C(6)	1.383(5)
C(6)–C(7)	1.393(5)
C(7)–C(8)	1.379(5)
C(9)–C(14)	1.387(5)
C(9)–C(10)	1.406(5)
C(10)–C(11)	1.379(5)
C(11)–C(12)	1.381(5)
C(12)–C(13)	1.384(5)
C(13)–C(14)	1.390(5)
C(15)–C(16)	1.355(5)
C(15)–C(17)	1.442(5)
C(16)–C(18)	1.432(5)
C(19)–C(20)	1.517(5)
C(20)–C(21)	1.514(5)
C(21)–C(22)	1.520(5)
C(23)–C(24)	1.517(5)
C(24)–C(25)	1.520(5)
C(25)–C(26)	1.504(5)
C(27)–C(28)	1.526(5)
C(28)–C(29)	1.528(5)
C(29)–C(30)	1.525(5)
C(31)–C(32)	1.516(5)
C(32)–C(33)	1.514(5)
C(33)–C(34)	1.519(5)

---

**Table 34. Bond angles (°) for 7 at 100(2) K with estimated standard deviations in parentheses.**

Label	Angles
S(2)–Ni(1)–S(1)	90.70(4)
S(2)–Ni(1)–S(3)	87.20(4)
S(1)–Ni(1)–S(3)	177.49(4)
S(2)–Ni(1)–S(4)	179.10(4)
S(1)–Ni(1)–S(4)	88.87(3)
S(3)–Ni(1)–S(4)	93.24(4)
C(1)–S(1)–Ni(1)	105.39(12)
C(2)–S(2)–Ni(1)	105.71(12)
C(15)–S(3)–Ni(1)	102.68(12)
C(16)–S(4)–Ni(1)	102.63(12)
C(23)–N(1)–C(27)	111.3(3)
C(23)–N(1)–C(31)	109.5(3)
C(27)–N(1)–C(31)	108.5(2)
C(23)–N(1)–C(19)	108.0(2)
C(27)–N(1)–C(19)	108.4(2)
C(31)–N(1)–C(19)	111.2(3)
C(2)–C(1)–C(9)	124.4(3)
C(2)–C(1)–S(1)	119.4(3)
C(9)–C(1)–S(1)	115.9(2)
C(1)–C(2)–C(3)	126.1(3)
C(1)–C(2)–S(2)	118.6(3)
C(3)–C(2)–S(2)	115.0(2)
C(4)–C(3)–C(8)	118.2(3)
C(4)–C(3)–C(2)	119.9(3)
C(8)–C(3)–C(2)	121.7(3)
C(5)–C(4)–C(3)	121.2(3)
C(6)–C(5)–C(4)	119.9(3)
C(5)–C(6)–C(7)	119.4(3)
C(8)–C(7)–C(6)	121.0(3)
C(7)–C(8)–C(3)	120.3(3)
C(14)–C(9)–C(10)	118.7(3)
C(14)–C(9)–C(1)	121.9(3)
C(10)–C(9)–C(1)	119.3(3)
C(11)–C(10)–C(9)	120.5(3)
C(10)–C(11)–C(12)	120.5(3)
C(11)–C(12)–C(13)	119.5(3)

C(12)–C(13)–C(14)	120.5(3)
C(9)–C(14)–C(13)	120.3(3)
C(16)–C(15)–C(17)	122.3(3)
C(16)–C(15)–S(3)	121.2(3)
C(17)–C(15)–S(3)	116.6(3)
C(15)–C(16)–C(18)	122.6(3)
C(15)–C(16)–S(4)	120.3(3)
C(18)–C(16)–S(4)	117.1(3)
N(2)–C(17)–C(15)	177.4(4)
N(3)–C(18)–C(16)	177.8(4)
C(20)–C(19)–N(1)	115.3(3)
C(21)–C(20)–C(19)	111.4(3)
C(20)–C(21)–C(22)	112.0(3)
N(1)–C(23)–C(24)	117.0(3)
C(23)–C(24)–C(25)	109.7(3)
C(26)–C(25)–C(24)	112.8(3)
N(1)–C(27)–C(28)	116.2(3)
C(27)–C(28)–C(29)	109.2(3)
C(30)–C(29)–C(28)	112.8(3)
C(32)–C(31)–N(1)	115.6(3)
C(33)–C(32)–C(31)	110.5(3)
C(32)–C(33)–C(34)	111.9(3)

**Table 35. Bond lengths (in Å) for compound 8 at 100(2) K with estimated standard deviations in parentheses.**

Ni1 – S3	2.1557(6)	Ni1 – S4	2.1616(6)
Ni1 – S1	2.1702(7)	Ni1 – S2	2.1728(6)
S1 – C1	1.7617(19)	S2 – C6	1.7819(18)
S2 – C7	1.8273(18)	S3 – C10	1.7753(19)
S3 – C9	1.8309(18)	S4 – C15	1.7534(19)
C1 – C2	1.397(3)	C1 – C6	1.399(2)
C2 – C3	1.382(3)	C2 – H14	0.95
C3 – C4	1.394(3)	C3 – H1	0.95
C4 – C5	1.388(3)	C4 – H13	0.95
C5 – C6	1.386(3)	C5 – H12	0.95
C7 – C8	1.523(2)	C7 – H11	0.99

C7 – H2	0.99	C8 – C9	1.522(3)
C8 – H4	0.99	C8 – H3	0.99
C9 – H6	0.99	C9 – H5	0.99
C10 – C11	1.388(3)	C10 – C15	1.397(3)
C11 – C12	1.385(3)	C11 – H7	0.95
C12 – C13	1.390(3)	C12 – H10	0.95
C13 – C14	1.383(3)	C13 – H9	0.95
C14 – C15	1.401(3)	C14 – H8	0.95

---

**Table 36. Bond angles (in °) for compound 8 at 100(2) K with estimated standard deviations in parentheses.**

S3–Ni1–S4	92.41(2)	S3–Ni1–S1	168.83(2)
S4–Ni1–S1	88.06(2)	S3–Ni1–S2	90.84(2)
S4–Ni1–S2	173.55(2)	S1–Ni1–S2	89.83(2)
C1–S1–Ni1	102.74(6)	C6–S2–C7	102.77(9)
C6–S2–Ni1	103.53(6)	C7–S2–Ni1	107.89(6)
C10–S3–C9	103.05(9)	C10–S3–Ni1	105.04(6)
C9–S3–Ni1	107.43(6)	C15–S4–Ni1	103.75(6)
C2–C1–C6	118.12(16)	C2–C1–S1	121.47(13)
C6–C1–S1	120.41(14)	C3–C2–C1	120.15(16)
C3–C2–H14	119.9	C1–C2–H14	119.9
C2–C3–C4	121.13(17)	C2–C3–H1	119.4
C4–C3–H1	119.4	C5–C4–C3	119.41(17)
C5–C4–H13	120.3	C3–C4–H13	120.3
C6–C5–C4	119.26(17)	C6–C5–H12	120.4
C4–C5–H12	120.4	C5–C6–C1	121.92(17)
C5–C6–S2	122.22(14)	C1–C6–S2	115.68(14)
C8–C7–S2	111.42(12)	C8–C7–H11	109.3
S2–C7–H11	109.3	C8–C7–H2	109.3
S2–C7–H2	109.3	H11–C7–H2	108.0
C9–C8–C7	116.72(15)	C9–C8–H4	108.1
C7–C8–H4	108.1	C9–C8–H3	108.1
C7–C8–H3	108.1	H4–C8–H3	107.3
C8–C9–S3	110.75(13)	C8–C9–H6	109.5

S3–C9–H6	109.5	C8–C9–H5	109.5
S3–C9–H5	109.5	H6–C9–H5	108.1
C11–C10–C15	122.18(17)	C11–C10–S3	120.72(14)
C15–C10–S3	116.98(14)	C12–C11–C10	119.17(18)
C12–C11–H7	120.4	C10–C11–H7	120.4
C11–C12–C13	119.74(18)	C11–C12–H10	120.1
C13–C12–H10	120.1	C14–C13–C12	120.67(18)
C14–C13–H9	119.7	C12–C13–H9	119.7
C13–C14–C15	120.76(17)	C13–C14–H8	119.6
C15–C14–H8	119.6	C10–C15–C14	117.41(16)
C10–C15–S4	121.32(14)	C14–C15–S4	121.24(14)

**Table 37. Torsion angles (in °) for compound 8 at 100(2) K with estimated standard deviations in parentheses.**

Ni1–S1–C1–C2	164.38(14)	Ni1–S1–C1–C6	–15.51(16)
C6–C1–C2–C3	0.8(3)	S1–C1–C2–C3	–179.09(15)
C1–C2–C3–C4	–1.0(3)	C2–C3–C4–C5	–0.1(3)
C3–C4–C5–C6	1.4(3)	C4–C5–C6–C1	–1.6(3)
C4–C5–C6–S2	–176.58(15)	C2–C1–C6–C5	0.5(3)
S1–C1–C6–C5	–179.61(15)	C2–C1–C6–S2	175.78(14)
S1–C1–C6–S2	–4.3(2)	C7–S2–C6–C5	–50.59(18)
Ni1–S2–C6–C5	–162.83(15)	C7–S2–C6–C1	134.14(15)
Ni1–S2–C6–C1	21.90(15)	C6–S2–C7–C8	–174.52(13)
Ni1–S2–C7–C8	–65.54(13)	S2–C7–C8–C9	68.81(19)
C7–C8–C9–S3	–69.95(19)	C10–S3–C9–C8	178.70(13)
Ni1–S3–C9–C8	68.09(13)	C9–S3–C10–C11	64.86(18)
Ni1–S3–C10–C11	177.24(15)	C9–S3–C10–C15	–119.09(15)
Ni1–S3–C10–C15	–6.71(16)	C15–C10–C11–C12	2.6(3)
S3–C10–C11–C12	178.48(15)	C10–C11–C12–C13	–0.5(3)
C11–C12–C13–C14	–1.5(3)	C12–C13–C14–C15	1.4(3)
C11–C10–C15–C14	–2.7(3)	S3–C10–C15–C14	–178.68(14)
C11–C10–C15–S4	179.19(15)	S3–C10–C15–S4	3.2(2)
C13–C14–C15–C10	0.6(3)	C13–C14–C15–S4	178.75(15)
Ni1–S4–C15–C10	2.04(17)	Ni1–S4–C15–C14	–176.02(14)

## REFERENCES

- [1] K. Rajeshwar, R. McConnell, S. Licht, Solar hydrogen generation, *Toward a Renewable Energy Future*. Springer: New York. (2008).
- [2] P. Atkins, J. De Paula, *Elements of physical chemistry*, Oxford University Press, USA, 2013.
- [3] 800px-Solar\_spectrum\_en.svg.png 800×600 pixel, (n.d.).  
[https://upload.wikimedia.org/wikipedia/commons/thumb/e/e7/Solar\\_spectrum\\_en.svg/800px-Solar\\_spectrum\\_en.svg.png](https://upload.wikimedia.org/wikipedia/commons/thumb/e/e7/Solar_spectrum_en.svg/800px-Solar_spectrum_en.svg.png) (accessed August 20, 2017).
- [4] A.J. Bard, R. Parsons, J. Jordan, *Standard Potentials in Aqueous Solution*, Taylor & Francis, 1985.
- [5] G. Stochel, Z. Stasicka, M. Brindell, W. Macyk, K. Szacilowski, *Bioinorganic photochemistry*, John Wiley & Sons, 2009.
- [6] J.M. Berg, J. Tymoczko, *Stryer: Biochemistry*, WH Freeman and Company. 5 (2002) 306–307.
- [7] Y. Umena, K. Kawakami, J.-R. Shen, N. Kamiya, Crystal structure of oxygen-evolving photosystem II at a resolution of 1.9 Å, *Nature*. 473 (2011) 55–60. doi:10.1038/nature09913.
- [8] R. Eisenberg, H.B. Gray, Noninnocence in Metal Complexes: A Dithiolene Dawn, *Inorg. Chem.* 50 (2011) 9741–9751. doi:10.1021/ic2011748.
- [9] S. Sproules, K. Wieghardt, Dithiolene radicals: Sulfur K-edge X-ray absorption spectroscopy and Harry's intuition, *Coordination Chemistry Reviews*. 255 (2011) 837–860. doi:10.1016/j.ccr.2010.12.006.
- [10] M.S. Queen, B.D. Towey, K.A. Murray, B.S. Veldkamp, H.J. Byker, R.K. Szilagy, Electronic structure of [Ni(II)S<sub>4</sub>] complexes from S K-edge X-ray absorption spectroscopy, *Coordination Chemistry Reviews*. 257 (2013) 564–578. doi:10.1016/j.ccr.2012.07.020.
- [11] C.A. Mitsopoulou, Identifying of charge-transfer transitions and reactive centers in M(diimine)(dithiolate) complexes by DFT techniques, *Coordination Chemistry Reviews*. 254 (2010) 1448–1456. doi:10.1016/j.ccr.2009.12.035.

- [12] M. Gomez-Mingot, J.-P. Porcher, T.K. Todorova, T. Fogeron, C. Mellot-Draznieks, Y. Li, M. Fontecave, Bioinspired Tungsten Dithiolene Catalysts for Hydrogen Evolution: A Combined Electrochemical, Photochemical, and Computational Study, *J. Phys. Chem. B.* (2015). doi:10.1021/acs.jpcc.5b01615.
- [13] R. Humphry-Baker, C.A. Mitsopoulou, D. Katakis, E. Vrachnou, Photophysical study of the decomposition of water using visible light and tungsten tris(dithiolenes) as photosensitizers-catalysts, *Journal of Photochemistry and Photobiology A: Chemistry.* 114 (1998) 137–144.
- [14] D. Katakis, C. Mitsopoulou, E. Vrachnou, Photocatalytic splitting of water: increase in conversion and energy storage efficiency, *Journal of Photochemistry and Photobiology, A: Chemistry.* 81 (1994) 103–106. doi:10.1016/1010-6030(94)03777-9.
- [15] D.F. Katakis, C. Mitsopoulou, J. Konstantatos, E. Vrachnou, P. Falaras, Photocatalytic splitting of water, *Journal of Photochemistry and Photobiology, A: Chemistry.* 68 (1992) 375–388. doi:10.1016/1010-6030(92)85246-Q.
- [16] R. Henning, W. Schlamann, H. Kisch, Photolysis of Water Catalyzed by Transition Metal Dithiolenes, *Angew. Chem. Int. Ed. Engl.* 19 (1980) 645–646. doi:10.1002/anie.198006452.
- [17] D. Sellmann, M. Geck, M. Moll, Transition-metal complexes with sulfur ligands. 62. Hydrogen evolution upon reaction of protons with sulfur-coordinated iron(II) complexes. Investigation of the proton, hydrogen and hydride interactions with iron 1,2-benzenedithiolate complexes, *J. Am. Chem. Soc.* 113 (1991) 5259–5264. doi:10.1021/ja00014a019.
- [18] A. Vlček Jr., A.A. Vlček, Metal-localized protonation of  $Mmnt_3-2$  ( $M = Rh, Co$ ) complexes, *Inorganica Chimica Acta.* 41 (1980) 123–131. doi:10.1016/S0020-1693(00)88441-8.
- [19] E. Lyris, D. Argyropoulos, C.-A. Mitsopoulou, D. Katakis, E. Vrachnou, New catalysts in the photo-oxidation of water, *Journal of Photochemistry and Photobiology A: Chemistry.* 108 (1997) 51–54.
- [20] C. Mitsopoulou, E. Lyris, S. Veltsos, D. Katakis, An investigation of the reaction of Cu (II) ions with tris (4-methoxy)-and tris-(4-dimethylamino) 2-diphenyl-

dithiolenato-S, S') tungsten (VI) complexes, *Inorganic Reaction Mechanisms*. 3 (2001) 99–106.

[21] J.A. McCleverty, *Prog. Inorg. Chem.* 10 (1968) 49–221.

[22] K. Arumugam, J.E. Bollinger, M. Fink, J.P. Donahue, Preparation and Isolation of Dithiolene Thiophosphoryl Molecules as Stable, Protected Forms of Dithiolene Ligands, *Inorg. Chem.* 46 (2007) 3283–3288. doi:10.1021/ic0700203.

[23] E.I. Stiefel, *Dithiolene Chemistry, Progress in Inorganic Chemistry*. 52 (2004).

[24] T.M. Cocker, R.E. Bachman, Photochemical and chemical oxidation of  $\alpha$ -dimine-dithiolene metal complexes: Insight into the role of the metal atom, *Inorganic Chemistry*. 40 (2001) 1550–1556. doi:10.1021/ic000884n.

[25] W.B. Connick, H.B. Gray, Photooxidation of platinum(II) diimine dithiolates, *Journal of the American Chemical Society*. 119 (1997) 11620–11627. doi:10.1021/ja9723803.

[26] Y. Zhang, K.D. Ley, K.S. Schanze, Photooxidation of Diimine Dithiolate Platinum(II) Complexes Induced by Charge Transfer to Diimine Excitation, *Inorganic Chemistry*. 35 (1996) 7102–7110.

[27] F. Neese, T. Petrenko, D. Ganyushin, G. Olbrich, Advanced aspects of ab initio theoretical optical spectroscopy of transition metal complexes: Multiplets, spin-orbit coupling and resonance Raman intensities, *Coordination Chemistry Reviews*. 251 (2007) 288–327. doi:10.1016/j.ccr.2006.05.019.

[28] P. Surawatanawong, S. Sproules, F. Neese, K. Wieghardt, Electronic structures and spectroscopy of the electron transfer series  $[\text{Fe}(\text{NO})\text{L}_2]_z$  ( $z = 1+, 0, 1-, 2-, 3-$ ;  $\text{L} =$  dithiolene), *Inorganic Chemistry*. 50 (2011) 12064–12074. doi:10.1021/ic201565d.

[29] K. Ray, S. DeBeer George, E.I. Solomon, K. Wieghardt, F. Neese, Description of the ground-state covalencies of the bis(dithiolato) transition-metal Complexes from X-ray absorption spectroscopy and time-dependent density-functional calculations, *Chemistry - A European Journal*. 13 (2007) 2783–2797. doi:10.1002/chem.200601425.

[30] K. Ray, T. Weyhermüller, F. Neese, K. Wieghardt, Electronic Structure of Square Planar Bis(benzene-1,2-dithiolato)metal Complexes  $[\text{M}(\text{L})_2]_z$  ( $z = 2-, 1-, 0$ ;

M = Ni, Pd, Pt, Cu, Au): An Experimental, Density Functional, and Correlated ab Initio Study, *Inorg. Chem.* 44 (2005) 5345–5360. doi:10.1021/ic0507565.

[31] G.C. Papavassiliou, G.C. Anyfantis, G.A. Mousdis, Neutral Metal 1,2-Dithiolenes: Preparations, Properties and Possible Applications of Unsymmetrical in Comparison to the Symmetrical, *Crystals*. 2 (2012). doi:10.3390/cryst2030762.

[32] J.A. Denny, M.Y. Darensbourg, Metallodithiolates as Ligands in Coordination, Bioinorganic, and Organometallic Chemistry, *Chem. Rev.* 115 (2015) 5248–5273. doi:10.1021/cr500659u.

[33] M.J. Baker-Hawkes, E. Billig, H.B. Gray, Characterization and Electronic Structures of Metal Complexes Containing Benzene-1,2-dithiolate and Related Ligands, *J. Am. Chem. Soc.* 88 (1966) 4870–4875. doi:10.1021/ja00973a021.

[34] W.R. McNamara, Z. Han, C.-J. (Madeline) Yin, W.W. Brennessel, P.L. Holland, R. Eisenberg, Cobalt-dithiolene complexes for the photocatalytic and electrocatalytic reduction of protons in aqueous solutions, *Proceedings of the National Academy of Sciences*. 109 (2012) 15594–15599. doi:10.1073/pnas.1120757109.

[35] S. Curreli, P. Deplano, C. Faulmann, A. Ienco, C. Mealli, M.L. Mercuri, L. Pilia, G. Pintus, A. Serpe, E.F. Trogu, Electronic Factors Affecting Second-Order NLO Properties: Case Study of Four Different Push-Pull Bis-Dithiolene Nickel Complexes, *Inorg. Chem.* 43 (2004) 5069–5079. doi:10.1021/ic0496469.

[36] D. Espa, L. Pilia, C. Makedonas, L. Marchiò, M.L. Mercuri, A. Serpe, A. Barsella, A. Fort, C.A. Mitsopoulou, P. Deplano, Role of the acceptor in tuning the properties of metal [M(II) = Ni, Pd, Pt] dithiolato/dithione (donor/acceptor) second-order nonlinear chromophores: Combined experimental and theoretical studies, *Inorganic Chemistry*. 53 (2014) 1170–1183. doi:10.1021/ic402738b.

[37] L. Pilia, D. Espa, A. Barsella, A. Fort, C. Makedonas, L. Marchiò, M.L. Mercuri, A. Serpe, C.A. Mitsopoulou, P. Deplano, Combined experimental and theoretical study on redox-active d8 metal dithione-dithiolato complexes showing molecular second-order nonlinear optical activity, *Inorganic Chemistry*. 50 (2011) 10015–10027. doi:10.1021/ic2007765.

[38] P. Deplano, L. Pilia, D. Espa, M.L. Mercuri, A. Serpe, Square-planar d8 metal mixed-ligand dithiolene complexes as second order nonlinear optical chromophores:

Structure/property relationship, *Coordination Chemistry Reviews*. 254 (2010) 1434–1447. doi:10.1016/j.ccr.2009.12.022.

[39] A. Vogler, H. Kunkely, J. Hlavatsch, A. Merz, Mixed-Ligand 1,2-diimine Ethylene-1,2-dithiolate Complexes of Nickel, Palladium, and Platinum, *Inorganic Chemistry*. 23 (1984) 506–509. doi:10.1021/ic00172a026.

[40] A. Vogler, H. Kunkely, A 1,2-Dithiolenenickel Complex with Different Substituents—a Novel Type of Mixed-Valence Compounds, *Angew. Chem. Int. Ed. Engl.* 21 (1982) 77–77. doi:10.1002/anie.198200771.

[41] G.C. Anyfantis, G.C. Papavassiliou, A. Terzis, C.P. Raptopoulou, V. Psycharis, P. Paraskevopoulou, Preparation and characterization of Ni(dpdt)(pddt) and Ni(dpdt)(pddt)·CS<sub>2</sub>, where dpdt is diphenylethylenedithiolate and pddt is 6,7-dihydro-5H-1,4-dithiepin-2,3-dithiolate, *Polyhedron*. 29 (2010) 969–974. doi:10.1016/j.poly.2009.11.014.

[42] D. Sellmann, J. Sutter, Dithiolenes in more complex ligands, in: *Dithiolene Chemistry*, John Wiley & Sons, Inc., 2004: pp. 585–681.

[43] Q. Wang, J.E. Barclay, A.J. Blake, E.S. Davies, D.J. Evans, A.C. Marr, E.J.L. McInnes, J. McMaster, C. Wilson, M. Schröder, The Synthesis and Electronic Structure of a Novel [Ni<sup>II</sup>S<sub>4</sub>Fe<sub>2</sub>(CO)<sub>6</sub>] Radical Cluster: Implications for the Active Site of the [NiFe] Hydrogenases, *Chem. Eur. J.* 10 (2004) 3384–3396. doi:10.1002/chem.200305738.

[44] S. Canaguier, V. Fourmond, C.U. Perotto, J. Fize, J. Pécaut, M. Fontecave, M.J. Field, V. Artero, Catalytic hydrogen production by a Ni-Ru mimic of NiFe hydrogenases involves a proton-coupled electron transfer step, *Chemical Communications*. 49 (2013) 5004–5006. doi:10.1039/c3cc40987b.

[45] S. Canaguier, M. Fontecave, V. Artero, Cp\*--ruthenium-nickel-based H<sub>2</sub>-evolving electrocatalysts as bio-inspired models of NiFe hydrogenases, *European Journal of Inorganic Chemistry*. (2011) 1094–1099. doi:10.1002/ejic.201000944.

[46] S. Canaguier, M. Field, Y. Oudart, J. Pécaut, M. Fontecave, V. Artero, A structural and functional mimic of the active site of NiFe hydrogenases, *Chemical Communications*. 46 (2010) 5876–5878. doi:10.1039/c001675f.

[47] S. Canaguier, L. Vaccaro, V. Artero, R. Ostermann, J. Pécaut, M.J. Field, M.

Fontecave, Cyclopentadienyl ruthenium-nickel catalysts for biomimetic hydrogen evolution: Electrocatalytic properties and mechanistic DFT studies, *Chemistry - A European Journal*. 15 (2009) 9350–9364. doi:10.1002/chem.200900854.

[48] S. Canaguier, V. Artero, M. Fontecave, Modelling NiFe hydrogenases: Nickel-based electrocatalysts for hydrogen production, *Dalton Transactions*. (2008) 315–325. doi:10.1039/b713567j.

[49] V. Fourmond, S. Canaguier, B. Golly, M.J. Field, M. Fontecave, V. Artero, A nickel-manganese catalyst as a biomimic of the active site of NiFe hydrogenases: A combined electrocatalytical and DFT mechanistic study, *Energy and Environmental Science*. 4 (2011) 2417–2427. doi:10.1039/c0ee00736f.

[50] P. Haquette, B. Talbi, S. Canaguier, S. Dagorne, C. Fosse, A. Martel, G. Jaouen, M. Salmain, Functionalized cationic ( $\eta^6$ -arene)ruthenium(II) complexes for site-specific and covalent anchoring to papain from papaya latex. Synthesis, X-ray structures and reactivity studies, *Tetrahedron Letters*. 49 (2008) 4670–4673. doi:10.1016/j.tetlet.2008.05.043.

[51] L. Vaccaro, V. Artero, S. Canaguier, M. Fontecave, M.J. Field, Mechanism of hydrogen evolution catalyzed by NiFe hydrogenases: Insights from a Ni-Ru model compound, *Dalton Transactions*. 39 (2010) 3043–3049. doi:10.1039/b912690b.

[52] A.D. McNaught, A.D. McNaught, *Compendium of chemical terminology*, Blackwell Science Oxford, 1997.

[53] K. Kalyanasundaram, M. Grätzel, *Photosensitization and photocatalysis using inorganic and organometallic compounds*, Springer Science & Business Media, 2013.

[54] M. Chanon, *Homogeneous photocatalysis*, Wiley, 1997.

[55] T.M. McCormick, Z. Han, D.J. Weinberg, W.W. Brennessel, P.L. Holland, R. Eisenberg, Impact of Ligand Exchange in Hydrogen Production from Cobaloxime-Containing Photocatalytic Systems, *Inorg. Chem.* 50 (2011) 10660–10666. doi:10.1021/ic2010166.

[56] Z. Han, L. Shen, W.W. Brennessel, P.L. Holland, R. Eisenberg, Nickel Pyridinethiolate Complexes as Catalysts for the Light-Driven Production of Hydrogen from Aqueous Solutions in Noble-Metal-Free Systems, *J. Am. Chem. Soc.* 135 (2013) 14659–14669. doi:10.1021/ja405257s.

- [57] C. Kefalidi, E. Koutsouri, L. Marchiò, A. Zarkadoulas, S. Efstathiadou, C.A. Mitsopoulou, Synthesis, characterization and crystal structure of rhenium (I) tricarbonyl diimine complexes coupled with their efficiency in producing hydrogen in a photocatalytic system, *Polyhedron*. 110 (2016) 157–164.
- [58] A. Fihri, V. Artero, A. Pereira, M. Fontecave, Efficient H<sub>2</sub>-producing photocatalytic systems based on cyclometalated iridium- and tricarbonylrhenium-diimine photosensitizers and cobaloxime catalysts, *Dalton Trans.* (2008) 5567–5569. doi:10.1039/B812605B.
- [59] W.R. McNamara, Z. Han, P.J. Alperin, W.W. Brennessel, P.L. Holland, R. Eisenberg, A Cobalt–Dithiolene Complex for the Photocatalytic and Electrocatalytic Reduction of Protons, *J. Am. Chem. Soc.* 133 (2011) 15368–15371. doi:10.1021/ja207842r.
- [60] R.S. Khnayzer, C.E. McCusker, B.S. Olaiya, F.N. Castellano, Robust Cuprous Phenanthroline Sensitizer for Solar Hydrogen Photocatalysis, *J. Am. Chem. Soc.* 135 (2013) 14068–14070. doi:10.1021/ja407816f.
- [61] M.K. Panda, K. Ladomenou, A.G. Coutsolelos, Porphyrins in bio-inspired transformations: Light-harvesting to solar cell, *Coordination Chemistry Reviews*. 256 (2012) 2601–2627. doi:10.1016/j.ccr.2012.04.041.
- [62] J.L. Dempsey, B.S. Brunshwig, J.R. Winkler, H.B. Gray, Hydrogen Evolution Catalyzed by Cobaloximes, *Acc. Chem. Res.* 42 (2009) 1995–2004. doi:10.1021/ar900253e.
- [63] W.T. Eckenhoff, W.R. McNamara, P. Du, R. Eisenberg, Cobalt complexes as artificial hydrogenases for the reductive side of water splitting, *Biochimica et Biophysica Acta (BBA) - Bioenergetics*. 1827 (2013) 958–973. doi:10.1016/j.bbabi.2013.05.003.
- [64] A. Mahammed, B. Mondal, A. Rana, A. Dey, Z. Gross, The cobalt corrole catalyzed hydrogen evolution reaction: surprising electronic effects and characterization of key reaction intermediates, *Chem. Commun.* 50 (2014) 2725–2727. doi:10.1039/C3CC48462A.
- [65] D.W. Wakerley, M.A. Gross, E. Reisner, Proton reduction by molecular catalysts in water under demanding atmospheres, *Chem. Commun.* 50 (2014) 15995–

15998. doi:10.1039/C4CC06159D.

[66] C.S. Letko, J.A. Panetier, M. Head-Gordon, T.D. Tilley, Mechanism of the Electrocatalytic Reduction of Protons with Diaryldithiolene Cobalt Complexes, *J. Am. Chem. Soc.* 136 (2014) 9364–9376. doi:10.1021/ja5019755.

[67] A. Zarkadoulas, E. Koutsouri, C.A. Mitsopoulou, A perspective on solar energy conversion and water photosplitting by dithiolene complexes, *Coordination Chemistry Reviews*. 256 (2012) 2424–2434.

[68] A. Zarkadoulas, M.J. Field, C. Papatriantafyllopoulou, J. Fize, V. Artero, C.A. Mitsopoulou, Experimental and Theoretical Insight into Electrocatalytic Hydrogen Evolution with Nickel Bis (aryldithiolene) Complexes as Catalysts, *Inorganic Chemistry*. 55 (2016) 432–444.

[69] A. Zarkadoulas, M.J. Field, V. Artero, C.A. Mitsopoulou, Proton-Reduction Reaction Catalyzed by Homoleptic Nickel–bis-1,2-dithiolate Complexes: Experimental and Theoretical Mechanistic Investigations, *ChemCatChem*. 9 (2017) 2308–2317. doi:10.1002/cctc.201601399.

[70] E. Koutsouri, C.A. Mitsopoulou, Photocatalytic Hydrogen Evolution by tris-dithiolene tungsten complexes, *Open Chemistry*. 14 (2016) 393–403.

[71] Y. Pellegrin, F. Odobel, Sacrificial electron donor reagents for solar fuel production, *Comptes Rendus Chimie*. 20 (2017) 283–295. doi:10.1016/j.crci.2015.11.026.

[72] B. Probst, A. Rodenberg, M. Guttentag, P. Hamm, R. Alberto, A Highly Stable Rhenium–Cobalt System for Photocatalytic H<sub>2</sub> Production: Unraveling the Performance-Limiting Steps, *Inorg. Chem.* 49 (2010) 6453–6460. doi:10.1021/ic100036v.

[73] E. Hontzopoulos, J. Knostantatos, E. Vrachnou-Astra, D. Katakis, Homogeneous catalytic action of a nickel dithiolene complex, leading to dihydrogen formation from N,N'-dimethyl-4,4'-dipyridinium radical ion solutions, *Journal of Molecular Catalysis*. 31 (1985) 327–333. doi:10.1016/0304-5102(85)85115-4.

[74] E. Hontzopoulos, E. Vrachnou-Astra, J. Konstantatos, D. Katakis, A new photosensitizer-catalyst for the photochemical cleavage of water, *Journal of Photochemistry*. 30 (1985) 117–120. doi:10.1016/0047-2670(85)87010-6.

- [75] C. Mitsopoulou, J. Konstantatos, D. Katakis, E. Vrachnou, Dithiolenes: A cheap alternative to platinum for catalytic dihydrogen formation. The case of tris-[1-(4-methoxyphenyl)-2-phenyl-1,2-ethylenedithiolenic-S,S'] tungsten, *Journal of Molecular Catalysis*. 67 (1991) 137–146. doi:10.1016/0304-5102(91)85041-Y.
- [76] W.T. Eckenhoff, W.W. Brennessel, R. Eisenberg, Light-Driven Hydrogen Production from Aqueous Protons using Molybdenum Catalysts, *Inorg. Chem.* 53 (2014) 9860–9869. doi:10.1021/ic501440a.
- [77] A. Das, Z. Han, W.W. Brennessel, P.L. Holland, R. Eisenberg, Nickel Complexes for Robust Light-Driven and Electrocatalytic Hydrogen Production from Water, *ACS Catal.* 5 (2015) 1397–1406. doi:10.1021/acscatal.5b00045.
- [78] H. Lv, T.P.A. Ruberu, V.E. Fleischauer, W.W. Brennessel, M.L. Neidig, R. Eisenberg, Catalytic Light-Driven Generation of Hydrogen from Water by Iron Dithiolene Complexes, *J. Am. Chem. Soc.* 138 (2016) 11654–11663. doi:10.1021/jacs.6b05040.
- [79] H. Rao, Z.-Y. Wang, H.-Q. Zheng, X.-B. Wang, C.-M. Pan, Y.-T. Fan, H.-W. Hou, Photocatalytic hydrogen evolution from a cobalt/nickel complex with dithiolene ligands under irradiation with visible light, *Catal. Sci. Technol.* 5 (2015) 2332–2339. doi:10.1039/C4CY01574F.
- [80] K. Ladomenou, M. Natali, E. Iengo, G. Charalampidis, F. Scandola, A.G. Coutsolelos, Photochemical hydrogen generation with porphyrin-based systems, *Coordination Chemistry Reviews*. 304 (2015) 38–54. doi:10.1016/j.ccr.2014.10.001.
- [81] G. Landrou, A.A. Panagiotopoulos, K. Ladomenou, A.G. Coutsolelos, Photochemical hydrogen evolution using Sn-porphyrin as photosensitizer and a series of Cobaloximes as catalysts, *J. Porphyrins Phthalocyanines*. 20 (2016) 534–541. doi:10.1142/S1088424616500243.
- [82] A.A. Panagiotopoulos, E.G. Fasoulakis, E.E. Vardalachaki, A.G. Coutsolelos, Photocatalytic hydrogen production based on a water-soluble porphyrin derivative as sensitizer and a series of Wilkinson type complexes as catalysts, *J. Porphyrins Phthalocyanines*. 20 (2016) 1200–1206. doi:10.1142/S1088424616500905.
- [83] T. Lazarides, M. Delor, I.V. Sazanovich, T.M. McCormick, I. Georgakaki, G. Charalambidis, J.A. Weinstein, A.G. Coutsolelos, Photocatalytic hydrogen production

from a noble metal free system based on a water soluble porphyrin derivative and a cobaloxime catalyst, *Chem. Commun.* 50 (2014) 521–523. doi:10.1039/C3CC45025B.

[84] X. Li, M. Wang, S. Zhang, J. Pan, Y. Na, J. Liu, B. Åkermark, L. Sun, Noncovalent Assembly of a Metalloporphyrin and an Iron Hydrogenase Active-Site Model: Photo-Induced Electron Transfer and Hydrogen Generation, *J. Phys. Chem. B.* 112 (2008) 8198–8202. doi:10.1021/jp710498v.

[85] L.-C. Song, L.-X. Wang, M.-Y. Tang, C.-G. Li, H.-B. Song, Q.-M. Hu, Synthesis, Structure, and Photoinduced Catalysis of [FeFe]-Hydrogenase Active Site Models Covalently Linked to a Porphyrin or Metalloporphyrin Moiety, *Organometallics.* 28 (2009) 3834–3841. doi:10.1021/om900141x.

[86] P. Poddutoori, D.T. Co, A.P.S. Samuel, C.H. Kim, M.T. Vagnini, M.R. Wasielewski, Photoinitiated multistep charge separation in ferrocene-zinc porphyrin-iron hydrogenase model complex triads, *Energy Environ. Sci.* 4 (2011) 2441–2450. doi:10.1039/C1EE01334C.

[87] A.M. Kluwer, R. Kapre, F. Hartl, M. Lutz, A.L. Spek, A.M. Brouwer, P.W.N.M. van Leeuwen, J.N.H. Reek, Self-assembled biomimetic [2Fe2S]-hydrogenase-based photocatalyst for molecular hydrogen evolution, *Proceedings of the National Academy of Sciences.* 106 (2009) 10460–10465.

[88] P. Zhang, M. Wang, C. Li, X. Li, J. Dong, L. Sun, Photochemical H<sub>2</sub> production with noble-metal-free molecular devices comprising a porphyrin photosensitizer and a cobaloxime catalyst, *Chem. Commun.* 46 (2010) 8806–8808. doi:10.1039/C0CC03154B.

[89] P. Zhang, M. Wang, X. Li, H. Cui, J. Dong, L. Sun, Photochemical hydrogen production with molecular devices comprising a zinc porphyrin and a cobaloxime catalyst, *Science China Chemistry.* 55 (2012) 1274–1282. doi:10.1007/s11426-012-4514-0.

[90] K. Peuntinger, T. Lazarides, D. Dafnomili, G. Charalambidis, G. Landrou, A. Kahnt, R.P. Sabatini, D.W. McCamant, D.T. Gryko, A.G. Coutsolelos, D.M. Guldi, Photoinduced Charge Transfer in Porphyrin–Cobaloxime and Corrole–Cobaloxime Hybrids, *J. Phys. Chem. C.* 117 (2013) 1647–1655. doi:10.1021/jp311766s.

- [91] J.C. Manton, C. Long, J.G. Vos, M.T. Pryce, Porphyrin-cobaloxime complexes for hydrogen production, a photo- and electrochemical study, coupled with quantum chemical calculations, *Dalton Trans.* 43 (2014) 3576–3583. doi:10.1039/C3DT53166J.
- [92] M. Natali, M. Orlandi, C. Chiorboli, E. Iengo, V. Bertolasi, F. Scandola, Porphyrin-cobaloxime dyads for photoinduced hydrogen production: investigation of the primary photochemical process, *Photochem. Photobiol. Sci.* 12 (2013) 1749–1753. doi:10.1039/C3PP50184A.
- [93] M. Natali, R. Argazzi, C. Chiorboli, E. Iengo, F. Scandola, Photocatalytic Hydrogen Evolution with a Self-Assembling Reductant–Sensitizer–Catalyst System, *Chem. Eur. J.* 19 (2013) 9261–9271. doi:10.1002/chem.201300133.
- [94] J.-M. Savéant, *Elements of molecular and biomolecular electrochemistry: an electrochemical approach to electron transfer chemistry*, John Wiley & Sons, 2006.
- [95] A.J. Bard, Inner-Sphere Heterogeneous Electrode Reactions. Electrocatalysis and Photocatalysis: The Challenge, *J. Am. Chem. Soc.* 132 (2010) 7559–7567. doi:10.1021/ja101578m.
- [96] K. Izutsu, *Electrochemistry in nonaqueous solutions*, John Wiley & Sons, 2009.
- [97] V. Fourmond, P.-A. Jacques, M. Fontecave, V. Artero, H<sub>2</sub> Evolution and Molecular Electrocatalysts: Determination of Overpotentials and Effect of Homoconjugation, *Inorg. Chem.* 49 (2010) 10338–10347. doi:10.1021/ic101187v.
- [98] A. Begum, G. Moula, S. Sarkar, A Nickel(II)–Sulfur-Based Radical-Ligand Complex as a Functional Model of Hydrogenase, *Chem. Eur. J.* 16 (2010) 12324–12327. doi:10.1002/chem.201001812.
- [99] A. Begum, S. Sarkar, An Iron(III) Dithiolene Complex as a Functional Model of Iron Hydrogenase, *Eur. J. Inorg. Chem.* 2012 (2012) 40–43. doi:10.1002/ejic.201100879.
- [100] L. Gan, T.L. Groy, P. Tarakeshwar, S.K.S. Mazinani, J. Shearer, V. Mujica, A.K. Jones, A Nickel Phosphine Complex as a Fast and Efficient Hydrogen Production Catalyst, *J. Am. Chem. Soc.* 137 (2015) 1109–1115. doi:10.1021/ja509779q.

- [101] A. Kochem, T. Weyhermüller, F. Neese, M. van Gastel, EPR and Quantum Chemical Investigation of a Bioinspired Hydrogenase Model with a Redox-Active Ligand in the First Coordination Sphere, *Organometallics*. 34 (2015) 995–1000. doi:10.1021/acs.organomet.5b00039.
- [102] J.-P. Porcher, T. Fogeron, M. Gomez-Mingot, E. Derat, L.-M. Chamoreau, Y. Li, M. Fontecave, A Bioinspired Molybdenum Complex as a Catalyst for the Photo- and Electroreduction of Protons, *Angew. Chem. Int. Ed.* 54 (2015) 14090–14093. doi:10.1002/anie.201505607.
- [103] K. Koshiba, K. Yamauchi, K. Sakai, A Nickel Dithiolate Water Reduction Catalyst Providing Ligand-Based Proton-Coupled Electron-Transfer Pathways, *Angew. Chem. Int. Ed.* 56 (2017) 4247–4251. doi:10.1002/anie.201700927.
- [104] M. Fang, M.H. Engelhard, Z. Zhu, M.L. Helm, J.A.S. Roberts, Electrodeposition from Acidic Solutions of Nickel Bis(benzenedithiolate) Produces a Hydrogen-Evolving Ni–S Film on Glassy Carbon, *ACS Catal.* 4 (2014) 90–98. doi:10.1021/cs400675u.
- [105] K.J. Lee, B.D. McCarthy, E.S. Rountree, J.L. Dempsey, Identification of an Electrode-Adsorbed Intermediate in the Catalytic Hydrogen Evolution Mechanism of a Cobalt Dithiolene Complex, *Inorganic Chemistry*. 56 (2017) 1988–1998. doi:10.1021/acs.inorgchem.6b02586.
- [106] A.J. Clough, J.W. Yoo, M.H. Mecklenburg, S.C. Marinescu, Two-Dimensional Metal–Organic Surfaces for Efficient Hydrogen Evolution from Water, *J. Am. Chem. Soc.* 137 (2015) 118–121. doi:10.1021/ja5116937.
- [107] C.A. Downes, S.C. Marinescu, One dimensional metal dithiolene (M = Ni, Fe, Zn) coordination polymers for the hydrogen evolution reaction, *Dalton Trans.* 45 (2016) 19311–19321. doi:10.1039/C6DT03257E.
- [108] S.C. Eady, S.L. Peczonczyk, S. Maldonado, N. Lehnert, Facile heterogenization of a cobalt catalyst via graphene adsorption: robust and versatile dihydrogen production systems, *Chem. Commun.* 50 (2014) 8065–8068. doi:10.1039/C4CC02920H.
- [109] S.C. Eady, M.M. MacInnes, N. Lehnert, A Smorgasbord of Carbon: Electrochemical Analysis of Cobalt–Bis(benzenedithiolate) Complex Adsorption and

Electrocatalytic Activity on Diverse Graphitic Supports, *ACS Appl. Mater. Interfaces*. 8 (2016) 23624–23634. doi:10.1021/acsami.6b05159.

[110] W.L. Armarego, Purification of laboratory chemicals, Butterworth-Heinemann, 2017.

[111] S. Cobo, J. Heidkamp, P.-A. Jacques, J. Fize, V. Fourmond, L. Guetaz, B. Jusselme, V. Ivanova, H. Dau, S. Palacin, M. Fontecave, V. Artero, A Janus cobalt-based catalytic material for electro-splitting of water, *Nat Mater*. 11 (2012) 802–807. doi:10.1038/nmat3385.

[112] Oxford Diffraction, CrysAlis CCD and CrysAlis RED. (2001).

[113] G.M. Sheldrick, Program for Crystal Structure Solution. (1997).

[114] L.J. Farrugia, WinGX suite for small-molecule single-crystal crystallography, *Journal of Applied Crystallography*. 32 (1999) 837–838.

[115] C.F. Macrae, I.J. Bruno, J.A. Chisholm, P.R. Edgington, P. McCabe, E. Pidcock, L. Rodriguez-Monge, R. Taylor, J. Van De Streek, P.A. Wood, Mercury CSD 2.0 - New features for the visualization and investigation of crystal structures, *Journal of Applied Crystallography*. 41 (2008) 466–470. doi:10.1107/S0021889807067908.

[116] F. Neese, The ORCA program system, *WIREs Comput Mol Sci*. 2 (2012) 73–78. doi:10.1002/wcms.81.

[117] S. Sinnecker, A. Rajendran, A. Klamt, M. Diedenhofen, F. Neese, Calculation of Solvent Shifts on Electronic  $g$ -Tensors with the Conductor-Like Screening Model (COSMO) and Its Self-Consistent Generalization to Real Solvents (Direct COSMO-RS), *J. Phys. Chem. A*. 110 (2006) 2235–2245. doi:10.1021/jp056016z.

[118] S.J. Konezny, M.D. Doherty, O.R. Luca, R.H. Crabtree, G.L. Soloveichik, V.S. Batista, Reduction of Systematic Uncertainty in DFT Redox Potentials of Transition-Metal Complexes, *J. Phys. Chem. C*. 116 (2012) 6349–6356. doi:10.1021/jp300485t.

[119] G. Sumrell, J.I. Stevens, G.E. Goheen, Benzoin Condensation of Anisaldehyde, *The Journal of Organic Chemistry*. 22 (1957) 39–41.

[120] T.-T. Bui, B. Garreau-de Bonneval, K.I. Moineau-Chane Ching, Synthesis and

preliminary physical properties of new neutral tetraalkoxy-substituted nickel bis(1,2-dithiolene) complexes, *New J. Chem.* 34 (2010) 337–347. doi:10.1039/B9NJ00519F.

[121] M.K. Johnson, *Vibrational Spectra of Dithiolene Complexes*, in: *Dithiolene Chemistry*, John Wiley & Sons, Inc., 2003: pp. 213–266. doi:10.1002/0471471933.ch4.

[122] C.W. Schlaepfer, K. Nakamoto, Infrared spectra and normal-coordinate analysis of 1,2-dithiolate complexes with nickel, *Inorg. Chem.* 14 (1975) 1338–1344. doi:10.1021/ic50148a028.

[123] M.L. Kirk, R.L. McNaughton, M.E. Helton, *The Electronic Structure and Spectroscopy of Metallo-Dithiolene Complexes*, in: *Dithiolene Chemistry*, John Wiley & Sons, Inc., 2003: pp. 111–212. doi:10.1002/0471471933.ch3.

[124] Q. Miao, J. Gao, Z. Wang, H. Yu, Y. Luo, T. Ma, Syntheses and characterization of several nickel bis(dithiolene) complexes with strong and broad Near-IR absorption, *Inorganica Chimica Acta.* 376 (2011) 619–627. doi:10.1016/j.ica.2011.07.046.

[125] G.N. Schrauzer, V.P. Mayweg, Coordination Compounds with Delocalized Ground States. Bisdithioglyoxalnickel and Related Complexes 1a,b, *J. Am. Chem. Soc.* 87 (1965) 3585–3592. doi:10.1021/ja01094a011.

[126] B. Garreau-de Bonneval, K.I. Moineau-Chane Ching, F. Alary, T.-T. Bui, L. Valade, Neutral d8 metal bis-dithiolene complexes: Synthesis, electronic properties and applications, *Coordination Chemistry Reviews.* 254 (2010) 1457–1467. doi:10.1016/j.ccr.2010.02.019.

[127] C.L. Beswick, J.M. Schulman, E.I. Stiefel, Structures and Structural Trends in Homoleptic Dithiolene Complexes, in: *Dithiolene Chemistry*, John Wiley & Sons, Inc., 2003: pp. 55–110. doi:10.1002/0471471933.ch2.

[128] R.K. Szilagyi, B.S. Lim, T. Glaser, R.H. Holm, B. Hedman, K.O. Hodgson, E.I. Solomon, Description of the Ground State Wave Functions of Ni Dithiolenes Using Sulfur K-edge X-ray Absorption Spectroscopy, *J. Am. Chem. Soc.* 125 (2003) 9158–9169. doi:10.1021/ja029806k.

[129] B.S. Lim, D.V. Fomitchev, R.H. Holm, Nickel Dithiolenes Revisited: Structures and Electron Distribution from Density Functional Theory for the Three-

Member Electron-Transfer Series  $[\text{Ni}(\text{S}_2\text{C}_2\text{Me}_2)_2]_{0,1,2}$ , *Inorg. Chem.* 40 (2001) 4257–4262. doi:10.1021/ic010138y.

[130] G.A. Bowmaker, P.D.W. Boyd, G.K. Campbell, Electrochemical and ESR studies of the redox reactions of nickel(II), palladium(II), and platinum(II) complexes of 1,2-diphenyl-1,2-ethenedithiolate(2-)-S,S', *Inorg. Chem.* 22 (1983) 1208–1213. doi:10.1021/ic00150a014.

[131] A. Davison, R.H. Holm, R.E. Benson, W. Mahler, Metal Complexes Derived from cis-1,2-dicyano-1,2-ethylenedithiolate and Bis(Trifluoromethyl)-1,2-dithiete, in: *Inorganic Syntheses*, John Wiley & Sons, Inc., 1967: pp. 8–26. doi:10.1002/9780470132418.ch3.

[132] A. Davison, J.A. McCleverty, E.T. Shawl, E.J. Wharton, Ligand-Exchange Reactions of Bis(cis-1,2-disubstituted ethylene-1,2-dithiolato)nickel Complexes, *J. Am. Chem. Soc.* 89 (1967) 830–832. doi:10.1021/ja00980a017.

[133] D. Sellmann, S. Funfgelder, G. Pohlmann, F. Knoch, M. Moll, Transition-metal complexes with sulfur ligands. 55. Nickel complexes with thiolato-thioether ligands including nitrogen and oxygen donors in S<sub>6</sub>, S<sub>5</sub>, OS<sub>4</sub>, NS<sub>4</sub>, and S<sub>4</sub> donor sets. Syntheses, properties, and x-ray structure determinations of  $[\text{Ni}(\text{S}_6^*)]$ ,  $[\text{Ni}(\text{S}_5^*)]$ ,  $[\text{Ni}(\text{OS}_4^*)]_2$ ,  $[\text{Ni}(\text{S}_4\text{-C}_5^*)]_2$ , and  $[\text{Ni}(\text{S}_4\text{-C}_3^*)]$ , *Inorg. Chem.* 29 (1990) 4772–4778. doi:10.1021/ic00348a036.

[134] C. Zhang, H.K. Reddy, R.K. Chadha, G.N. Schrauzer, Synthesis, Structures and Dynamic Properties of Trimethylene- And Tetramethylene-Bis(CIS-Stilbene-1,2-Dithiolato)Nickel(II), *Journal of Coordination Chemistry.* 26 (1992) 117–126. doi:10.1080/00958979209407920.

[135] K. Wang, Electrochemical and Chemical Reactivity of Dithiolene Complexes, in: *Dithiolene Chemistry*, John Wiley & Sons, Inc., 2003: pp. 267–314. doi:10.1002/0471471933.ch5.

[136] M.T.S. de Mello, M.C. Ribeiro, P.S. Santos, Resonance Raman spectroscopy of benzenedithiolate complexes: evidences of extensive delocalization of the chromophore, *Journal of Molecular Structure: THEOCHEM.* 372 (1995) 1–7. doi:10.1016/0166-1280(95)90646-0.

[137] D. Sellmann, D. Häussinger, F. Knoch, M. Moll, Transition Metal Complexes

with Sulfur Ligands. 117.1 A Reaction Cycle for Nickel Mediated Thioester Formation from Alkyl, CO, and Thiolate Groups Modeling the Acetyl-Coenzyme A Synthase Function of CO Dehydrogenase, *J. Am. Chem. Soc.* 118 (1996) 5368–5374. doi:10.1021/ja952598u.

[138] D. Sellmann, S. Fünfgelder, F. Knoch, M. Moll, Transition Metal Complexes with Sulfur Ligands, LXXVI Redox and Addition Reactions of Nickel Complexes with Multidentate Thioether-Thiolato Ligands. X-Ray Structure Determinations of  $(\text{NMe}_4)_2[\text{Ni}(\text{S}_2')_2]$  and  $[\text{Ni}(\text{S}_4 - \text{C}_3)(\text{PMe}_3)]$ , *Zeitschrift Fur Naturforschung - Section B Journal of Chemical Sciences.* 46 (1991) 1601–1608. doi:10.1515/znb-1991-1203.

[139] M. Cha, J. Sletten, S. Critchlow, J.A. Kovacs, Synthesis and structure of a thiolate-ligated Ni cluster which contains an unusual thiolate bridging mode and an exposed Ni site, *Inorganica Chimica Acta.* 263 (1997) 153–159. doi:10.1016/S0020-1693(97)05646-6.

[140] N. Robertson, S. Parsons, K. Awaga, W. Fujita, Structural characteristics of dithiolene and nitronyl nitroxide salts: a unique oxygenation?deoxygenation process, *CrystEngComm.* 2 (2000) 121–124. doi:10.1039/B004549G.

[141] A.D. Adler, F.R. Longo, J.D. Finarelli, J. Goldmacher, J. Assour, L. Korsakoff, A simplified synthesis for meso-tetraphenylporphine, *J. Org. Chem.* 32 (1967) 476–476. doi:10.1021/jo01288a053.

[142] B. Ventura, L. Flamigni, G. Marconi, F. Lodato, D.L. Officer, Extending the porphyrin core: synthesis and photophysical characterization of porphyrins with [small pi]-conjugated [small beta]-substituents, *New J. Chem.* 32 (2008) 166–178. doi:10.1039/B707505G.

[143] C. Makedonas, C.A. Mitsopoulou, An investigation of the reactivity of [(diimine)(dithiolato)M] complexes using the Fukui functions concept, *European Journal of Inorganic Chemistry.* (2006) 590–598. doi:10.1002/ejic.200500664.

[144] C. Costentin, G. Passard, M. Robert, J.-M. Saveant, Concertedness in proton-coupled electron transfer cleavages of carbon-metal bonds illustrated by the reduction of an alkyl cobalt porphyrin, *Chem. Sci.* 4 (2013) 819–823. doi:10.1039/C2SC21788K.

- [145] J.B. Allen, R.F. Larry, *Electrochemical methods: fundamentals and applications*, Department of Chemistry and Biochemistry University of Texas at Austin, John Wiley & Sons, Inc. (2001) 156–176.
- [146] B.D. McCarthy, C.L. Donley, J.L. Dempsey, Electrode initiated proton-coupled electron transfer to promote degradation of a nickel(II) coordination complex, *Chemical Science*. 6 (2015) 2827–2834. doi:10.1039/c5sc00476d.
- [147] T. Yamaguchi, S. Masaoka, K. Sakai, Hydrogen production from water catalyzed by an air-stable di-iron complex with a bio-relevant Fe<sub>2</sub>(μ-S)<sub>2</sub> core, *Chemistry Letters*. 38 (2009) 434–435. doi:10.1246/cl.2009.434.
- [148] C. Wombwell, E. Reisner, Synthesis, structure and reactivity of Ni site models of [NiFeSe] hydrogenases, *Dalton Trans.* 43 (2014) 4483–4493. doi:10.1039/C3DT52967C.
- [149] K. Kaupmees, I. Kaljurand, I. Leito, Influence of Water Content on the Acidities in Acetonitrile. Quantifying Charge Delocalization in Anions, *J. Phys. Chem. A*. 114 (2010) 11788–11793. doi:10.1021/jp105670t.
- [150] B.D. McCarthy, D.J. Martin, E.S. Rountree, A.C. Ullman, J.L. Dempsey, Electrochemical Reduction of Brønsted Acids by Glassy Carbon in Acetonitrile—Implications for Electrocatalytic Hydrogen Evolution, *Inorg. Chem.* 53 (2014) 8350–8361. doi:10.1021/ic500770k.
- [151] C.A. Downes, S.C. Marinescu, Efficient Electrochemical and Photoelectrochemical H<sub>2</sub> Production from Water by a Cobalt Dithiolene One-Dimensional Metal–Organic Surface, *J. Am. Chem. Soc.* 137 (2015) 13740–13743. doi:10.1021/jacs.5b07020.
- [152] A.V. Marenich, J. Ho, M.L. Coote, C.J. Cramer, D.G. Truhlar, Computational electrochemistry: prediction of liquid-phase reduction potentials, *Phys. Chem. Chem. Phys.* 16 (2014) 15068–15106. doi:10.1039/C4CP01572J.
- [153] B.H. Solis, S. Hammes-Schiffer, Computational Study of Anomalous Reduction Potentials for Hydrogen Evolution Catalyzed by Cobalt Dithiolene Complexes, *J. Am. Chem. Soc.* 134 (2012) 15253–15256. doi:10.1021/ja306857q.
- [154] D. Argyropoulos, C.-A. Mitsopoulou, D. Katakis, Stereochemical Nonrigidity and Geometrical Isomerism in Six-Coordinate Trigonal Prismatic Complexes: The

Case of Asymmetric Molybdenum and Tungsten Tris(dithiolenes), *Inorganic Chemistry*. 35 (1996) 5549–5554.

[155] J. Kamenicek, F. Valach, B. Kratochvíl, Z. Zak, Syntheses and structure of Ni (III) complexes with 1-toluene-3, 4-dithiole. Bond-valence approach to the oxidation state of the central atom, *Polish Journal of Chemistry*. 76 (2002) 483–490.

[156] J. Ochocki, P. Chaudhuri, W.L. Driessen, R.A.G. De Graaf, F.B. Hulsbergen, J. Reedijk, Synthesis, spectroscopy and magnetism of mixed-valence Ni(II)–Ni(III) compounds with (benz)imidazolethioether, acetates and dithiolates as ligands. Crystal structure of (acetato)(1,6-bis(benzimidazol-2-yl)-2,5-dithiahexane)nickel(II) bis(toluen-3,4-dithiolato)niccolate(III), *Inorganica Chimica Acta*. 167 (1990) 15–20. doi:10.1016/S0020-1693(00)83932-8.

[157] R.E. Marsh, Space group Cc: an update, *Acta Cryst. B*. 60 (2004) 252–253. doi:10.1107/S0108768104003878.

[158] A.L. Rheingold, K.S. Beall, P.J. Riggs, S.E. Groh, Bis(tetraethylammonium) nickel tetrakis thiophenolate: a new polymorph, *Acta Crystallographica Section C*. 49 (1993) 542–543. doi:10.1107/S0108270192007704.

[159] A. Bhattacharjee, E.S. Andreiadis, M. Chavarot-Kerlidou, M. Fontecave, M.J. Field, V. Artero, A Computational Study of the Mechanism of Hydrogen Evolution by Cobalt(Diimine-Dioxime) Catalysts, *Chem. Eur. J.* 19 (2013) 15166–15174. doi:10.1002/chem.201301860.

[160] E.J. Sundstrom, X. Yang, V.S. Thoi, H.I. Karunadasa, C.J. Chang, J.R. Long, M. Head-Gordon, Computational and Experimental Study of the Mechanism of Hydrogen Generation from Water by a Molecular Molybdenum-Oxo Electrocatalyst, *J. Am. Chem. Soc.* 134 (2012) 5233–5242. doi:10.1021/ja210949r.

[161] B.H. Solis, A.G. Maher, T. Honda, D.C. Powers, D.G. Nocera, S. Hammes-Schiffer, Theoretical Analysis of Cobalt Hangman Porphyrins: Ligand Dearomatization and Mechanistic Implications for Hydrogen Evolution, *ACS Catal.* 4 (2014) 4516–4526. doi:10.1021/cs501454y.

[162] L. Ridder, A.J. Mulholland, J. Vervoort, I.M.C.M. Rietjens, Correlation of Calculated Activation Energies with Experimental Rate Constants for an Enzyme Catalyzed Aromatic Hydroxylation, *J. Am. Chem. Soc.* 120 (1998) 7641–7642.

doi:10.1021/ja980639r.

[163] A. Bhattacharjee, A.K.H. Weiss, V. Artero, M.J. Field, T.S. Hofer, Electronic Structure and Hydration of Tetramine Cobalt Hydride Complexes, *J. Phys. Chem. B.* 118 (2014) 5551–5561. doi:10.1021/jp502651s.

[164] M. Cha, S.C. Shoner, J.A. Kovacs, Nickel-promoted reductive carbon-sulfur bond cleavage: a model for the first step in the reaction promoted by methyl coenzyme M reductase, *Inorg. Chem.* 32 (1993) 1860–1863. doi:10.1021/ic00061a052.

[165] J.R. Lakowicz, *Principles of Fluorescence Spectroscopy*, Springer US, 2007. <https://books.google.gr/books?id=-PSybuLNxcAC>.

[166] G.M. Shkolnik, W.E. Geiger, Molecular charge-transfer complexes of metalloporphyrins with bis(cis-1,2-trifluoromethylethylene-1,2-dithiolato)nickel, *Inorg. Chem.* 14 (1975) 313–317. doi:10.1021/ic50144a021.

